Solar fuels production by CO2 and H2O splitting via thermochemical processes

Anita Haeussler

THÈSE

Pour obtenir le grade de

Docteur

Délivré par

UNIVERSITE DE PERPIGNAN VIA DOMITIA

Préparée au sein de l'école doctorale
Énergie et Environnement ED 305

Et de l'unité de recherche
PROMES-CNRS UPR 8521

Spécialité :
Sciences de l'ingénieur

Présentée par
Anita Haeussler

Solar fuels production by CO_2 and H_2O splitting via thermochemical processes

Soutenue le 05/03/2021 devant le jury composé de

M. Pierre-Marie GEFFROY, DR-CNRS, CEC, Limoges	Rapporteur
M. François VALDIVIESO, Pr, Mines de Saint-Etienne	Rapporteur
M. André AYRAL, Pr, IEM (Pr. UM, IEM), Montpellier	Examinateur
M. Fernando COSTA OLIVEIRA, DR, LNEG, Lisbonne, Portugal	Examinateur
M. David FARRUSSENG, DR-CNRS, IRCELYON, Villeurbanne	Président du jury
Me. Anne JULBE, DR-CNRS, IEM, Montpellier	Co-directeur de thèse
M. Stéphane ABANADES, DR-CNRS, PROMES, Odeillo	Directeur de thèse

Solar fuels production by CO_2 and H_2O splitting via thermochemical processes

Acknowledgements

Cette thèse n'aurait pas été possible sans le soutien de nombreuses personnes, que je tenais à remercier, en espérant ne pas en oublier.

Premièrement, j'aimerais remercier Stéphane Abanades pour m'avoir donné l'opportunité de réaliser cette thèse sous sa direction. Ses précieux conseils et sa grande disponibilité ont été essentiels au succès de ce travail. J'adresse aussi mes remerciements à Anne Julbe pour avoir contribué à superviser cette thèse ainsi que pour ses relectures consciencieuses.

Je souhaitais remercier toutes les personnes qui ont eu un rôle actif dans le projet SUNFUEL : Stéphane Abanades, André Ayral, Anne Julbe, Christophe Charmette, Julien Jouannaux, Martin Drobek, Jade Valls, Adrien Serve et Bruno Cartoixa.

Je tenais aussi à remercier Roger Garcia, Emmanuel Guillot, Nicolas Boullet et Eric Bêche du laboratoire PROMES pour leur soutien technique durant cette thèse.

Un grand merci à Jean Pascal Pernel et Didier Rives pour avoir cuisiné des plats tous plus délicieux les uns que les autres (à l'exception des endives braisées). Il ne serait pas ici possible de nommer tout le monde, mais je souhaiterais remercier toutes les bonnes fées du laboratoire PROMES, qui par leur gentillesse et leur dévouement ont contribué à rendre mon séjour en Cerdagne des plus agréables.

Mon expérience au laboratoire n'aurait pas été la même sans : Alex, Alexis, Axel, Charlène, Chuan, Clémence, Damien, Dounia, Gabi, Hadrien, Inma, Johann, José, Lester, Magali, Paul, P-H, Ségolène, Srirat, Thibaut et Timothée. Merci à vous pour tous les moments extraordinaires que nous avons partagés ensemble et d'avoir supporté mes blagues plus ou moins drôles.

Merci à toi.

Enfin et surtout, je voudrais témoigner toute ma gratitude à ma famille pour leur soutien sans faille, même à l'autre bout de la France. Cette thèse n'aurait pas pu avoir lieu sans vous, ce travail vous ait dédié.

A toi Mamy qui a attendu que ce travail soit achevé pour t'envoler.

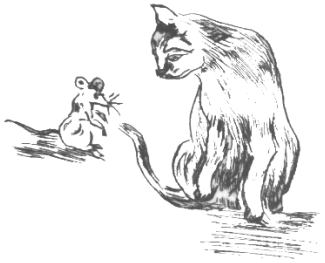

Table of content

Nomenclature

Latin letters

A	Kinetic parameter, preexponential factor
E_a	Kinetic parameter, activation energy (J/mol)
E_α	Kinetic parameter, activation energy for a fix conversion extent (J/mol)
ΔH_i	Enthalpy variation of the reaction i (kJ/mol)
HHV_i	High heating value of the specie i (J/mol)
ΔG_i	Standard Gibbs free energy variation of the reaction i (kJ/mol)
K_i	Constant of the reaction i
p_i	Partial pressure of the specie i (Pa, bar)
P	Pressure (Pa, bar)
$P°$	Standard pressure (Pa, bar)
R	Universal constant gas (J/mol/K)
ΔS	Entropy variation (J/mol/K/)
T	Temperature (°C, K)
ΔT	Temperature swing (°C, K)

Greek letters

α	Extent of conversion
δ	Oxygen non-stoichiometry extent

Abbreviations

CDS	Carbon dioxide splitting
CSP	Concentrated solar power
DNI	Direct normal irradiation
EDS	Energy-dispersive spectroscopy
FESEM	Field emission scanning electron microscopy
PV	Photovoltaic
RPC	Reticulated porous ceramic
SEM	Scanning electron microscopy
SSA	Specific surface area
TGA	Thermogravimetric analysis
TR	Thermal reduction
WS	Water splitting
XRD	X-ray diffraction
CDS	Carbon dioxide splitting
CSP	Concentrated solar power

List of figures

List of tables

Introduction

The climate change and global warming due to fossil fuels utilization for energy production is one of the most important problems facing the humanity. To overpass this issue, the scientific community has drawn attention to the necessity to reduce greenhouse gas emissions. Thus, the carbon-free economy should be developed, in particular with a drastic decrease of the CO_2 emission in the energy sector. Indeed, the worldwide energy production is mainly based on fossil fuel combustion which induces issues associated with the limited fossil fuel resources and the produced greenhouse gas emissions due to the combustion process. Several studies have focused on the CO_2 capture and sequestration (CCS); however, this technology is only implementable for centralized CO_2 emitters, but not for diffuse emissions such as those of the transportation sector, impeding to drastically reduce the global CO_2 emissions in the atmosphere. Beside of that, it appears more convenient to directly use renewable fuels to reach a carbon-free economy. Di-hydrogen appears as very interesting energy vector as its conversion only produces water. In addition, hydrogen is one of the most abundant elements on earth, however it only exists combined with other atoms such as carbon (e.g. hydrocarbons) or oxygen (e.g. water). Therefore, di-hydrogen can be produced from a variety of sources (water, fossil fuels or biomass). Hereafter, "di-hydrogen" is designated by "hydrogen" for simplification. Nowadays, H_2 production is mainly based on the utilization of fossil fuels (such as methane reforming or partial oxidation) or, to a lesser extent, non-decarbonized or nuclear electricity (electrolysis). Therefore, sustainable H_2 production pathways are worth investigating. The simplest way to produce hydrogen from a decarbonized feedstock without greenhouse gas emissions is water dissociation into hydrogen and oxygen. As hydrogen is only an energy carrier, its production requires an input of energy, which should be as well sustainable to satisfy the production of green H_2. In this aim, solar energy is especially attractive because its utilization does not imply any CO_2 emissions, its source is not limited and it is available everywhere on earth, however being intermittent, diffuse and unevenly distributed. Therefore, the conversion of solar energy into chemical energy via the production of solar fuels permits to alleviate intermittent issues through long-term solar energy storage into dispatchable chemical fuels. Indeed, solar fuels can be stored easily, transported over long distances and used on demand.

Thermochemical processes coupling H_2O dissociation with concentrated solar power (CSP) systems appear as a promising solution to produce sustainable H_2. Similarly, such processes are also able to dissociate CO_2, thus up grading CO_2 to CO and forming syngas when combined with H_2, which can yield hydrocarbon fuels via Fischer-Tropsch process. The process based on thermochemical redox cycles is composed of two reactions, involving a metal oxide acting as reaction intermediate that is recycled. First, a thermal reduction of the metal oxide at high temperature is performed, resulting in the production of O_2. This reaction is thermally activated by the concentrated solar heat supplied to the system. Secondly, the reduced form of the metal oxide is re-oxidized by H_2O or CO_2, leading to the production of H_2 or CO in an exothermic reaction. The only inputs in the thermochemical process are the abundant and low-cost

feedstock (H_2O or CO_2) and solar heat, making it a carbon-neutral process. The thermochemical H_2O or CO_2 splitting processes offer high theoretical efficiency and do not require electricity utilization. Therefore, they could be an ideal long-term pathway to decarbonize worldwide energy production. Nowadays, technological locks still need to be overcome before considering any large scale application for hydrogen or syngas production using solar thermochemical processes. The major challenge is to develop reliable thermochemical processes with high and stable fuel production along with fast reaction rates, meeting industrial requirements.

This PhD thesis was part of SUNFUEL project (N°ANR-16-CE06-0010) supported by the French National Research Agency. This project aims to develop solar thermochemical conversion of H_2O and CO_2 for the production of high-value solar fuels, using non-stoichiometric metal oxides as chemical intermediates. Together with the PROMES-CNRS laboratory (project coordinator), where this thesis has been realized, the Institut Européen Membranes (IEM) and the ALSYS-CTI company were involved as project partners in the SUNFUEL project. Another PhD at IEM was devoted to the preparation and characterization of coated porous materials and membranes for fuels production. The project tasks include:

(i) the evaluation of perovskite and ceria materials potential for thermochemical cycles via a study of their redox activity, in order to select the best redox materials to be integrated in a solar reactor;

(ii) the synthesis and shaping of the reactive materials as porous structures and dense membranes;

(iii) the design and construction of scalable and flexible reactor prototypes based on two different concepts and operation modes:

- monolithic configuration with temperature-swing redox cycling
- membrane configuration with mixed ionic-electronic conducting membrane for isothermal and continuous operation.

The key objective of the project was to demonstrate the H_2O and CO_2 splitting process using the two configurations during on-sun operation of the solar reactors and to compare their performance. The company ALSYS-CTI was in charge of providing the reactive materials as cylindrical foams and tubular membranes, whereas IEM laboratory was responsible for the development of perovskite thin layers and dense membranes, materials characterization, optimization of their properties and investigation of the oxygen mobility mechanisms involved in densified membranes. The evaluation of the thermochemical performance of the redox materials, integrated within the developed solar reactors, was realized by PROMES-CNRS laboratory.

This thesis manuscript focuses on the investigation and optimization of solar fuels production by H_2O and CO_2 splitting reactions using non-stoichiometric redox materials as oxygen carriers. The different key research areas involved in thermochemical processes were investigated including: the chemical composition and the microstructure/morphology of the oxygen carrier,

the reactor design and the operating parameters controlling the solar process performance as a function of the process configuration (temperature-swing redox cycling versus isothermal thermolysis via oxygen-conducting membrane).

The first chapter presents the different pathways for solar fuels production using solar energy with their advantages and drawbacks. Then a state of the art of thermochemical cycles using non-stoichiometric oxides is detailed including thermodynamics, chemical composition and morphology of the reactive redox materials (based on ceria and perovskites), and solar reactor technologies developed to perform thermochemical cycles.

The second chapter focusses on the evaluation and the selection of suitable non-stoichiometric metal oxides for thermochemical cycles. The redox activities of different perovskite materials are experimentally investigated. Thermodynamic and kinetic studies are also performed to provide a better understanding of the mechanisms involved in the thermochemical cycles.

Then a detailed parametric study of the monolithic configuration of the solar reactor integrating the shaped redox material undergoing two-step thermochemical cycling (with alternation of redox steps) is presented in chapter 3. The thermochemical fuel production performance of reticulated porous ceramic structures in the form of ceria foams or additive-manufactured ordered porous structures are determined for both CO_2 and H_2O splitting. The effect of perovskite coating (dual-phase foams) or hierarchical porosity structures is also addressed (chapter 3).

In addition, the chapter 4 focuses on the experimental performance analysis of divided particulate materials made of ceria in packed-bed tubular or cavity-type solar reactors with either direct or indirect heating of the reacting materials. The fuel production rates and yields from CO_2 and H_2O dissociation are compared as a function of the shape of the microstructured ceria material (e.g., templated foams, sintered fibers, cork-templated granules, porous microspheres).

Finally, the chapter 5 demonstrates the feasibility of isothermal and continuous CO_2 (and H_2O) splitting using reactive redox ion-conducting membranes. Tubular dead-end membranes are used for *in-situ* separation of the reaction products via oxygen transfer through the membrane, from the oxidation side to the reduction side. A parametric study of the solar membrane reactor configuration is performed to investigate the relevant operating parameters impacting the thermochemical system performance. The experimental performance analysis of reactive uncoated and perovskite-coated ceria membranes is carried out to determine their fuel production capacity in the solar membrane reactor configuration.

A series of reactive ceria materials with different macro/microstructures has been considered, including cork-templated ceria, RPC foam, commercial fiber boards, commercial pellets and microspheres. The ceria fibers yielded the highest reduction extent (averaged oxygen nonstoichiometry up to $\delta \sim 0.055$), thereby leading to superior fuel production yield (above 300 μmol/g in the first cycle, but decreasing in next cycles). This was attributed to the low thermal conductivity of the material and high thermal gradient across its height. It was

demonstrated that, for these fibers, the surface directly irradiated by concentrated sunlight reached much higher temperatures than the target temperature (1400 °C). This was also confirmed by a thermogravimetric analysis, highlighting that both O_2 and CO production yields were compliant with the other ceria materials under the same conditions. Furthermore, the fuel yield declined during cycling because of sintering, denoting that this material is not suitable for achieving stable cycling performance. Noticeably, the cork-templated ceria, the ceria foam and ceria pellets offered a good resistance to sintering, with no performance decline over cycles and a complete re-oxidation (fuel production of ~130 µmol/g, for a reduction step at 1400 °C - atmospheric pressure, yielding δ~0.022-0.026). Biomimetic CTCe showed a higher fuel production rate compared to the other investigated materials, attributed to the favorable microstructure of the cork-derived ceramic. The morphology obtained from the cork structure led to improved redox activity, demonstrating the relevance of this material for thermochemical H_2O and CO_2 splitting cycles. Furthermore, two synthesis routes for ceria ecoceramic were investigated (multiple infiltration steps using water as solvent *vs* single infiltration step using acetone as solvent). The multiple infiltration route used water instead of acetone but required longer time and more energy than the single infiltration step route. The first method led to higher production yields (74 µmol/g of O_2 and 157 µmol/g H_2) with higher H_2 production rate (typically 1.4 mL/min/g) than the second method (63 µmol/g, 126 µmol/g and 1.1 mL/min/g, respectively). Due to the high flowability of CeMS microspheres that can escape from the cavity zone, the global fuel production rate based on the actual mass of CeMS material was somewhat low in comparison with other tested materials, despite its porous structure. The CeMS shape could be however adapted for fluidized bed reactors in order to favor the access of the oxidant gas to the reactive surface and thus favor the oxidation kinetic. Finally, it was demonstrated that commercial ceria pellets can be used as reactive material for thermochemical cycles since high fuel production rates were reached (up to 9.5 mL/min/g). This is advantageous for industrial implementation, as reactive materials should be commercially available at large scale in order to reduce fuel production costs.

Chapitre 1 - State of the art[1]

1.1 Introduction

One of the main challenges of this century is to limit the global warming caused by anthropic greenhouse gas emissions. The energy sector represents 68% of the greenhouse gas emissions, while CO_2 emissions due to fossil fuel combustion rose by 57.5% since 1990 [1]. Therefore, to reduce these emissions, the transition from fossil fuels to green energy production is essential. Solar energy is an interesting alternative to fossil fuels, as it is free, non-exhaustive and available everywhere on Earth. Furthermore, the solar energy reaching the Earth surface is superior to the energy demand and it does not yield greenhouse gas emissions. However, solar energy is not homogenously distributed on Earth surface and it is diffuse and intermittent, making its direct exploitation incompatible with energy demand. For this reason, conversion and storage of solar energy into chemical fuels is an attractive solution, as chemical fuels are transportable and available on demand.

1.2 Solar processes to generate solar fuels

In order to convert solar energy to solar fuels, numerous processes have been investigated and they can be classified according to the involved physico-chemical phenomena, as presented in Figure 1-1. All these processes lead to the production of H_2 or/and CO. Hydrogen can be directly used as a fuel (*e.g.*, in fuel cells), whereas syngas (mixture H_2/CO) can be used as feedstock to drive chemical reactions such as synthetic fuel production (via the Fischer–Tropsch process [2]) or methanol synthesis [3], etc...

[1] Most of the content of this chapter has been published in two peer-reviewed articles:

- A. Haeussler, S. Abanades, J. Jouannaux and A. Julbe. *Catalysts*, 2018, **8**, 611–631
- A. Haeussler, S. Abanades, J. Jouannaux, M. Drobek, A. Ayral and A. Julbe. *AIMS Mater Sci*, 2019, **6**, 657–684

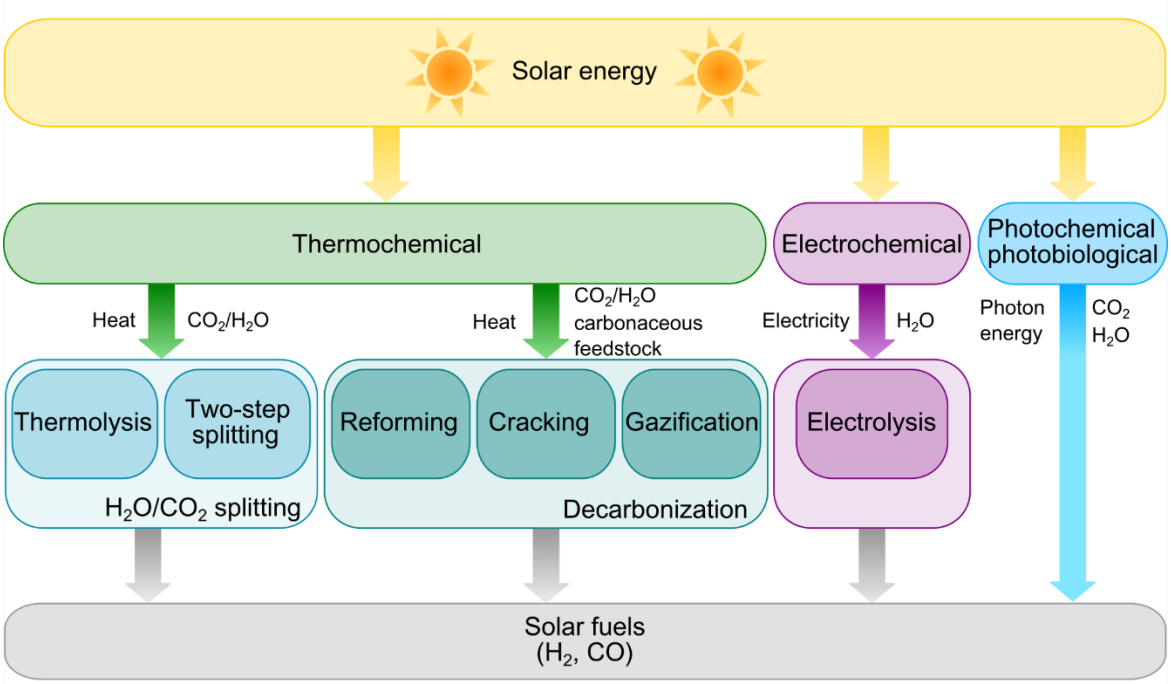

Figure 1-1: Solar thermochemical routes using solar energy for CO and H_2 production, adapted from [4]

1.2.1 Electrochemical processes

Solar electrochemical processes use electricity produced from solar energy (either photovoltaic (PV) panels or CSP (concentrated solar power) technology) to perform electrolysis, resulting in the production of H_2 by water splitting. Electrolysis has the advantage of being a simple process, producing high purity H_2 [5]. Notwithstanding, electrolysis process requires high amount of electricity per amount of H_2 produced [6], thus strongly limiting the global solar-to-hydrogen energy conversion efficiency.

1.2.1.1 Low temperature electrolyzers

Electrochemical water splitting bypasses high temperature limitations encountered in thermal H_2 production routes and avoids gas recombination issues thanks to separate generation of H_2 and O_2 at distinct electrodes. Low temperature electrolysis is typically carried out at temperatures in the range 20-100°C [7]. Different electrolyzer technologies exist and they are classified according to the operating temperature and the electrolyte material used. At low temperature, alkaline electrolysis [8], proton exchange membrane electrolysis [9] and anion exchange membrane electrolysis [10] are the main technologies developed. The electrolysis efficiency was estimated up to 73 % for alkaline technology [11]. The global warming potential of hydrogen produced by electrolysis mainly depends on the source used to provide electricity [12]. In the aim to decrease the environmental impact for H_2 production, the photovoltaic (PV) technology was coupled with electrolysis, namely PV-electrolysis. Therefore, it associates two single step processes: the PV panels produce electricity to supply electrolyzers and produce H_2 by water splitting. For H_2 produced by PV electrolysis, the global solar-to-H_2 efficiency is ~16%, and it mainly depends on the PV panel efficiency [11].

1.2.1.2 High temperature electrolyzers

The water splitting is an endothermic reaction, thus it requires an energy input, depending on the reaction enthalpy (ΔH_r). The reaction enthalpy can be decomposed in two parts as described by equation (1):

$$\Delta H_r = \Delta G_r + T\Delta S_r \quad (1)$$

where ΔG_r corresponds to the free energy of the reaction (*i.e.* the minimum share of ΔH_r which has to be applied as work) and $T\Delta S_r$ is the product of the reaction temperature and the reaction entropy (*i.e.* the share of energy provided by heat). The electricity required to perform water splitting is proportional to ΔG_r. Therefore, increasing the operating temperature permits to decrease the electricity input in the system, as presented in Figure 1-2 [13].

Increasing the temperature during electrolysis enhances the system performance. Therefore, coupling electricity and heat supply from solar energy improves the solar-to-fuel conversion efficiency. In high temperature electrolysis, solid oxide electrolyte is used to perform electrolysis in the temperature range 700-1000°C [14]. To achieve high temperatures in electrolysis, different strategies have been investigated: either heat the system with electricity from PV panels or Rankine cycle using CSP, or directly heat the gas with CSP [15]. High-temperature electrolysis thus appears to be an interesting solution for H_2 production in the long-term due to the high efficiency of water decomposition. It should be underlined that CO_2 splitting (typically coupled with H_2O splitting) is also possible with high temperature electrolysis. However, further investigations are required to enhance the durability and decrease the cost of the electrolysis cells [13]

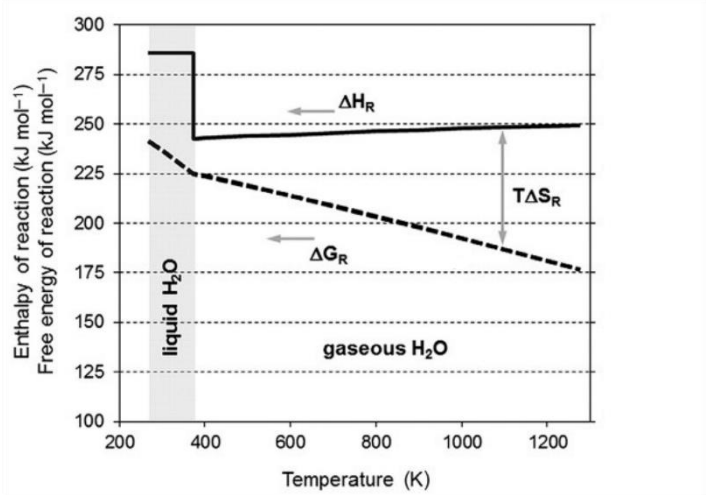

Figure 1-2: Evolution of enthalpy (ΔH) along with free energy of reaction (ΔG) as a function of the temperature for water splitting reaction [13]

1.2.2 Photochemical and photobiological processes

Photochemical and photobiological pathways use photon energy of the solar light to separate electrons and holes, namely charge separation, which is further used to drive chemical reactions. Indeed, photons present the advantage to be high-energy particles as they move at light speed. Therefore, they represent an important energy source.

1.2.2.1 Photobiological process

The photobiological route converts solar energy into fuels, using microorganisms. With the solar energy, the microorganisms proceed like synthetic photosynthesis, resulting in fuel production [16]. The photobiological research field is still in the phase of fundamental research and further development is required to offer a viable pathway for solar fuels production. The solar-to-hydrogen energy conversion efficiency achieved by the photobiological route is below 1%, due to issue with light penetration in dense microalgae culture [17]. Furthermore, it produces a mixture of O_2 and H_2 that requires further separation [18]. One of the major bottlenecks to unblock is the long-term stability of the microorganisms used [19].

1.2.2.2 Photocatalysis

Photochemical routes are based on the activation of catalysts by photo-energy provided by solar light. The catalyst is typically a semi-conductor material. Photon absorption (its energy is superior to the gap between the valence band and the conduction band) creates electron-hole pairs in the semi-conductor. Afterward, the electron-hole pairs migrate to the surface without generation. Finally, H^+ and H_2O are reduced and oxidized, forming H_2 and O_2, respectively, by photogenerated electrons and holes. The principal reactions can be described as follows:

$$\text{Catalyst} + h\nu \rightarrow h^+ + e^- \quad (1)$$

$$H_2O + 2h^+ \rightarrow 2H^+ + \frac{1}{2}O_2 \quad (2)$$

$$2H^+ + 2e^- \rightarrow H_2 \quad (3)$$

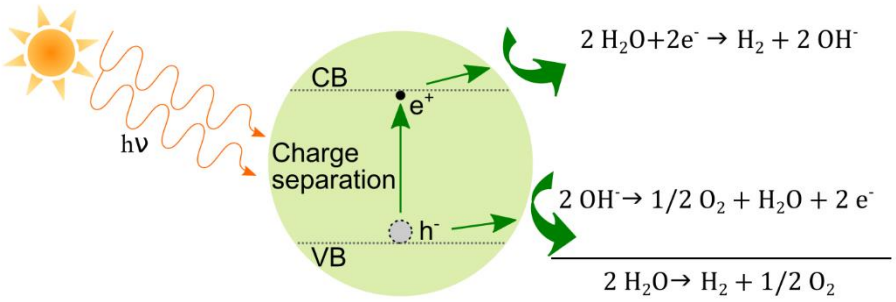

Figure 1-3: Photocatalytic pathway for water splitting (adapted from [18]), where CB represents the conduction band and VB the valence band

The efficiency depends on the bandgap and the band structure of the semiconductor along with the electron transfer process. The bottom of the conduction band should be lower than the reduction potential of water to generate H_2, whereas the top of the valence band should be higher than the oxidation potential of water to generate O_2 [20]. Among the semiconductors used for H_2 production by photocatalysis, TiO_2 and $SrTiO_3$ have been largely studied. Doping strategies were investigated to enhance solar-to-fuel efficiency, such as N-doped TiO_2 nanoparticles [21]. To avoid recombination, the use of sacrificial reagents (*e.g.* ethylenediaminetetraacetic acid) were proposed. One of the main advantages of photocatalysis is the possibility to proceed at low temperature (20-60°C). However, it suffers from the low stability and lifetime of the catalysts [18].

1.2.3 Thermochemical processes

Different highly endothermic reactions have been investigated to produce solar fuels, requiring high temperature [22]. Due to the diffuse aspect of solar energy and its radiation spread on the whole electromagnetic spectrum, the solar energy requires to be concentrated to exploit the heat.

1.2.3.1 Overview of concentrated solar power technologies

The concentrated solar power (CSP) technologies are introduced hereafter to provide a better understanding of thermochemical processes. CSP collects the incoming solar radiation and concentrates it into a solar receiver with large reflective surface. This implies that only the direct normal irradiation (DNI) is exploitable for high temperature applications. Among the technologies available to concentrate solar power, three categories permit to reach high temperatures (>250°C) and are industrially implementable: parabolic trough, central receiver and dish/engine (Figure 1-4).

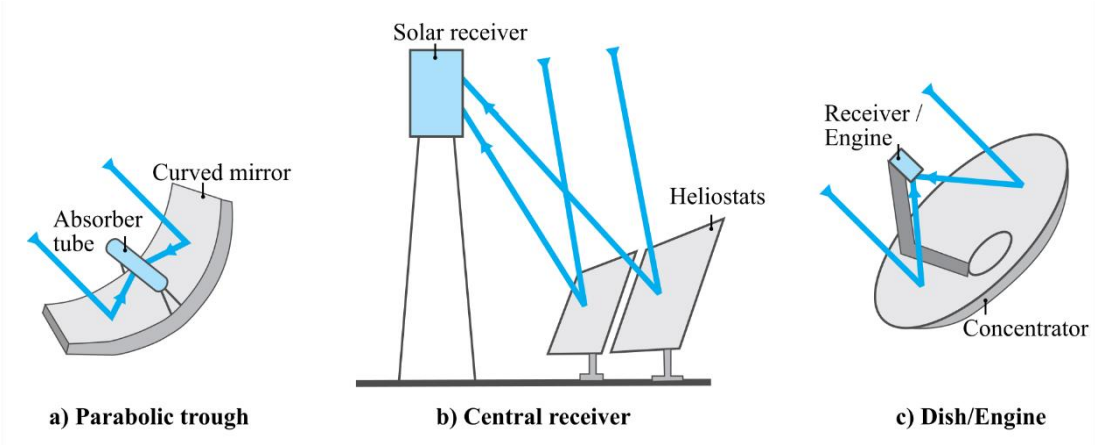

Figure 1-4: Principal concentrated solar power technologies: a) parabolic trough, b) central receiver and c) dish/engine [23]

The parabolic trough system is based on parabolic-shaped collectors which concentrate the sunlight onto a focal line where is placed an absorber tube, acting as a receiver. A calorific fluid circulates through the absorber tube to be heated. The heated fluid can be used to drive a turbine. The absorber tube is connected to the reflector and all the system tracks the sun along one-axis. It allows to reach temperature in a range of 250-450°C with concentrating factors in a range of 60-100 times. Another alternative to the parabolic trough is the linear Fresnel reflector system, where flat plane mirrors are divided into multiple parts to track the sunlight which is further reflected onto a secondary reflector concentrating the sunlight onto the absorber tube [22, 24].

Central receiver consists of a solar receiver placed at the top of a tower. The incident sunlight is tracked by elementary mobile mirrors, named heliostats, and it is reflected into the solar receiver. The heliostats are usually slightly focusing the solar energy. The solar receiver is composed of radiative/convective heat exchangers to transfer the energy to a thermal fluid. In comparison with parabolic trough, central receiver technology allows reaching higher temperature (up to 1000°C) and concentration factor (in the range 600-1000). However, it requires additional cost due to independent tracking for each heliostat [22, 24].

The last technology is the dish solar concentrator. A parabolic dish reflects and concentrates the sunrays into a solar receiver placed at the focal point of the dish collector. An additional heliostat can be used to track and reflect the solar energy into the dish avoiding the motion of the dish (solar furnace). This technology enables to achieve high temperature (above 1000°C) and concentration ratio (1000-5000) in comparison with other technologies, but dish solar concentrator power is limited by the size of the dish [22, 24]. In this work, the operating temperature was typically 1400°C, therefore a solar furnace technology was employed.

1.2.3.2 Decarbonization processes

In order to free the energy market from fossil fuels and adopt a carbon neutral economy, decarbonization routes for mid-term applications have been developed. In this way, solar-upgrading of carbonaceous feedstocks (natural gas, oil, coal, biomass) is an interesting avenue. Indeed, solar cracking, reforming and gasification allow producing H_2 or syngas from hydrocarbons with solar energy. In addition to the production of solar fuels, the decarbonization processes can optionally sequestrate carbon from carbonaceous feedstock [3].

Solar cracking

Solar cracking corresponds to the thermal decomposition of carbonaceous feedstocks, such as natural gas, oil, or other hydrocarbons, according to the equation (4).

$$C_xH_y \rightarrow xC + \frac{y}{2}H_2 \quad (4)$$

Other side reactions can occur due to the presence of impurities in the reactant. The thermal decomposition of carbon-rich materials leads to the production of hydrogen-rich gas phase and a carbon solid phase, enabling an easy carbon sequestration. Unlike other decarbonization processes, the solar cracking process sequestrates carbon in a single-step [25]. With methane, a conversion extent of 99% under argon atmosphere was achieved by [26]. The almost complete conversion of CH_4 allows the production of H_2 without greenhouse gas emission. The thermal decomposition route has a high theoretical maximum solar-to-fuel conversion efficiency of 55% [27]. The solar cracking route is suitable for natural gas and hydrocarbons with high H/C ratio (such as CH_4), due to the important energy loss involved in the carbon sequestration.

Solar reforming

Hydrocarbons used in reforming process are generally methane or natural gas, because they generate a hydrogen-rich gas phase. The reaction can be described by the net simplified reaction (5) which is highly endothermic.

$$C_xH_y + xH_2O \rightarrow \left(\frac{y}{2} + x\right)H_2 + xCO \quad (5)$$

The steam reforming shows fast reaction and high conversion extent, making it widely used in industry to produce syngas. The steam reforming reaction is typically carried out in the temperature range 800-1000°C and pressure range 3-25 bar, using a catalyst (such as Ni–Mo/Al_2O_3 or Co–Mo/Al_2O_3). Dry-reforming, *i.e.* using CO_2 instead of steam, can also be used according to reaction (6).

$$C_xH_y + xCO_2 \rightarrow \frac{y}{2}H_2 + 2xCO \quad (6)$$

The choice between steam- and dry- reforming depends on the final target application [28]. In solar reforming, the heat required to perform the reforming reaction is provided by the concentrated solar power, whereas conventional reforming is performed auto-thermally by partial combustion of hydrocarbon feedstock. Solar reforming using non-stoichiometric oxides as catalysts has also been investigated. In a first step, the reactive material (oxygen carrier such as ceria) is reduced under reducing atmosphere (i.e. typically methane) to produce syngas, and in a second step the reactive material is re-oxidized under H_2O or CO_2. Therefore the process can occur isothermally, alleviating the thermal stress and heat losses induced by temperature swing used in thermochemical cycles [29].

Solar gasification

The gasification process converts carbonaceous materials to syngas. It is composed of two steps consisting of a pyrolysis reaction followed by char gasification [30], represented by the ideal simplified net reaction:

$$C_xH_yO_z + (x-z)H_2O \rightarrow \left(\frac{y}{2} + x - z\right)H_2 + xCO \quad (7)$$

The feedstock employed for solar gasification can be solid fossil fuels or renewable fuel such as biomass, allowing a carbon neutral syngas production. This process targets the production of syngas, but other compounds may be formed (*e.g.* H_2S, tars) due to side reactions or impurity in the carbon-rich materials. The pyrolysis reaction corresponds to the thermal decomposition of the solid (from 300 to1000°C), resulting in the production of hydrogen-rich gaseous phase (containing also CH_4, C_2H_6, ...), condensable compounds (tars) and pure solid carbon (char). Afterward, the char gasification occurs, corresponding to carbon-steam gasification reaction, i.e. reaction (8). Due to the complexity of the reaction mechanism involved, other intermediate competing reactions should be considered (such as reactions (9)-(12)).

$$C + H_2O \rightarrow CO + H_2 \quad (8)$$
$$C + 2H_2 \rightarrow CH_4 \quad (9)$$
$$C + CO_2 \rightarrow 2CO \quad (10)$$
$$CO + H_2O \rightarrow CO_2 + H_2 \quad (11)$$
$$CH_4 + H_2O \rightarrow CO + 3H_2 \quad (12)$$

In contrast to the conventional gasification which employs a significant part (~30-45%) of the feedstocks into the combustion for process heat, in solar gasification all the feedstocks are devoted to the gasification reaction as the required heat is provided by solar energy. This leads to feedstock savings, enhanced syngas purity as contamination by byproducts is avoided with solar gasification, and increased amount of syngas produced per unit of feedstock. Furthermore, concentrated solar energy allows to perform the gasification reaction at higher temperatures than for the conventional gasification, resulting in an improvement of the reaction kinetics and the syngas quality [22]. Different pilot scale reactors have been tested for solar gasification [31, 32].

1.2.3.3 Thermochemical H_2O/CO_2 splitting processes

Contrary to decarbonization processes, H_2O/CO_2 splitting processes do not involve any hydrocarbon feedstock, but only H_2O or CO_2. Therefore, the solar fuels produced through this pathway can be considered as carbon-free and represent the ideal long-term alternative to store intermittent renewable energy [3].

Solar thermolysis

The solar thermolysis process consists of the direct thermal decomposition of water. As the process is reversible, a separation of the products (O_2 and H_2) is necessary to avoid their recombination. Two different options have been investigated: the quenching of the gas mixture or the removal of one of the products from the gas mixture at high temperature (using membrane, centrifugation or supersonic jet) [33]. Two drawbacks have impeded the development of this process: the required high temperature (>2200 C) to reach a reasonable dissociation extent and the necessity to separate O_2 and H_2 at high temperature to avoid undesirable reverse reaction or mixture explosion [22]. Consequently, this process is considered as not being implementable at large-scale for industry.

Solar two-step thermochemical splitting cycles

Thermochemical cycles based on metal oxides encompass two steps. First, a solar-activated thermal reduction (TR) of the material at high temperature produces O_2, according to reaction (13). Concentrated solar energy can be used as the external source of high temperature heat to drive the reaction. The second step is an exothermic reaction, in which the material is re-oxidized by H_2O or CO_2, according to reaction (14). The metal oxide is not consumed in the overall H_2O and CO_2 splitting process, and thus acts as a "catalyst" in the global reaction.

$$M_xO_y \rightarrow M_xO_{y-\delta} + \frac{\delta}{2}O_2 \quad (13)$$

$$M_xO_{y-\delta} + \delta CO_2 (\text{or } H_2O) \rightarrow M_xO_y + \delta CO (\text{or } H_2) \quad (14)$$

The two-step pathway enables to decrease the operating temperature in comparison with direct thermolysis, allowing operation at moderately high temperatures. In addition, O_2 and CO/H_2 are produced separately, eliminating the risk of recombination. Furthermore, the theoretical solar-to-fuel energy conversion efficiency is high [34]. Redox pairs investigated for thermochemical cycles are volatile metal oxides (ZnO/Zn and SnO_2/SnO [35]), or non-volatile stoichiometric and non-stoichiometric redox materials ($CeO_2/CeO_{2-\delta}$ [36, 37], Fe_3O_4/FeO, ferrites [38–40], such as $NiFe_2O_4$ [41], perovskites [42–44]). Thermochemical cycles using a volatile redox pair involve a reduction temperature higher than the vaporization temperature of the product. The use of volatile redox pairs is mainly limited by the necessity to operate with a rapid quenching of the gaseous phase to avoid products recombination. Regarding non-volatile redox pairs, reactants and products remain in solid state during the overall cycle (O_2 is thus released alone in the gas phase). In the case of a stoichiometric redox pair, a crystallographic phase change occurs between the reduction and the oxidation steps. The change in the crystallographic structure induces poor thermal stability and slow oxidation kinetics. For a non-

stoichiometric redox pair, oxygen vacancies are created in the oxide while the crystallographic structure is maintained [45].

To date, the highest experimental solar-to-fuel energy conversion efficiency has reached 5% for ceria reticulated porous foams [46], while the efficiency should be at least 20% to permit industrialization and to compete with photovoltaic technology combined with electrolysis [47].

Solar-driven two-step thermochemical cycles are relevant to produce "green" H_2 or syngas, as the only inputs are H_2O, CO_2 and solar energy. Among the thermally based H_2 production pathways, thermochemical cycles are the closest to the ideal H_2 production for the global warming reduction potential, production cost, and low environmental impact. However, the energy and exergy efficiencies of thermochemical cycles can be further enhanced [48]. Solar thermochemical water splitting cycles are considered as a long-term solution to produce H_2 at large scale [49]. This work focusses on the investigation and performance enhancement of thermochemical cycles using non-stoichiometric oxides.

1.3 Thermodynamics

In this part, the thermodynamics of thermochemical cycles are described to provide a better understanding of the mechanisms involved in thermochemical cycles. Investigating thermodynamics allows predicting the theoretical maximum fuel production that can be reached in thermochemical cycles, as a function of the reduction and oxidation temperatures and partial pressure of oxygen. In order to achieve spontaneous reactions, it is required to satisfy criteria (15) and (16), where $\Delta G°$ represents the standard Gibbs free enthalpy variation, P_{O_2} the oxygen partial pressure, T the temperature, and the subscripts *TR*, *WS*, and *CDS* refer to the thermal reduction, the water splitting, and the carbon dioxide splitting, respectively [50]. Figure 1-5 represents the Gibbs free energy in standard conditions for CO_2 splitting using $La_{0.6}Sr_{0.4}MnO_3$ during the reduction and oxidation steps. The Gibbs free energy of the reduction reaction is computed with values of $\Delta H°$ and $\Delta S°$ found in the literature [42]. Concerning the CO_2 splitting, its Gibbs free energy comes from the thermochemical database of HSC chemistry software®. The Gibbs free energy of oxidation corresponds to the difference between the Gibbs free energies of CO_2 splitting and of $La_{0.6}Sr_{0.4}MnO_3$ reduction. It can be seen that the thermal reduction is favorable for temperature higher than T_{high} and the oxidation step is promoted for temperature lower than T_{low} [51].

$$\Delta G°_{TR}\left(p_{O_2,TR}, T_{TR}\right) < 0 \quad (15)$$

$$\Delta G°_{WS}\left(p_{O_2,WS}, T_{WS}\right) < -\Delta G°_{H_2O}\left(p_{O_2,WS}, T_{WS}\right) \quad (16a)$$

$$\Delta G°_{CDS}\left(p_{O_2,CDS}, T_{CDS}\right) < -\Delta G°_{CO_2}\left(p_{O_2,CDS}, T_{CDS}\right) \quad (16b)$$

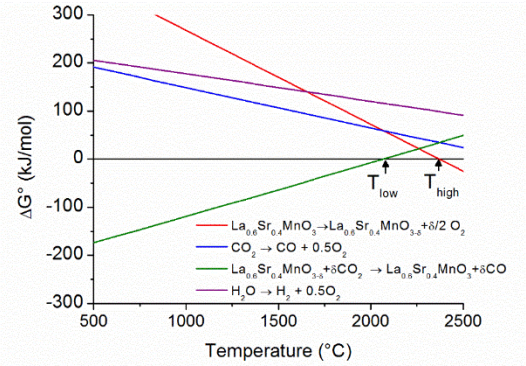

Figure 1-5: Schematic plot of the Gibbs energy for carbon dioxide splitting, water splitting, and two-step thermochemical redox cycling of $La_{0.6}Sr_{0.4}MnO_3$ in standard conditions

The Gibbs energy variation for the reduction and the oxidation steps are defined by Equations (17) and (18), respectively, whereas Equations (19) and (20) define the enthalpy and entropy variations of the overall cycle:

$$\Delta G^\circ_{TR,T_{TR}} = \Delta H^\circ_{TR} - T_{TR}\left(\Delta S^\circ_{TR} + \frac{1}{2}S^{O_2}_{T_{TR}}\right) \quad (17)$$

$$\Delta G^\circ_{WS,T_{WS}} = -\Delta H^\circ_{red} - \Delta H^{H_2O}_{f,T_{WS}} - T_{WS}(S^{H_2}_{T_{WS}} - S^{H_2O}_{T_{WS}} - \Delta S_{red}) \quad (18a)$$

$$\Delta G^\circ_{CDS,T_{CDS}} = -\Delta H^\circ_{red} - \Delta H^{CO_2}_{f,T_{CDS}} + \Delta H^{CO}_{f,T_{CDS}} - T_{CDS}(S^{CO}_{T_{CDS}} - S^{CO_2}_{T_{CDS}} - \Delta S_{red}) \quad (18b)$$

$$\Delta H^\circ_{cycle} = \Delta H^\circ_{TR} + \Delta H^\circ_{WS} \quad (19)$$

$$\Delta S^\circ_{cycle} = \Delta S^\circ_{TR} + \Delta S^\circ_{WS} \quad (20)$$

where ΔH° and ΔS° correspond to the standard enthalpy and entropy variations, T_i is the temperature during the WS or TR reaction. From Equation (6), the oxidation step is exothermic because the oxidation step is entropically unfavorable and the two steps have to be exergonic. Due to $\Delta H_{WS} < 0$, ΔH_{TR} has to be at least higher than ΔH_{CO_2} in order to have $\Delta H_{cycle} > \Delta H_{CO_2}$ [52–54]. At non-standard pressures, the effect of oxygen partial pressure on the entropy variation can be expressed as Equation (21), where P° is the reference pressure:

$$\Delta S_{TR} = \Delta S^\circ_{TR} - \frac{1}{2}R\ln\left(\frac{p_{O_2}}{P^\circ}\right) \quad (21)$$

The enthalpy variation can be considered as pressure-independent, which conducts to express the Gibbs free enthalpy variation in non-standard pressures, as Equation (22) [55].

$$\Delta G_{TR} = \Delta H^\circ_{TR} - T\Delta S^\circ_{TR} + \frac{1}{2}RT\ln\left(\frac{p_{O_2}}{P^\circ}\right) \quad (22)$$

When the reduction step is at equilibrium, the Gibbs free enthalpy is nil which allows writing the Equation (17) in the form of Equation (23) for a given value of δ.

$$\ln\left(\frac{p_{O_2}}{P^\circ}\right) = \frac{2\Delta S_{red}}{R} - \frac{2\Delta H_{red}}{RT}\Big|_{\delta=\delta_{cte}} \quad (23)$$

The oxygen non-stoichiometry is plotted in Figure 1-6 as a function of the logarithm of the oxygen partial pressure at different temperatures. Then, it is possible to plot the logarithm of the oxygen partial pressure as a function of the reverse temperature for a constant δ value, and

to determine both ΔH_{red} and ΔS_{red} via Equation (23) [45]. For the oxidation step, the contribution of the amount of oxidant gas can be expressed as in Equation (24), where P_{CO}, P_{CO_2} P_{H_2} and P_{H_2O} are the carbon monoxide, carbon dioxide, hydrogen and steam partial pressure, respectively [55]. From Equation (24), it can be evidenced that the increase of the oxidant gas ratio tends to decrease ΔG_{WS} which favors the oxidation reaction. However, increasing the oxidant gas in excess amount may negatively impact the thermochemical cycle efficiency, due to the low conversion yield of the oxidant gas to the splitting products.

$$\Delta G_{WS} = \Delta H°_{WS} - T\Delta S°_{WS} + RT \ln\left(\frac{P_{H_2}}{P_{H_2O}}\right) \quad (24.a)$$

$$\Delta G_{CDS} = \Delta H°_{CDS} - T\Delta S°_{CDS} + RT \ln\left(\frac{P_{CO}}{P_{CO_2}}\right) \quad (24.b)$$

Thus, an ideal redox material must have a low enthalpy variation $\Delta H°_{red}$ which permits to increase the reduction extent at a lower temperature. In contrast, a high entropy variation $\Delta S°_{red}$ is required, thereby allowing smaller temperature variation between the reduction and the re-oxidation steps, which is critical for overall efficiency [45]. The Gibbs free enthalpy variation can be adjusted by changing the operating conditions (lower oxygen partial pressure or oxidant excess) but this induces energy penalty.

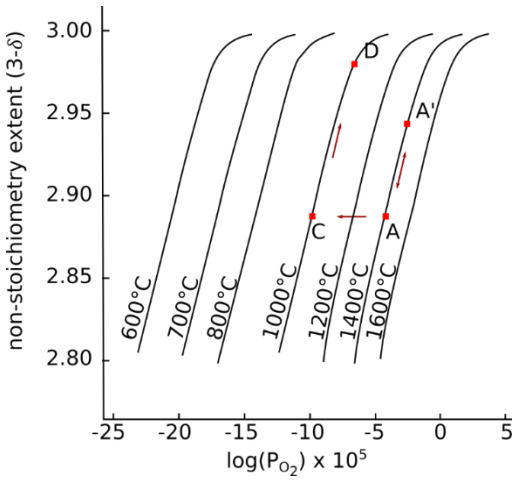

*Figure 1-6: Oxygen non-stoichiometry of $La_{0.6}Sr_{0.4}MnO_{3-\delta}$ as a function of the logarithm of oxygen partial pressure at different temperatures (adapted from Reference [56]). Pressure-swing vs. temperature-swing thermochemical pathways: isothermal cycle at 1400 °C with pressure swing operation between **A** and **A'**, two-temperature cycling with quenching (**A** to **C**), oxidation at 1000 °C (**C** to **D**) and reduction at 1400 °C (**D** to **A**) [57]*

1.4 Non-stoichiometric materials: ceria and its dopant

Ceria-based materials have been studied for a large number of applications, such as catalysis [58], solid electrolytes [59], solid oxide fuel cells [60]. Ceria has a cubic fluorite structure with a face centered cubic unit cell ($Fm\bar{3}m$), as represented in Figure 1-7. The lattice parameter increases linearly with the concentration of Ce^{3+} due to its larger ionic radius (1.143 Å) in comparison with the ionic radius of Ce^{4+} (0.97 Å) [61, 62]. It retains its crystalline phase over a wide range of oxygen non-stoichiometry and reduction extent. The reachable non-stoichiometry depends on both the oxygen partial pressure and the temperature. Figure 1-8

shows the influence of temperature and pressure on ceria non-stoichiometry [55, 63, 64]. Reduced ceria forms a continuum of oxygen-vacancy in the non-stoichiometric oxide. Due to the non-stoichiometry, there is a distortion of the fluorite structure. A redox cycle based on the complete thermal reduction of CeO_2 to Ce_2O_3 was first highlighted [65]. A non-stoichiometric partial reduction of Ce^{4+} to Ce^{3+} was then performed at lower temperatures [66]. This reaction scheme has been largely studied due to its advantageous combination of characteristics such as favorable oxidation thermodynamics, rapid reaction kinetics, complete reversibility and stability. The reduction step of ceria-based thermochemical cycles commonly requires a temperature between 1400 and 1500 °C with an oxygen partial pressure below 10^{-5} atm [45, 63, 67–69]. Chueh et al. [68] demonstrated stable and fast fuel production over 500 cycles with a solar-to-fuel efficiency in the range 0.7–0.8%. The average O_2 and H_2 production rates over 500 cycles (oxygen partial pressure during the reduction: 10^{-5} atm, reduction and oxidation temperatures: 1500 °C and 800 °C, respectively) are represented in Figure 1-9. After a decrease of the production rates for both O_2 and H_2 during the first hundred cycles, the average production rates are then stabilized. The authors suggest that the efficiency could be increased by modifying the design and up-scaling the process, as far as chemistry was not the limiting step [68].

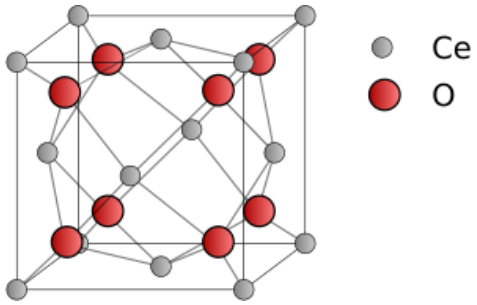

Figure 1-7: Crystallographic structure of pure ceria

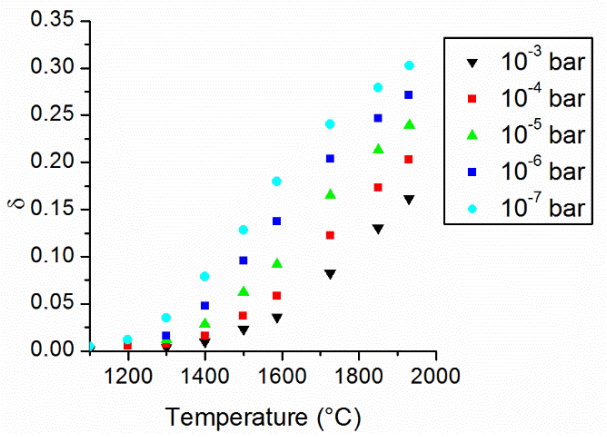

Figure 1-8: Non-stoichiometry in ceria (δ) as a function of temperature for different oxygen partial pressures [63]

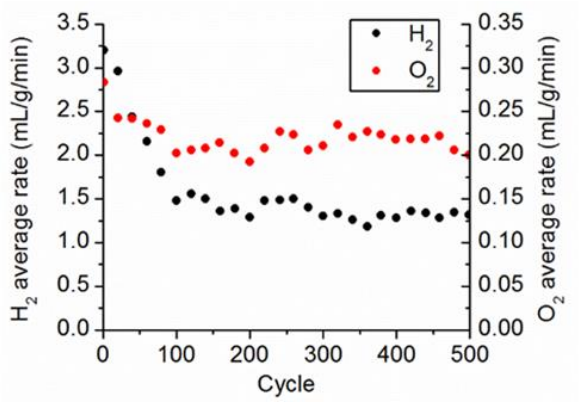

Figure 1-9 : Average O_2 and H_2 production rates over 500 successive cycles performed with ceria, with a reduction temperature of 1500 °C and an oxidation temperature of 800 °C [68]

Rhodes et al. [70] demonstrated the ability of porous ceria to perform 2000 successive thermochemical cycles (reduction temperature at 1450 °C, oxidation with CO_2 at 1100 °C). The average extent of non-stoichiometry for the last 50 cycles was 86.4% of the average value for the first 50 cycles. The porous structure was maintained in spite of an apparent decrease of specific surface area. The obtained mean non-stoichiometry was δ=0.0197. After repeated cycles, it was observed that the oxidation of ceria tends to be more and more homogeneous through the bulk [70]. Furler et al. [67] also demonstrated the ability of ceria to perform consecutive cycles with stable syngas production.

Ceria has a high entropy change compared to other non-stoichiometric materials, which provides a lower temperature swing requirement between reduction and oxidation. Ceria also provides more favorable oxidation reaction thermodynamics than perovskites [45].

In summary, pure ceria retains a stable fluorite phase over a large range of oxygen vacancy concentration. Furthermore, its re-oxidation is thermodynamically favorable. However, ceria suffers from low reduction extents and thus requires high reduction temperature, limiting the global solar-to-fuel energy conversion efficiency. To overcome these drawbacks, different dopants have been considered to lower the reduction temperature and thus to favor the oxygen release, as presented in the next paragraph.

1.4.1 Doped ceria

Numerous elements have been incorporated as dopants into ceria, trying to both enhance fuel production and decrease the reduction temperature. In order to improve ceria performance by modifying its bulk properties, partial substitution of ceria with aliovalent or isovalent elements was investigated [71]. For the sake of brevity, all the investigated dopants for ceria are not developed here. The detailed screening about ceria dopants was published in a review article as part of this thesis work [72].

Meng et al. [73] pointed out that a small ionic radius for divalent, trivalent and tetravalent dopants is beneficial to promote the released amount of oxygen. Furthermore, high valence dopants also enhance the reduction extent. A dopant with high valence and small ionic radius favors the reduction extent of doped ceria. This is due to the Coulombic forces determining the

attraction between oxygen-ions and doping cation, which is proportional to the charges and to the reverse of cation ionic radius. Thus, Ce–O bonds formed around dopants with small ionic radius and high valence tend to break more easily [74].

A summary of the effect of the different doping cations into ceria is given in Table SA-1. Direct comparison of the cations impact in a quantitative way would not be relevant as it may be biased by strong differences in both operation conditions (reaction temperatures, oxygen partial pressure, gas composition, etc.) and dopant concentrations. Thus, Table SA-1 rather provides information about the qualitative influence of the cations with positive and negative effects on the reactions.

1.4.1.1 Monovalent dopant

Meng et al. [74] studied the effect of monovalent Li^+ ion on ceria thermochemical performance. They showed that up to a dopant concentration of 5 at.% Li, the amount of produced oxygen increased. Conversely, maximum H_2 production was obtained for the minimum Li concentration tested (2.5%). However, the authors did not compare Li-doped ceria to pure ceria. Therefore, it is necessary to remain cautious when reporting that 2.5% of Li may increase the H_2 production in comparison with pristine CeO_2.

1.4.1.2 Divalent dopants

Kaneko et al. [75] highlighted that Cu dopant in ceria improved O_2 release compared with pure ceria due to a partial reduction of Cu species from Cu(I) to Cu(0). However, Cu_2O does not take part during the oxidation step. Hence, H_2 production from Cu-doped ceria is similar to pure ceria performance [75], and the addition of Cu dopant in ceria does not provide any beneficial interest for the improvement of the solar-to-fuel efficiency.

The effect of cerium substitution with strontium and calcium on thermochemical performance was also studied [76, 77]. It appears that the amount of O_2 released by $Ce_{0.9}Sr_{0.1}O_2$ is slightly lower than with CeO_2. Similarly, the reduction extent of $Ce_{0.9}Ca_{0.1}O_2$ is lower than for pure CeO_2. It is noteworthy that Sr-doped ceria was expected to produce lower oxygen amount than Ca-doped ceria due to the larger ionic radius of Sr^{2+} than Ca^{2+}. This finding can be explained by the higher thermal stability of Sr-doped ceria compared to Ca-doped ceria [77]. These results were confirmed by Scheffe and Steinfeld [76] who stated that Ca and Sr incorporation into CeO_2 did not improve the solar-to-fuel energy conversion efficiency.

The use of the Mg^{2+} ion as dopant in ceria increases the O_2 production yield (1.98 mL/g) at 1500 °C in comparison with pure ceria (1.77 mL/g). The bulk conductivity of ceria is improved by the increase of the oxygen vacancy concentration due to the incorporation of Mg^{2+} cation. The lower valence state of Mg^{2+} compared to Ce^{4+} leads to an increase in the amount of intrinsic oxygen vacancies. Therefore, Mg-doped ceria outperforms pristine ceria and presents good stability over cycles [77]. However, the solubility of Mg^{2+} is limited due to the important difference between the ionic radii of Ce^{4+} and Mg^{2+}, 0.97 Å and 0.89 Å, respectively [78].

1.4.1.3 Trivalent dopant

The influence of scandium as a dopant in ceria is shown in Figure 4 [79]. The introduction of Sc in ceria is limited to 20 at.%. The small ionic radius of Sc^{3+} compared to Ce^{3+} permits to relieve the lattice strain induced by the reduction reaction of cerium ion. The scandium ion favors the reduction extent by decreasing lattice strain. However, when introducing up to 7% Sc^{3+}, the O_2 production decreases due to a decrease of Ce content [77]. The H_2 production and re-oxidation yield are increased compared to pure ceria, from 3.19 to 4.06 mL/g with 10% of Sc [77]. The Sc-doped ceria presents a rapid oxidation rate similar to pure ceria, although the addition of a dopant in ceria generally decreases the oxidation rate compared to pure ceria [80]. However, Scheffe et al. [58] found that Ce substitution by Sc does not enhance significantly the thermochemical performance.

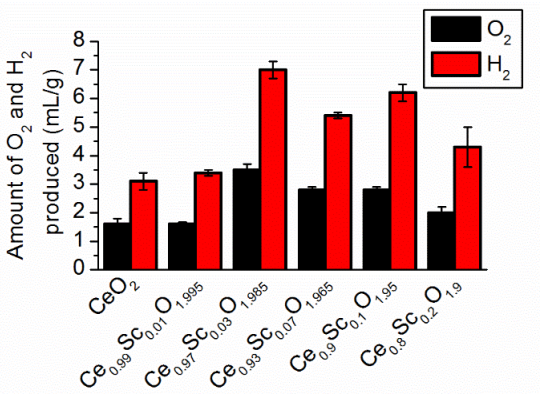

Figure 1-10. Amounts of O_2 and H_2 produced by Sc-doped ceria and pure ceria, with a reduction and oxidation temperature of 1500 °C and 500 °C, respectively [79]

Other trivalent ions were investigated for ceria doping such as Y^{3+} [76, 81, 82], Co^{3+} [83], La^{3+} [81, 82], Pr^{3+} [84–87], Gd^{3+} [84, 88], Tb^{3+} [84, 87, 89], Dy^{3+} [77], Er^{3+} [84]. None of these trivalent dopants present a significant enhancement of the fuel production and the thermal stability, thus resulting in no significant improvement of the thermochemical performance in comparison with pristine ceria.

Muhich and Steinfeld [89] stated that divalent and trivalent elements were not suitable dopants. Indeed, two electrons must be promoted to the Ce f-band upon reduction if the energy required to drive water splitting is not sufficient. Divalent and trivalent elements did not promote two electrons to the Ce f-band. The authors rather suggested to use tetravalent dopants to improve significantly the thermochemical performance of ceria [89]. Among the trivalent dopants presented previously, only Sc showed a significant improvement of the thermochemical performance of ceria.

1.4.1.4 Tetravalent dopants

The use of tetravalent cations with ionic radius smaller than Ce^{4+}, as ceria dopants, can increase ceria thermochemical performance. Their small ionic radius permits to decrease the oxygen diffusion barrier and facilitates vacancy formation, thus enhancing O_2 production. The onset reduction temperature is lowered for ceria doped with tetravalent cation compared with pure ceria [81, 90]. The incorporation of tetravalent cations into ceria favors the formation of active

oxygen vacancies and decreases the energy of vacancy formation [87, 90]. When focusing on redox-active materials, the Zr-concentration in ceria-zirconia is generally limited to 50%, and beyond there is no beneficial effect on the thermochemical performance. The reduction extent of Zr-doped ceria is enhanced with the increase of Zr concentration (Figure 1-11) [36, 53, 80, 91]. The 10% Zr-doped ceria presents a lower onset temperature (~750 °C) compared to pure ceria (1000 °C) [80, 92]. The reduction temperature can thus be decreased below 1500 °C by Zr incorporation [36, 93]. The enhancement of the reduction step is due to an improved oxygen mobility caused by lattice distortion and the favored oxygen vacancies due to the incorporation of the Zr dopant [93, 94]. Ceria doped with 10% Zr has a faster oxygen production rate than pure ceria due to a lower activation energy (162 kJ/mol) in comparison with pure ceria (235 kJ/mol) [82]. Jiang et al. [81] evidenced that Zr^{4+} doped ceria shows the highest O_2 production compared to ceria doped with other tetravalent ions (Ti^{4+}, Sn^{4+}, Hf^{4+}). In contrast, Muhich et al. [95] predicted a lower reduction capability for Zr-CeO_2 in comparison with Hf-CeO_2 [95]. The addition of Zr in ceria promotes bulk reduction at lower temperature than for undoped ceria [96].

Conversely, the incorporation of Zr may have a negative effect on the oxidation step. The required oxidation temperature is generally lowered, thus leading to higher temperature swing [53, 97], while the oxidant gas has to be supplied in excess [98] when compared with pure ceria. The slow oxidation of Zr-doped ceria is explained by a thermodynamically less favorable reaction than for pristine ceria [53] because of decreasing Ce(III) ions concentration at the ceramic surface induced by Zr dopant [80, 82, 96]. The CO production with $Ce_{0.75}Zr_{0.25}O_2$ was found to be higher than for undoped ceria at an oxidation temperature of 1200 °C and 1300 °C. However, for an oxidation temperature of 1400 °C, undoped ceria showed higher CO production than $Ce_{0.75}Zr_{0.25}O_2$ [81]. The Zr-doped ceria may also show a reactivity decrease over cycles due to its lower thermal resistance in comparison with pure ceria [99].

A few studies [97, 98, 100] have evaluated the solar-to-fuel energy conversion efficiency of Zr-doped ceria using a thermodynamic analysis. It was shown that Zr-doped ceria materials offer higher efficiency than pure ceria in most conditions [97, 98, 100].

Zr-doped ceria shows a higher maximum non-stoichiometry than pristine ceria. However, the oxidation kinetics are slower than for undoped ceria. To overcome this issue, a number of studies investigated the incorporation of a second dopant. Call et al. [37] used lower valence cations in $Ce_{0.85}Zr_{0.15}O_2$, but they concluded that this route was not beneficial for enhancing O_2 and CO production. The incorporation of larger trivalent ions leads to an increase of the lattice strain, which decreases the amount of produced oxygen, compared to $Ce_{1-x}Zr_xO_2$. However, $Ce_{1-x}Zr_xO_2$ doped with lower valence cation can reduce the decrease of reactivity of $Ce_{1-x}Zr_xO_2$ upon cycling [37].

The impact of the incorporation of Y, La, Pr and Sm in Zr-doped ceria was studied. It was highlighted that these dopants did not provide any improvement on the oxide reducibility, although they had a beneficial impact on its thermal stability [37, 96].

The incorporation of 1% of Gd ($Ce_{0.74}Zr_{0.25}Gd_{0.01}O_2$) improved the oxide reduction extent (200 µmol/g of O_2 produced at 1400 °C) when compared with pure ceria and 25% Zr-doped ceria (75.0 µmol/g and 179.4 µmol/g, respectively). Moreover, during the oxidation step the quantity of H_2 produced with $Ce_{0.74}Zr_{0.25}Gd_{0.01}O_2$ (338 µmol/g) was higher than for both CeO_2 and $Ce_{0.75}Zr_{0.25}O_2$ (128.0 µmol/g and 323.0 µmol/g, respectively). The crystallite growth was hindered due to the presence of Gd and the performance was reported to decrease for higher Gd concentration [88]. On the contrary, Call et al. [37] reported that the incorporation of Gd dopant into $Ce_{0.85}Zr_{0.15}O_2$ results in lower O_2 and CO production in comparison with pristine $Ce_{0.85}Zr_{0.15}O_2$.

Kang et al. [101] investigated the effect of Ni, Fe, Mn and Mg as dopants in ceria-zirconia. They reported that these dopants increase the O_2 production during the first cycle compared with ceria-zirconia. Nevertheless, $Ce_{1-x}Zr_xO_2$ doped with Ni, Fe, and Mn shows a weak CO/O_2 ratio (e.g., 0.35 for $Ce_{0.7}Zr_{0.2}Mn_{0.1}O_2$). Only the Mg dopant presents a good CO/O_2 ratio (1.52 and 1.99 for the first and second cycles, respectively). The CO production increases from 4.65 to 5.64 mL/g with 10% addition of Mg in $Ce_{0.8}Zr_{0.2}O_2$ [101]. The introduction of Mg in Zr-doped ceria engenders lattice defects in the crystalline structure, which increases oxygen mobility. The thermal stability is also improved by the incorporation of Mg. Calcium dopant was also identified by Kang et al. [102] to be beneficial for both the oxygen mobility and the thermal stability of Zr-doped ceria [102].

The addition of Hf^{4+} in Zr-doped ceria improve the thermochemical performance in comparison with undoped ceria-zirconia (the best performance was reported for $Ce_{0.895}Zr_{0.046}Hf_{0.053}O_{1.988}$). A grain growth was observed during the first cycle due to sintering, but then no further grain growth occurred during the 19 following cycles [103].

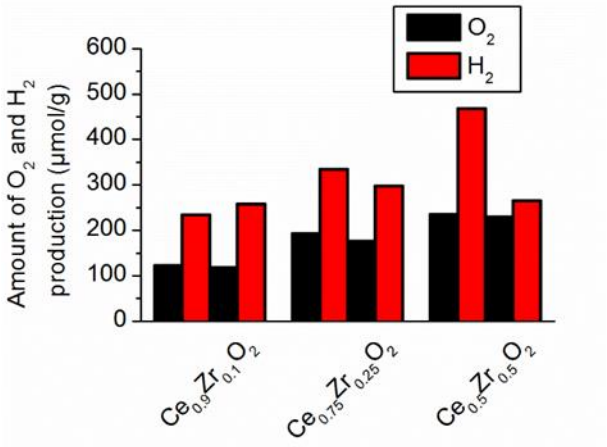

Figure 1-11: O_2 and H_2 production during two thermochemical cycles using $Ce_{1-x}Zr_xO_2$ (x = 0.1, 0.25 and 0.5) with reduction and oxidation temperatures of 1400 °C and 1050 °C, respectively [77].

The dopant radius has an influence on the thermochemical properties of ceria. The radius able to give the best performance was calculated by Jacot et al. [87] to be around 0.8 Å. The Hf^{4+} cation (8-fold coordination) has a ionic radius of 0.83 Å, and should thus provide attractive thermochemical performance [87]. The reduction extent of Hf-doped ceria increases with Hf dopant concentration [80]. The onset reduction temperature increases with the Hf concentration,

reaching 930 °C for $Ce_{0.8}Hf_{0.2}O_2$. At the same time, the increase of Hf concentration leads to an increase of the time required to fully oxidize the doped ceria. This trend is illustrated in Figure 1-12 [86]. The oxidation kinetics for $Ce_{0.93}Hf_{0.07}O_2$ were observed to be slower than for undoped ceria [87]. H_2 production is increased by the larger non-stoichiometry reached during the reduction step compared with pure ceria. However, the re-oxidation yield of Hf-doped ceria is lower than for undoped ceria [77].

The incorporation of lower valence dopants (Li^+, Mg^{2+}, Ca^{2+}, Er^{3+} and Y^{3+}) into $Ce_{0.95}Hf_{0.05}O_2$ was investigated by Jacot et al. [104], aiming to improve the redox reaction kinetics. For all the investigated dopants, the reduction kinetic was not improved whereas the oxidation kinetic enhancement was weak [104]. However, the addition of Li^+ dopant into Hf-doped CeO_2 helps to preserve the interconnected porosity compared with undoped ceria. The lithium reduces the cation mobility at high temperature, thus maintaining the interconnected porosity [86].

Meng and Tamaura [105] studied the addition of Pr into Hf-doped ceria. The introduction of 10% Pr into $Ce_{0.9}Hf_{0.1}O_2$ increased the H_2 production (5.72 mL/g) in comparison with the pristine $Ce_{0.9}Hf_{0.1}O_2$ (4.50 mL/g). The multivalent states of Pr cation led to the enhancement of thermochemical properties by eliminating residual gaseous oxygen (Pr^{3+} oxidation into Pr^{4+}) and improving the ionic conductivity of the oxide [105].

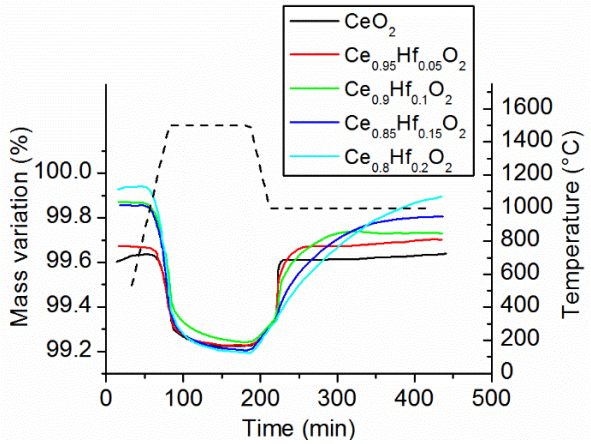

Figure 1-12: Thermogravimetric analysis of $Ce_{1-x}Hf_xO_2$ during a reduction at 1500 °C followed by an oxidation under CO_2 at 1000 °C [86]

The incorporation of Sn or Ti into ceria enhances the reduction extent achieved by ceria. However, in both cases a new phase is formed ($Ce_2Ti_2O_7$ and $Ce_2Sn_2O_7$, respectively) leading to a lower quantity of CO produced in comparison with pristine ceria [81, 87, 90].

The tungsten cation used as ceria dopant does not provide any significant enhancement of thermochemical performance compared with pure ceria [61]. Rhodium has been studied as ceria dopant by Lin et al. [94] who reported that this dopant increased the formation of oxygen vacancies in ceria [94]. However, Jacot et al. [66] reported that $Ce_{0.9}Rh_{0.2}O_2$ suffers from important and irreversible mass loss during thermogravimetric analysis, thus altering the re-oxidation step [66]. Furthermore, rhodium is one of the rarest and most valuable precious metals and its use may thus be not favorable for process economics.

With the addition of Cr, Si, Ge and Rh into ceria, a higher reduction extent was obtained in comparison with pure ceria [87, 90, 106, 107]. Ramos-Fernandez et al. [61] found that the use of chromium as ceria dopant does not improve the thermochemical performance. The CO generation rate was not increased and the amount of fuel produced was similar to pure ceria [81]. The use of Cr may not be advised, as it can be dangerous for health and environment.

1.4.1.5 Pentavalent dopants

The incorporation of Nb^{5+} cation into ceria contributes to increase the reduction extent in comparison with pure ceria [87, 104]. However, the Nb dopant might also form clusters. In this configuration, only the oxygen vacancies situated far from the Nb dopant are able to drive water-splitting, thus leading to weak H_2 production [89]. Furthermore, Nb may be toxic, limiting its application in future industrial processes.

Hoes et al. [108] investigated the introduction of a second dopant (La, Y, Sc) in Nb-doped ceria. They showed that the reduction extent achieved by these oxides decreases in the following order: $Ce_{0.9}Sc_{0.05}Nb_{0.05}O_2$ > $Ce_{0.9}Y_{0.05}Nb_{0.05}O_2$ > $Ce_{0.95}La_{0.025}Nb_{0.025}O_2$ > $Ce_{0.75}La_{0.125}Nb_{0.125}O_2$ > CeO_2. The highest calculated energy efficiency was achieved by $Ce_{0.9}Y_{0.05}Nb_{0.05}O_2$ (31% with H_2O vapor as oxidant) in comparison with 26% for pure ceria [108].

The use of tantalum cation as dopant into CeO_2 increases the reduction extent [87, 88, 104]. Doping ceria with 10% Ta increases the H_2 production compared with undoped ceria (142 µmol/g of H_2 produced at 1040 °C after a reduction at 1450 °C). However, Jacot et al. [87] noticed that the re-oxidation kinetics of $Ce_{0.93}Ta_{0.07}O_2$ was slower compared to pure ceria [87]. Upon cycling, Ta-doped ceria presents a decrease of the weight loss during O_2 release (0.580% to 0.470%), which may be attributed to the formation of Ce-rich phases prone to evaporate [91]. Muhich and Steinfeld [56] predicted that the addition of Ta into ceria does not enhance its thermochemical performance [89].

Likewise, the use of vanadium as ceria dopant does not improve the ceria redox activity [89].

1.4.2 Dopants with multiple oxidation states

Manganese has been studied as ceria dopant: during the first cycle, ceria doped with 30% Mn showed an improved O_2 production (13.2 Ncm^3/g) compared with pure ceria (4.8 Ncm^3/g) at a reduction temperature of 1500 °C. However, during the second cycle the O_2 production of Mn-doped ceria fell down to 5.4 Ncm^3/g, i.e., similar to pure ceria. In addition, the H_2 amount produced was smaller with Mn-doped ceria (7.9 Ncm^3/g) than with undoped ceria (8.7 Ncm^3/g) at 1150 °C [83].

Iron was another investigated dopant: ceria doped with 30% Fe presents a high O_2 production (10.5 Ncm^3/g) compared with pure ceria (4.8 Ncm^3/g) at 1500 °C. However, the material melted at this temperature [83]. The presence of Fe^{2+} and Fe^{3+} in the crystal lattice increases the oxygen mobility, thus leading to enhanced O_2 and H_2 productions. However, both O_2 and H_2 productions were not influenced by the Ce:Fe ratio [109].

Ceria doped with 30% Ni shows a weak enhancement of O_2 and H_2 productions (4.4 Ncm^3/g and 9.0 Ncm^3/g, respectively) compared with pure ceria (4.8 Ncm^3/g and 8.7 Ncm^3/g, respectively) at temperatures of 1500 °C and 1150 °C, respectively [83]. Kaneko and Tamaura [110] highlighted the highest O_2 and H_2 amounts obtained (1.4 Ncm^3/g and 2.5 Ncm^3/g, respectively) with a molar Ce:Ni ratio of 9.5:0.5. The Ni cation is involved in the formation of anionic defects that promote the oxygen mobility [110].

The addition of Zn into ceria was also investigated. A significant amount of ZnO was detected in the fresh sample, but after few cycles, the ZnO phase sublimated (traces of ZnO were still present afterwards) while Zn was still present as dopant in the ceria solid solution. The ZnO phase had an adverse effect on the H_2 and CO productions. However, the Zn dopant contributed to increase the ceria redox activity. Furthermore, Zn-doped ceria showed a stable fuel production over consecutive cycles [111].

1.4.3 Paired charge compensating strategy

Muhich et al. [95] investigated a doping strategy of ceria using paired charge compensating dopants. Ceria was co-doped with a trivalent cation (Sc, Y, or La) and a pentavalent cation (V, Nb or Ta). The trivalent dopant has an important impact on the reduction step, caused by the decrease of the ionic attraction between trivalent cation and oxygen anion in comparison with Ce^{4+} and O^{2-}. Inversely, the pentavalent cation has only a small effect on the reduction step. Among the compositions investigated, $Ce_{0.9}Sc_{0.05}X_{0.05}O_2$ (with X = V, Nb or Ta) exhibits the highest reduction capability. However, it still remains lower than Hf-doped ceria [95].

The thermochemical performance of ceria needs to be improved in order to reach an economically viable solar fuel production. However, modifying ceria properties with dopants is complex, as dopants influence more than one property. None of the dopants presented so far allows a significant improvement of ceria performance. However, some of them appear promising, especially zirconium that increases the reduction extent at the expense of a decrease of the oxidation rate and thermal stability. Scandium may also be attractive since it increases O_2 production and promotes thermal stability. Hafnium increases the reduction extent as well, while decreasing the onset temperature. However, the re-oxidation yield decreases over cycles. Another important lever to improve thermochemical performance is the shaping of the reactive ceria-based materials for tailoring both their microstructure and morphology.

1.5 Perovskite formulations investigated for thermochemical cycles

Since a few years ago, perovskites have been investigated for solar fuel production from thermochemical cycles [112]. Perovskites have the general formula ABO_3, where A and B are cations. The A cation is 12-fold coordinated with oxygen and it is larger than the B cation. The latter is 6-fold coordinated with oxygen anion. Ideal perovskites present a cubic structure with space group Pm3m, as represented in Figure 1-13 [113]. Different elements can occupy the A and B sites of the perovskite according to their ionic radius. The ionic radius of the A cation is comprised between 1.10 and 1.80 Å, whereas the ionic radius of the B cation is comprised between 0.62 and 1.00 Å [114]. The Goldschmidt tolerance factor (Equation (25)) determines whether the perovskite structure can be formed according to the ionic radii. In this equation, r_A,

r_B, and r_O are the ionic radii of cation A, cation B, and oxygen anion, respectively. This factor has to be close to one, so that the perovskite can be formed and equals one in the case of an ideal perovskite structure. Rhombohedral perovskites can be formed if t is approximately greater than 1.02. Orthorhombic and tetragonal perovskites can be formed if $t < 1$.

$$t = \frac{r_A + r_O}{\sqrt{2}(r_B + r_O)} \quad (25)$$

The large non-stoichiometry of perovskites is a very interesting property for thermochemical cycles [115]. Due to the large number of dopant insertion options (27 possibilities for the A site and 35 possibilities for the B site), their composition can be tuned to optimize fuel production [116, 117]. For the sake of brevity, all the investigated perovskites for thermochemical cycles are not developed here. The detailed screening about perovskites used as reactive materials in thermochemical cycles was published in a review article [118].

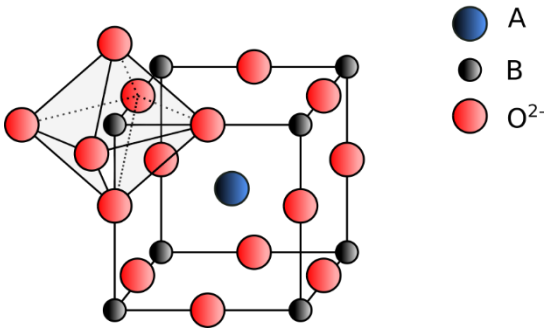

Figure 1-13: Ideal cubic perovskite structure ABO_3, with an octahedral site

1.5.1 Manganese based perovskite

1.5.1.1 A-site substituted materials

Among the lanthanum–manganese perovskites series, the most studied are $La_{1-x}Sr_xMnO_3$ and $La_{1-x}Ca_xMnO_3$. $LaMnO_3$ presents a very low reduction extent, which prevents the fuel production. The presence of Sr or Ca in the A-site increases the oxidation state of Mn, due to the lower charge of Sr^{2+} or Ca^{2+} compared to La^{3+}. The increase of Mn oxidation state permits to increase the reduction extent. The reduction extent thus increases with the Sr or Ca content [56, 119–124]. $La_{1-x}Ca_xMnO_3$ presents a higher reduction extent than $La_{1-x}Sr_xMnO_3$, because of the larger decrease of the Gibbs' free enthalpy [125–128]. This can be attributed to the smaller ionic radius of Ca^{2+} compared to Sr^{2+} [42, 129–131]. The substitution of lanthanum by calcium also permits to diminish the reduction temperature [132]. The optimum content for Sr substituting La is comprised between 0.3 and 0.5 [56, 119–121]. The increase of Sr or Ca content adversely affects the re-oxidation yield [133]. Figure 1-14 represents the CO production for different Sr contents in $La_{1-x}Sr_xMnO_3$, and for undoped and Zr-doped CeO_2 as reference materials. All $La_{1-x}Sr_xMnO_3$ perovskites present higher CO production in comparison with pure ceria during cycles. $La_{0.5}Sr_{0.5}MnO_3$ presents the highest CO production and can compete with $(Ce,Zr)O_2$ [134]. The CO production is lower when Ca is used as dopant (210 µmol/g) instead of Sr (269 µmol/g) [125, 132].

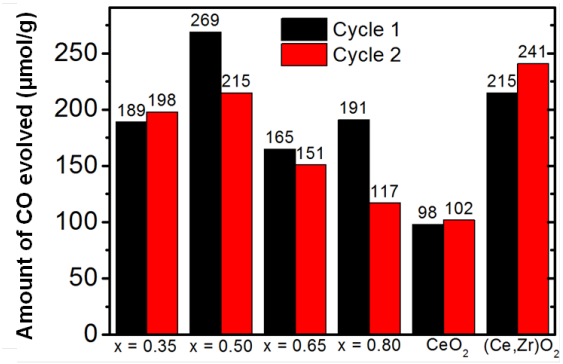

Figure 1-14: CO production at 1050 °C (with T_{red} = 1400 °C) for the $La_{1-x}Sr_xMnO_3$ series and in comparison with fluorite materials as reference during two cycles [134]

Another possible dopant for the A-site in lanthanum–manganese perovskites is Ba^{2+}, leading to the $La_{1-x}Ba_xMnO_3$ series. The presence of Ba^{2+} does not show any beneficial effect on the reduction extent when compared with Sr and Ca dopants. For instance, an O_2 production of 203 µmol/g was measured for $La_{0.5}Ba_{0.5}MnO_3$, while Sr and Ca containing materials produced 248 µmol/g and 311 µmol/g, respectively (Figure 1-15). Another point is that the re-oxidation yield is also reduced compared with Sr or Ca-doped lanthanum–manganese perovskites [125].

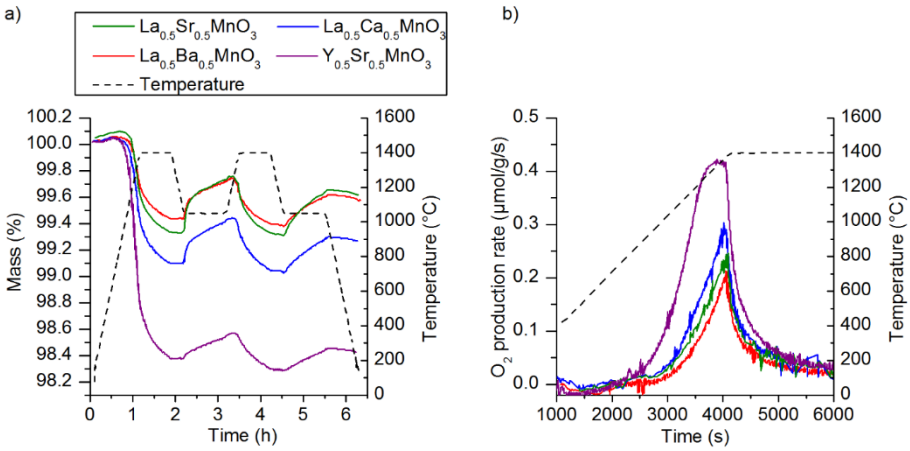

*Figure 1-15: (a) Thermogravimetric analysis (TGA) for $La_{0.5}Ca_{0.5}MnO_3$, $La_{0.5}Ba_{0.5}MnO_3$, $Y_{0.5}Sr_{0.5}MnO_3$, and $La_{0.5}Sr_{0.5}MnO_3$ during reduction at 1400 °C under Ar, followed by oxidation with CO_2 at 1050 °C (two cycles), (**b**) O_2 production rates derived from TGA data of the same materials [125]*

1.5.1.2 B-site substituted materials

As shown previously, lanthanum–manganese perovskites do not show complete re-oxidation. In order to improve the re-oxidation yield, the B-site was doped with aluminum element. The presence of Al also permits to increase the reduction extent [42, 125, 129, 135–137]. In the case of $(La,Sr)MnO_3$ perovskites, the presence of Al^{3+} cation in the B-site permits to increase the reaction kinetics. The introduction of Al^{3+} in the structure leads to strong atomic interaction due to the decrease of the unit cell volume, which leads to a better stability. Nevertheless, it also diminishes the amount of Mn cation, thus reducing the redox capacity [138]. In addition, reduction of $La_{1-x}Sr_xMn_{1-y}Al_yO_3$ has an onset temperature 300 °C lower than CeO_2 revealing a lower reduction enthalpy, which promotes the reduction extent [136]. The presence of Al^{3+} enables the reduction of Mn^{4+} to Mn^{3+} but prevents the reduction of Mn^{3+} to Mn^{2+} [139].

McDaniel et al. [136] performed 80 cycles with $La_{0.6}Sr_{0.4}Mn_{0.6}Al_{0.4}O_3$ and they obtained a constant CO production, proving that the material was not deactivated. Using density functional theory calculation, Deml et al. [140] presented $La_{0.6}Sr_{0.4}Mn_{0.6}Al_{0.4}O_3$ as the optimal composition for thermochemical cycles. In an experimental study using the same material composition, the fuel production was not stable and the re-oxidation yield dropped from 57% to 35% between the first and second cycle for $La_{0.6}Sr_{0.4}Mn_{0.4}Al_{0.6}O_3$ [125]. A low H_2 production for this material was also highlighted by Sugiyama et al. [141]. Furthermore, Nair and Abanades [142] found that the use of Al did not improve the reactivity compared to $La_{1-x}Sr_xMnO_3$ perovskites. The Al^{3+} cation was also used as B-site dopant in $La_{1-x}Ca_xMnO_3$. Takacs et al. [42] found that the O_2 production of $La_{1-x}Ca_xMn_{1-y}Al_yO_3$ was superior to the one of $La_{1-x}Ca_xMnO_3$ and $La_{1-x}Sr_xMn_{1-y}Al_yO_3$. However, the oxidation temperature must be lower than 850 °C for a complete re-oxidation, which induces energy penalty due to the necessity to reheat the material [135]. The optimal composition was found to be $La_{0.6}Ca_{0.4}Mn_{0.6}Al_{0.4}O_3$ which produces more hydrogen (429 µmol/g) than ceria (56 µmol/g) in similar experimental conditions (reduction at 1400 °C, oxidation at 1000 °C) [143]. For both $La_{1-x}Ca_xMnO_3$ and $La_{1-x}Sr_xMnO_3$ with Al dopant on the B-site, it was also proved that the presence of the dopant in the B-site avoids the carbonate formation at low temperature during CO_2 splitting [144].

Gallium was also considered as B-site dopant in $La_{1-x}Ca_xMnO_3$. The introduction of Ga^{3+} allowed increasing O_2 and CO production. The $La_{0.6}Ca_{0.4}Mn_{0.8}Ga_{0.2}O_3$ perovskite produced 212 µmol/g of O_2, while the undoped perovskite produced only 167 µmol/g (at T_{red} = 1300 °C). During the oxidation step at 900 °C, the Ga-doped perovskite produced 401 µmol/g of H_2 whereas the undoped perovskite produced 339 µmol/g. The fuel production was promoted by the high specific surface area of the perovskite, as it favors solid–gas interactions. However, the substitution of Mn by Ga was limited to 30% in the Sr-doped lanthanum–manganese perovskite [145].

The beneficial effect of the Mg^{2+} cation as dopant in the B-site of $La_{1-x}Sr_xMnO_3$ was also highlighted [125]. Mg^{2+} does not participate to the redox reactions, but it improves the resistance to sintering and the thermal stability. It can be noticed in Figure 1-16 that during the first cycle $La_{0.6}Sr_{0.4}Mn_{0.4}Al_{0.6}O_3$ produced the highest CO amount while $La_{0.6}Sr_{0.4}Mn_{0.83}Mg_{0.17}O_3$ kept the highest CO production during the second cycle, showing a stable fuel production upon two cycles (209 and 207 µmol/g, respectively). Furthermore, the use of Mg permits to reduce grain growth during cycles and to obtain smaller grain size compared to the undoped perovskite. Smaller grain sizes induce higher specific surface areas, and thus, promote the oxidation step. Notwithstanding this effect, the use of Mg dopant is limited to ~15–20% due to its low solubility [125].

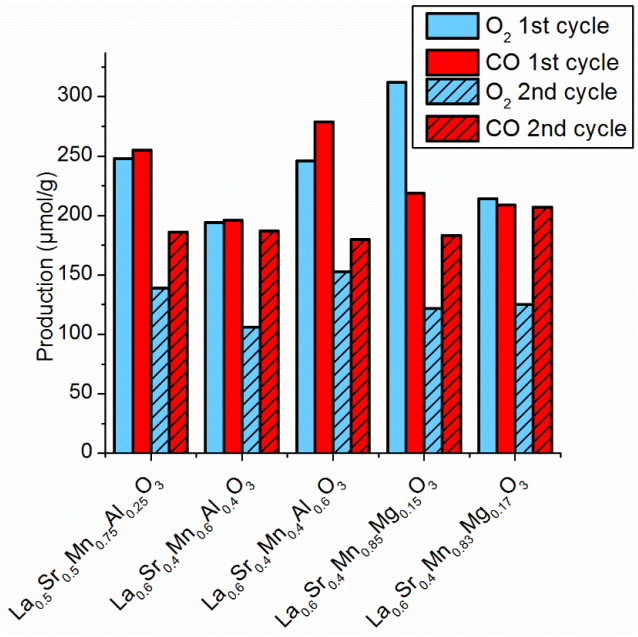

Figure 1-16: Comparison of O_2 and CO productions for $La_{1-x}Sr_xMn_{1-y}Al_yO_3$ and $La_{1-x}Sr_xMn_{1-y}Mg_yO_3$ perovskite series (T_{red} = 1400 °C and T_{ox} = 1050 °C) [125]

Scandium was also considered as B-site dopant in Sr-doped lanthanum–manganese perovskite, but its content was limited to 10% due to its low solubility. Despite this, the introduction of only 5% of Sc increases the O_2 production by a factor of two when compared with $La_{0.5}Sr_{0.5}MnO_3$, according to Dey et al. [146]. However, the authors also present an almost full and very fast re-oxidation whatever the investigated materials, which may be due to flaws in the experimental procedure given that the re-oxidation with either H_2O or CO_2 is never complete for such materials (as opposed to the re-oxidation with O_2). Accordingly, the presence of residual oxygen in the system when switching the gas atmosphere must be avoided in order to prevent the swift material re-oxidation. Thus, the observed mass gain may not be attributed to CO_2 splitting only, and a quantification by gas analysis of the amount of CO produced would be necessary to confirm the results.

The $La_{1-x}Sr_xMn_{1-y}Fe_yO_3$ perovskite was also investigated [147]. The starting reduction temperature of this perovskite was reduced when increasing the Fe content, which in turn promoted the reduction extent. As an illustration, $La_{0.6}Sr_{0.4}Mn_{0.8}Fe_{0.2}O_3$ produced 286 µmol/g of O_2 at 1350 °C while $La_{0.6}Sr_{0.4}Mn_{0.2}Fe_{0.8}O_3$ produced 333 µmol/g. The CO amount produced tended to decrease with the increase of the Fe content. For instance, $La_{0.6}Sr_{0.4}MnO_3$ doped with 20% Fe produced 329 µmol/g of CO while $La_{0.6}Sr_{0.4}MnO_3$ doped with 60% Fe produced 277 µmol/g [147].

In order to improve the fuel production during the re-oxidation step, Mn substitution by Cr ion was investigated. $La_{0.7}Sr_{0.3}Mn_{0.7}Cr_{0.3}O_3$ was reported by Sugiyama et al. [141] to yield a similar O_2 production as $La_{0.7}Sr_{0.3}Mn_{0.7}Al_{0.3}O_3$ but a higher H_2 production. The presence of Cr in the B-site permits to increase the oxidation extent when compared to Al.

1.5.2 Lanthanum–cobalt perovskites

Lanthanum–cobalt perovskites were studied in thermochemical cycles. $LaCoO_3$ presents a high O_2 production (369 µmol/g at T_{red} = 1300 °C) during the first reduction step. However, the CO production is low and it decreases quickly over cycles: 86 and 22 µmol/g of CO during the first and second cycles, respectively [134].

Lanthanum–cobalt perovskites substituted in the A or/and B-site were investigated. Regarding the impact of Ca dopant in the A-site, the increase of Ca content promoted oxygen production (715 µmol/g for $La_{0.8}Ca_{0.2}CoO_3$ and 1213 µmol/g for $La_{0.2}Ca_{0.8}CoO_3$ at 1300 °C). Figure 1-17.a reveals that the increase of Ca content increases the O_2 production rate. Nonetheless, the H_2 production dropped for Ca content above 40%, as shown in Figure 1-17b. For example, the H_2 production was 587 µmol/g for 40% Ca content versus only 204 µmol/g for 80% Ca content at 900 °C. Wang et al. [148] selected $La_{0.6}Ca_{0.4}CoO_3$ as the most promising material among Ca-doped lanthanum–cobalt perovskites according to both O_2 and CO production.

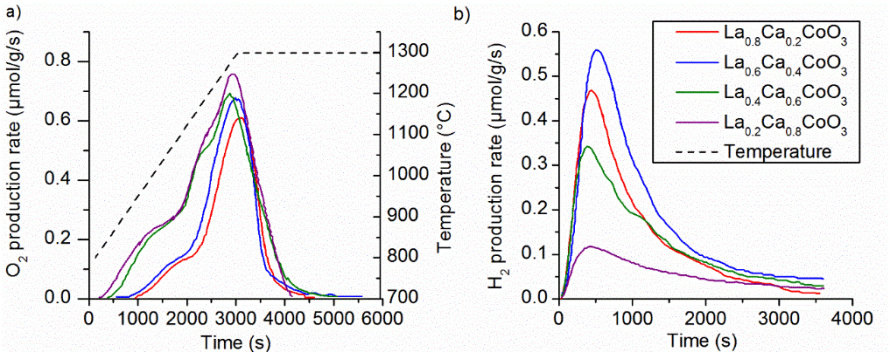

*Figure 1-17: (**a**) O_2 production rate (T_{red} = 1350 °C) and (**b**) H_2 production rate (T_{ox} = 900 °C), for $La_{0.8}Ca_{0.2}CoO_3$, $La_{0.6}Ca_{0.4}CoO_3$, $La_{0.4}Ca_{0.6}CoO_3$, and $La_{0.2}Ca_{0.8}CoO_3$ [148].*

Substitution of lanthanum by Sr in lanthanum–cobalt perovskites was also considered. The $La_{0.8}Sr_{0.2}CoO_3$ perovskite presents a mass loss (1.5%) higher than $La_{0.8}Sr_{0.2}MnO_3$ (0.1%), meaning a higher reduction extent [149]. Furthermore, $La_{0.6}Sr_{0.4}CoO_3$ offers higher H_2 production (514 µmol/g) than $La_{0.6}Sr_{0.4}MnO_3$ (234 µmol/g) [150]. However, Orfila et al. [63] highlighted a decrease of the production after four consecutive cycles, due to the formation of a pure Co oxide phase that impairs both O_2 and CO/H_2 production [149]. In addition, Demont et al. [121] pointed out a partial decomposition of the $La_{0.8}Sr_{0.2}CoO_3$ perovskite to form a Ruddlesden–Popper phase according to reaction (26). However, Ruddlesden–Popper phases are subjected to topotactic oxygen release which can be suitable for thermochemical cycles [121].

$$2(La,Sr)CoO_3 \rightarrow (La,Sr)_2CoO_4 + CoO + 1/2\ O_2 \qquad (26)$$

Iron was also investigated as another dopant in lanthanum–cobalt perovskites. It appears that the presence of Fe decreases the oxygen production. For example, $LaCoO_3$ releases 369 µmol/g of O_2 at 1300 °C, whereas $LaFe_{0.75}Co_{0.25}O_3$ releases 59 µmol/g. In addition, the oxidation step was not enhanced by the introduction of Fe. Nair and Abanades [134] emphasized that the use of Fe as dopant in $LaCoO_3$ neither improves the perovskite stability, nor the re-oxidation yield.

In addition to the use of Fe dopant in B-site, the introduction of Sr in the A-site was tested. It tends to enhance the reduction extent reached by the reactive material but the CO production yield remains low (90 µmol/g) and decreases over cycles [121, 134].

$La_{1-x}Sr_xCo_{1-y}Cr_yO_3$ was also studied for fuel production. Bork et al. [151] noticed that the increase of Co content promoted the O_2 production. In addition, increasing the Co content up to 20% increased the CO production. An optimum composition was thus deduced for fuel production: $La_{0.6}Sr_{0.4}Co_{0.2}Cr_{0.8}O_3$. This perovskite offered a CO production of 157 µmol/g with a reduction temperature of 1200 °C and an oxidation temperature of 800 °C. This performance is similar to ceria (CO production: 168 µmol/g) with reduction and oxidation temperatures of 1500 °C and 1000 °C, respectively. Thus, comparable CO production as ceria can be obtained with $La_{0.6}Sr_{0.4}Co_{0.2}Cr_{0.8}O_3$ at lower temperatures.

1.5.3 Yttrium–manganese perovskites

Strontium was studied as a B-site dopant in yttrium–manganese perovskites. $Y_{0.5}Sr_{0.5}MnO_3$ shows a reduction extent higher (539 µmol/g of O_2 produced) than $La_{0.5}Sr_{0.5}MnO_3$ (256 µmol/g of O_2 produced) in similar conditions [142]. The improvement of the reduction extent can be explained by a smaller ionic radius of Y^{3+} ($r = 1.08$ Å [40]) in comparison with La^{3+} ($r = 1.36$ Å [152]). Demont and Abanades [125] observed that the O_2 production peak was reached at 1315 °C (Figure 1-15a), suggesting that the reduction temperature can be lowered without diminishing the O_2 production. Nair and Abanades [142] also pointed out a low re-oxidation yield (14%), which is in agreement with Rodenbough and Chan [153].

Substitution of yttrium by calcium was also investigated, yielding $Y_{1-x}Ca_xMnO_3$ perovskite. Both yttrium and calcium tend to increase the reduction extent in comparison with lanthanum and strontium, respectively. The O_2 production was 573 µmol/g for $Y_{0.5}Ca_{0.5}MnO_3$ (at T_{red} = 1400 °C) while it was only 312 µmol/g and 481 µmol/g for $La_{0.5}Ca_{0.5}MnO_3$ and $Y_{0.5}Sr_{0.5}MnO_3$, respectively [130].

1.5.4 Other perovskites

The most largely investigated perovskite series were presented in the previous sections. Other perovskites were also investigated as reactive materials in thermochemical cycles such as $BaMn_{1-y}Ce_yO_3$. It was highlighted that the $BaCe_{0.25}Mn_{0.75}O_3$ formulation had higher reduction ability than ceria for a temperature below 1400 °C. Furthermore, this perovskite produces three times more H_2 (140 µmol/g) than ceria with a reduction temperature of 1350 °C and an oxidation temperature of 850 °C. Compared with $La_{0.6}Sr_{0.4}Mn_{0.6}Al_{0.4}O_3$ perovskite, $BaCe_{0.25}Mn_{0.75}O_3$ offers similar production, but its oxidation kinetics are faster. Barcellos et al. [154] investigated the ability of this material to produce H_2 under high-conversion conditions. The H_2O:H_2 ratio required to drive the thermochemical cycle has to be below 1000:1. To realize this condition, different H_2O:H_2 ratios were used in the reaction chamber. $La_{0.6}Sr_{0.4}Mn_{0.6}Al_{0.4}O_3$ showed a rapid decrease of H_2 production with the decrease of H_2O:H_2 ratio and H_2 production stopped for H_2O:H_2 < 500, whereas $BaCe_{0.25}Mn_{0.75}O_3$ also showed a decrease of H_2 production as the H_2O:H_2 ratio decreased but it still had comparable H_2 production as ceria with a H_2O:H_2 ratio of 285. The fuel productions for $La_{0.6}Sr_{0.4}Mn_{0.6}Al_{0.4}O_3$, $BaCe_{0.25}Mn_{0.75}O_3$, and ceria under

various H_2O:H_2 ratios are illustrated in Figure 1-18. Thus, $BaCe_{0.25}Mn_{0.75}O_3$ perovskite is able to perform water splitting under milder conditions in the aim of future large-scale implementation [154].

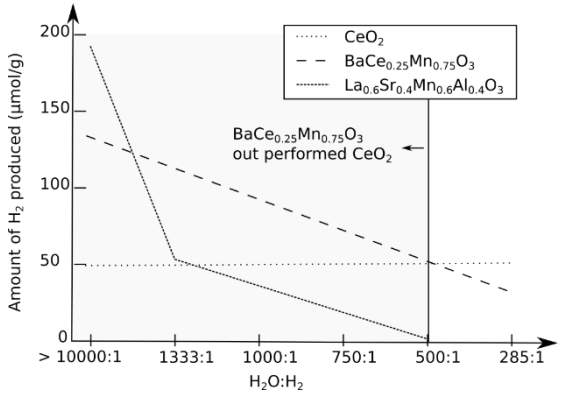

Figure 1-18: H_2 production as a function of the H_2O:H_2 ratio for $La_{0.6}Sr_{0.4}Mn_{0.6}Al_{0.4}O_3$, $BaCe_{0.25}Mn_{0.75}O_3$, and ceria at T_{red} = 1350 °C and T_{ox} = 850 °C (adapted from Reference [154]).

The influence of the cation in A-site was studied by Dey *et al.* [130] who tested a set of perovskites in the series $Ln_{0.5}A_{0.5}MnO_3$ (Ln = La, Nd, Sm, Gd, Dy, Y, and A = Sr, Ca). They showed that the decrease of the rare-earth ionic size improves the reduction extent. Consequently, the maximal O_2 production was reached by $Y_{0.5}Ca_{0.5}MnO_3$ (573 µmol/g) and $Y_{0.5}Sr_{0.5}MnO_3$ (481 µmol/g), because yttrium has the smallest ionic radius among the rare-earth tested. As a comparison, $La_{0.5}Ca_{0.5}MnO_3$ and $La_{0.5}Sr_{0.5}MnO_3$ produced 312 µmol/g and 198 µmol/g of O_2, respectively, in the same experimental conditions (T_{red} = 1400 °C). Nair and Abanades [134] found that the re-oxidation yield was very low (10% for $Y_{0.5}Sr_{0.5}MnO_3$). The very low re-oxidation extent for $Y_{0.5}Sr_{0.5}MnO_3$ in comparison with $La_{0.5}Sr_{0.5}MnO_3$ and $La_{0.5}Ca_{0.5}MnO_3$ can be observed in Figure 1-19.

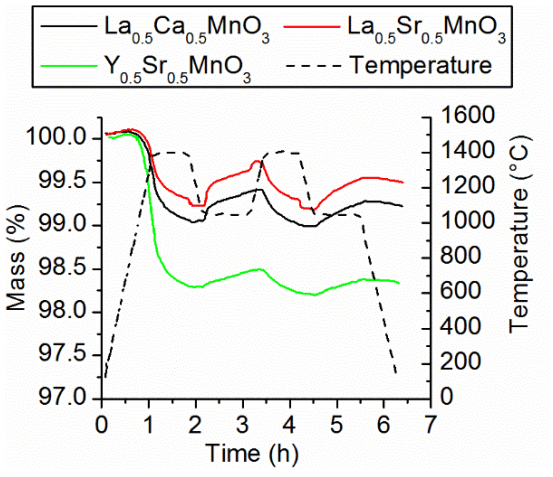

Figure 1-19: TGA of $La_{0.5}Sr_{0.5}MnO_3$, $La_{0.5}Ca_{0.5}MnO_3$, and $Y_{0.5}Sr_{0.5}MnO_3$ during two thermochemical cycles (T_{red} = 1400 °C and T_{ox} = 1050 °C) [134].

The $Ba_{1-x}Sr_xFeO_3$ perovskite was also studied for thermochemical cycles. This perovskite showed a high reduction extent (582 µmol/g of O_2 produced) with a low reduction temperature (1000 °C), and it was able to produce CO (136 µmol/g) in an isothermal cycle (1000 °C).

Nevertheless, a low stability was observed for this perovskite, with decreasing CO production [134].

Wang et al. [150] studied the impact of the cation (Cr, Mn, Fe, Ni, and Co) occupying the B-site of Sr-doped lanthanum perovskites. They reported that the $La_{0.6}Sr_{0.4}CoO_3$ perovskite can accommodate more oxygen vacancies than $La_{0.6}Sr_{0.4}BO_3$ perovskites (with B = Cr, Mn, Fe, and Ni), which is due to a low energy of oxygen vacancy formation. Furthermore, $La_{0.6}Sr_{0.4}CoO_3$ presents a lower onset temperature (~900 °C) than $La_{0.6}Sr_{0.4}MnO_3$ (~1020 °C) in similar conditions. The reported H_2 production is also higher for $La_{0.6}Sr_{0.4}CoO_3$ (514 µmol/g) at 900 °C (with T_{red} = 1300 °C) than for other $La_{0.6}Sr_{0.4}BO_3$ perovskites (Ni: 368 µmol/g; Fe: 349 µmol/g; Cr: 280 µmol/g and Mn: 234 µmol/g) [150].

To date, a large number of perovskite formulations have been studied for thermochemical cycles, and the most important results are summarized in Table SA-2. Perovskites can accommodate a wide range of oxygen non-stoichiometry. However, the high vacancy formation ability is usually associated to a slow re-oxidation step, impeding complete re-oxidation and resulting in low CO/H_2 production rates. In other words, a favored reduction capability can be obtained at the expense of lower oxidation extent and vice-versa. A compromise between maximum achievable oxygen non-stoichiometry and fuel production yield has to be considered, and the key outcomes may arise from an optimization of the perovskite's composition. The recent results presented above show that the high number of possible perovskite formulations leaves space for the finding of suitable materials for thermochemical cycles.

1.6 Morphology

The solar-to-fuel energy conversion efficiency is not only influenced by the chemical composition of the reactive compound, but also by the material shaping that mostly determines the available surface area for the solid/gas reaction (the material oxidation mechanism is mainly governed by surface reaction). The diffusion length and specific surface area affect respectively the reduction and oxidation steps. They depend on the morphology of the reactive material. Accordingly, the main relevant options for materials shaping are summarized in this section.

1.6.1 Felts and fibers

Furler et al. [67] used porous CeO_2 felt to perform thermochemical cycles. Over ten cycles, 2.89 mL/g of O_2 and 5.88 mL/g of fuel were produced in average. Due to low heat absorption and the presence of hot spots, ceria sublimates and forms an opaque film on the optical window, contributing to a decrease of temperature. The solar-to-fuel efficiency was 0.09% for ten consecutive cycles [67]. Such a low efficiency was attributed to the low thermal conductivity of the felt, leading to heat transfer limitations. Hence, the reaction is mainly limited to the near surface directly exposed to the concentrated sunlight [45, 155].

Gibbons et al. [156] investigated electrospun ceria-based fibers in order to maintain both high surface area and small grain sizes. The fiber diameter is in the range 100 nm–2 µm. The oxidation reaction kinetic was increased by the specific surface area of the fibers. The electrospun structure impedes the sintering responsible for the decreasing production of fuel

over cycles. The specific surface area of $Ce_{0.975}Zr_{0.025}O_2$ drops to 0.60 m^2/g after a thermal reduction at 1400 °C. This is mainly due to an increase of grain sizes along the fiber axis. However, the decrease of specific surface area does not cause a decrease in CO production. During long-term cycling, the CO production rate declines from 30 after few cycles to 13–14 mL min^{-1} g^{-1} after 60 cycles [156].

Gladen and Davidson [157] studied the use of ceria fibers made with a commercially suitable manufacturing process for the aim of producing fibers applicable to different reactor types. In isothermal conditions (1500 °C), the microstructure was still open and porous with a porosity of 73% after 1000 cycles, although the specific surface area dropped from 0.143 to 0.078 m^2/g. Regardless of the weak surface area, the fiber-mat design remained an appropriate strategy in isothermal conditions, as fuel production was governed by thermodynamics. In the case of temperature-swing redox cycling (from 800 to 1500 °C), the specific surface area dropped to 0.057 m^2/g after 1000 cycles. However, the open and porous structure of the fiber-mat was still retained [157].

1.6.2 Reticulated porous foams

In order to avoid the inherent limitations induced by the use of a felt material, several studies focused on the application of reticulated porous foams [2, 45, 46, 155, 157–162]. The use of ceria-based reticulated porous ceramics (RPC) with a macroporous structure (mm-pore sized) improves the penetration and the volumetric absorption of incident concentrated solar radiation. In this way, the temperature gradient through the foam structure is lowered, thus promoting O_2 production during homogeneous reduction of the whole loaded material [45]. The reduction duration of RPC ceria was predicted to be in the order of seconds, namely longer than with reactive particles due to the longer bulk diffusion lengths [50]. Furler et al. [159] obtained a solar-to-fuel energy conversion efficiency of about 1.73% (with 2.8–3.8 kW power input), almost 17 times higher than for ceria felt. However, the maximal fuel production rate was 9 times lower for a RPC foam than for a felt. The oxidation reaction is a surface-controlled reaction and the RPC structure has a low specific surface area, yielding slow oxidation rates [159]. Takacs et al. [160] obtained the highest heat transfer with large pore sizes, i.e., foam with 8 pores per inch (ppi), although the highest O_2 amount produced was obtained with a 10 ppi foam thanks to its higher pore density [160]. Cho et al. [161] developed a MgO partially-stabilized zirconia foam coated with reactive ceria to perform thermochemical cycles. Over seven cycles, the foam produced 4573 mL of H_2 in total (for 82.88 g of loaded reactive ceria), with a reduction temperature in the range 1400–1600 °C and an oxidation temperature in the range 900–1100 °C [161].

Foams with only macropores feature good solar absorption properties, thus promoting the reduction step. However, the oxidation step is not favored due to the poor specific surface area of the reticulated foam. In order to improve the oxidation rate, dual-scale porosity RPC foams were developed by Furler et al. [158] with combined macro-scale (mm-pore sized) and micro-scale porosity (µm-pore sized). Firstly, millimetric pores permit volumetric absorption of concentrated sunlight and efficient heat transfer to the reactive material. Secondly, micrometric

pores improve the specific surface area, which promotes the oxidation step by improving the reaction kinetics [2, 46, 158, 162]. Furler et al. [158] obtained reduced cycling time and solar-to-fuel efficiency of 1.72% without sensible heat recovery [158]. Marxer et al. [2] carried out 291 cycles with stable redox performance, yielding the production of 700 NL of syngas. The reactive material undergoes sintering, resulting in an increase of grain size, but micro-scale pores still remain open. Dual-scale RPC provides faster oxidation rate (0.75 mL min^{-1} g^{-1}) and higher fuel amount produced (4.41 mL/g) in comparison with single-scale RPC (0.37 mL min^{-1} g^{-1} and 4.11 mL/g, respectively). However, regarding the study of Marxer et al. [2], the mass loaded of dual-scale RPC in the reactor (948 g) is lower than the one of single-scale RPC (1413 g). This leads to an absolute amount of CO produced by dual scale RPC (4.18 L) lower than for single scale RPC (5.80 L) [2]. It should be noticed that the use of polymer templates to synthesize the reticulated porous foams is not environmentally friendly and should be replaced by bio-based templates for proposing sustainable processes.

1.6.3 Nanostructured powders

Venstrom et al. [163, 164] developed a nanocrystalline three-dimensionally ordered macroporous (3DOM) ceria powder. The powder has a surface area of 29.9 m^2/g before cycling with average grain sizes of 14 nm and an interconnected ordered porous network. The authors carried out the reduction at 1100 K under 5% H_2 in Ar, followed by an isothermal oxidation with either H_2O or CO_2 [163, 164]. In comparison with commercial ceria powder, the H_2 (CO) production rate is 126% (260%) faster with 3DOM powder, as observed in Figure 1-20. This is due to the high specific surface area (10.2 m^2/g) of the 3DOM powder remaining after the reduction. The powder morphology clearly affects the oxidation kinetic. However, the amount of fuel produced is comparable between the 3DOM and the commercial powder (23 Ncm^3/g of CO and 20 Ncm^3/g of H_2). However, the ordered structure is not stable after 1h thermal treatment at 1250 °C, but porosity is still present [163].

Costa Oliveira et al. [165] investigated 3DOM ceria particles prepared from cork template. The CO production of the 3DOM structure is twice higher than with reticulated porous ceria, proving that the 3DOM morphology enhances oxidation kinetic. Ceria granules were able to produce stable amount of CO over 11 solar-driven cycles and the ordered structure was retained after cycling. The CO peak production rate of 3DOM particles was three times higher than the value reported for dual-scale reticulated porous ceria [165].

Hierarchical pore structure of ceria was developed by Malonzo et al. [166] using wood template. The structure, consisting of micrometer-thick walls, pore size of 10 µm and a specific surface area of 0.1 m^2/g, is retained after undergoing cycles up to 1400 °C. For a reduction temperature of 1500 °C, the CO production rate decreases due to an important decrease of the specific surface area. The CO production rate of nanostructured ceria was observed to be 6 times higher than for non-porous ceria, with a reduction temperature of 1400 °C. It is similar to electrospun fibers under comparable operating conditions. Furthermore, the density of wood-templated ceria is higher than for fibers, allowing the loading of more reactive material. The performance stability of the wood-templated ceria was demonstrated by conducting 21 cycles [166].

To some extent, the advantages of nanostructured powders in terms of reactivity and kinetics can be constrained by some issues. Indeed, homogenous heating of the reactive powders is challenging and their processing in two-step cycles may require particle transport to carry out both reaction steps.

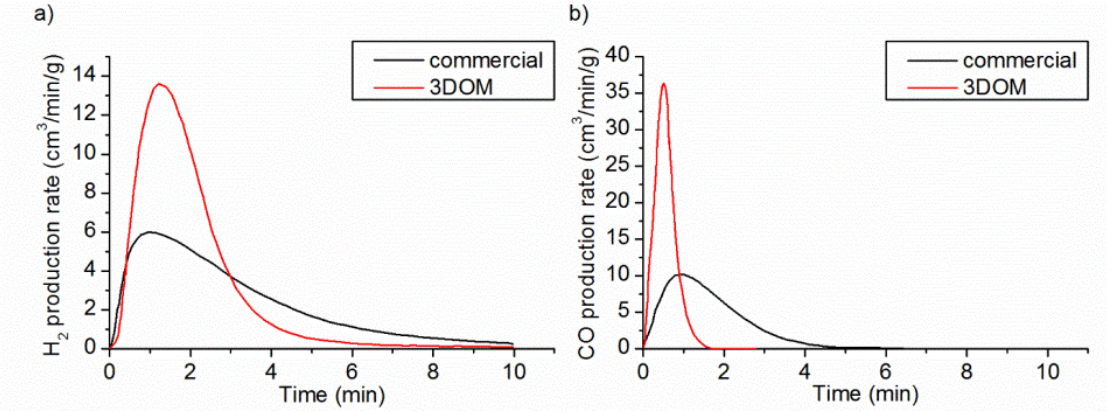

Figure 1-20 : Comparison between 3DOM and commercial ceria powders performance in thermochemical cycles : (a) H_2 production rate and (b) CO production rate, oxidation at 1100 °C [163]

In summary, the shaped materials should provide a good solar absorptivity favoring homogeneous heating, along with a high specific surface area favoring solid-gas reactions. A long-term thermal stability is also required for the considered ceria structures regardless of the involved shaping method. To achieve an economically viable solar fuel production, the enhancement of the thermochemical performance must be balanced with the additional cost caused by the materials shaping.

1.7 Solar reactors

The design of the solar reactor is also a key parameter in the thermochemical performance of redox cycles, as it directly impacts the heat losses, therefore the solar-to-fuel conversion efficiency. The reactor should be able to provide solar thermal energy as well as reactant gases to the reactive material with the minimum heat dissipation while maintaining its structural integrity. In this section the principal solar reactors used for two-step thermochemical cycles are presented [3].

1.7.1 Monolithic reactors

The monolithic solar reactor used self-supported reactive materials. Cho et al. [161] designed a 45 kW_{th} solar reactor to perform two-step thermochemical cycles using inert zirconia foam coated with reactive ceria, as presented in Figure 1-21. The solar reactor consisted of a cylindrical stainless-steel body sealed by a quartz window to allow the concentrated sunlight to access the solar absorber cavity. This cavity was placed at the reactor center and the reactive RPC (reticulated porous ceramic) was placed inside. An inert zirconia foam partially stabilized by MgO was coated with CeO_2 (20 wt%) and used as reactive material. The temperature measurements were achieved by thermocouples placed at different locations of the foam. Thermochemical cycles were typically performed at reduction temperatures in the range 1400-

1600°C, followed by an oxidation at 900-1100°C with water as oxidant gas. The highest H_2 production achieved 443 mL for 190 g of ceria.

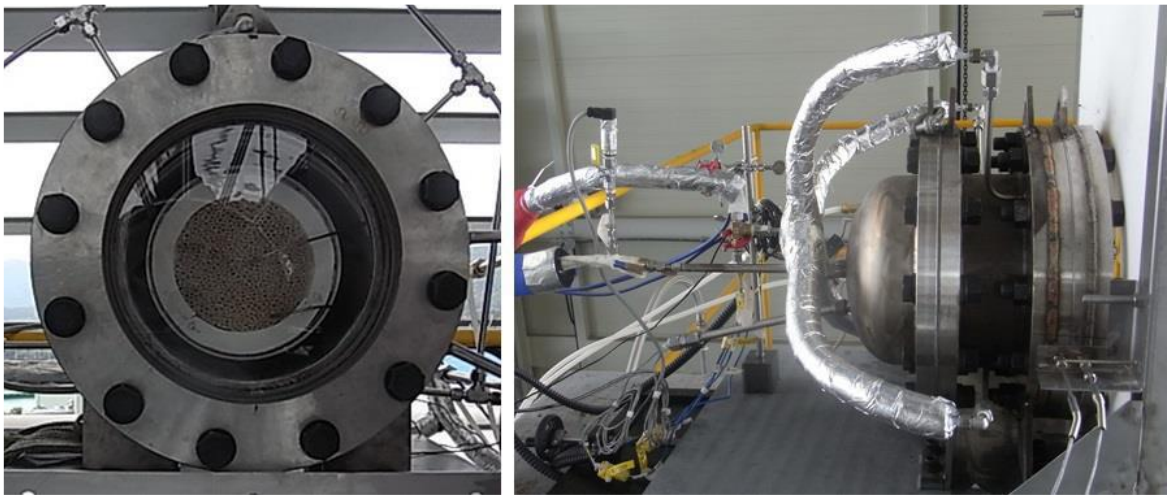

Figure 1-21: Photographs of the monolithic solar reactor developed by Cho et al. [161]

A 4.4 kW isothermal reactor performing CO_2 splitting was developed by Hathaway et al. [167, 168], as illustrated in Figure 1-22. The reactor was composed of two parts: a solar receiver cavity and a heat recovery section. Co-axial dense alumina tubes were placed in the cavity and directly heated by the concentrated solar radiation. Six tubular assemblies were placed in the cavity. They were composed of an outer dead-end tube and an inner open tube. The annular region present in the cavity was filled with ceria particles to form a packed bed. The other portion of the assembly was filled with reticulated porous ceramic made of alumina acting as a heat recovery system. During the reduction, an inert gas swept the tubular assemblies (from the inlet tube to the annular region, Figure 1-22) and the inert gas was switched to CO_2 during the oxidation step. CO was produced continuously by alternating the reaction in the assembled tubes. A solar simulator was used to heat the reactor. At 1750 K in steady state, the CO production rate reached 360 mL/min (*i.e.* 0.1 mL/min/g) over 45 cycles. The solar-to-fuel conversion efficiency achieved 1.64%. The authors pointed out a theoretical limit of 2 % efficiency for isothermal CO_2 splitting, making the isothermal approach inappropriate for thermochemical cycles. Instead, they suggested to develop heat recovery system and non-isothermal process with continuous fuel production [167, 168].

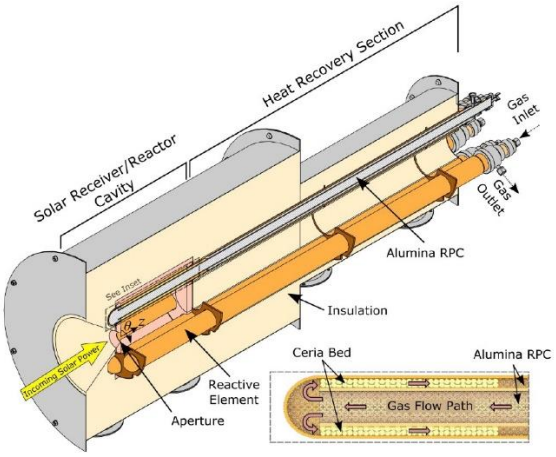

Figure 1-22: Isothermal solar reactor using a heat recovery system developed by Hathaway et al. [167]

At ETH Zürich, a monolithic reactor was developed using reticulated porous ceramic made of ceria (Figure 1-23). The reactive foam structure was located at the bottom and the walls of the cavity to allow for a good volumetric absorption of the concentrated radiation and uniform heating. A quartz window sealed the reactor, allowing the concentrated radiation to reach the cavity. During the reduction step, the temperature was in the range 1450-1500°C and the pressure was in the range 10-1000 mbar. During the oxidation step, the reactor was freely cooled and CO_2 was injected for temperatures in the range 700-1000°C. With this reactor, the authors achieved the benchmark solar-to-fuel energy conversion efficiency of 5.25% with a peak CO production rate at 1.2 mL/min/g for a reduction at 1500°C under 10 mbar, with dual-scale porosity foam made of ceria [46].

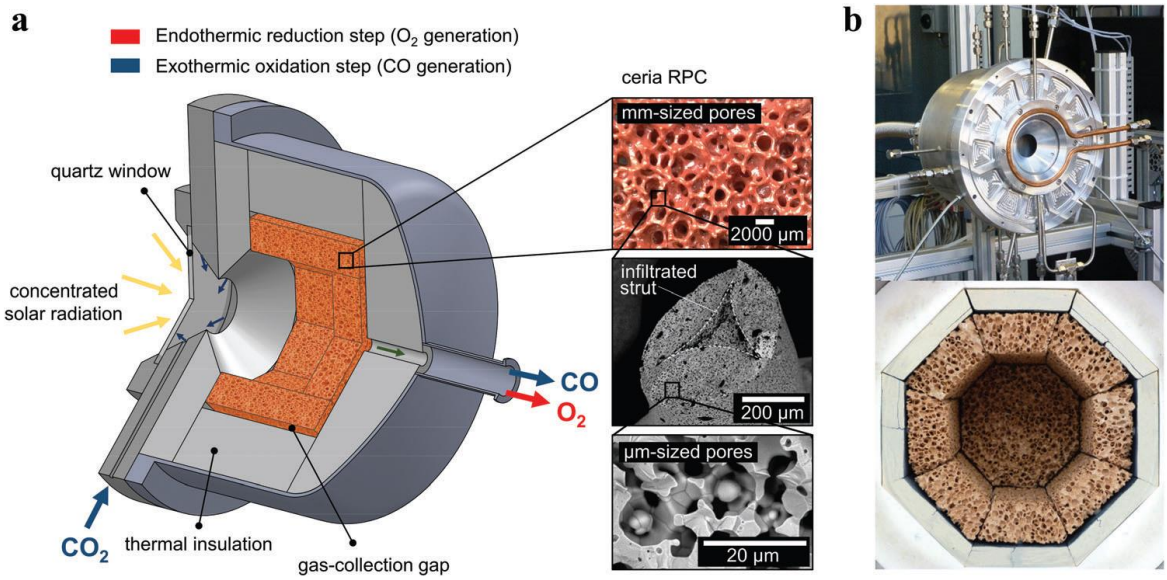

Figure 1-23: a) schematic and b) photographs of the monolithic solar reactor developed at ETH Zürich [46]

A solar reactor using counter-rotating rings coated with reactive material was proposed by Diver et al. [169, 170], using ferrite as oxygen carrier. The upper part of the rings was heated by concentrated light and the reduction occurred, whereas the oxidant gas swept the lower part of the rings, resulting in fuel production. The slow rotation of the rings moved the oxygen

carrier material alternatively to the reduction and oxidation chambers. In addition, the counter rotation of the rings in opposite direction permits heat recovery. With this system, the solar-to-fuel conversion efficiency achieved 29.9 % [170].

1.7.2 Particle reactors

Particle reactors use dispersed particles as reactive materials. They can be used to perform the reduction and the oxidation reactions separately in different reaction chambers, which is advantageous due to the different reaction kinetics in order to optimize the fuel production.

Koepf et al. [171] proposed beam-down reactor at experimental scale, as illustrated in Figure 1-24. The reactor used reactive particles that were fed by the top and carried to the cavity center with gravity and vibrations, while being heated, forming a moving bed. The reactor was tested with ZnO particles. When the particles were reduced, the resulting Zn vapor was recovered at the gas exit (⑦ in Figure 1-24), whereas unreacted particles were recovered at the annular region of the gas exit (⑤ in Figure 1-24).

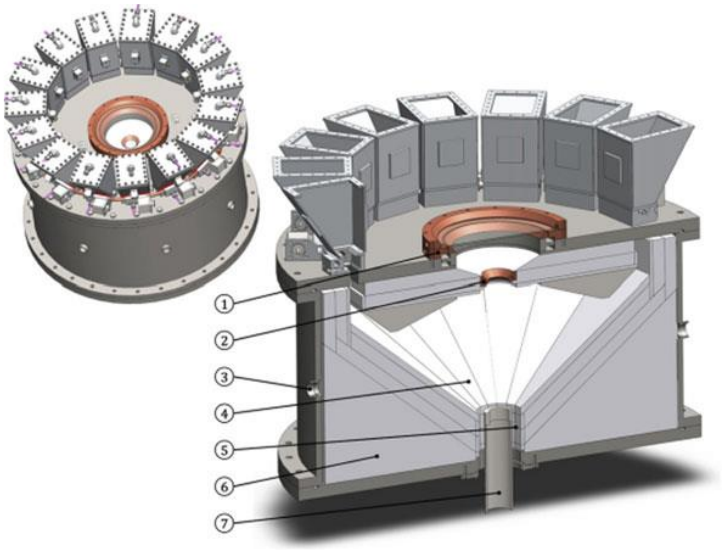

Figure 1-24: Gravity-fed particles solar reactor proposed by Koepf et al. [171]

A fluidized bed reactor using $NiFe_2O_4$ or CeO_2 particles was also proposed by Gokon et al. [172]. The reactive particles were placed in the cavity and directly irradiated by the concentrated light provided by a solar simulator. They were fluidized by a gas injection from the reactive chamber bottom, and a draft tube was placed at the center of the chamber to favor the intermixing. The reduction and the oxidation steps were alternatively performed in the same cavity. However, non-homogeneous heat distribution occurred in the reactor, limiting the thermochemical performance. Ermanoski et al. [173] developed another particle-based reactor concept. The reactor featured distinct reduction and oxidation chambers, where the reactive particles were transported between them by a screw elevator. The rotating part of the reactor was pointed out as a major drawback of this concept due to the risk of failure at high temperature [174]. Chambon et al. [175] proposed a moving-front piston reactor to perform the reduction of volatile oxides. They used pellets of ZnO and SnO_2 as reactive materials. The reactor was composed of a solar absorber cavity irradiated by concentrated sunlight through a window. The

reactive pellets were carried in the cavity with an ascending piston. During the reduction, the reduced species (Zn or SnO) volatilized and were transported by the carrier gas for quenching. Then the solid particles were condensed and recovered in a filter, to be re-oxidized in a further step [175].

1.8 Conclusion

Thermochemical redox cycles are promising for converting solar energy into chemical energy in the form of sustainable solar fuels that can be stored long-term, transported long-range, and used on-demand. In order to enhance global energy conversion efficiency, the optimization of the reactive material is required.

Ceria is the benchmark material for thermochemical fuel production due its ability to produce oxygen vacancies while retaining its fluorite structure during reversible oxidation states, and its oxidation is thermodynamically favorable. Different studies investigated the thermodynamic and kinetic properties of ceria during thermochemical cycles. The oxygen non-stoichiometry reachable by ceria is the main issue limiting the fuel production yield. To enhance its overall reduction extent, numerous dopants were studied for improving oxygen mobility. The most promising are Zr^{4+}, Hf^{4+} and Sc^{3+} cations and their incorporation is generally beneficial to the reduction step, by increasing the reduction extent. However, it has generally a negative impact on the oxidation step, with a decrease of both the oxidation rate and the re-oxidation yield. The cation doping process requires carefully considering solubility, phase diagrams and phase stability.

As alternative redox materials, perovskites represent a promising class of materials for thermochemical fuel production cycles. Such materials have a high thermal stability and can accommodate large oxygen non-stoichiometry in their structure owing to high oxygen exchange properties, thereby allowing for large fuel production. Furthermore, the reduction temperature can be decreased compared with other materials like ceria, while keeping comparable fuel productivities. The main drawback associated with the use of perovskites is generally the incomplete re-oxidation yield due to low kinetics and low thermodynamic driving forces. The large number of possible perovskite formulations and the discovery of novel materials make possible tuning the redox properties to optimize the fuel production. Perovskites based on lanthanum–manganese, lanthanum–cobalt, yttrium–manganese associated with different dopants (Al, Ga, Ba, Mg, Sr, Ca, Ce, Cr, Fe) are the principal materials that were studied for thermochemical cycles application. Therefore, perovskites constitute a promising class of materials in the context of solar thermochemical fuel production. Further advancements in the discovery and characterization of new and better performing redox materials are of critical importance, while complying with: favorable thermodynamics, rapid reaction kinetics, and crystallographic stability over thermochemical cycling.

Another important parameter influencing the fuel production capability is the material shaping and design. Different morphologies including fibers, felts, nanostructured powders, and reticulated porous foams (with single and dual-scale porosity) have been considered in the literature. The fiber and felt materials have a high specific surface area that favors the oxidation

step. Nevertheless, the solar absorption in the structure volume is low, yielding temperature gradients into the material and limiting the reduction step efficiency. On the contrary, reticulated porous foams with single-scale porosity (mm-pore size) show good solar radiation absorption, which favors the reduction step. However, their oxidation is limited due to the low specific surface area. To further improve the oxidation rate, micro-scale porosity has been introduced in reticulated porous foams (dual-scale foam) to increase the specific surface area while enabling volumetric solar radiation absorption. Nanostructured powders also exhibit a high specific surface area that promotes the oxidation step, but the nanostructure tends to be damaged at high temperatures. Moreover, the material shaping process represents an additional step required for the preparation of tailored materials (such as porous structures or dense membranes) and for their incorporation in suitable solar reactors, which could have an impact on the process economics. The design of optimized and thermally stable oxide structures with controlled morphologies and microstructures is thus a huge challenge for their large-scale implementation in high-temperature solar reactors applied to synthetic fuel production.

Chapitre 2 - Selection of reactive materials for two-step thermochemical cycles

2.1 Introduction

A main challenge for two-step thermochemical cycles is to develop a reactive material able to dissociate water and/or CO_2 with fast reaction rate and performance stability over cycles. Thus to be usable in thermochemical cycles, a reactive material should satisfy the following criteria:

- low reduction temperature (<1400 °C);
- capacity to produce high amount of H_2 and/or CO during the oxidation step;
- fast kinetic rate;
- thermal stability;
- low cost;
- non-toxic;
- largely available and abundant [174].

Typical redox catalysts used in thermochemical splitting are metal oxides based on either volatile (e.g. ZnO/Zn and SnO_2/SnO [176]) or non-volatile stoichiometric and non-stoichiometric redox pairs (CeO_2/$CeO_{2-\delta}$ [36, 37], Fe_3O_4/FeO, ferrites [38–40], such as $NiFe_2O_4$ [41]). More exhaustive lists of relevant material formulations can be found in the literature [55, 118, 177]. Recently, non-stoichiometric ceramics with $ABO_{3-\delta}$ perovskite structure have attracted significant attention, thanks to their suitable redox properties, durability and reliability at high processing temperatures. Perovskites formulations such as $La_{0.5}Ca_{0.5}MnO_3$ (LCM) and $La_{0.5}Sr_{0.5}MnO_3$ (LSM) with or without any dopant have been tested for either H_2O or CO_2 splitting [119, 125, 135, 144, 145]. Insertion of aluminum in the B site [136] was found to increase both H_2 production and reaction kinetics, with stable production rate after 80 cycles. The insertion of Ga in the B site (limited to 30% due to its low solubility) [146] was found to increase the tolerance factor, with beneficial influence on the reduction rate. Nair and Abanades [142] pointed out that Mg as dopant in the B site does not increase the fuel production rate but improves thermal stability. A detailed overview of the best performing perovskite formulations, with a special focus on their ability to produce solar fuel with high yield and stable performance was recently published by Haeussler et al. [118].

This chapter aims to present an experimental screening of the promising materials compositions found in literature in order to identify suitable materials for thermochemical cycles. First, a study on the Pechini-derived synthesis method used to prepare the reactive powders is developed. Then, the reactivity of the selected powders is investigated through the study of their redox behavior. Promising materials are finally selected to perform kinetic and thermodynamic

studies in order to provide better understanding of the mechanisms involved in the thermochemical cycles.

2.2 Method

2.2.1 Material synthesis

The perovskite powders were synthesized by a Pechini-derived method [178, 179] based on the utilization of nitrate metal salts (M), citric acid (CA) as a chelating agent, and ethylene glycol (EG) as a complexing agent. Two different solution formulations with the following molar ratios: M:CA:EG=1:1.5:1 (P1 method) and M:CA:EG=1:5:20 (P2 method) have been applied. In a typical synthesis, the given quantity of metal nitrates was dissolved in water with the fixed M:H_2O mass ratio of 1:6.

LSM powders (with or without Mg or Al dopant) were first prepared by the P1 method. The mixture of nitrate salts and CA (CA:M=1.5:1) was heated to 60 °C and stirred for 10 min. Then, EG was added to the solution in the molar ratio EG:CA=0.66:1.

In parallel, LSM and LCM powders were prepared by P2 method at IEM (Montpellier), in which large excess of CA was added to the metal salts solution (CA:M=5:1). The mixture was heated to 60 °C and stirred for 10 min. Then, a large excess of EG was added to the solution in the molar ratio EG:CA=4:1.

For both methods, the final mixture was heated at 120 °C until a viscous colored sol was obtained, which was further heated at 250 °C for 2 h to form a polymeric resin (polyesterification step). The as-obtained resin was crushed using an agate mortar and subsequently treated in successive thermal treatment steps in air atmosphere: 1) 600 °C for 1 h with a 3 °C/min ramp yielding a porous ceramic powder, 2) 1400 °C for 1 h with a 5 °C/min ramp, yielding the final perovskite material which was used in two step thermochemical CO_2 splitting reactions.

All sample references, corresponding formulations and synthesis methods are reported in Table 2-1.

2.2.2 Characterization methods

The main physico-chemical characteristics (morphology, chemical composition, crystalline structure, and microstructure) of the P1 and P2 powders prepared at either 600 °C or 1400 °C have been determined and compared. The powders morphology and grain sizes were observed by Field Emission Scanning Electron Microscopy (FESEM – Hitachi S4800). Materials microstructure was analyzed by N_2 physisorption (Micromeritics ASAP-2000), after outgassing at 200 °C overnight. The BET method [180] was used to estimate the specific surface area (S_{BET}) of the powders.

The crystallographic structure of the investigated powders was analyzed at room temperature with X-ray diffraction (XRD) thanks to PANalytical XPert Pro diffractometer (Cu Kα radiation, $\lambda = 0.15418$ nm). A 20°-75° angular range was used with θ-θ symmetrical scan. The X-ray diffractograms obtained were recorded and investigated with the PANalytical software (Data

collector and HighScorePlus). The collected XRD patterns are presented in the appendix section.

Particle sizes distributions were analyzed by laser diffraction (Mastersizer 3000) coupled with a fluid dispersion system (Hydro EV). The system was operated at two wavelengths (633 nm and 470 nm). Ultrasounds were used to operate powder dispersion in water and the particle size distribution was determined by applying the Fraunhofer diffraction theory [181].

The thermochemical CO_2 splitting reactivity of the powders obtained at 1400 °C was studied via thermogravimetric analysis (TGA – SETARAM SETSYS) using a platinum crucible. Around 100 mg of powders was used for each TGA experiment. The temperature was first increased to 1400 °C (20 °C/min) under argon (99.999% purity, < 2 ppm of O_2, 0.020 NL/min) to perform the thermal reduction. After 45 min plateau at 1400 °C, the temperature was decreased to 1050 °C (20 °C/min). A mixture of CO_2 and Ar (1:1) was then introduced (0.010 NL/min for each) in the system to perform the oxidation step, during 60 min. Then the temperature was increased again to 1400 °C under argon, and the thermal reduction and CO_2 splitting reaction cycle was operated again. The mass variation due to oxygen release during the thermal reduction step and oxygen uptake during CO_2 splitting step was recorded continuously, and the amounts of O_2 and CO produced were calculated.

The O_2 amount (n_{O2}) produced per gram of perovskite during the reduction step was calculated by the equation (1):

$$n_{\mathrm{O_2}} = \frac{\Delta m_{loss}}{m \cdot M_{\mathrm{O_2}}} \tag{27}$$

where Δm_{loss} is the mass loss measured by TGA during the reduction step; $M_{\mathrm{O_2}}$ is the molecular weight of O_2 and m is the initial mass of perovskite powder in the crucible. The amount of CO (n_{CO}) produced per gram of perovskite during the oxidation step was calculated by the equation (2):

$$n_{\mathrm{CO}} = \frac{\Delta m_{gain}}{m \cdot M_{\mathrm{O}}} \tag{28}$$

where Δm_{gain} is the mass gain during the re-oxidation step and M_{O} is the molecular weight of oxygen.

Two successive redox cycles were performed for each sample with the same reaction conditions as those mentioned above. All the production yields measured with the TGA are presented in Table SB-1.

In addition, thermochemical cycles were performed in an electric tubular furnace, using around 0.8 g of reactive material in an alumina crucible, as shown in Figure 2-1. Argon was used as a sweep gas in the furnace (continuous Ar flow rate of 0.2 L/min). The temperature was increased to 1400 °C with a ramp of 10 °C/min. The released oxygen was analyzed continuously at the furnace output with a zirconium oxide sensor (range: 10-10000 ppm, calibrated with 5000 ppm

O_2 in N_2). At the end of the reduction step, the temperature was decreased to 1050 °C. Then, water was injected (50% mole fraction of H_2O in Ar) thanks to a liquid mass flow controller. In order to protect the analytical instrumentation, the water in excess at the reactor exit was removed thanks to an iced water bubbler combined with a desiccant column. The produced hydrogen was analyzed with H_2 catharometer analyzer based on thermal conductivity detection (calibrated for Ar/H_2 binary mixture, scale: 0–10%, precision: 1% of full scale). After few minutes, the hydrogen production ended (content below 0.1%) and water injection was stopped. The second cycle was conducted with the same conditions as the first one.

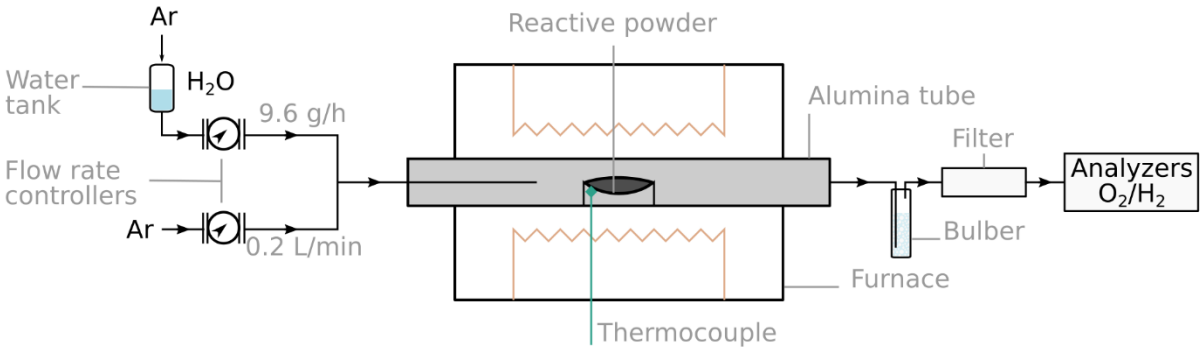

Figure 2-1: Schematic representation of the tubular furnace for two-step H_2O splitting cycles

2.3 Experimental results

In this section, a comparative study was first performed to elucidate the influence of the modified Pechini method used for reactive powder synthesis on the materials reactivity. Then, the most promising materials and dopants were investigated for thermochemical cycles application. All the selected reactive compositions are reported in Table 2-1, along with the abbreviations used in this chapter. The selected compositions were synthesized with a modified Pechini method, and their crystallographic structure was characterized with XRD analysis. The redox behavior was investigated via TGA, and structure stability was assessed via XRD analysis after thermochemical cycles, in order to highlight an eventual crystallographic phase change. SEM was also applied to characterize materials microstructure and detect any possible changes in morphologies. Finally, promising materials were selected for further thermodynamic and kinetic studies.

Table 2-1: List of materials and abbreviations of the different chemical compositions studied in this chapter

Material composition	Synthesis method	Material abbreviation
Perovskites		
Lanthanum-manganese perovskites		
$La_{0.5}Sr_{0.5}MnO_3$	P2	LSM-P2
$La_{0.5}Sr_{0.5}Mn_{0.6}Al_{0.4}O_3$	P2	LSMAl-P2
$La_{0.5}Sr_{0.5}Mn_{0.6}Cr_{0.4}O_3$	P2	LSMCr-P2
$La_{0.5}Sr_{0.5}Mn_{0.6}Al_{0.2}Cr_{0.2}O_3$	P2	LSMAlCr-P2
$La_{0.5}Sr_{0.5}Mn_{0.8}Ga_{0.2}O_3$	P2	LSMGa-P2
$La_{0.5}Sr_{0.5}Mn_{0.9}Mg_{0.1}O_3$	P2	LSMMg-P2
$La_{0.5}Sr_{0.5}MnO_3$	P1	LSM-P1
$La_{0.5}Sr_{0.5}Mn_{0.6}Al_{0.4}O_3$	P1	LSMAl-P1
$La_{0.5}Sr_{0.5}Mn_{0.9}Mg_{0.1}O_3$	P1	LSMMg-P1
$La_{0.5}Ca_{0.5}MnO_3$	P2	LCM-P2
$La_{0.5}Ca_{0.5}Mn_{0.6}Al_{0.4}O_3$	P2	LCMAl-P2
$La_{0.5}Ca_{0.5}Mn_{0.6}Cr_{0.4}O_3$	P2	LCMCr-P2
$La_{0.5}Ca_{0.5}Mn_{0.8}Ga_{0.2}O_3$	P2	LCMGa-P2
$La_{0.5}Ca_{0.5}Mn_{0.9}Mg_{0.1}O_3$	P2	LCMMg-P2
Strontium manganese perovskites		
$Pr_{0.75}Sr_{0.25}MnO_3$	P1	PrSrM75
$Pr_{0.50}Sr_{0.50}MnO_3$	P1	PrSrM50
$Pr_{0.25}Sr_{0.75}MnO_3$	P1	PrSrM25
$Sm_{0.50}Sr_{0.50}MnO_3$	P1	SmSrM50
$Sm_{0.75}Sr_{0.25}MnO_3$	P1	SmSrM75
Yttrium manganese perovskites		
$Y_{0.9}Ce_{0.1}MnO_3$	P1	YCeM
$Y_{0.97}La_{0.03}MnO_3$	P1	YLaM
$Y_{0.97}La_{0.03}Sr_{0.1}MnO_3$	P1	YLaSrM
$Y_{0.9}Sr_{0.1}MnO_3$	P1	YSrM
Lanthanum cobalt perovskite		
$La_{0.5}Sr_{0.5}CoO_3$	P1	LSCo
$LaMn_{0.5}Co_{0.5}O_3$	P1	LMCo
Barium manganese perovskite		
$BaCe_{0.5}Mn_{0.5}O_3$	P1	BaCeMn
Calcium manganese perovskite		
$Ca_{0.5}Sr_{0.5}MnO_3$	P1	CSM
$Ca_{0.5}Sr_{0.5}Mn_{0.5}Fe_{0.5}O_3$	P1	CSMF
Ceria		
CeO_2	P2	CeO_2
$Ce_{0.63}Zr_{0.27}Al_{0.1}O_2$	P2	$CeZrAlO_2$
$Ce_{0.63}Zr_{0.37}O_2$	P2	$CeZr37O_2$
$Ce_{0.85}Zr_{0.15}O_2$	P2	$CeZr15O_2$

2.3.1 Influence of the synthesis method on powder shaping and reactivity

In order to select the most adapted perovskite formulation and microstructure providing both a suitable shaping depending on the targeted application (involving either porous microstructures or densified membrane materials) and good redox reactivity for CO_2 splitting, the characteristics and redox activity of the powders prepared by the P1 and P2 modified-Pechini methods have been investigated. First, the sinterability of LSM, LSMMg and LSMAl powders has been compared up to 1550 °C. These compositions have been selected from the literature based on their promising redox activity [118, 125, 136].

The sinterability of the powders prepared at 600 °C by the P1 and P2 modified Pechini methods has been investigated by optical dilatometry using pressed pellets, from room temperature up

to 1550 °C [182]. Measurements have been realized by IEM (Montpellier). The dilatometric results clearly evidence that the P1-powders offer very low sinterability and poor densification below 1400 °C whereas the P2-powders show enhanced sintering at this point. Accordingly, uniform pellets were thus easily obtained by compaction and sintering of P2-powders. On the other hand, formation of porous pellets with the P1-powders was almost impossible and hardly controllable using conventional uniaxial pressing and sintering conditions.

In order to explain the strong differences in the sintering behavior of P1 and P2-powders, a comparative analysis of their microstructure, morphology and crystallographic structure has been performed at IEM. The morphology, microstructure and structure of the P1 and P2 powders obtained at either 600 °C or 1400 °C have been compared [182]. Results revealed the strong influence of the synthesis parameters on the powder homogeneity and sinterability. The P2 powders obtained at 600 °C were found to be uniform in both morphology and composition, with high specific surface area and already a well-defined cubic perovskite structure. These powders were easily shaped as pellets and their sintering was controllable up to enhanced densification at about 1400 °C. In contrast, the P1 powders were found to present heterogeneities and a spongy microstructure due to combustion reactions during their synthesis [183]. Furthermore, no significant difference in specific surface area was evidenced between P1 powders obtained at 600 °C and 1400 °C.

A comparison of the redox activity of both P1 and P2-powders for CO_2 splitting reaction has been performed. When P1 and P2 powders were thermally treated at 1400 °C, their specific surface area and main crystalline phase became almost comparable and thus their performance for CO_2 splitting were expected to be similar. The results of TGA (Figure 2-2) for two redox cycles are reported in Table 2-2 for LSM, LSMAl and LSMMg powders prepared by P1 and P2 methods at 1400 °C. The associated O_2/CO productions and re-oxidation yields are also reported.

Table 2-2: Comparison of O_2 and CO production during two redox cycles (TGA) for LSM-based powders obtained at 1400 °C. Influence of Al and Mg dopants.

Powder sample	1st cycle			2nd cycle		
	O_2 production (µmol/g)	CO production (µmol/g)	Re-oxidation yield (%)	O_2 production (µmol/g)	CO production (µmol/g)	Re-oxidation yield (%)
LSM-P1	193	184	48	161	185	57
LSM-P2	232	190	41	104	195	94
LSMAl-P1	310	198	32	129	212	82
LSMAl-P2	302	200	33	109	203	93
LSMMg-P1	287	219	38	112	217	97
LSMMg-P2	269	214	40	111	215	97

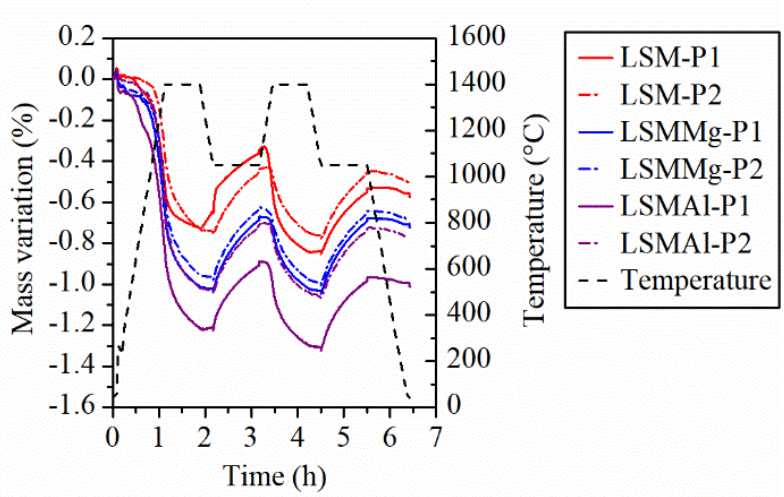

Figure 2-2: Thermogravimetric analysis of redox cycles for CO_2 splitting with LSM-based powders prepared at 1400 °C. Influence of Al and Mg dopants.

The TGA measurements showed that both P1 and P2 powders exhibit similar fuel production yield during the two step thermochemical cycles. However, slight differences were noticed depending on the dopant. The highest CO amount (215-217 µmol/g) was produced by LSMMg powders with an almost complete re-oxidation yield for both P1 and P2 powders (97%), thereby confirming cycling stability. For all samples, the CO production yield during the first and second cycle was similar. It is important to underline the low re-oxidation yield of LSM-P1 due to an incomplete reduction of the material after the first cycle.

These results clearly demonstrate that the reactivity of LSM-based powders is not altered by the synthesis protocol, despite strongly different sintering behavior of the P1 and P2 derived powders. The powders stabilization at 1400 °C before the redox cycling experiment is a key asset to provide comparable reactivity.

This statement represents a real advantage concerning the shaping processes of powders for two step thermochemical cycling. Indeed, it offers on one hand the possibility of controlling the sintering/densification without altering the perovskite redox reactivity (at temperatures ~1400 °C) and on the other hand the possibility to select the most suitable synthesis method for each type of material shaping (powder, porous structure, or dense membrane).

2.3.2 Influence of the chemical composition and dopants on the redox activity

2.3.2.1 Lanthanum manganese perovskites

Lanthanum manganite perovskites have been investigated for numerous applications such as electrodes of solid oxide fuel cells [184], metal-air batteries [185], gas and ion sensors [186, 187] or high performance materials for catalysis [188]. For two-step thermochemical cycles, Sr-based and Ca-based lanthanum manganite perovskites have been widely studied. However, their low re-oxidation extent is an issue. Thus, to enhance the thermochemical performance, the following dopants have been selected on the basis of their promising behavior reported in the literature: Al, Cr, Ga, and Mg.

Ca-based perovskites

Lanthanum-calcium manganite perovskites are able to achieve high reduction extent [135, 145]. The following perovskites were investigated in this work: $La_{0.5}Ca_{0.5}Mn_{0.6}Al_{0.4}O_3$ (LCMAl-P2), $La_{0.5}Ca_{0.5}Mn_{0.6}Cr_{0.4}O_3$ (LCMCr-P2), $La_{0.5}Ca_{0.5}Mn_{0.8}Ga_{0.2}O_3$ (LCMGa-P2), and $La_{0.5}Ca_{0.5}Mn_{0.9}Mg_{0.1}O_3$ (LCMMg-P2). $La_{0.5}Ca_{0.5}MnO_3$ (LCM-P2) was used as reference. The crystallographic structure of these materials was studied by XRD analysis (Figure SB-1). All powders exhibit an orthorhombic phase with a lattice parameter *a* in the range 5.346-5.431 Å, *b* in range 5.362-5.432 Å and *c* in range 7.593-7.693 Å. Figure 2-3 compares the mass variation during two thermochemical cycles, as well as the O_2 and CO production yields for the series of Ca-based perovskites. Table SB-1 reports the corresponding O_2 and CO production yields. The reduction extent reached during the first cycle is enhanced by Al^{3+} and Mg^{2+} dopants: O_2 production is 449 µmol/g and 394 µmol/g, respectively compared with 325 µmol/g for LCM-P2. The O_2 evolution rate is presented in Figure SB-2. The maximum O_2 rate reached by the reactive material depends on the reduction extent. Except LCMAl-P2, the O_2 production starts at 900 °C for all the other Ca-based perovskites. The O_2 production for LCMAl-P2 starts at 650 °C, i.e. 250 °C less than for other perovskites, unveiling a lower reduction enthalpy. This explains the higher reduction extent reached by LCMAl-P2 in comparison with other Ca-based perovskites. Concerning the oxidation step, only the Ga dopant offers higher CO production yield (215 µmol/g) in comparison with LCM-P2 (175 µmol/g). The other dopants (Al, Cr, and Mg) negatively impact the amount of CO produced. The re-oxidation extent achieved during the first cycle does not exceed 40%. During the second cycle, the CO production yield of LCMGa is lower (200 µmol/g) than during the first cycle (215 µmol/g), indicating a slight decrease in performance stability. In summary, none of the investigated dopants was able to enhance the performance of the reference material LCM-P2.

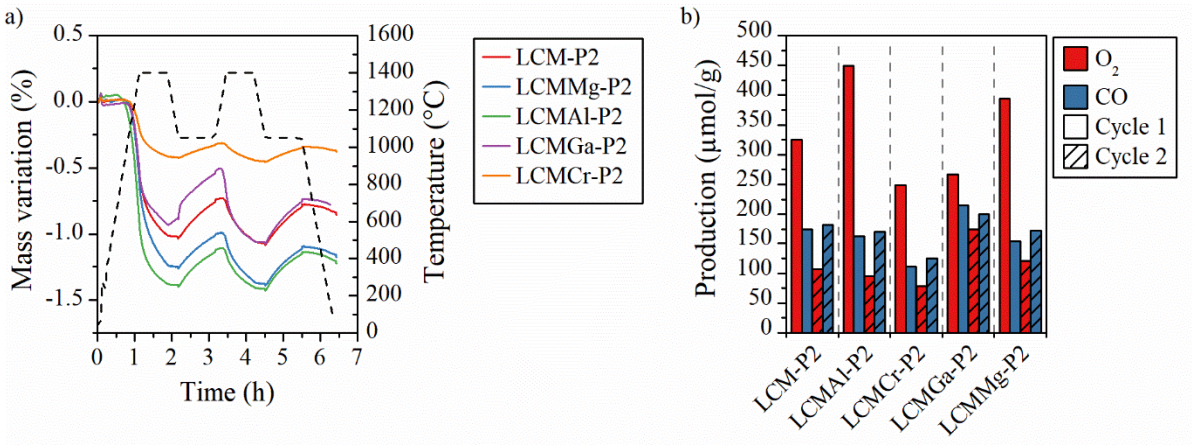

Figure 2-3: a) Thermogravimetric reduction and re-oxidation profiles for CO_2 splitting, and b) O_2 and CO production yields for Ca-based perovskites

Initially, LCM-P2, LCMAl-P2, LCMGa-P2, and LCMMg-P2 had different Mn oxidation states (respectively +3.50, +3.83, +3.63 and +3.67) due to their different dopant content. The Mn oxidation state was not calculated for perovskites containing Cr that shows different oxidation states, able to interfere with the Mn oxidation state. After the first reduction, the Mn oxidation

state reached respectively +3.25, +3.22, +3.36, and +3.34 in the series LCM-P2, LCMAl-P2, LCMGa-P2, and LCMMg-P2. The LCMAl-P2 sample had a high initial Mn oxidation state compared to LCM-P2 and this was related to the high amount of O_2 produced during the reduction step. After the reduction, the Mn oxidation state in both LCMAl-P2 and LCM-P2 were similar. After the oxidation step, the Mn oxidation state was respectively +3.32, +3.33, +3.47 and +3.40 in the series LCM-P2, LCMAl-P2, LCMGa-P2, and LCMMg-P2. Due to incomplete re-oxidation, none of the materials was able to recover its initial Mn oxidation state. The final oxidation state was comparable for all samples and this explained why similar CO productions were achieved within this series despite strong differences in the re-oxidation yields. These results suggest that the CO production capability is not directly governed by the final oxygen non-stoichiometry achieved (depending on distinct capabilities for oxygen vacancy formation), but is rather governed by the final oxidation state of the redox-active Mn cation after reduction.

Sr-based perovskites

Lanthanum-strontium manganite perovskites have been investigated for microelectrodes [189] and thermochemical cycles [56]. The following perovskites have been investigated in this work: $La_{0.5}Sr_{0.5}Mn_{0.6}Al_{0.4}O_3$ (LSMAl-P2), $La_{0.5}Sr_{0.5}Mn_{0.6}Cr_{0.4}O_3$ (LSMCr-P2), $La_{0.5}Sr_{0.5}Mn_{0.6}Al_{0.2}Cr_{0.2}O_3$ (LSMAlCr-P2), $La_{0.5}Sr_{0.5}Mn_{0.8}Ga_{0.2}O_3$ (LSMGa-P2), and $La_{0.5}Sr_{0.5}Mn_{0.9}Mg_{0.1}O_3$ (LSMMg-P2). The $La_{0.5}Sr_{0.5}MnO_3$ (LSM-P2) was used as reference. The crystallographic structure of these materials was studied by XRD analysis (Figure SB-3). All the powders exhibit a cubic phase, with a lattice parameter *a* in the range 3.840-3.864 Å. Figure 2-4 presents the thermogravimetric profiles during two thermochemical cycles. The obtained O_2 and CO production yields are compared in Table SB-1. The Mg^{2+} and Al^{3+} dopants allow an enhancement of the reduction extent reached during the first cycle in comparison with LSM perovskite. On the contrary, LSMGa-P2 and LSMAlCr-P2 have a similar O_2 production yield than LSM, thereby revealing no improvement of Ga^{3+} and Al/Cr dopant on the reduction step. The Cr dopant is even unfavorable for the reduction step, as evidenced by a lower O_2 production yield of LSMCr-P2 (215 µmol/g) compared with LSM-P2 (232 µmol/g). Figure SB-4 shows the O_2 evolution rate during the first cycle as a function of time and temperature. The maximum O_2 rate reached by the reactive material depends on its reduction extent. The O_2 production starts at 800 °C for all the Sr-based perovskites. Concerning the oxidation step, the Mg^{2+}, Ga^{3+} and Al^{3+} dopants lead to an enhancement of the CO production yield (214 µmol/g, 195 µmol/g, and 200 µmol/g, respectively) in comparison with LSM-P2 (190 µmol/g). In contrast, doping with Cr or Al/Cr decreases the CO amount produced (134 µmol/g and 164 µmol/g, respectively) in comparison with undoped LSM-P2. The re-oxidation extent during the first cycle is low, with the highest value of 42% for LSMGa. Between the first and second cycles, the O_2 productions of all Sr-based perovskites drop from the range 215-302 µmol/g to 134-214 µmol/g, due to the low re-oxidation extent reached during the first cycle. The CO production yields obtained during the first and the second cycle are similar, confirming the thermochemical stability of the perovskite series. The re-oxidation extents reached during the second cycles are above 90% except for LSMAl that only reaches 83% due

to its low CO production yield. Therefore, apart from Cr and Cr/Al^{3+} dopants, Ga^{3+}, Al^{3+} and Mg^{2+} are able to enhance LSM performance. In this series, LSMMg seems to be the most promising material since it offers both the highest CO production yield and enhanced performance stability.

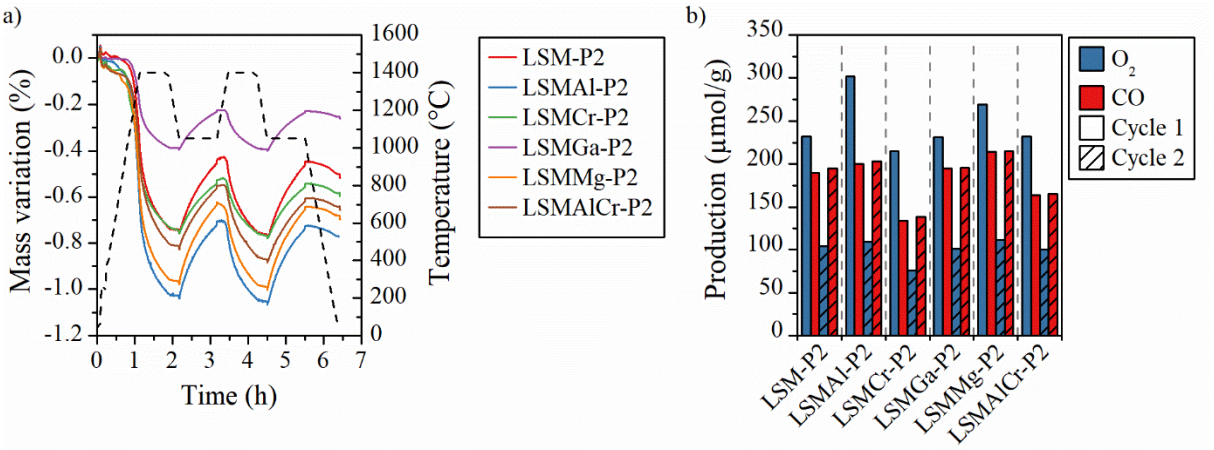

Figure 2-4: a) Thermogravimetric reduction and re-oxidation profiles for CO_2 splitting, and b) O_2 and CO production yields for Sr-based perovskites

Initially, LSM-P2, LSMMg-P2, LSMGa-P2 and LSMAl-P2 had different Mn oxidation states (respectively +3.50, 3.67, 3.63 and 3.83) due to their different dopant contents. After the first reduction, the Mn oxidation state decreased to +3.30, 3.41, 3.37 and 3.42, respectively. After the oxidation step, the Mn oxidation states were +3.38, 3.36, 3.48 and 3.56, respectively. After the oxidation, the LSM-P2, LSMMg-P2, LSMGa-P2 and LSMAl-P2 samples did not recover their initial Mn oxidation state.

The TGA points out the promising redox behavior of LSMMg. In order to further provide insights into the thermochemical reactions of LSMMg, two thermochemical H_2O splitting cycles were carried out in an electric tubular furnace (Figure 2-1). The system permits to directly analyze the gas produced at the outlet, thus yielding the production rate values. The results are presented in Figure 2-5. The reduction step was performed at 1400 °C after a heating ramp of 10 °C/min, with Ar flow rate of 0.2 L/min. The oxidation step was performed at 1050 °C for 40 min under 50% of H_2O. Around 0.8 g of reactive material was used to perform the analysis. The O_2 and H_2 production yields obtained with the tubular furnace were in the same order of magnitude than the O_2 and CO production yields measured by TGA (207 µmol/g against 269 µmol/g for O_2, and 236 µmol/g for H_2 against 215 µmol/g for CO, in tubular furnace and TGA, respectively). In the 2nd cycle, O_2 and H_2 yields were 123 and 251 µmol/g, confirming complete re-oxidation. The oxygen production rate increased with the increase of temperature and reached a peak value at the target temperature. Then, the O_2 production decreased slowly until reaching a sufficiently low production rate value and the temperature was then decreased for the oxidation step. The H_2 production rate reached a peak few seconds after steam injection and then slowly decreased. This fits with kinetic studies on perovskites reported in the literature [119, 137]. The H_2 production rate reached a maximum value of 0.31 mL/min/g during both cycles, denoting good production stability for LSMMg-P1.

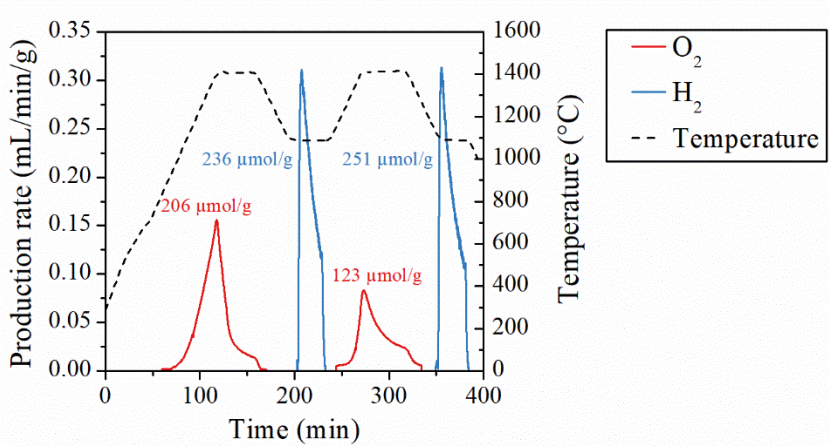

Figure 2-5: O_2 and H_2 production rates during two consecutive thermochemical cycles for H_2O splitting, performed in a tubular furnace with LSMMg-P1

To explain the good thermochemical performance of LSMMg-P1, FESEM was used to explore its microstructure. Figure 2-6 presents the FESEM observations of LSMMg-P1 powder before and after TGA (i.e. 2 redox cycles). The spongy microstructure results from the decomposition of nitrate during the Pechini synthesis method. Such a powder morphology is typically obtained by combustion reactions [183]. The grain size was measured in the range 0.5-1 µm. Furthermore, it can be observed that the two thermochemical cycles performed during TGA did not induce sintering, as confirmed by the limited grain growth. The presence of Mg^{2+} ions as stabilizer in the perovskite structure could explain this behavior. Indeed the strong Mg-O bond, resulting in high melting temperature for MgO (2800 °C), could explain its good thermal resistance [125]. Thermal resistance is a key asset for further process implementation, as the reactive material should undergo multiple cycles while maintaining stable performance. Thus, LSMMg-P1 appears as a promising candidate for this purpose.

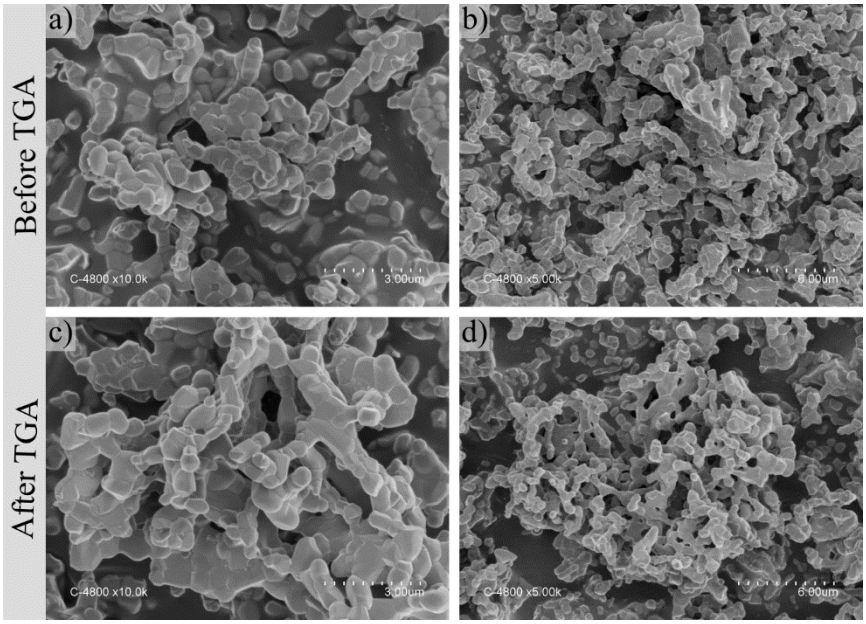

Figure 2-6: FESEM observations of LSMMg-P1 powder: a) and b) before, c) and d) after TGA for CO_2 splitting

The grain size distribution is another important characteristic of the reactive powder, with direct influence its specific surface area. Indeed, a high specific surface area promotes the oxidation step production rate since the oxidation reaction is surface-controlled. The particle size distribution of both fresh and cycled LSMMg-P1 powders was investigated by laser diffraction, using the Fraunhofer diffraction theory and the assumption of spherical particles. Results are presented in Figure 2-7. For the fresh sample, a bimodal distribution of particle sizes is observed with two maximums centered at 5.9 µm and 27.4 µm. After two thermochemical cycles (TGA for CO_2 splitting), the proportion of small particles strongly decreased in favor of larger ones, attributed to slight densification effect. The two initial distributions shift, combine and form a single distribution, centered at 40.1 µm. In comparison with the small grain sizes (0.5-1 µm) observed by SEM [182], the large particle sizes measured by laser diffraction correspond to consolidated aggregates of grains partially sintered. It appears clearly in Figure 2-6 that these porous aggregates are more efficiently consolidated (sintered) after cycling although the size of grains within the aggregates remain almost unchanged.

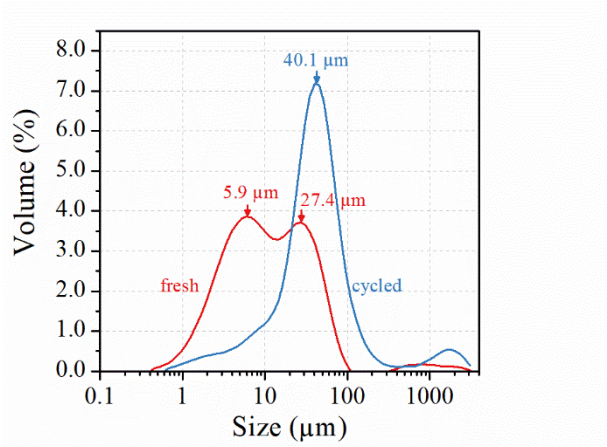

Figure 2-7: Particle size distribution of fresh (red) and cycled (blue) LSMMg-P1 powder

To sum up, Ca-doped perovskites offer higher reduction extent than Sr-doped perovskites. Conversely, Sr-based perovskites show higher re-oxidation yield than Ca-based perovskites. The use of Mg dopant in B site is promising. Mg^{2+} is not involved in the redox reactions but it enhances the oxidation degree of Mn (compared with Ga^{3+} and Al^{3+}), thus favoring both the reduction and oxidation extents. Mg^{2+} also acts as a sintering inhibitor as the LSMMg powder remain well dispersed and not cohesive after TGA cycling, although other powders tend to sinter.

2.3.2.2 Strontium manganese perovskites

Numerous studies have investigated perovskites with lanthanum in the A site. In this work, other rare earth elements such as samarium or praseodymium have been investigated instead of lanthanum in order to reach higher thermochemical performance. Five compositions have been selected: $Sm_{0.75}Sr_{0.25}MnO_3$ (SmSrM75), $Sm_{0.5}Sr_{0.5}MnO_3$ (SmSrM50), $Pr_{0.75}Sr_{0.25}MnO_3$ (PrSrM75), $Pr_{0.5}Sr_{0.5}MnO_3$ (PrSrM50) and $Pr_{0.25}Sr_{075}MnO_3$ (PrSrM25). The P1 method was used to synthesize the materials. It should be noted that an attempt to synthesize $Sm_{0.25}Sr_{0.75}MnO_3$ formulation was also done, but XRD analysis showed that the perovskite

structure did not form. The crystallographic structure of these materials was studied by XRD analysis (Figure SB-5).

Figure 2-8 shows the TGA of the strontium manganese perovskites series (including LSM for comparison). First, the Sr content influences the non-stoichiometry extent reached by the reactive material. A high Sr content induces a high amount of oxygen released, for example PrSrM25 ($Pr_{0.25}Sr_{075}MnO_3$) produces 668 µmol/g of O_2 against 146 µmol/g for PrSrM75 ($Pr_{0.75}Sr_{0.25}MnO_3$). As highlighted in the literature, increasing the Sr content increases the Mn oxidation state in B site. As the reduction reaction depends on the reduction from Mn^{4+} to Mn^{3+}, an increase of Sr content enhances the reduction extent [56, 119–124, 190]. However, increasing Sr content does not enhance the CO yield. For a fixed Sr content, the amount of O_2 released depends on the Sr-substitution element in the A site. With 50% Sr, the O_2 production yield increases in the following order: LSM (232 µmol) < PrSrM50 (268 µmol/g) < SmSrM50 (377 µmol/g). Using Sm^{3+} or Pr^{3+} in the A site enhances the reduction step in comparison with La^{3+}. The CO production during the first cycle increases in the following order: PrSrM50 (153 µmol/g) < SmSrM50 (169 µmol/g) < LSM (190 µmol/g). The highest O_2 production yield is obtained with PrSrM25 (668 µmol/g) whereas the highest CO production yield is obtained with SmSrM75 (180 µmol/g). Thus, Sm and Pr in A site (instead of La) have a beneficial impact on the reduction step but they decrease the amount of CO produced during the oxidation step, impeding the enhancement of thermochemical performance.

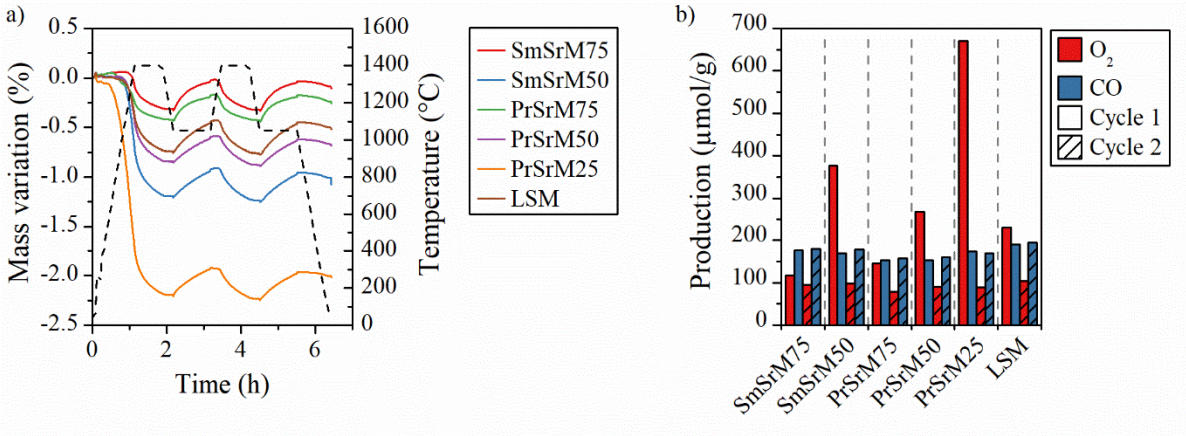

Figure 2-8: a) Thermogravimetric reduction and re-oxidation profiles for CO_2 splitting and b) O_2 and CO production yields for strontium manganite perovskites

2.3.2.3 Lanthanum cobalt perovskites

Lanthanum cobalt perovskites were studied for their attractive magnetic properties [191] or for their performance as cathode materials in high temperature fuel cells [192]. Due to their high oxygen exchange capacities, lanthanum cobalt perovskites also appear as potentially attractive reactive materials in thermochemical cycles. Both $La_{0.5}Sr_{0.5}CoO_3$ (LSCo) and $LaMn_{0.5}Co_{0.5}O_3$ (LMCo) have been selected for tests in thermochemical cycles. The XRD patterns of LSCo and LMCo confirm the formation of the expected crystallographic structure (Figure SB-7). Figure 2-9 compares the mass variation during two thermochemical cycles along with the O_2 and CO production yields for LSCo and LMCo. The LSCo cycles have been carried at a lower reduction

temperature (1300 °C) due to the melting risk of this material at higher temperatures. The oxidation temperature was also decreased down to 950 °C in order to maintain a similar temperature swing in comparison with all the other performed TGA. The CO production yield of LMCo is low (~100 µmol/g) due to the weak non-stoichiometry extent reached during the reduction step (δ=0.021). On the contrary, LSCo reached a high reduction extent during the first cycle (1191 µmol/g) and high subsequent mass uptake (1141 µmol/g) despite a low re-oxidation extent (48%) ascribed to carbonate formation. In a previous work in our group, this material has been tested for H_2O splitting and low H_2 production was measured [121]. In addition, strong sintering or partial melting occurred in the crucible after TGA performed with CO_2. The XRD pattern of LSCo after the thermochemical cycles highlighted the decomposition of $La_{0.5}Sr_{0.5}CoO_3$ to $LaSrCoO_4$ and CoO (Figure SB-7), as previously pointed out in [121].

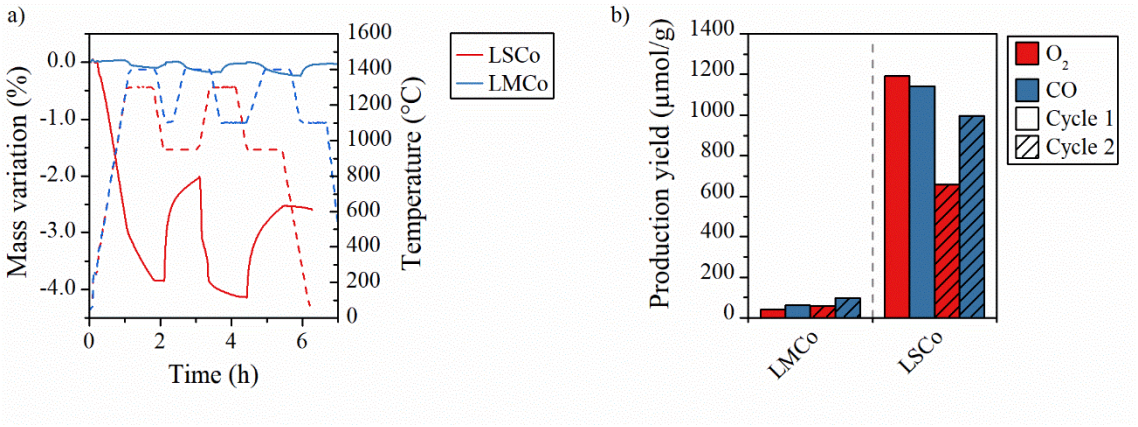

Figure 2-9: a) Thermogravimetric profiles (solid lines) and associated temperatures (dashed lines), b) production yields for lanthanum cobalt perovskites (the unusual high mass uptake of LSCo is ascribed to carbonate formation rather than CO production)

2.3.2.4 Yttrium manganese perovskites

Yttrium manganese perovskites have been widely studied for air separation applications due to their ability to selectively absorb, store and release significant amounts of oxygen [193]. The oxygen exchange capacity is a key parameter for reactive materials in thermochemical cycles. In this respect, due to their high oxygen exchange capacity, series of yttrium manganese perovskites were investigated for thermochemical CO_2 splitting cycles. Four promising compositions were selected: $Y_{0.97}La_{0.03}MnO_3$ (YLaM), $Y_{0.9}Ce_{0.1}MnO_3$ (YCeM), $Y_{0.87}Sr_{0.1}La_{0.03}MnO_3$ (YLaSrM), and $Y_{0.9}Sr_{0.1}MnO_3$ (YSrM). The XRD patterns of the prepared yttrium-manganite perovskite series are shown in Figure SB-8 and correspond to the space group P63cm (01-070-4962). YSrM shows a peak shift due to the substitution of Y^{3+} by Sr^{2+} in comparison with $YMnO_3$, inducing the following lattice parameters: a=6.11 Å and c=11.25 Å. After thermochemical cycles, the lattice parameters slightly increase, with a=6.16 Å and c=11.47 Å. Both YLaM and YCeM show increased lattice parameters in comparison with $YMnO_3$ due to the higher ionic radii of La (1.03 Å) and Ce (1.01 Å) in comparison with Y (0.90 Å) [152]. This leads to an increase in lattice parameters (a=6.16 Å and 6.21 Å; c=11.48 Å and 11.98 Å, respectively) in comparison with $YMnO_3$ (a=6.13 Å; c=11.40 Å). Similarly, to YSrM, both YLaM and YCeM present a decrease in lattice parameters after thermochemical cycles: a=6.15 Å and c=11.43 Å for YLaM and a=6.20 Å and c=11.94 Å for YCeM.

Figure 2-10 shows the mass variation during two thermochemical cycles, along with the O_2 and CO production yields. The TGA of YCeM was aborted after the first cycle due to very low re-oxidation extent. A strong mass loss was observed during the first part of the reduction step (until 1128 °C) and thus, only the mass variation measured during the second part of the reduction step (above 1128 °C) was taken into account to calculate the oxygen yield. Among the tested yttrium manganese perovskites, YLaSrM reached the highest reduction extent with 145 µmol/g of O_2 in comparison with 54 µmol/g, 47 µmol/g, and 127 µmol/g for YLaM, YCeM, and YSrM, respectively. The CO production yields follow the same trend than the O_2 production yields, suggesting that CO production depends on the achieved non-stoichiometry, with the following yields: YLaSrM (135 µmol/g) > YSrM (118 µmol/g) > YLaM (86 µmol/g) > YCeM (33 µmol/g). Despite its low reduction extent, YLaM displays high re-oxidation extent (77%) during the 1st cycle in comparison with YSrM (46%). Furthermore, both O_2 and CO production yields for YSrM during the second cycle are lower (106 µmol/g and 106 µmol/g, respectively) than those of the first cycle (127 µmol/g and 118 µmol/g, respectively). On the contrary YLaM exhibits an increase of both O_2 and CO production yields when comparing the first and second cycles (from 54 to 60 µmol/g and from 86 to 107 µmol/g, respectively). This can be explained by a slow reduction rate of the material. Indeed, during the first cycle, YLaM does not reach its maximum reduction extent. So, the non-stoichiometry extent continues to increase during the second step. Among the yttrium manganese perovskites investigated, YLaSrM offers the best performance with the highest CO production yield (137 µmol/g). Furthermore, the CO production yield is stable between the first and the second cycle, highlighting the thermochemical stability of this perovskite material. The re-oxidation extent of YLaSrM during the second cycle reached 91%. Consequently, YLaSrM appears as the most promising reactive material among the investigated yttrium manganese perovskite series.

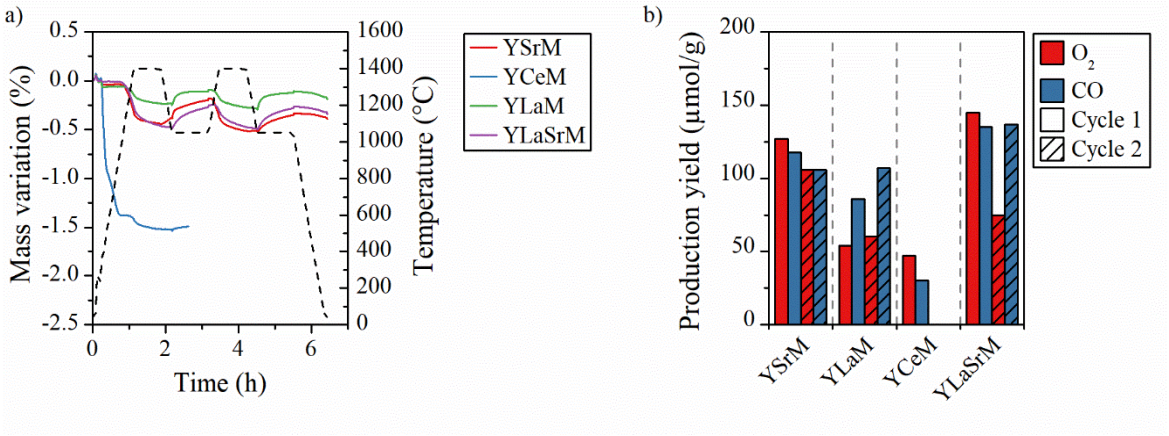

Figure 2-10: a) Thermogravimetric reduction and re-oxidation profiles with CO_2 (solid lines) and associated temperatures (dashed lines), b) O_2 and CO production yields for yttrium manganite perovskite series

2.3.2.5 Barium manganese perovskites (BaCe0.5Mn0.5O3)

Barcellos et al. identified cerium-doped barium manganese perovskite as a promising water-splitting material due to its appropriate oxygen bonding strength [154]. To investigate this new perovskite type, $BaCe_{0.5}Mn_{0.5}O_3$ (BaCeMn) was synthesized by the Pechini method. As reported in [154], a mixture of two phases $BaCe_{0.5}Mn_{0.5}O_3$ and CeO_2 was evidenced in the XRD

patterns (Figure SB-9). Two TGA cycles were carried out as presented in Figure 2-11. During the first cycle, 220 µmol/g and 154 µmol/g of O_2 and CO were produced, respectively. These values are in accordance with those obtained for lanthanum manganese perovskites [56]. However, during the second cycle, CO production yield fell to 110 µmol/g and a poor re-oxidation yield was achieved. Such a decrease in performance is not consistent with the good stability highlighted by Barcellos et al. [154]. This may be explained by the slightly higher reduction temperature used here (1400 °C) in comparison with Barcellos work (1350 °C). Indeed, higher temperatures can induce sintering that could hinder re-oxidation reaction. Furthermore, the XRD pattern after cycling (Figure SB-9) highlights the decomposition of the BaCeMn crystallographic structure with the formation of $BaCeO_3$ and MnO_3 phases, explaining the degradation of thermochemical performance.

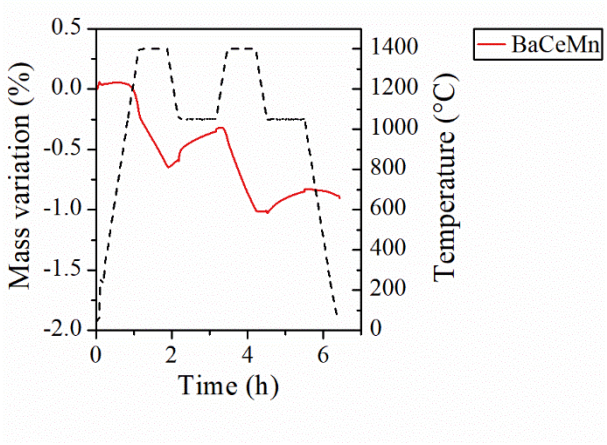

Figure 2-11: Thermogravimetric reduction and re-oxidation profiles with CO_2 (solid lines) and associated temperature (dashed lines) for BaCeMn

2.3.2.6 Ceria and doped-ceria

Currently, ceria is considered as the state-of-art material for two-step thermochemical cycles, due to the stability of its crystallographic structure over a large range of non-stoichiometry and working conditions. However, it suffers from a low reduction extent impeding high fuel production yield [45, 63, 67–69]. Numerous doping strategies have been explored to improve ceria thermochemical performances [93, 194, 195]. Three promising compositions have been selected from the literature and synthesized via Pechini method (P2): $Ce_{0.85}Zr_{0.15}O_2$ (CeZr15), $Ce_{0.63}Zr_{0.37}O_2$ (CeZr37) and $Ce_{0.63}Zr_{0.27}Al_{0.1}O_2$ (CeZr27Al10). Ceria (CeO_2) was used as reference material. The formation of a fluorite structure was checked by XRD for all the selected formulations (Figure SB-10). Figure 2-12 shows the thermogravimetric profiles of both ceria and doped ceria along with the O_2 and CO production yields. All the doped ceria materials present an enhancement of the reduction extent during the first cycle (in the range of 116-176 µmol/g compared with 55 µmol/g for pristine ceria). The reduction extent increases with the increase of Zr concentration in ceria, from 55 µmol/g for pure ceria to 176 µmol/g for CeZr37. Doping with Zr has a beneficial impact on ceria reduction extent. The lattice distortion induced by the incorporation of Zr^{4+} enhances the oxygen mobility, explaining the high O_2 yield of Zr-doped ceria [93, 94].

The total amount of dopant in CeZr27Al10 and CeZr37 is similar (37%), however the O_2 released by CeZr27Al10 (129 µmol/g) is significantly lower than the value measured for CeZr37 (176 µmol/g). Thus, incorporation of both Al and Zr into ceria is not beneficial to the reduction extent. Concerning the oxidation step, the CO production yield increases in the following order: CeZr37 (72 µmol/g) < CeO_2 (95 µmol/g) ≈ CeZr27Al10 (86 µmol/g) < CeZr15 (144 µmol/g). Doped ceria-based materials offer low re-oxidation extent (in the range of 20-62%) in comparison with pristine ceria (77%). During the second cycle, CeZr37 and CeZr27Al10 show a decrease of the amount of CO produced (69 µmol/g and 57 µmol/g, respectively) in comparison with the first cycle (72 µmol/g and 86 µmol/g, respectively). Such performance results from the low thermal stability of the microstructure of these materials (synthesized via P2 method, favoring strong sintering), making them not suitable for consecutive cycling operation. It is expected that the thermal stability of the microstructure of these ceria-based materials could be enhanced with the use of an adequate synthesis method (P1) limiting sintering. However, similarly to LSM, the P1 method is not expected to result in significantly enhanced CO production yield.

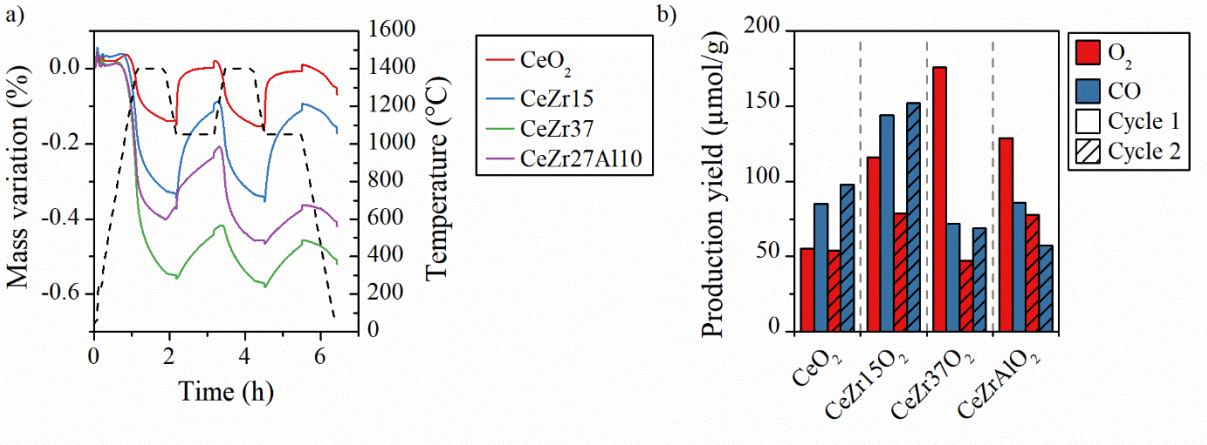

Figure 2-12 : a) Thermogravimetric reduction and re-oxidation profiles (solid lines) and associated temperatures (dashed lines), b) O_2 and CO production yields for ceria and ceria doped materials

2.4 Thermodynamic study

As explained in the previous chapter, determination of thermodynamic properties is interesting to predict both the theoretical reduction extent and the fuel production yield. Two materials have been selected for performing a thermodynamic study: LSMMg-P1 that appeared as the most promising material studied here, and $Ca_{0.5}Sr_{0.5}MnO_3$ (CSM). Indeed, CSM was studied for thermochemical energy storage applications due to its excellent oxygen exchange capacity and associated heat storage capacity [115, 123]. After a reduction at 1400 °C under 10 ppm O_2, the final non-stoichiometry extent reached by CSM leads to an O_2 production yield of 1302 µmol/g (Figure 2-13.a). Its re-oxidation yield is very weak (less than 20%) and a large temperature swing is required to favor the oxidation step and produce significant amounts of CO (~350 µmol/g at 600 °C after a reduction plateau up to 1400 °C for CSM, Fig. 13a). Similarly, $Ca_{0.5}Sr_{0.5}Mn_{0.5}Fe_{0.5}O_3$ (CSMF) displays an O_2 yield of 913 µmol/g at 1300 °C under 10 ppm O_2 and a CO production yield of 315 µmol/g at 600 °C (Figure SB-11). This highlights the need to use a large temperature swing to obtain acceptable CO production, which is

inappropriate for rapid cycling due to the required heating/cooling stages between reaction steps of thermochemical cycles. These results confirm that the redox behavior of CSM is very different from LSMMg. Thus, it appears relevant to study and compare the thermodynamic properties of these two materials in order to explain the differences in their redox behavior. To evaluate the enthalpy and entropy as a function of the non-stoichiometry, the Van't Hoff method was applied according to equation (29). If $\Delta H°(\delta)$ and $\Delta S°(\delta)$ are independent of temperature, as often observed, an Arrhenius plot of a set of T-pO_2 pairs at a given δ yields a linear curve, with the enthalpy and entropy of reduction given by the slope and intercept, respectively. To this aim, three steps are required, as represented in Figure 2-13 for CSM material. Firstly, thermogravimetric analyses with temperature steps (1000 °C, 1100 °C, 1200 °C, 1300 °C and 1400 °C) under different oxygen partial pressures should be carried out. In this study, different oxygen partial pressures were used: 10 ppm, 250 ppm, 2000 ppm and 10000 ppm. Figure 2-13.a and b present the thermogravimetric analysis of CSM under 10 ppm O_2 and 250 ppm O_2, respectively. At the different temperatures, from all the couples (T, p_{O_2}), the non-stoichiometry at the equilibrium is determined (by numerical extrapolation for low p_{O2} conditions because equilibrium is hardly reached). When the equilibrium state was not reached at the end of the temperature step, curves were extrapolated with an exponential function to obtain the non-stoichiometry extent at the equilibrium. Secondly, for all the oxygen partial pressures investigated, the non-stoichiometry extent was plotted as a function of the temperature and a curve fits the experimental data, as represented in Figure 2-13c. Finally, for each non-stoichiometry extent δ, the logarithm plot of oxygen partial pressure versus the inverse temperature can be fitted by linear regression from which the enthalpy and entropy of reduction can be extracted from the analysis, as represented in Figure 2-13d. For a fixed δ, both the entropy and enthalpy were obtained with a linear regression. Thus, enthalpy and entropy can be calculated for all the stoichiometric extent values. Likewise, the different data used to compute the thermodynamic constant of LSMMg are represented in Figure 2-14.

$$\ln\left(\frac{p_{O_2}}{P^{\circ}}\right)_{\delta} = \frac{2\Delta S_o(\delta)}{R} - \frac{2\Delta H_o(\delta)}{RT} \quad (29)$$

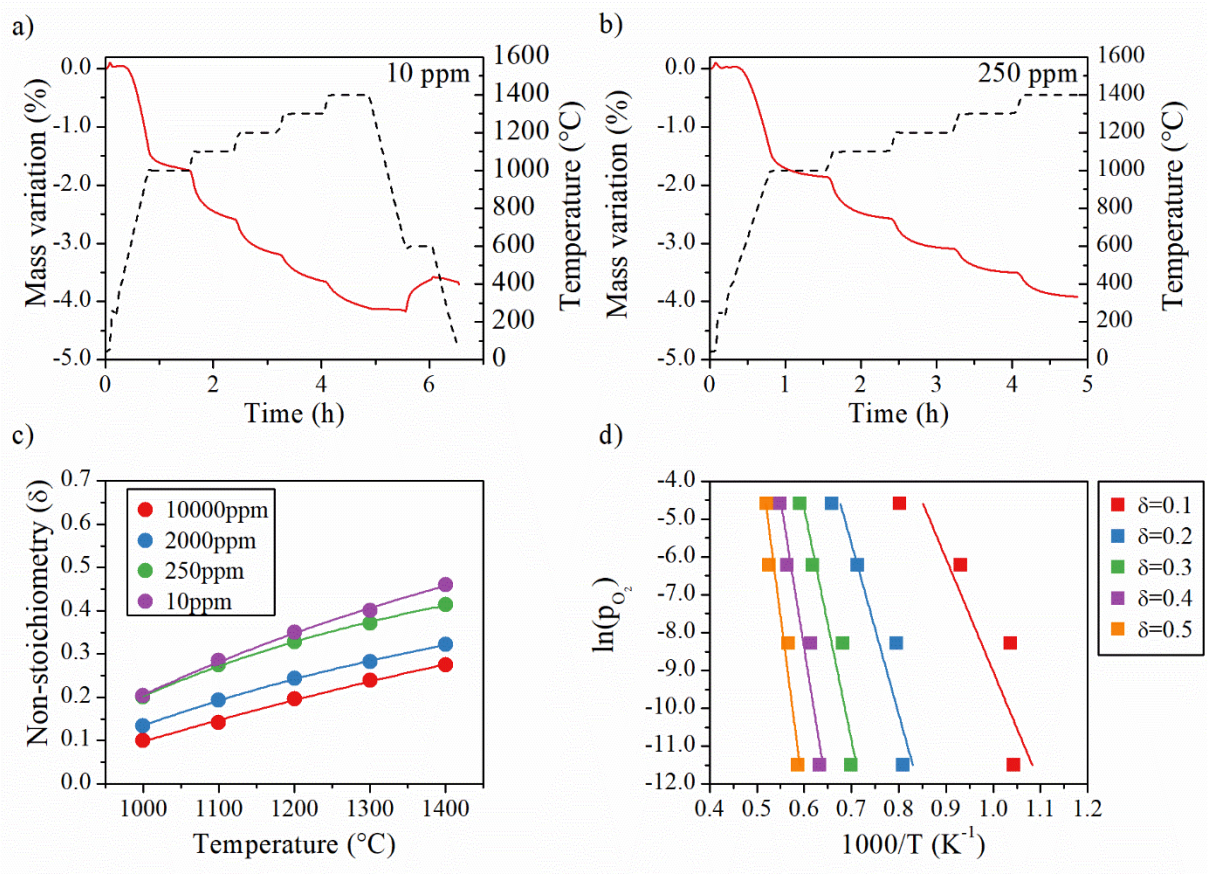

Figure 2-13: a) TGA of CSM under 10 ppm O_2, b) TGA of CSM under 250 ppm O_2 with five temperature steps, c) non-stoichiometry extent as a function of temperature and d) logarithm of oxygen partial pressure versus inverse temperature for CSM

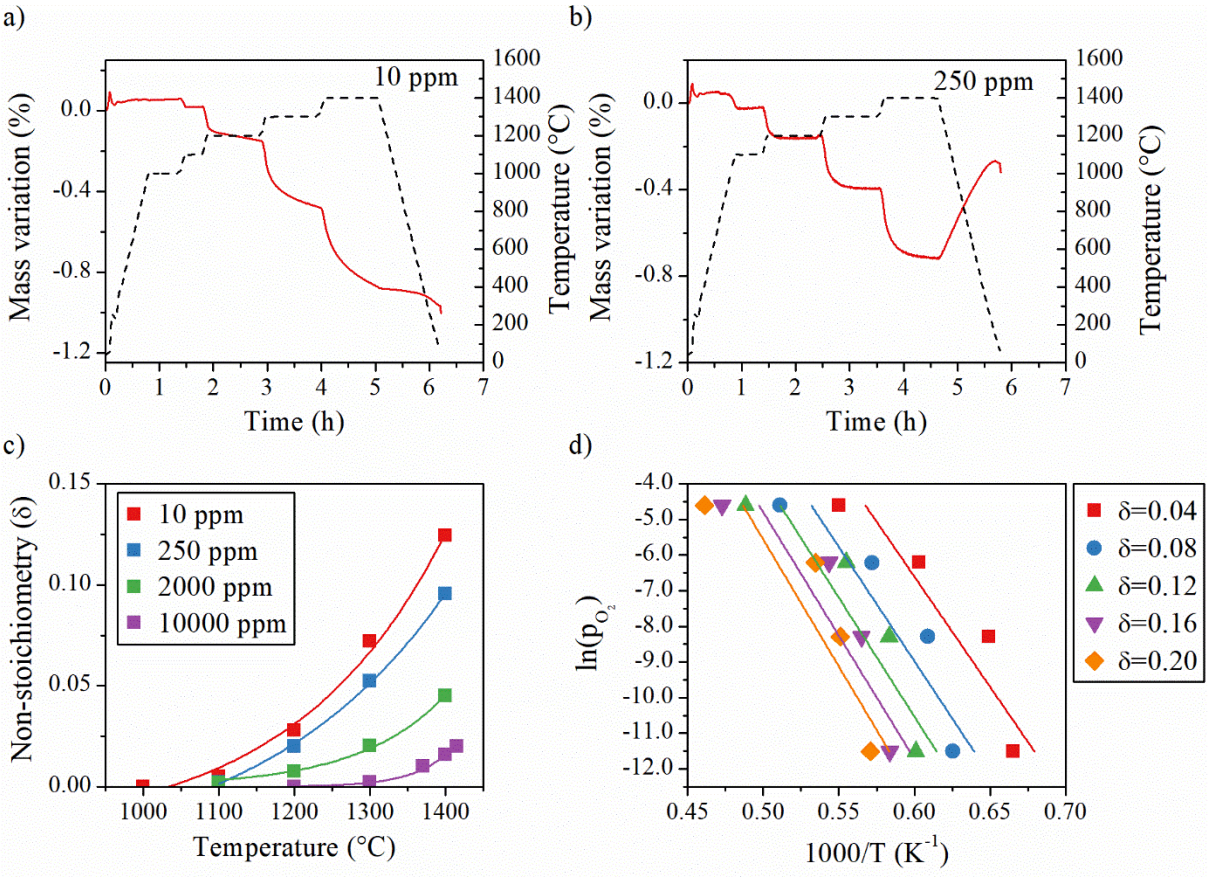

Figure 2-14: a) TGA of LSMMg under 10 ppm O_2, b) TGA of LSMMg under 250 ppm O_2, with five temperature steps, c) non-stoichiometry extent as a function of temperature and d) logarithm of oxygen partial pressure versus inverse temperature for LSMMg

The thermodynamic properties of both materials have been investigated with the calculation of their enthalpies and entropies as a function of non-stoichiometry (Figure 2-15). The enthalpy and entropy values for CeO_2 and $La_{0.5}Sr_{0.5}MnO_3$ (LSM) calculated by [119, 196] are also plotted. Both CSM and LSMMg-P1 present an increase of the entropy and enthalpy with the increase of non-stoichiometry. Figure 2-16 presents the evolution of the Gibbs free enthalpy as a function of the non-stoichiometry extent for a temperature of 1400 °C under 10 ppm O_2. In both cases, ΔG constantly increases with the increase of non-stoichiometry. This can be explained by the fact that increasing the non-stoichiometry requires to increase the energy input to the reaction.

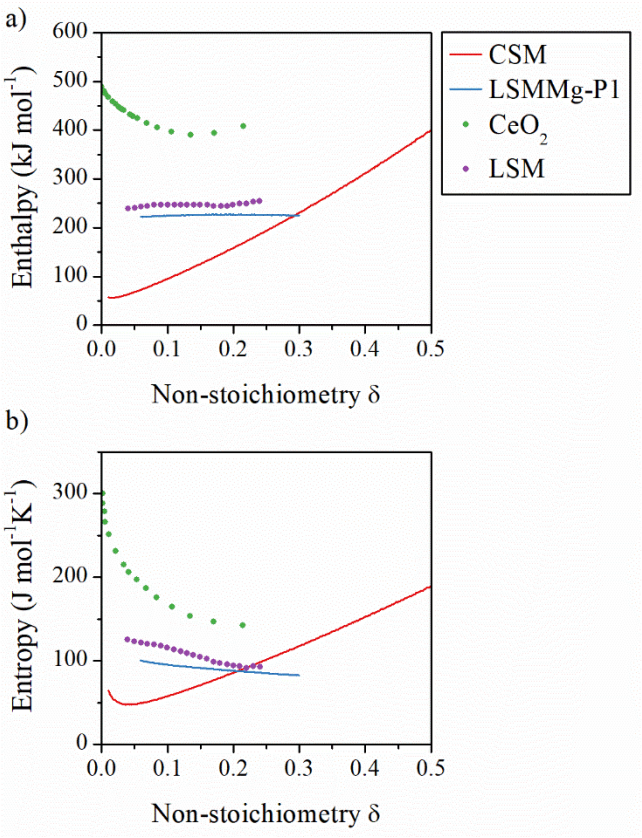

Figure 2-15: a) Enthalpy and b) entropy of reduction as a function of the non-stoichiometry for CSM and LSMMg. Data for CeO_2 and LSM issued from [119, 196] are added for comparison

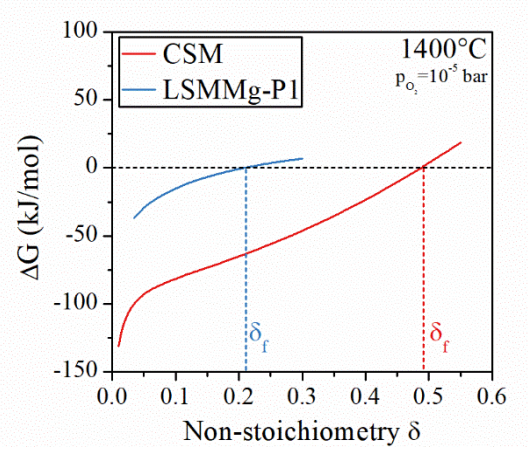

Figure 2-16: Non-standard Gibbs free enthalpy at 1400 °C under 10 ppm O_2 along with the non-stoichiometry extent for CSM and LSMMg

From the knowledge of the enthalpy and entropy values, it is possible to determine the theoretical maximum non-stoichiometry extent for both oxidation and reduction steps. In the following, the reduction extent and the re-oxidation yield of CSM and LSMMg in similar conditions than the TG analysis (reduction at 1400 °C under 10 ppm O_2 with a re-oxidation step at 1050 °C) are predicted thanks to the thermodynamic properties extracted from the previous analysis. At the reaction equilibrium, the Gibbs free enthalpy of the reaction is null. To obtain the final non-stoichiometry extent (δ_f), the non-standard Gibbs free enthalpy needs to be determined as a function of the non-stoichiometry. Thus, for fixed operating conditions, the

reduction extent at equilibrium, which corresponds to a null Gibbs free enthalpy, is the final reduction extent obtained from equation (30).

$$\Delta G_{\mathrm{o}}(\delta_f) = \Delta H_{\mathrm{o}}(\delta_f) - T_{red}\Delta S_{\mathrm{o}}(\delta_f) + \frac{1}{2}RT\ ln\left(\frac{p_{\mathrm{O_2}}}{P^{\circ}}\right) = 0 \quad (30)$$

The determination of the final non-stoichiometry of CSM and LSMMg after reduction step is represented in Figure 2-16 by the vertical dashed lines.

Concerning the oxidation step, it is also possible to determine the non-stoichiometry reached after the re-oxidation reaction (δ_{ox}). The re-oxidation of the reduced material ($\mathrm{M_xO_{y-\delta_{red}}}$) with CO_2 (reaction 31) is the sum of the material oxidation with O_2 (reaction 32) and the CO_2 dissociation (reaction 33).

$$\frac{1}{\Delta\delta}\mathrm{M}_x\mathrm{O}_{y-\delta_{red}} + \mathrm{CO_2} \rightarrow \frac{1}{\Delta\delta}\mathrm{M}_x\mathrm{O}_{y-\delta_{ox}} + \mathrm{CO} \quad (31)$$

$$\frac{1}{\Delta\delta}\mathrm{M}_x\mathrm{O}_{y-\delta_{red}} + \frac{1}{2}\mathrm{O_2} \rightarrow \frac{1}{\Delta\delta}\mathrm{M}_x\mathrm{O}_{y-\delta_{ox}} \quad (32)$$

$$\mathrm{CO_2} \rightarrow \mathrm{CO} + \frac{1}{2}\mathrm{O_2} \quad (33)$$

Thus, the Gibbs enthalpy of re-oxidation reaction is the sum of Gibbs enthalpy of the two previous reactions, as defined by the equation (34),

$$\Delta G^{\circ}_{re-ox} = -\Delta G^{\circ}_{\mathrm{o}}(\delta_{ox}) + \Delta G^{\circ}_{\mathrm{CO_2}} \quad (34)$$

where ΔG°_{re-ox}, ΔG°_{ox} and $\Delta G^{\circ}_{\mathrm{CO_2}}$ are the standard free energy of the reactions (31), (32) and (33) respectively. The equilibrium constant of the CO_2 dissociation can be expressed at 1 atm as:

$$K_{diss} = \frac{p_{\mathrm{CO}} * p_{\mathrm{O_2}}^{1/2}}{p_{\mathrm{CO_2}} * P^{\circ 1/2}} \quad (35)$$

where K_{diss} is the dissociation constant, p_{CO}, $p_{\mathrm{O_2}}$, and $p_{\mathrm{CO_2}}$ the partial pressure of CO, O_2 and CO_2. The equilibrium CO yields can be determined by expressing the oxygen partial pressure in terms of the dissociation constant, the CO_2 and CO partial pressures, as shown by equation (36).

$$\Delta G_O(\delta_{red} - \Delta\delta) = RT_{ox}\ ln\left[\frac{K_{diss}p_{\mathrm{CO_2}}}{p_{\mathrm{CO}}}\right] \quad (36)$$

The different partial pressures can be expressed according to the following equations:

$$p_{\mathrm{CO_2}} = \frac{n_{\mathrm{CO_2},i} - n_{\mathrm{CO}}}{n_g} \quad (37)$$

$$p_{\mathrm{CO}} = \frac{n_{\mathrm{CO}}}{n_g} \tag{38}$$

where $n_{\mathrm{CO}_2,i}$, n_{CO}, n_g are the initial amount of CO_2, the amount of CO and the total amount of gas per mole of reactive material, respectively. Combining the equations (36), (37) and (38) allows to determine the amount of CO produced per mole of material, and corresponding to $\Delta\delta$. It assumes that the reaction occurs in a closed-system and the spontaneous CO_2 dissociation is not significant at the oxidation temperature. Similar reasoning can be applied for an oxidation step using water as oxidant gas [42, 51, 53, 76]. Using the method previously exposed, the theoretical reduction extent and fuel production yield for CSM and LSMMg were computed (Table 2-3). The operation conditions inputted in the thermodynamic model are the followings: reduction step at 1400 °C under 10^{-5} bar of O_2 partial pressure, followed by a re-oxidation at 1050 °C. The initial amount of oxidant gas is assumed to be in large excess at $n_{\mathrm{CO}_2,i} = 1000\delta_{red}$ as used in [42]. These operation conditions correspond to those used in TGA. The theoretical final non-stoichiometry extents after the reduction step were calculated at 0.475 and 0.231 for CSM and LSMMg-P1, respectively. Thus, CSM reached a higher reduction extent (1469 µmol/g) than LSMMg-P1 (542 µmol/g) at equilibrium, which is due to the lower enthalpy for CSM in comparison with LSMMg-P1, that permits to reach higher final non-stoichiometry. Concerning the oxidation step, LSMMg-P1 presents a high re-oxidation yield (72%), whereas it is only 32% for CSM at 1050 °C. Indeed, CSM exhibits a too low enthalpy to allow full re-oxidation. However, the comparison between the theoretical and experimental values obtained with TGA shows a large disparity. This can be explained by the limited cycling duration used in TGA, impeding reaction completion, whereas the thermodynamic study does not consider reaction kinetics. Secondly as the reduction step is not complete, then during the re-oxidation step, the non-stoichiometry variation is lower. Thus, the thermodynamic study is a relevant approach to highlight interesting reactive materials for thermochemical cycles, but it must be completed with experimental data and kinetic study of thermochemical cycles.

Table 2-3: Theoretical non-stoichiometry extents and O_2 and CO production yields derived from a thermodynamic study (T_{red}=1400 °C, $p_{O2,\,red}$=10^{-5} bar, T_{ox}=1050 °C under CO_2 excess)

Compound	Reduction step		Oxidation step		
	δ_{red}	O_2 produced (µmol/g)	δ_{ox}	$\Delta\delta$	CO produced (µmol/g)
CSM	0.475	1469	0.321	0.154	927
LSMMg-P1	0.231	542	0.064	0.167	784

2.5 Kinetic study

The kinetics of redox reactions was investigated to predict the amount of fuel produced by a reactive material as a function of the cycling time. However, the study of reaction kinetics is complex due to the high number of involved parameters. The kinetic rate of a reaction is defined by equation (39),

$$\frac{d\alpha}{dt} = A\,exp\left(-\frac{E_a}{RT}\right) f(\alpha) \tag{39}$$

where α is the conversion extent, f a mathematical function representing the reaction mechanism, E_a the activation energy, A the pre-exponential factor and T the temperature.

The main reaction models used in solid-state kinetics are presented in

Table 2-4. The nucleation models describe reactions such as crystallization, crystallographic transition or adsorption. The geometrical contraction models assume that the reaction is controlled by the progression of the reaction interface toward the center of a reactive particle. Diffusion models represent the kinetic mechanism in a reaction that is controlled by the thickness of the product barrier. While in the order-based models, the reaction rate is proportional to the concentration of remaining reactants.

Table 2-4: Usual kinetic models for solid-state reactions [197, 198]

Model	**Code**	$f(\alpha)$
Nucleation models		
Power law	P4	$4\alpha^{3/4}$
Power law	P3	$3\alpha^{2/3}$
Power law	P2	$2\alpha^{1/2}$
Power law	P2/3	$2/3\alpha^{-1/2}$
Avrami-Erofeev	A4	$4(1-\alpha)[-\ln(1-\alpha)]^{3/4}$
Avrami-Erofeev	A3	$3(1-\alpha)[-\ln(1-\alpha)]^{2/3}$
Avrami Erofeev	A2	$2(1-\alpha)[-\ln(1-\alpha)]^{1/2}$
Reaction order models		
Mampel (first order)	F1	$1-\alpha$
Second order	F2	$(1-\alpha)^2$
Third order	F3	$(1-\alpha)^3$
Diffusion models		
One-dimensional diffusion	D1	$1/2\alpha^{-1}$
Two-dimensional diffusion	D2	$[-\ln(1-\alpha)]^{-1}$
Three-dimensional diffusion	D3	$3/2(1-\alpha)^{2/3}\left[1-(1-\alpha)^{1/3}\right]^{-1}$
Geometrical contraction models		
Contracting sphere	R3	$3(1-\alpha)^{2/3}$
Contracting cylinder	R2	$2(1-\alpha)^{1/2}$

In this study, two approaches are proposed to investigate the kinetics of the reduction reaction. The first one is a simple method requiring experimental data with only one heating rate, which gives a first evaluation of the activation energy. The second method requires performing the reduction reaction with at least three different temperature ramps and it permits to obtain the activation energy as a function of the conversion extent.

2.5.1 Simple method for determining the activation energy

The first method developed permits to calculate the activation energy of the reduction reaction by assuming that the reaction mechanism is unchanged during the process. Rewriting the general kinetic equation (39) gives the equation (40).

$$\ln\left(\frac{d\alpha/dt}{f(\alpha)}\right) = \ln(A) - \frac{E_a}{RT} \quad (40)$$

By plotting $\ln\left(\frac{d\alpha/dt}{f(\alpha)}\right)$ as a function of $1/T$, the activation energy is calculated by linear regression. This method requires knowing the reaction model function, thus the contracting sphere model (R3) was used, assuming that the reaction proceeds from the external surface to the core of particles [199]. Indeed, the contracting sphere model (R3) offers the best fitting of experimental data (presented in Figure SB-12), unlike other models that do not fit correctly the experimental data. The activation energies for all the investigated materials were calculated with this method thanks to TGA data. Figure 2-17 represents the activation energy for the reduction of reactive materials plotted as function of O_2 production yield. The hollowed scatters represent data with high residual standard deviation value during the linear regression. Within a material family, the increase of activation energy was correlated with the decrease of O_2 production yield. Indeed, the activation energy represents the energy barrier that should be overpassed to perform a reaction. Consequently, the activation energy can be used as an indicator to predict the non-stoichiometry reached by a reactive material. However, it does not give any indication on the oxidation step, impeding to predict the amount of fuel produced.

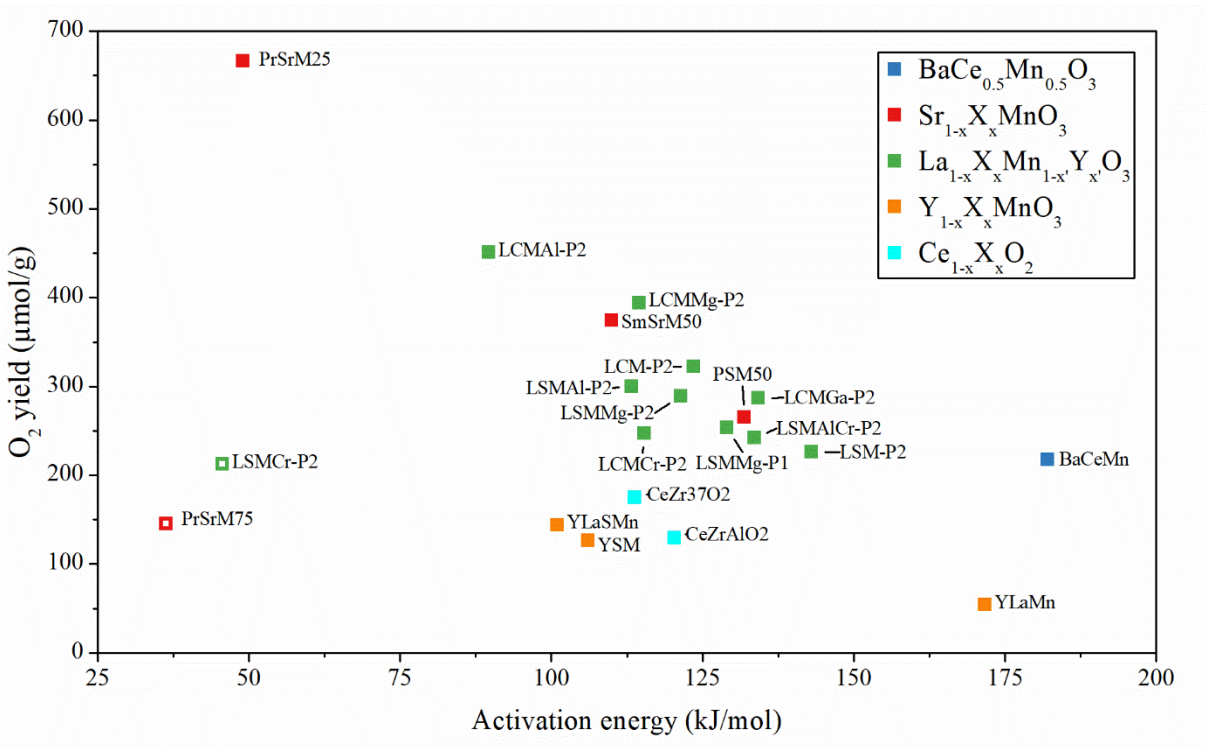

Figure 2-17: Experimental O_2 yield as a function of activation energy for the series of investigated reactive materials.

2.5.2 Iso-conversion method to calculate the activation energy

The activation energy as a function of the conversion extent can be obtained thanks to the iso-conversion method. It assumes that, for a fixed conversion extent, the reaction rate only depends on the temperature, as expressed by equation (41).

$$\left[\frac{\partial \ln\left(\frac{\mathrm{d}\alpha}{\mathrm{d}t}\right)}{\partial T^{-1}}\right]_{\alpha} = -\frac{E_{\alpha}}{R} \tag{41}$$

Numerous iso-conversional computational methods exist, using the same principle. In this study, the differential iso-conversional method developed by Friedman [200] was used. It is based on the following equation:

$$\ln\left(\frac{\mathrm{d}\alpha}{\mathrm{d}t}\right)_{\alpha,i} = \ln[f(\alpha)A_{\alpha}] - \frac{E_{\alpha}}{RT_{\alpha,i}} \tag{42}$$

where i denotes the ramp temperature, $T_{\alpha,i}$ is the temperature at which α is reached under the temperature ramp i. Plotting $\ln\left(\frac{\mathrm{d}\alpha}{\mathrm{d}t}\right)_{\alpha,i}$ as a function of $1/T_{\alpha,i}$ permits to obtain the activation energy for each α value determined from the slope of the plot (Figure 2-19). The method is model-free as it does not require to assume any reaction model. Complex reaction mechanisms can even be highlighted by a discontinuity of the activation energy as a function of the conversion extent. Three temperature ramps were performed in TGA, as illustrated in Figure 2-18. The conversion extent was defined as the ratio of the non-stoichiometry extent to the final non-stoichiometry extent. The latter was assumed to be the theoretical final non-stoichiometry extent at 1400 °C under 10 ppm O_2 calculated in the thermodynamic study. The non-stoichiometry evolution as a function of temperature for 3 °C/min and 5 °C/min ramps (Figure 2-18) are very similar (but different) because the temperature ramps are close. The non-stoichiometry interval in which the activation energy was determined corresponds to the non-stoichiometry values reached at the different temperatures during the heating, since the iso-conversional method required using different temperatures for a given α value.

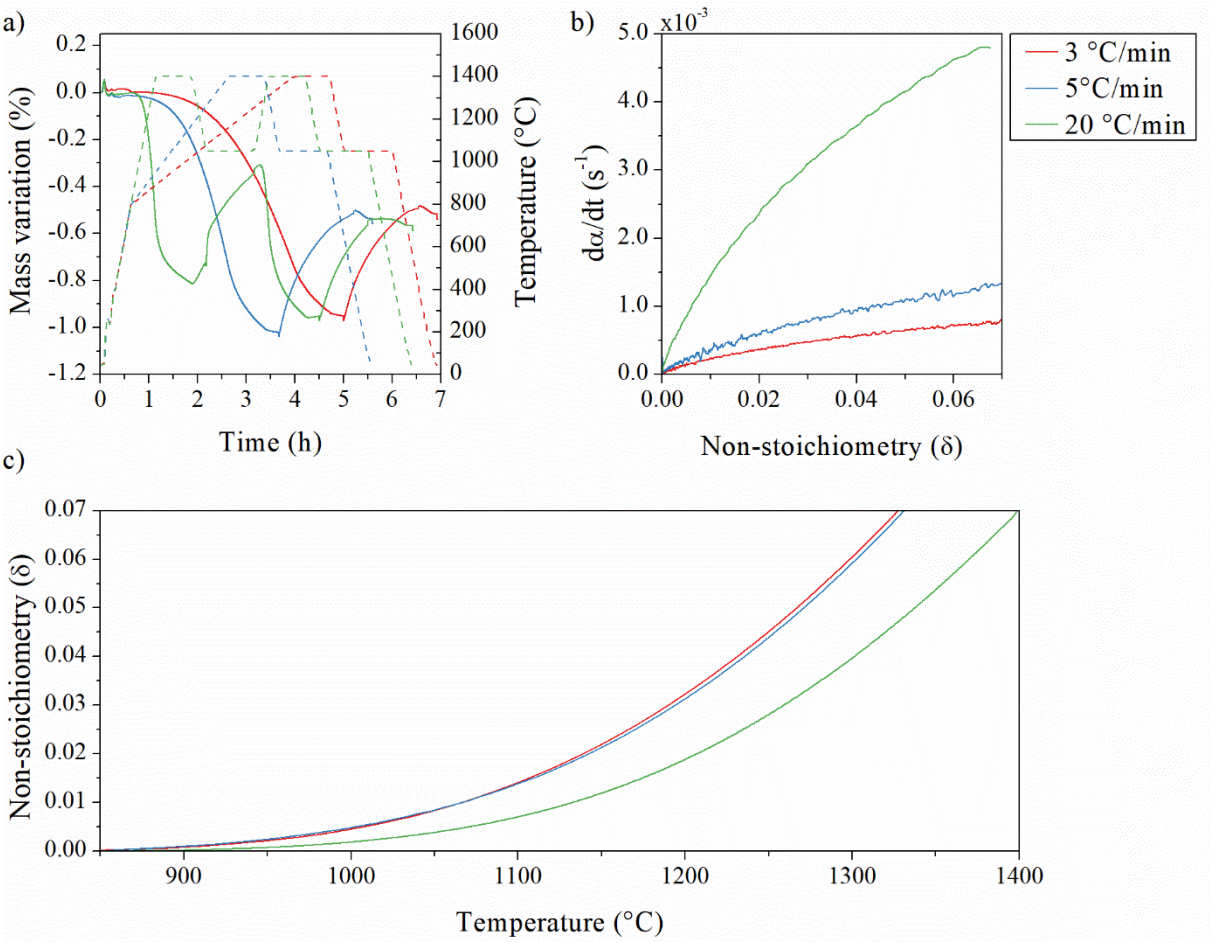

Figure 2-18: a) Mass variation during TGA of LSMMg for different heating rates under Ar (3 °C/min, 5 °C/min, and 20 °C/min) along with the associated temperature profiles. The mass loss during the first reduction step at the different heating rates was used for kinetic analysis (after reduction, the material was re-oxidized at 1050 °C under 50% CO_2 in Ar) b) associated conversion extent as function of non-stoichiometry, c) associated non-stoichiometry extent as a function of temperature

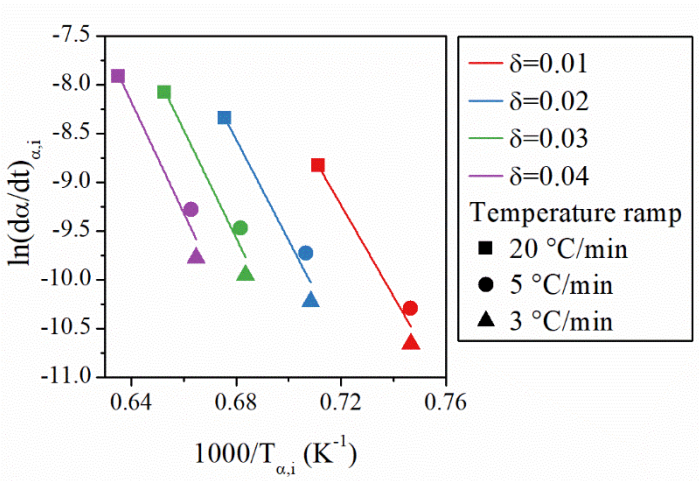

Figure 2-19: Logarithm of the reaction rate as a function of the inverse temperature for different non-stoichiometry extents at constant heating rates

The activation energy for the reduction of LSMMg-P1 was computed with this method, as presented in Figure 2-20. The evolution of the activation energy versus non-stoichiometry extent does not show any discontinuity, revealing a single reaction mechanism during the

reduction step. The activation energy is not constant with the evolution of the reduction extent: it increases from ~300 kJ/mol up to ~500 kJ/mol when non-stoichiometry increases. This means that, through the reduction reaction, the activation energy increases as the oxide reduction progresses. In other words, reduction of LSMMg-P1 becomes more kinetically limited as oxygen extraction proceeds, and the reduction reaction is thus increasingly hindered. This study thus confirms the relevance of the determination of the activation energy versus non-stoichiometry during the reduction reaction. The iso-conversion method provides relevant information about the kinetic behavior of reactive materials used in thermochemical cycles. Regarding the oxidation step, such methods are not applicable because the oxidation step is favored by a temperature decrease in the investigated temperature range, thus implying a thermodynamic control of the reaction.

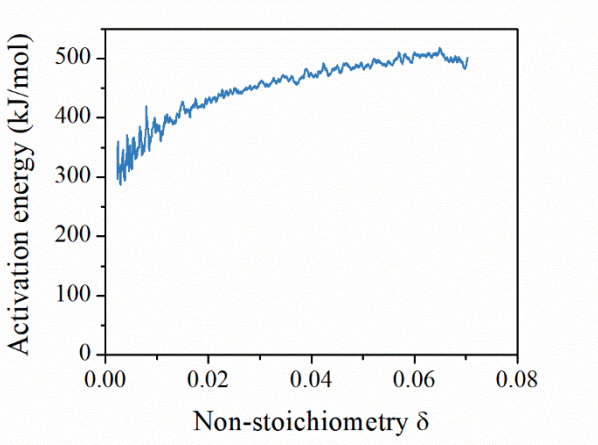

Figure 2-20: Activation energy of LSMMg reduction as a function of the non-stoichiometry extent

2.6 Conclusion

In this chapter, a large range of materials compositions was probed in order to identify suitable materials for thermochemical cycles with potentially high solar-to-fuel conversion efficiency. First, the influence of the derived-Pechini method was investigated. It was highlighted that large excess in citrate agent (P2 method) leads the increase of powder sinterability, which can be suitable to realize dense layers. In contrast, the P1 method appears to be more suitable to synthesize reactive materials for stable thermochemical two-step cycles due to low powder sinterability.

The materials compositions were experimentally screened to unveil the variations in redox reactivity. In comparison with ceria considered as the benchmark material, numerous perovskites offer improved thermochemical performance, such as (La,A)(B,Mn)O_3 with A=Ca and Sr and B=Al, Al/Cr, Cr, Ga and Mg, (Pr,Sr)MnO_3, (Sm,Sr)MnO_3. LSMMg exhibits promising performance, because it offers a high reduction extent and high fuel production yield, combined with good thermal stability. In addition, $Ca_{0.5}Sr_{0.5}MnO_3$ (CSM) was also selected due to its high reduction capability and oxygen mobility, which could be of interest for applications requiring oxygen ion-conducting materials (ceramic membranes). Kinetic and/or thermodynamic properties of LSMMg and CSM were extracted from different experiments to provide further insights on the redox activity of these materials.

It has been demonstrated that in $A_{1-x}Sr_xMnO_3$ perovskites, Sm^{3+} and Pr^{3+} in A site permit to increase the reduction extent in comparison with La^{3+} but the re-oxidation yield is not enhanced as well. The extent of Sr^{2+} substitution impacts on the perovskite reduction extent as it modifies the Mn oxidation state. Among the lanthanum-manganite perovskites, Ca^{2+} dopant in A site permits to increase the amount of oxygen released in comparison with Sr^{2+} but not the fuel production yield. For LSM, doping with Ga^{3+}, Al^{3+} and Mg^{2+} brings about an improvement of the amount of oxygen and fuel produced. On the contrary, doping with Cr or Al/Cr negatively impacts on LSM thermochemical performance.

For doped ceria, the increase of Zr^{4+} incorporation enhances the reduction extent. The optimal Zr content appears to be 15% as it increases both the oxygen and fuel production yields. Conversely, co-doping with Al^{3+}/Zr^{4+} does not improve ceria thermochemical cycles.

It has been highlighted that the activation energy of the reduction step is correlated with the reduction extent of the reactive material. Moreover, the activation energy increases with the increase of non-stoichiometry extent during the progression of the reduction reaction. However, reduction kinetics does not allow anticipating the re-oxidation rate/yield which is also a key factor in determining materials suitability. In addition, the thermodynamic properties determination permits to predict the theoretical reduction and re-oxidation extent, but the experimentally obtained values can be lower than the predicted ones at thermodynamic equilibrium due to kinetic limitations. Thus, it is essential to combine both kinetic and thermodynamic studies, in order to provide the most complete overview of the redox behavior of the selected reactive materials.

Chapitre 3 - Thermochemical performance evaluation of reticulated porous ceria structures in a monolithic solar reactor[2]

3.1 Introduction

To date, different solar reactor concepts have been investigated for thermochemical cycles. Cho et al. [161, 201] performed 13 thermochemical cycles using a 40 kW_{th} solar furnace with CeO_2 reactive coating on inert zirconia foam, yielding an average H_2 production per cycle of about 2.1 mL/g. An isothermal thermochemical cycle was carried out in a 4.4 kW solar reactor using ceria [190], producing 360 mL/min of CO at constant temperature of 1477 °C. Using a gas-phase heat recovery system, the solar-to-fuel efficiency reached 1.64% without taking into account the inert gas energy costs [167]. An electrically-heated monolithic reactor irradiated by artificial light, with porous ceria as reactive material, was developed elsewhere [68, 159, 202]. Stable and rapid fuel production was demonstrated over 500 cycles with peak and average solar-to-fuel efficiencies of 3.53 % and 1.73%, respectively [159]. The highest efficiency of ~5% was obtained with T_{red}=1500 °C, T_{ox}=800 °C and a total pressure of 10 mbar during the reduction step [46]. A counter rotating ring reactor was also designed [169, 203, 204], yielding instant solar-to-fuel efficiency of 1.7% and peak CO production rate of 100 mL/min.

A novel 1.5 kW monolithic solar reactor was designed and developed at PROMES laboratory for two-step thermochemical H_2O and CO_2 splitting with non-stoichiometric metal oxides as oxygen carrier redox materials. A reticulated ceria foam was integrated inside the reactor cavity. Such a porous structure acting as the reactive material itself inherently combines the advantages of efficient volumetric radiative absorption, low pressure drop, high surface area, rapid reaction rates, and high mass loading of the reactive material. Low optical thickness (i.e., low opacity) for incident thermal radiation is desired to enable both volumetric radiative absorption and uniform heating of the porous structure. On the other hand, the oxidation step with H_2O or CO_2 is known to be largely surface dependent, and thus a large surface area is required to enhance reaction kinetics. Hence, a trade-off must be found between rapid reaction kinetics and efficient radiation heat transfer, by combining both of the desired properties, namely: low optical thickness for volumetric radiative absorption during reduction and high surface area for rapid

[2] Most of the results of this chapter have been published in three peer-reviewed articles:

- A. Haeussler, S. Abanades, A. Julbe, J. Jouannaux, M. Drobek, A. Ayral and B. Cartoixa. *Chem Eng Res Des*, 2020, **156**, 311–323
- A. Haeussler, S. Abanades, A. Julbe, J. Jouannaux and B. Cartoixa. *Energy*, 2020, **201**, 117649
- A. Haeussler, S. Abanades, A. Julbe, J. Jouannaux and B. Cartoixa. *Journal of CO_2 Utilization*, 2020, **41**, 101257

reaction rates during oxidation. In addition, low porosity is favorable for high material mass loading in the reactor. The above issues have to be considered when dealing with porous reactive structures. In this respect, the porous reticulated ceria foams offer both uniform cell size density (millimetric scale) for solar radiation volumetric absorption and granular microstructure (micron-sized grains forming an interconnected macroporous network) within the foam struts for enhanced oxidation reaction. The experimental performance assessment of the reactor has been conducted to determine the most relevant operating parameters encompassing the reactions temperatures, reduction pressure, type and concentration of oxidant, influencing solar fuel production. Indeed, the identification of suitable operating parameters to reach optimized thermochemical performance is essential for further process scale-up. Specifically, the amounts of produced fuel and fuel production rates have been optimized. Such a detailed parametric optimization, carried out on a real solar reactor operated with reticulated porous ceria structures under representative operating conditions has never been achieved to date.

3.2 Experimental method and set-up

3.2.1 Specifications of the solar reactor

The solar reactor consists of a cavity-type cylindrical absorber heated by concentrated solar energy (Figure 3-1). It is based on the directly-irradiated concept and it is chiefly composed of a vertical tubular cavity (80 mm height, 50 mm inside diameter, 60 mm outside diameter) acting as a blackbody solar receiver. Alumina was selected as the high-temperature wall material because it is thermally resistant while it is chemically inert in both reducing and oxidizing conditions. Thus, chemical interactions between the reactant and the reactor wall are avoided. A transparent hemispherical Pyrex glass window is fixed at the front of the reactor to allow solar radiation entering within the cavity while separating the cavity chamber from the surrounding air atmosphere. With this arrangement, the irradiated reaction zone in which the cycling redox reactions occur is maintained under controlled atmosphere. The window hemispherical shape is selected to position the window away from the focal point, thus avoiding glass overheating, which is requested for stable and reliable reactor operation during repeated cycles at the high-temperature processing conditions. The cavity made of alumina is designed to absorb the concentrated solar power via the front aperture plate also made of alumina (18 mm-diameter aperture). The aperture is placed at the focal point of the solar concentrating system (0.85 m from the parabolic mirror) where the solar flux density can reach over 10 MW/m^2, thus representing 1.5 kW of maximum thermal power absorbed by the cavity (for a direct normal irradiation DNI of 1 kW/m^2). The cavity walls are well insulated by using a porous alumino-silicate fibrous layer directly wrapping the ceramic cavity in order to minimize thermal conductive losses (total thickness of 3.6 cm on each side, 14 cm of external diameter and 14.6 cm height). A board of zirconia felt (2 mm thickness) is also used to insulate the front alumina wall of the aperture plate, thereby reducing the radiative losses at the upper front.

The height of the foam inside the cavity was about 50 mm and it was hollowed at its center to promote radiative heat transfer and absorption along the annular foam height, thereby favoring uniform heating of the whole reacting ceria structure.

The injected gas flows in the downward direction from the top to the bottom of the cavity to favor temperature homogenization. Ar gas flow is continually injected in the window area to provide inert gas atmosphere; it then enters the cavity via the aperture and sweeps the inner cavity volume. In addition, an auxiliary gas inlet (6 mm alumina tube) is positioned at the top of the cavity below the aperture for rapid gas composition switch between reduction and oxidation steps. Ar is injected during reduction step whereas a mixture of Ar and CO_2 (or steam) is injected during oxidation step. The gas then flows through the porous ceria structure inside the cavity and exits at the bottom via a single outlet port located at the center. The gas composition is controlled and adjusted via mass-flow controllers (MFC, Brooks Instruments model SLA5850S). Different MFCs are used to control the flowrates of purge gas (Ar, 99.999% purity, O_2 content below 2 ppm) and CO_2 (99.995% purity). Water is injected using a liquid mass flow controller (range 0-60 g/h, accuracy ±1% of full scale) via an alumina capillary settled inside the auxiliary tube inlet and heated by the nearby cavity. Water is thus vaporized inside the heated capillary and is then transported by the surrounding carrier gas to the cavity volume.

Different temperature sensors are used to control the reactor temperature at different locations and heights (at the external cavity wall and in contact with the reactive foam). The foam temperature is measured directly via three B-type (Pt–Rh) thermocouples (T1 at the bottom of the cylindrical part, i.e. 60 mm from the cavity top, T2 at the upper part, i.e. 40 mm from the cavity top, and T3 below the foam, i.e. 80 mm from the cavity top). Besides, an optical solar-blind pyrometer operating at 4.8-5.2 μm also monitors the temperature of the cavity by pointing in the central hollow foam via a CaF_2 porthole. The reactor pressure is measured by pressure transmitters placed at the gas inlets (window and auxiliary gas) and cavity. The reactor was operated at atmospheric pressure in the cavity (about 0.85 bar at the experimental site altitude, 1500 m) and the pressure drop due to the foam was negligible. In addition, low pressure experiments with flowing gas were also performed by continuously pumping at the reactor outlet (using a primary vacuum pump) in order to study the effect of pressure on the reduction extent and fuel production yield.

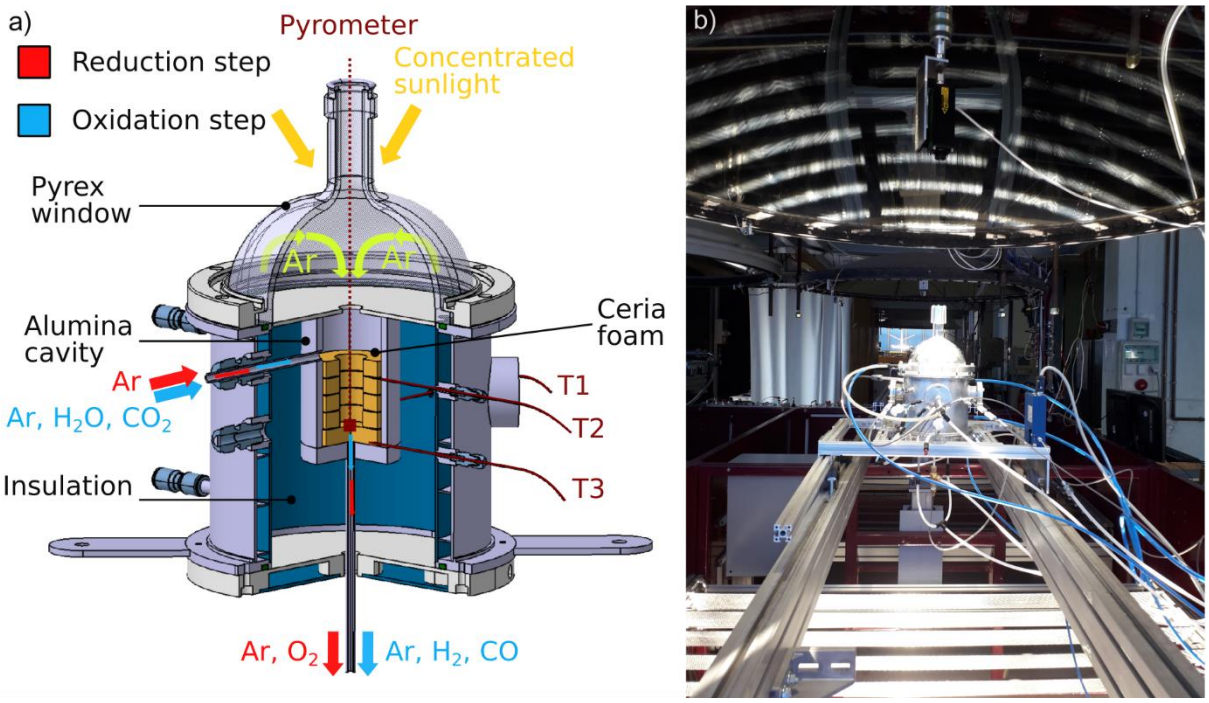

Figure 3-1: a) Schematic illustration of the 1.5 kW_{th} monolithic solar reactor for ceria redox cycling to produce H_2 and CO, b) SUNFUEL solar reactor during on-sun testing.

3.2.2 Materials and methods

The experiments were carried out at the focus of a vertical-axis medium size solar furnace comprising a sun-tracking heliostat and a parabolic dish solar concentrator (2 m-diameter, Gaussian flux density distribution). The focal point of the concentrator (0.85 m ahead of the parabolic mirror) was located at the cavity aperture for maximum solar radiation absorption inside the cavity receiver. The absorbed solar power that determines the reactor temperature was controlled and adjusted by the means of an intermediate shutter placed between the heliostat and the solar concentrator (below the reactor), thus enabling heating/cooling rates and temperature control. The reduction and oxidation steps were performed alternately via temperature-swing cycling while switching the gas flow between each cycle step.

The reactor was first connected to a vacuum pump to remove remaining air, and then purged with Ar inert gas before further solar heating. Complete removal of residual oxygen before starting the reduction step was ascertained by the O_2 concentration below 10 ppm in the flowing gas. A trace O_2 analyzer with electrochemical cell (Systech, range from 0.1 ppm to 1%, precision ±2% of reading) was used to measure online the O_2 concentration in the outlet gas. After purging, the reactor was gradually heated with a stable heating rate up to the maximal reduction temperature by stepwise shutter opening. During heating in Ar (Q_{Ar}=1.2 NL/min), O_2 was continuously released from ceria and its concentration increased steadily in response to the heating rate. The start of ceria reduction was detected after a period of reactor heating when approaching ~900 °C. The material reduction was continuously monitored by measuring the outlet O_2 concentration (used to calculate the O_2 production rate). Once reaching the temperature dwell, the O_2 concentration dropped smoothly because thermodynamic equilibrium was progressively reached when stabilizing the temperature. Then, the temperature was

decreased by closing the shutter, which fastened the drop of O_2 concentration. The reduction step was completed when O_2 concentration dropped to values below 10 ppm. The oxidation step was subsequently conducted by injecting the reactive gas flow (water steam or CO_2) to produce H_2 or CO. The oxidant gas was injected under either isothermal (i.e. once the targeted oxidation temperature was steady) or non-isothermal conditions (i.e. below a given temperature during free cooling with no solar energy input). The CO (and CO_2) concentrations in the exhaust gas were measured on-line (concentration vs. time profiles) by a specific analyzer with NDIR sensors (MGA3000, full scale: 0–30% for CO, 0-100% for CO_2, precision ±1% of full scale). H_2 was also analyzed continuously thanks to a specifically devoted H_2 analyzer based on thermal conductivity detection (catharometer for Ar/H_2 binary mixture, scale: 0-10%, precision: 1% of full scale), in order to quantify the H_2 produced during the reaction progress. H_2 or CO were detected few seconds after steam or CO_2 injection (< 10 s) and their concentration reached a maximum corresponding to the peak fuel production rate. After the peak, the concentration returned progressively to zero and the oxidizing gas injection was stopped to proceed to the next cycle by increasing the temperature again for the reduction step. Before gas analysis, the outlet gas flowed through a set including a bubbler to eliminate excess steam and a gas drying unit (desiccant column) to protect the analytical instrument. In the case of H_2O splitting, the excess water was entirely condensed and trapped and the gas analyzed was thus composed of a binary mixture Ar/H_2. In the case of CO_2 splitting, the outlet gas was composed of unreacted CO_2 in addition to Ar and CO. The whole process parameters (temperatures, pressures, gas flowrates, outlet gas concentrations) were recorded every seconds by an automated data acquisition system (Beckhoff).

The time-dependent gas production rates (F_i) were calculated from the inlet carrier gas flow rate (F_{Ar}) and the measured outlet gas mole fractions (y_i) according to equation (43):

$$F_i = F_{\mathrm{Ar}} . \frac{y_i}{1 - y_i} \tag{43}$$

where i denotes O_2 or H_2.

In the case of CO_2 splitting, the outlet CO production rate was determined as by equation (44):

$$F_{\mathrm{CO},outlet} = \left(F_{\mathrm{Ar}} + F_{\mathrm{CO_2},outlet} + F_{\mathrm{CO},outlet}\right) . y_{\mathrm{CO}} \tag{44}$$

where $F_{\mathrm{CO},outlet} + F_{\mathrm{CO_2},outlel} = F_{\mathrm{CO_2},inlet}$

The amounts of gas produced (O_2 and H_2 or CO) were then determined by time integration of the gas production rates over the duration of the reduction and oxidation steps ($\int F_i \mathrm{d}t$). The oxidant conversion defined as the molar ratio of oxidant decomposed to oxidant in the feed was also evaluated [205].

3.2.3 Materials synthesis

The ceria foams were fabricated following a standard replication method using polymer template commonly used for preparing commercial-grade porous catalysts and were supplied by ALSYS-CTI partner. The goal was to use standard commercial-grade foams usually

developed for catalytic applications, in order to demonstrate their efficiency in solar redox cycles for both H_2O and CO_2 splitting without any further microstructure optimization. Future utilization of such foams in industrial-scale processes should then be facilitated. The obtained foams after calcination of the polymer scaffold were fired in air at 1450 °C during 10h to sinter and stabilize their structure. After sintering, the open-cell foams were composed of fine agglomerated ceria grains with interconnected macroporous channels around the grains facilitating the passage of the reacting gas. This type of microstructure was particularly attractive for the targeted solar redox cycle application. Indeed, the large mm-scale cells were suitable for volumetric solar radiation absorption during the reduction reaction, while the µm-scale pores inside the foam struts favored the access of the reacting gas to the ceria bulk for the solid/gas oxidation reaction.

The foams were inserted at the center of the cavity so that the upper side was just below the auxiliary gas inlet. In this chapter, different sets of foams have been investigated:

- Ceria foams (reticulated porous ceramics, RPC) with uniform cell size;
- Ceria foams with axial cell size gradient;
- Perovskite-coated ceria foams;
- Ordered porous structures made of ceria prepared from 3D-printed polymer scaffolds with and without pore forming agent.

All the investigated foams are reported in Table 3-1. First, a set of ceria RPC foams (CF) with uniform cell density was considered as illustrated in Figure 3-2.a. The foams were provided by ALSYS-CTI. The set is composed of a cylindrical foam (45 mm diameter with 20 mm inner cavity diameter, 45 mm length) placed on a disk foam (10 mm height and 45 mm diameter). Two different configurations were considered: (i) a cylinder of 10 ppi and a disc of 10 ppi (CF-10), (ii) a cylinder of 20 ppi and a disc of 20 ppi (CF-20). A second set of CF aims to investigate the impact of axial cell density gradient (Figure 3-2.b) with foams provided by ALSYS-CTI. Three different configurations were considered:

(i) 4 different rings of 10, 20, 30, 45 ppi and a disc of 60 ppi,

(ii) 2 rings of 10 ppi, 2 rings of 20 ppi and a disc of 60 ppi,

(iii) 4 rings of 20 ppi and a disc of 10 ppi.

In the following, these structures are designated as ceria foam with high cell density gradient (CF-HG), medium gradient (CF-MG) and no gradient (CF-NG), respectively. It is expected that increasing the cell density toward the bottom (smaller cell size) enhances the optical thickness and reduces the radiation diffusion, thus increasing temperature gradient from the top to the bottom of the foam. Decreasing the cell size (higher ppi) also enhances foam density, which increases the mass of reacting material loaded in the reactor. The total load of ceria foam was about 55-65 g (mean apparent density of ~0.9-1.1 g/cm^3) in the case of pure ceria RPC (provided by Alsys-CTI), as indicated in Table 3-1 and Table SC-2.

The impact of perovskite coating on the surface of ceria foam was investigated with $La_{0.5}Sr_{0.5}Mn_{0.9}Mg_{0.1}O_3$ coated ceria foam (CF-LSMMg) and $Ca_{0.5}Sr_{0.5}MnO_3$ coated ceria foam (CF-CSM), as illustrated in Figure 3-2.c. The perovskite powder was synthesized by IEM using a modified liquid-phase Pechini process, as described previously [182]. The obtained perovskite powder (LSMMg) was then used as starting material to prepare the ceramic suspension able to coat uniformly the ceria foams (20 ppi) provided by Alsys-CTI [205]. The perovskite-coated foams were prepared at IEM. The perovskite powder was dispersed in water (45 wt %) using a polymethacrylate dispersing agent (DARVAN C-N®) and polyvinyl alcohol (Rhodoviol, 2wt%) as a binder/plasticizer. A SpeedMixer® (DAC 150.1 FVZ-K) was used to prepare fluid, uniform, stable and smooth slurries, suitable for casting. These suspensions were used to coat the surface of ceria foams (20 ppi) with a consolidated LSMMg layer. A set of 5 foams parts was used, comprising 4 rings and one disk (45 mm outer diameter, 20 mm inner diameter and 10 mm height) and all parts were weighted before and after the deposition and firing steps. A dip coating unit (Chemat Technology Dip Master 201) was used to perform the coating with a good repeatability. Ceramic parts were soaked into the LSMMg slurry for 90 seconds. The coated foams went through a multi-step thermal treatment with a final sintering step at 1500 °C for 8 h (2 °C/min ramp). The sintered samples were weighted again in order to calculate the effective amount of LSMMg coated at the surface of ceria foams, that was in the range 7.7-11.4 wt%. A similar procedure was applied in the case of CSM coating (the effective amount of CSM coated at the surface of ceria foams was in the range 5.7-7.7 wt%). Good adhesion of the perovskite coating on the ceria foam was confirmed by sonication tests. Moreover, the absence of interaction between the perovskite coating and the ceria foam was confirmed by X-Ray Diffraction [206].

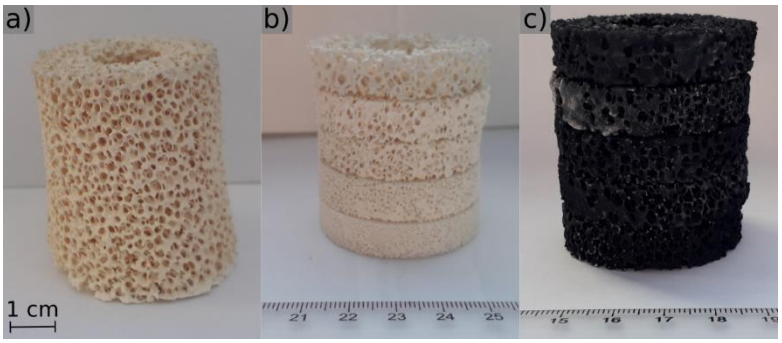

Figure 3-2: Images of reactive ceria foams: a) monolith with uniform cell size (CF-20), b) stack of discs with axial cell size gradient from 10 to 60 ppi (CF-HG) and c) stack of discs of perovskite-coated ceria foam with uniform cell size (CF-LSMMg)

A fourth type of ceria structure was prepared at PROMES to investigate the impact of ordered geometry. The ordered structures were manufactured with the well-known replication method on 3D-printed polymer scaffolds [207]. The cylindrical templates with ordered geometry (20 mm height, 67 mm diameter) were designed with Catia software and fabricated by additive manufacturing thanks to a powder bed fusion 3D-printer (Figure 3-3.a and Figure SC-1). The ceria slurry was realized with ceria powder purchased from Sigma Aldrich (particle size <5 µm, 99.9% purity), crushed in a mortar. The ceria powder and organic binder (Butvar™ B-98) were dissolved in ethanol with a mass ratio of 5:1. In the case of porogen addition, wood particles

(mix of pine and spruce wood, particle size 0-1000 µm) were added in the ceria slurry for 50% volume of ceria. Then, the templates were submerged several times in ceria slurry until ceria covered totally the surface (Figure 3-3.b). Finally, the ceria structures were fired in air at 1400 °C for 3 h. The ceria disc after the heating treatment and template firing was ~10 mm height and ~48 mm diameter (Figure 3-3.c). In the solar cavity absorber, 4 ordered ceria discs were stacked as follows: one 20 ppi disc, two 13 ppi discs and one 11 ppi disc. The geometry-ordered structures being brittle, their placement in the cavity required specific attention. To avoid unnecessary manipulations, the structures were placed on a cardboard insulation disk (~2cm thickness). Then, the alumina cavity was placed around the stacked ceria structures and their support in order to allow manipulation of the cavity with the reactive structured material inside. Afterward, the cavity was replaced in the reactor (Figure SC-2). Two sets of materials were investigated, corresponding to ceria foam with ordered-geometry with and without pore forming agent, abbreviated as CF-OGP and CF-OG respectively. Both ceria foams have a mean density of ~0.27 g/cm^3 and a porosity of ~98%.

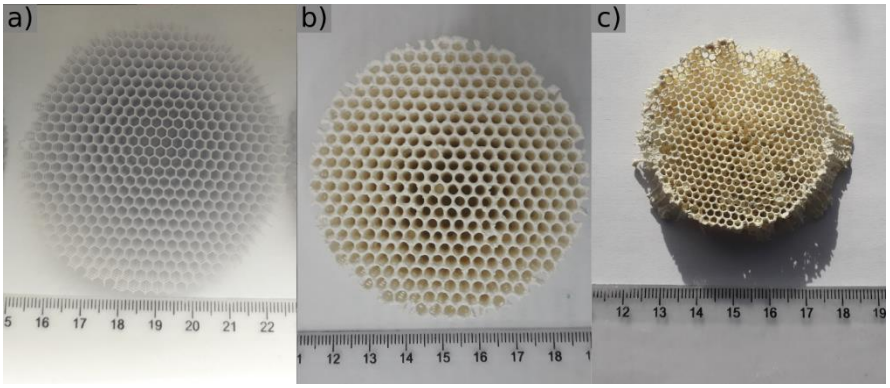

Figure 3-3: a) Ordered polymer template obtained from additive manufacturing, b) ceria impregnated template and c) final ceria structure with ordered-geometry after heat-treatment of b)

Table 3-1: Characteristics of the ceria foams investigated in the solar reactor, along with their abbreviation

Abbreviation	Foam material and geometry	Cell size	Density (g/cm^3)
CF-20	Ceria foam (1 cylinder hollowed + 1 disc)	20 ppi (cylinders +disc)	0.93
CF-10	Ceria foam (1 cylinder hollowed + 1 disc)	10 ppi (cylinders +disc)	0.92
CF-NG	Ceria foam (4 rings + 1 disc) with no cell size gradient	10 ppi (rings) and 20 ppi (disc)	0.95
CF-MG	Ceria foam (4 rings + 1 disc) with medium cell size gradient	10 ppi-20 ppi (rings) and 60 ppi (disc)	1.07
CF-HG	Ceria foam (4 rings + 1 disc) with high cell size gradient	10 ppi-60 ppi (rings) and 60 ppi (disc)	1.12
CF-LSMMg	Ceria foam (4 rings + 1 disc) coated with LSMMg,	20 ppi (rings +disc)	1.32
CF-CSM	Ceria foam (4 rings + 1 disc) coated with CSM	20 ppi (rings +disc)	1.45
CF-OG	Ceria porous structure with ordered geometry (4 stacked discs)	11-20 ppi (discs)	~0.27
CF-OGP	Ceria porous structure with ordered geometry and with pore former (4 stacked discs)	11-20 ppi (discs)	~0.27

3.3 Results and discussion

The experimental study was conducted to demonstrate the solar reactor reliability during continuous on-sun operation and to determine the thermochemical performance metrics as a function of the operating conditions including the temperatures (during reduction and oxidation), pressure during reduction, cell density of the foam, oxidant flow rate and inlet mole fraction in the gas feed. The reactor performance was appraised based on the fuel yield, production rates evolution and energy conversion efficiency as the main evaluation criteria.

Prior to fuel production tests, blank experiments without any reactive material (empty cavity) were performed to confirm that the gas species production only evolves from the reactions with ceria foam. As a result, no O_2 and H_2/CO were produced when heating the empty reactor in Ar up to 1400 °C and subsequently feeding with H_2O or CO_2 when decreasing the temperature, which confirms the absence of side reactions with the reactor materials.

3.3.1 Influence of the operating parameters

3.3.1.1 Parameters investigated during the reduction step

According to thermodynamics, the oxygen partial pressure and the reduction temperature are the key parameters determining the maximum reachable oxygen non-stoichiometry in the ceria structure [76, 196]. In order to study the influence of oxygen partial pressure, a vacuum pump was placed at the reactor output to lower the total operating pressure by about one order of magnitude compared with atmospheric pressure. The total inert gas flow was kept unchanged, in order to assess only the effect of the total pressure. The minimum pressure achievable with flowing gas (~100 hPa) is still reasonable and easily accessible in large-scale processes. Further decreasing the pressure would bring additional energy penalty (pumping work) and thus cannot

be considered when aiming the development of a scalable process. Figure 3-4a depicts the evolution of the oxygen non-stoichiometry *versus* temperature while heating the reactor at two different pressures during the reduction step. The temperature increase leads to the rise of oxygen non-stoichiometry for both pressures. Decreasing the pressure significantly increases the maximum non-stoichiometry reached by the reactive material at the final reduction temperature T1=1400 °C (δ=0.044 at 106 hPa versus 0.031 at 865 hPa). Furthermore, the onset temperature decreases by ~350 °C when decreasing the pressure from 865 hPa to 106 hPa. Figure 3-4b shows the O_2 and CO amounts produced for the two cycles performed at the different pressures during reduction. Decreasing the pressure during the reduction step significantly increases the produced oxygen amount (90 µmol/g to 128 µmol/g), which subsequently enhances CO production during the oxidation step. For a pressure of 106 hPa during the reduction step, a ceria reduction extent δ/δ_{max}=8.8% is reached at T1=1400 °C (δ_{max}=0.5 for complete reduction of Ce^{4+} to Ce^{3+}). This high reduction extent then boosts the amount of fuel produced during the oxidation step (from 160 µmol/g to 258 µmol/g). Moreover, the cycle performed at low pressure in Figure 3-4 shows a total CO_2 conversion extent of 7.5% and a CO_2 conversion peak of 36% measured at the peak rate of CO production (in comparison with 6.3% and 29%, respectively, for the cycle at atmospheric pressure). A reduced oxygen partial pressure thus shows a beneficial impact on both the reduction extent and fuel production yield achievable by the reactive ceria material.

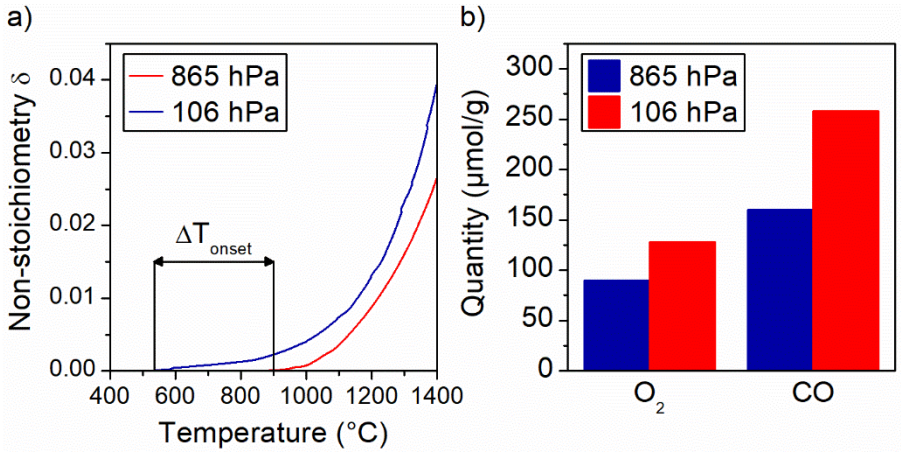

Figure 3-4: Investigation of CF-10 foam performance in the solar reactor (cycles #30 and #31). a) Evolution of non-stoichiometry as a function of temperature for two different operating pressures and b) amounts of O_2 and CO produced for different reduction pressures.

The reduction temperature is the other key parameter affecting the thermochemical cycle performance. Figure 3-5 illustrates the O_2 and CO production rates evolution for two cycles carried out at different reduction temperatures (1400 vs. 1450 °C, T1 was selected as the reference temperature measurement). Increasing the reduction temperature by 50 °C leads to an increase of the O_2 production from 126 µmol/g to 149 µmol/g. The reduction extent reached with a reduction temperature of 1450 °C is about δ=0.051 (at atmospheric pressure). As a result of the reduction extent being increased when the temperature increases, the amount of CO produced is also increased (from 260 µmol/g at 1400 °C up to 301 µmol/g at 1450 °C). Furthermore, the CO_2 conversion is increased from 8.7% to 10.9% together with the peak CO_2

conversion (from 38% to 47%). The increase of the reduction temperature thus shows a beneficial impact on the production of both O_2 and CO. Of course, such temperature increase must be limited due to the risk of the redox material sublimation and fastened ageing that may cause performance loss [65, 159]. Thus, the maximum temperature was kept at 1450 °C (measured by T1 thermocouple), while admitting that higher temperatures are reached in the upper part of the foam exposed to high-flux radiation (as evidenced by the higher temperature values, ~30-50 °C, measured by the pyrometer in the central foam cavity). Moreover, the increase of the reduction temperature implies an increase of the heat loss (increasing the reduction temperature by +50 °C results in increasing sensible heat losses for ceria and inert gas heating by ~27%) due to the increase of the temperature swing (ΔT) between redox cycle steps (sensible heat losses of 23 kJ for ΔT=400 °C vs. 29 kJ for ΔT=450 °C).

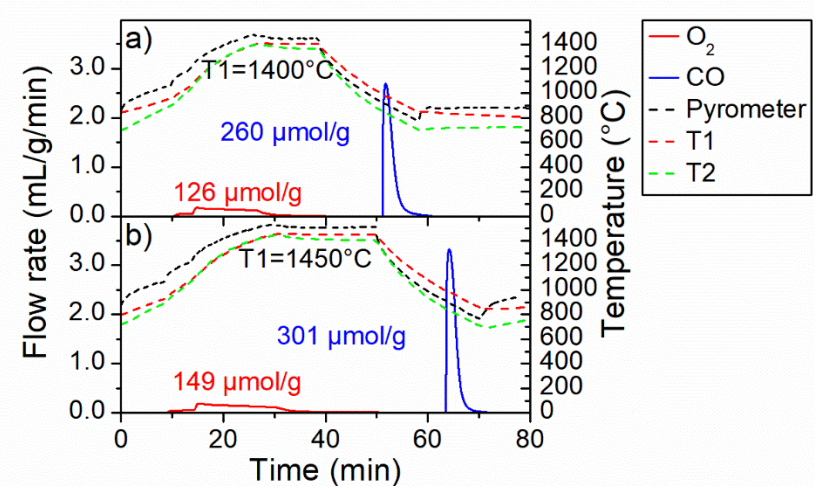

Figure 3-5: Evolution of O_2 and CO production rates along with the temperatures for two thermochemical cycles with reduction performed at a) 1400 °C (cycle #12) and b) 1450 °C (cycle #13) at atmospheric pressure for CF-20 foam.

The argon flow also impacts the oxygen partial pressure by diluting the O_2 released by ceria during the reduction step. As confirmed previously, the total pressure affects the oxygen partial pressure and sharply influences the ceria reduction extent. Varying the argon flow-rate is another way to tune the oxygen partial pressure. This parameter has thus been investigated to demonstrate its influence on the reduction step. Figure 3-6 shows the evolution of O_2 amount produced according to the argon flow-rate during the reduction step. An increasing argon flow lowers the oxygen partial pressure, which thereby significantly favors the reduction extent. This result can be explained by a higher dilution of the oxygen released during the reduction step (lower oxygen partial pressure). Indeed, increasing the argon flow-rate from 1.2 L/min to 2 L/min moderately increases the oxygen production yield from 99 to 117 µmol/g whereas the CO yield increases from 198 to 234 µmol/g. In comparison with the decrease of the total pressure, increasing the argon flow rate enhances the oxygen yield by 17%, whereas a pressure decrease from 865 hPa to 106 hPa improves the oxygen yield by 42%. This can be explained by a difference in oxygen partial pressure, which decreases only twice when doubling the Ar flow whereas it drops ~8 times when decreasing the total pressure from 865 to 106 hPa. Thus, the Ar flow rate would need to be dramatically increased to obtain the same effect as the total pressure reduction, which would cause considerable heat loss together with high inert gas

consumption. Therefore, decreasing the total pressure during the reduction step is more relevant than increasing the carrier gas flow-rate.

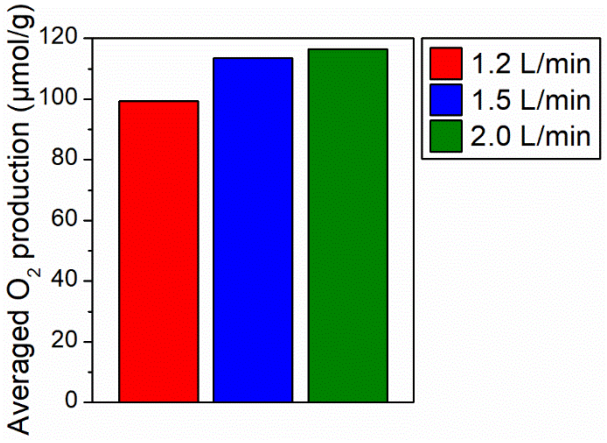

Figure 3-6: Influence of argon flow-rate on the average oxygen production for CF-10 foam (T_{red}~1400 °C, atmospheric pressure).

In summary, a reduction step at low pressure and high temperature is favorable to enhance fuel production yield. In contrast, the argon flow-rate does not impact significantly on the reduction step in comparison with total pressure reduction. In addition, significantly higher inert gas flow-rate would be required to obtain equivalent impact as total pressure reduction, although it is not realistic for process upscaling.

3.3.1.2 Parameters investigated during the oxidation step

The oxidation step was performed by adding the oxidant gas in the feed via the lateral gas inlet located above the ceria foam. Kinetics of CO_2 reduction over non-stoichiometric ceria has been investigated [208]. The CO_2 molar fraction (x_{CO_2}) injected in the reactor during the oxidation step is a key parameter mastering the fuel production rate. In order to highlight the influence of this parameter on CO production rate, three thermochemical cycles have been performed with the same reduction temperature (T1=1400 °C) and different CO_2 molar fractions (25%, 50%, and 100%) during the oxidation step. The results are presented in Figure 3-7a (for the oxidation test with pure CO_2, the argon flow usually injected in the window zone was replaced by CO_2). Increasing the CO_2 concentration results in a sharp increase of CO production rate, while the oxidation duration is concomitantly reduced (from 3.8 min to 1.7 min to obtain 90% of the maximum CO amount produced). The maximum CO production rate reached ~9.4 mL/g/min for oxidation in 100% CO_2 (cycle #28 in Table 1). This means that a 8 fold-increase of the fuel production rate was achieved with the studied micro-structured ceria foams (microstructural characterization provided in the next section), when compared to previously reported values [46, 201, 202, 209]. The fuel production rate can even be enhanced further (up to 9.9 mL/g/min for cycle #32) by increasing the total gas flow-rate (inducing products dilution). The peak of CO_2 to CO conversion reached 21%, 25% and 36% whereas the global CO_2 to CO conversion over the oxidation step duration reached 1.6%, 2.1% and 7.4% for CO_2 molar fractions of 1.00, 0.50 and 0.25, respectively. Furthermore, the produced CO amounts were similar regardless of the CO_2 molar fraction (in the range of 258-284 µmol/g), which denotes complete ceria

oxidation even though the kinetics is strongly dependent on the oxidant gas concentration. This result also means that the conversion of pure CO_2 streams (e.g. issued from post-combustion CO_2 capture processes) is particularly attractive to favor reaction kinetics. Increasing the CO_2 molar fraction increases the driving force of surface oxidation reaction (by increasing the amount of CO_2 available at the surface) and further promotes oxygen diffusion within ceria thanks to the gradient of oxygen concentration. In addition, it also decreases the $CO:CO_2$ ratio as shown in Figure 3-7b, which thermodynamically favors the oxidation step. In other words, larger CO_2 concentration favors the thermodynamic equilibrium towards CO production. However, considering an industrial process, a lower $CO:CO_2$ ratio will require higher amount of supplementary energy to separate CO from CO_2. In summary, a high CO_2 molar fraction in the oxidation step promotes kinetics, which leads to a fast (short-time duration) oxidation reaction, but at the expense of lower CO_2 to CO conversion extent.

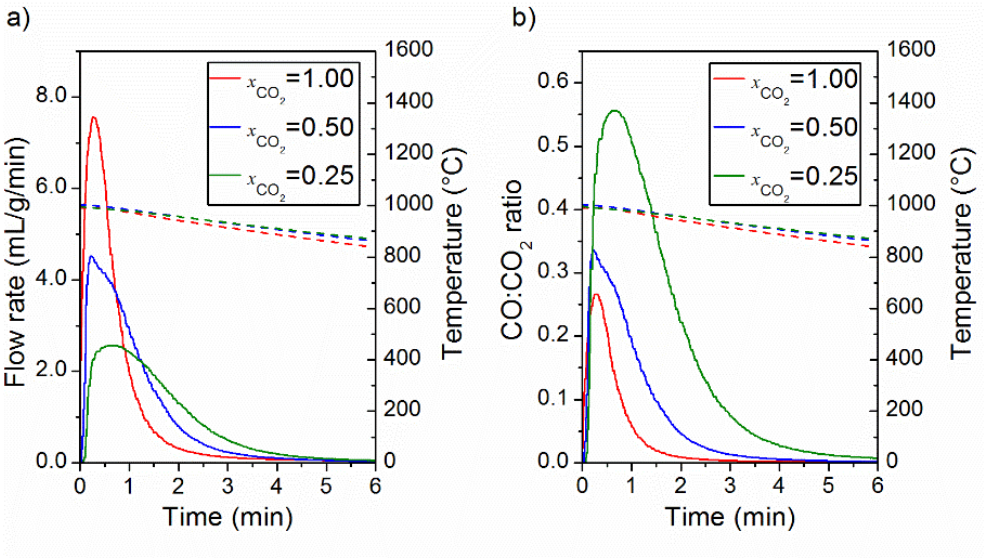

Figure 3-7: Evolution of a) CO production rates (solid lines) and b) CO to CO_2 ratio (solid lines) for different inlet CO_2 molar fractions (0.25, 0.50 and 1.00) along with T1 temperatures (dashed lines), during cycles #31, #33 and #35 with CF-10 foam, respectively.

Among the influencing parameters during the oxidation step, the gas flow-rates play a major role and their impact on the fuel production has never been investigated. First the effect of total flow rate (sum of inert and oxidant gas) was analyzed with a constant inlet molar fraction of the oxidant gas (CO_2). Figure 3-8 plots the CO production rates and $CO:CO_2$ mole ratio for two different total flow rates with an inlet CO_2 molar fraction of 0.5. Doubling the total gas flow rate led to an increase of the CO peak production rate from 3.2 to 4.6 mL/g/min while the $CO:CO_2$ ratio decreased (from 0.21 to 0.14 for the maximum). Low $CO:CO_2$ ratio (and CO dilution) thus favored the oxidation rate. However, the lower the total gas flow rate, the higher the CO_2 conversion extent and CO_2 conversion peak (3.62% and 18% for 2 L/min compared with 1.53% and 12% for 4 L/min, respectively). In both cases, the ceria foam exhibited a re-oxidation extent superior to 90%. Therefore, a high total gas flow rate enhanced the production rate despite a negative impact on the CO_2 conversion.

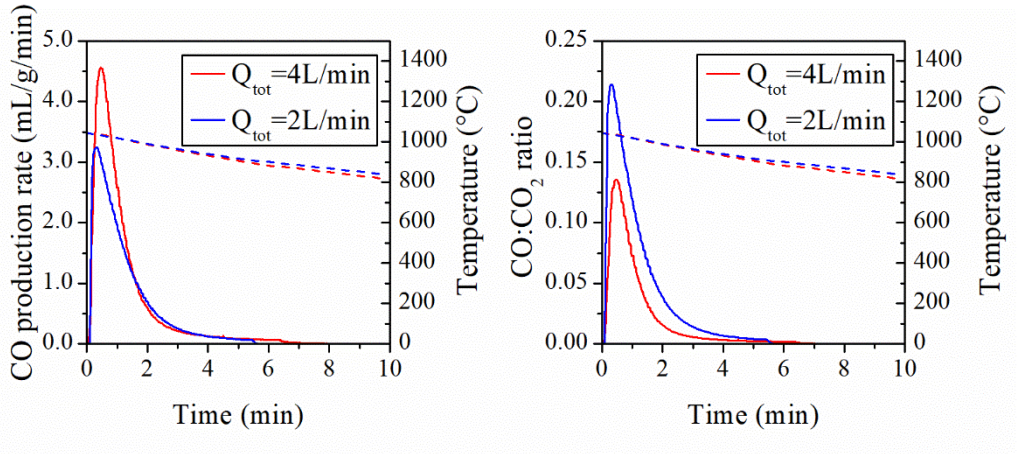

Figure 3-8: a) CO production rate (solid lines) and b) CO:CO_2 ratio (solid lines) along with T1 temperature (dashed lines) for total gas flow rates of 2 L/min (cycle #31) and 4 L/min (cycle #25) with CO_2 molar fraction of 0.5 for CF-NG.

During the oxidation step, the oxidizing gas can be diluted in inert gas. In order to study the impact of the Ar flow rate and dilution on the CO production rate, different Ar flow rates were used (0, 1, and 2 L/min) with fixed CO_2 flow rate (at 2 L/min), as represented in Figure 3-9. The peak CO production rate of 5.4 mL/min/g was achieved without any dilution whereas CO_2 dilution with Ar lowered the CO production rate. The CO production yield (in the range of 225-252 µmol/g) was not significantly impacted by the Ar dilution. Furthermore, the decrease of the CO_2 molar fraction arising from Ar dilution had an adverse impact and increasing the Ar flow did not show any beneficial effect on the oxidation step.

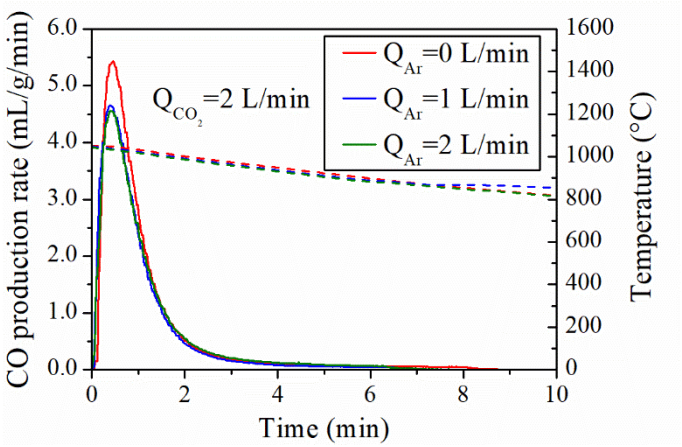

Figure 3-9: CO production rate (solid lines) along with T1 temperature (dashed lines) for different Ar flow rates (cycle #23 to #25 of CF-NG) at fixed CO_2 flow rate (2 L/min).

Finally, the CO_2 flow rate represents a key parameter during the oxidation step. In order to investigate its effect on the CO production rate, cycles were performed with different CO_2 flow rates (from 1 L/min to 3 L/min) with Ar flow rate fixed at 1 L/min, as represented in Figure 3-10. The higher the CO_2 flow rate, the higher the CO peak production rate (2-fold increase for CO_2 flow rate from 1 L/min to 3 L/min). The peak CO:CO_2 ratio reached 0.21 with CO_2 gas flow rate of 1 L/min (versus ~0.14 for cycles #30 and #24). The peak CO:CO_2 ratios are similar between 2 and 3 L/min of CO_2 gas flow because the higher amount of CO_2 is counterbalanced by the faster CO production rate. However, the CO_2 conversion extent is low when increasing

the CO_2 flow rate (~1% with 3 L/min), which is not favorable on the process viewpoint since additional energy would be required to separate CO from unconverted CO_2. Therefore, tuning the CO_2 flow rate represents a trade-off to reach both maximum CO production rate and acceptable CO_2 conversion extent.

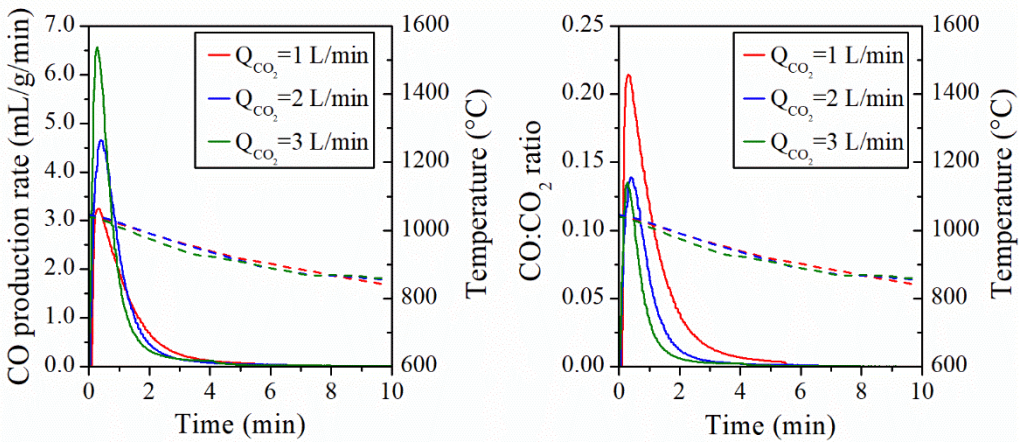

Figure 3-10: a) CO production rate (solid lines) and b) CO:CO_2 ratio (solid lines) along with T1 temperature (dashed lines) for CO_2 gas flow rate of 1 L/min (cycle #31), 2 L/min (cycle #24) and 3 L/min (cycle #30) at fixed Ar flow rate of 1 L/min (CF-NG).

As evidenced previously, a high CO_2 molar fraction during the oxidation step promotes a high CO production rate. The influence of the oxidizing gas was then investigated by carrying out the oxidation step with different water molar fractions (Figure 3-11). The H_2 production rate was only slightly increased when increasing over 2-fold the water molar fraction. The H_2 yield (in the range of 173-179 µmol/g) was not affected by water concentration. Moreover, the cycle performed with x_{H2O}=0.17 showed both higher H_2O conversion extent and peak conversion (5.6% and 15.5%, respectively) in comparison with the cycle performed with x_{H2O}= 0.40 (2.6% and 10.2%, respectively). Unlike the dissociation of CO_2, the steam molar fraction did not significantly impact the fuel production rate, and increasing the H_2O concentration did not provide strong benefit for improving thermochemical performance. Since high H_2O conversion is targeted and steam production consumes energy, a low H_2O concentration is thus preferable.

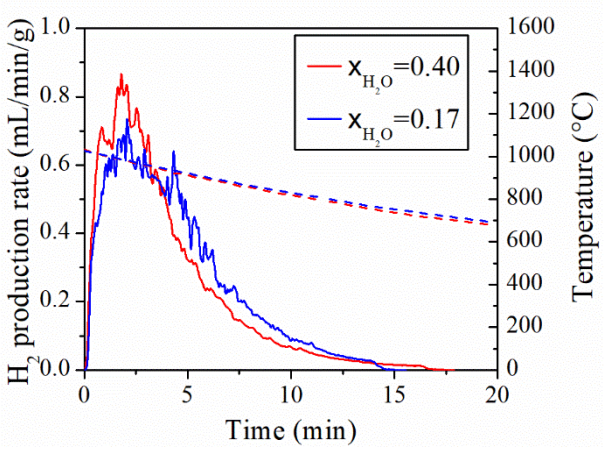

Figure 3-11: Influence of steam concentration on H_2 production rate along with T1 temperature for CF-NG (cycles #17 and #18).

The temperature plays a major role in the oxidation step performance. To study its influence on fuel production, three thermochemical cycles were carried out at different oxidation temperatures (T1=1150, 1050 and 950 °C), as shown in Figure 3-12a. The lower the oxidation temperature, the higher the amount of CO produced. For instance, CO production increases from 81 µmol/g to 197 µmol/g when the oxidation temperature decreases from 1150 °C to 950 °C. Furthermore, the CO peak production rate at 950 °C roughly increases by a factor x5 when compared with an oxidation performed at 1150 °C. Therefore, decreasing the oxidation temperature leads to fuel production enhancement by improving both the production rate and the fuel yield. On the other hand, decreasing the oxidation temperature increases the temperature swing (ΔT) between the reduction and oxidation steps, which induces sensible heat losses. This basically explains why isothermal or near-isothermal cycling has been commonly proposed based on theoretical efficiency calculations when kinetic aspects are not addressed [194, 210], despite other studies pointed out the lowest efficiencies for isothermal operation [211, 212]. Anyway, the strong effect of oxidation temperature on kinetics suggests that low temperature swing is definitely not appropriate to operate such redox cycle as the oxidation kinetics would be too slow and thus extend tremendously the reaction duration, which is unsuitable in practice. Conversely, high temperature swing inducing heat losses is often associated with a requirement for sensible heat recovery system, and the benefits of heat-recovery strategies on system efficiency [213], especially solid heat recovery for lower oxidation temperatures have been shown in thermodynamic analyses [214]. However, solar energy is freely available and decreasing the amount of solar energy between steps has in reality no impact on the global cycle performance, because it does not change the size/cost of the solar concentrating system which is primarily required for the reduction step only. Therefore, the sole parameter of importance being cycle duration, the reaction kinetics should be favored in priority as it mostly influences the amount of fuel produced during a working day. The global kinetic rate of the two-step process that determines the cycle duration thus mainly depends on both the heating rate (determining the rate of reduction step) and the oxidation rate (favored by low temperature and high oxidant concentration).

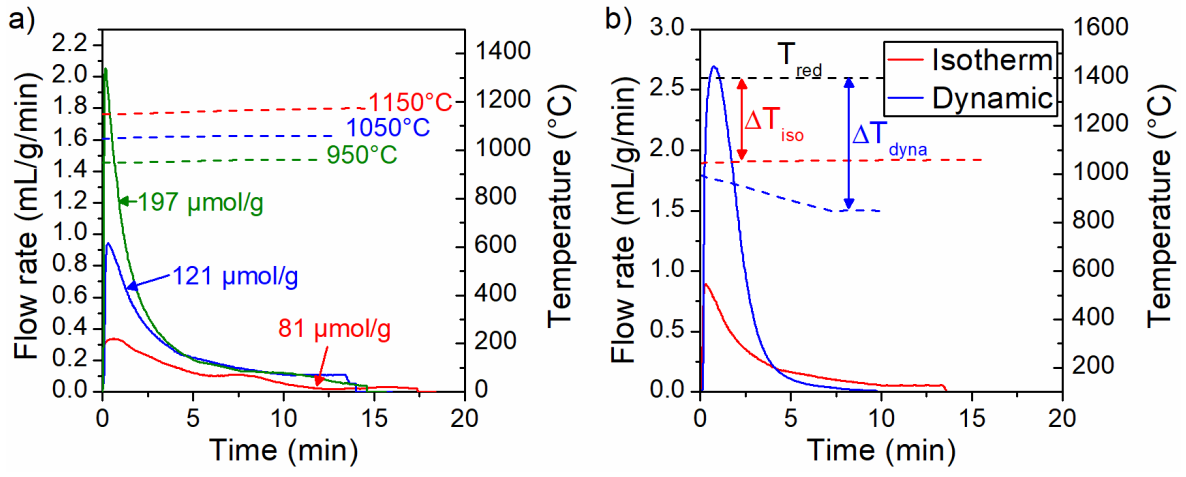

Figure 3-12: Evolution of CO production rate (solid lines) for (a) different oxidation temperatures T1 (dashed lines) in isothermal regime, during cycles #2, #3 and #4 with CF-20 foam, and (b) isothermal and dynamic thermal oxidation-regimes along with temperature T1 (dashed lines), for cycles #3 and #12 with CF-20 foam, respectively.

During the oxidation step, two temperature regimes were considered (isothermal and dynamic). The former consists of an oxidation at constant temperature maintained by solar energy input, whereas the latter proceeds with an oxidation during free cooling without any energy input. Figure 3-12b compares the CO production rate using either isothermal or dynamic regime. The maximal production rate in isothermal condition (at 1050 °C) is lower than in dynamic conditions. Moreover, the CO production in the dynamic regime occurs on shorter duration when compared with the isothermal one (CO_2 injection was started at ~1000 °C and stopped at ~850 °C). This is due to the higher oxidation temperatures (thermodynamically unfavorable) for isothermal conditions. In contrast, the constant temperature decrease during dynamic oxidation raises the thermodynamic driving force for the oxidation reaction. Moreover, the CO production yield during dynamic oxidation (260 µmol/g) is higher than under isothermal conditions (121 µmol/g). Fuel production is thus favored by the dynamic free cooling temperature regime. However, the temperature swing (ΔT) is higher with the dynamic regime, which induces sensible heat losses.

Both CO_2 and H_2O have been considered as oxidant gases for fuel production. Figure 3-13 compares H_2 and CO production rates in isothermal conditions at 900 °C and 1050 °C (after a reduction step at T1=1400 °C). A decrease in the oxidation temperature enhances markedly the fuel production rate for both CO_2 and H_2O. Regardless of the oxidation temperature, the peak production rate of CO is higher than the H_2 one. Considering thermodynamics, this phenomenon can be attributed to the more favorable CO_2 dissociation in comparison with H_2O dissociation. The output gas is a mixture of unconverted reactant and products that would require further separation step. While H_2 separation from H_2O is straightforward by steam condensation, CO removal from CO_2 requires additional energy and/or advanced separation technology.

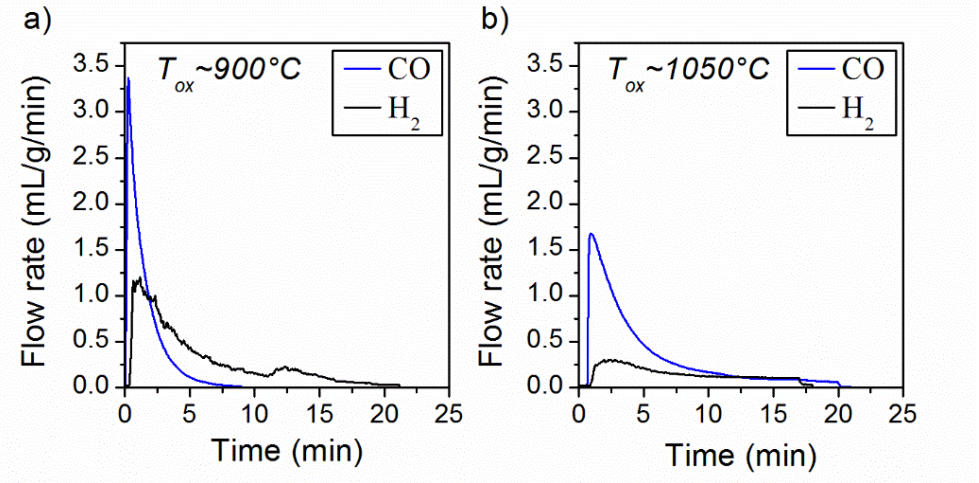

Figure 3-13: Evolution of H_2 and CO production rates vs. time, with an oxidation temperature of a) 900 °C (cycles #6 and #7 of CF-20) and b) 1050 °C (cycles #5 and #9 of CF-20).

In summary, the optimization of the operating parameters is crucial for improved thermochemical performance. The reduction extent achieved by the reactive material can be increased either by increasing the reduction temperature or by decreasing the oxygen partial

pressure during the reduction step, leading in both cases to enhanced fuel production yields. Besides, the oxidation step is favored by increasing CO_2 molar fraction, decreasing oxidation temperature or using high gas flow rates during the oxidation step.

3.3.2 Thermal stability of the porous ceria foams

Considering that industrial processes require reactive materials withstanding multiple cycles without any performance decline, consecutive cycles were performed with all the investigated foams as reported in Table SC-1-SC-4. Due to solar energy variability in a real solar process, the material cannot be subjected to strictly identical parameters from cycles to cycles, and it will thus have to sustain multiple changes in the cycling conditions, thereby favoring process flexibility. Typical results are shown in Figure 3-14 for CF-20 foam tested with the reduction steps carried out at ~1400 °C and 110 hPa, and oxidation steps from 1000 °C to 750 °C (dynamic conditions with CO_2 molar fraction of 0.5 for cycles #33 and #34, and 1.0 for cycles #35 and #36). Noticeably, repeatable results were obtained when using similar operating conditions. Furthermore, the CO production rate was remarkably high, in the range of 4 to 7 mL/g/min, representing the highest rates obtained to date with ceria and thus a strong improvement in the performance of solar fuel reactors based on reticulated porous ceria. In comparison, Furler et al. [46, 202, 209] obtained a maximal fuel production rate of 1.2 mL/g/min with more stringent operating conditions (1450 °C and 10 hPa) in an electrically-heated high-flux simulator using ceria foams with dual-scale porosity. In the present study, the microstructured ceria foams were subjected to real concentrated high-flux solar radiation in a scalable solar reactor and were found to sustain fuel production cycles without any loss of reactivity. Accordingly, in comparison with previously reported results, a considerable increase in the fuel production rate was achieved with the designed ceria foams exhibiting millimetric cells size and fine granular microstructure within the foam struts.

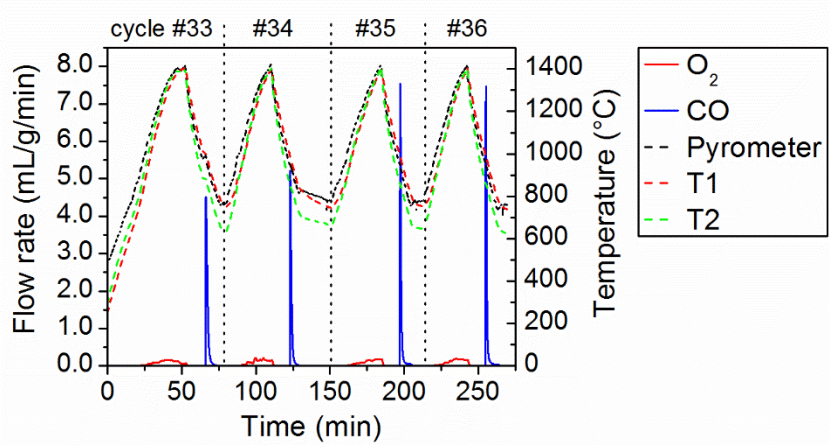

Figure 3-14: Evolution of CO and O_2 production rates for CF-20, during consecutive cycles performed with reduction at 1400 °C and 110 hPa, and oxidation during free cooling (CO_2 molar fraction was 0.5 for the two first cycles and 1.0 for the two last ones).

The studied foams (CF-10 and CF-20) underwent extended cycling during continuous on-sun operation under the various representative conditions reported in Table SC-1, without suffering any performance decline. Due to the good thermal stability of ceria that can withstand harsh process conditions, the material performance was not altered during consecutive redox cycles.

All the fuel production yields measured for both foams along the cycling experiments are plotted in Figure 3-15, thus highlighting the main parameters influencing the produced fuel amount. The pressure decrease and/or temperature increase during the reduction step both enhance the fuel production yield (>250 µmol/g). Conversely, unfavorable conditions (high oxidation or low reduction temperatures) generally result in the lowest fuel yields (<150 µmol/g).

The remarkably high achieved fuel production can be attributed to the monolithic reactor design integrating tailored ceria foam with morphology and microstructure favoring the oxidation step that is chiefly a surface-controlled reaction [68]. Figure 3-16a displays general, cross-section and surface views (Scanning Electron Microscopy – SEM Hitachi S-4800) of CF-10 foam struts before cycling. The grain sizes, struts porosity, and pore sizes were estimated by image analysis (ImageJ software). Grain sizes were in the range 3-10 µm for the fresh sample and a micro-scale interconnected porosity within the struts was evidenced (strut porosity ~13%, pore sizes in the range 1−5µm). The presence of hollow struts (cavities in the center of the struts) due to the departure of the organic template during calcination was noticeable, as well as surface cracks (ascribed to degassing during template calcination) which do contribute to enhance the available surface area for the oxidation step. After thermochemical cycling, white or grey zones were observed on the foams (Figure 3-15), depending mainly on their position in the reactor cavity (top or bottom part, respectively). SEM micrographs of the white part reveal high densification/sintering with residual closed porosity (Figure 3-16.b). This densification presumably results from the high temperature occurring in the upper part of the foam, close to the zone receiving highly concentrated solar radiation. Image analysis confirmed grain growth (sizes in the range 10−40 µm) and a decrease in struts porosity (7–8% with closed pores in the range 3−7 µm). The grey part of the foam is much less densified (Figure 3-16.c) as interconnected macro pores in the struts can still be observed (porosity~10%, pore size in the range 1−6 µm) and grain sizes are similar to those observed before cycling (3−12 µm). This could also mean that the structure has low thermal conductivity, leading to a lower internal densification as compared to the upper surface which is exposed to higher solar fluxes and temperatures. In the whole foam, the cavities (hollow struts) formed by the removal of the polymer template still remain after thermochemical reactions. The cracks observed at the surface of fresh samples (ascribed to degassing during template calcination) are still observed after cycling and do not evolve or collapse with time. The presence of both cracks and cavities remaining after cycles guarantees the access of the oxidant gas to the reactive ceria grains surface along cycles. The oxidation reaction being surface-controlled [68], a high available geometrical surface and interconnected macroporous network most likely explain the fast oxidation rates obtained with these microstructured ceria foams.

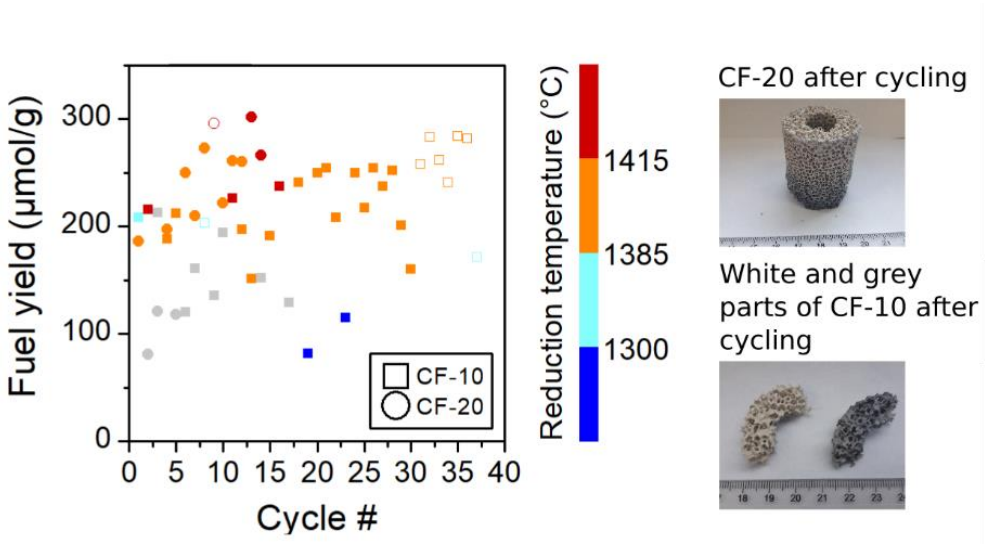

Figure 3-15: Fuel production yields measured for both CF-20 and CF-10 foams along cycling experiments. The color of symbols (from red to blue) indicates the reduction temperature (T1); symbols with emptied interior are related to low pressure during the reduction step, grey symbols are related to unfavorable high oxidation temperatures (T1>1050 °C), and symbol shape (square, circle) represents the foam type. (Right: pictures of foams after cycling).

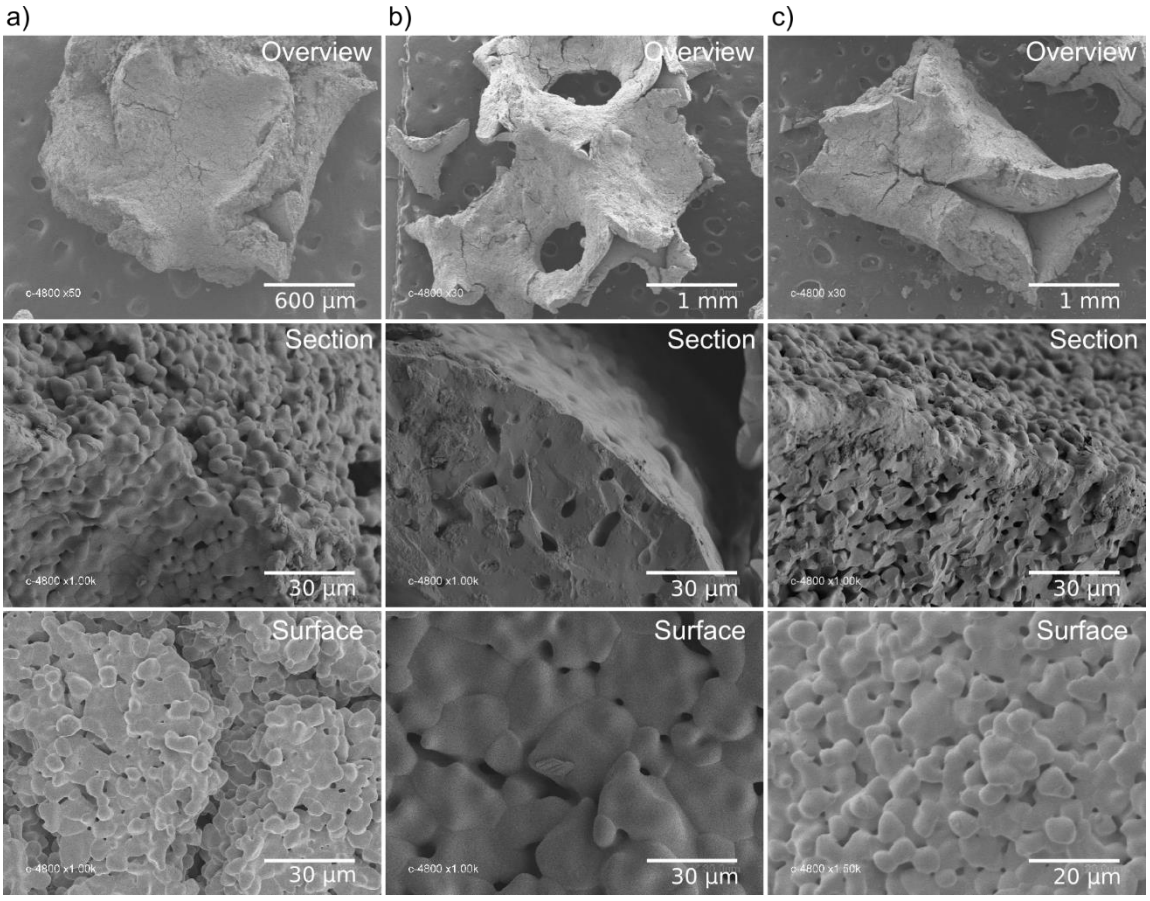

Figure 3-16: SEM images of CF-10 foam surface and cross-section at different magnifications: a) before cycling, b) white part after cycling, and c) grey part after cycling

3.3.3 Influence of foam cell size

Foam discs with different cell sizes were stacked to form a material with vertical graded porosity. These stacks were considered to assess the thermochemical reactor performance

according to the volumetric radiation absorption and resulting temperature distribution. Foams with large cell sizes at the top promote volumetric solar absorption while small cell sizes at the bottom increase foam density (amount of loaded ceria). Figure 3-17 shows thermochemical cycles performed with three foams exhibiting different porosity gradients (no gradient-NG, medium gradient-MG, and high gradient-HG). Increasing the cell size gradient led to higher temperature gradient within the ceria foam with temperature gaps from 150 °C to 245 °C (from the top to the bottom, as measured by the difference between T2 and T3). Increasing the cell density toward the bottom (CF-HG and CF-MG) enhanced the radiation attenuation, thus increasing the temperature gradient from the top to the bottom of the foam. In contrast, the foam with uniform cell density (20 ppi, CF-NG) led to the most uniform temperature distribution (as pointed out by the pyrometer temperature being similar to both T1 and T3), thereby favoring more homogeneous reduction within the whole reacting structure. The overall O_2 and CO production yields (86-94 µmol/g and 184-186 µmol/g, respectively) were not influenced by the cell size gradient. This means that the temperature gradient did not modify the average oxygen non-stoichiometry and associated fuel production capacity of the graded foam structure. The two considered foams with uniform cell densities (CF-20 and CF-10) also offered very similar fuel production performance at nominal conditions (typically ~200-250 µmol/g), which confirms the negligible effect of the considered foam cell sizes on the fuel production capacity.

Furthermore, the peak CO production rate achieved its highest value of 9.3 mL/g/min with the CF-NG foam, thus representing a 8-fold increase compared with previous published results (the highest fuel production rate reported to date, 1.2 mL/g/min, was obtained under more favorable conditions, i.e. temperature of 1500 °C and pressure of 10 mbar during reduction [46, 202, 209]). The fast re-oxidation rate can be explained by the favorable microstructure of the reactive foam exhibiting micro-scale interconnected porosity within the foam struts.

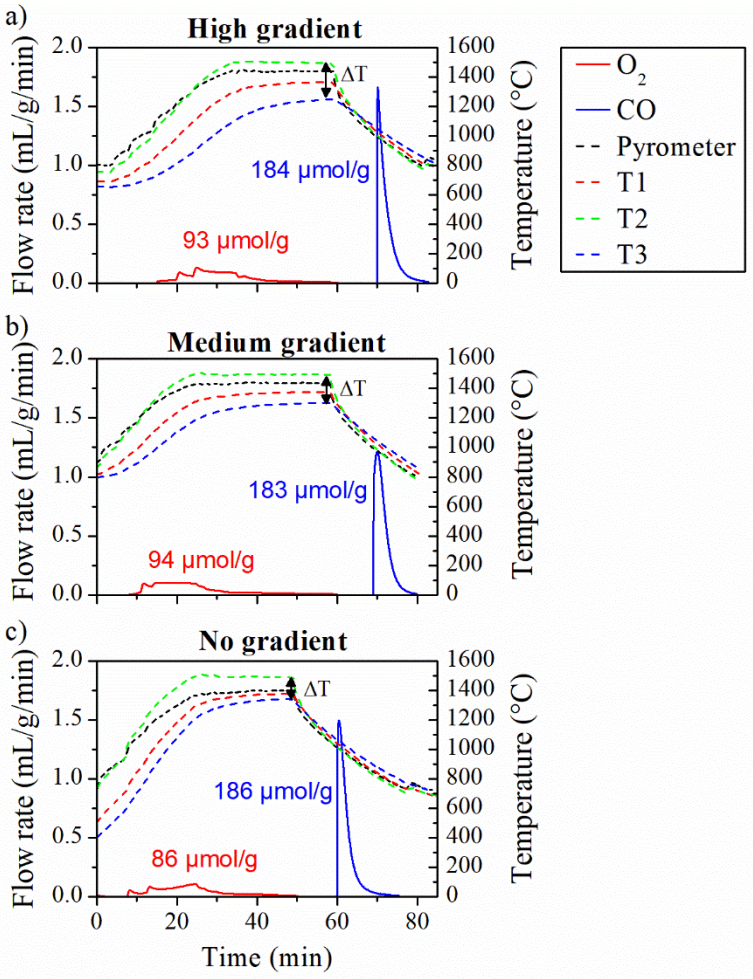

Figure 3-17: Thermochemical cycles performed at atmospheric pressure and T_{red}=1370 °C with a non-isothermal oxidation (~1000-800 °C) using a series of ceria foams with or with a gradient in their pore sizes : a) CF-HG (cycle #9), b) CF-MG (cycle #7) and c) CF-NG (cycle #20).

3.3.4 Dual phase foams

In order to promote the reduction extent in comparison with pure ceria, reticulated foams made of metal oxide dual-phase composites (CF-LSMMg and CF-CSM), have been experimentally investigated for thermochemical redox reactions in the solar reactor for the first time. Indeed an increase of both oxygen exchange capacity and reaction kinetics is required to further improve the thermochemical performance of ceria for solar-to-fuel production. In order to achieve this goal, the thermochemical performance in solar reactors, of ceria foams coated with LSMMg or CSM perovskite materials have been investigated. Such heterogeneous structures have never been investigated to date for solar thermochemical fuel production, and their shaping and testing as reticulated foams was never addressed. Significant efforts have thus been achieved to incorporate such materials in a reactor prototype and to evaluate their performance. The coated ceria foams were expected to combine the advantages of ceria for fast and complete re-oxidation, with the high reduction extent of perovskites [215].

3.3.4.1 Thermochemical cycling performance

Thermochemical performance of redox materials during solar-driven H_2O and CO_2 splitting cycles were experimentally determined. Solar-to-fuel conversion efficiency of ceria is limited

by its moderate reduction extent at reasonable reduction temperatures (up to 1400 °C). In contrast, perovskites offer higher oxygen exchange capacity and have thus been proposed as alternative materials for H_2O and CO_2 splitting. However, their re-oxidation step is slow and incomplete due to thermodynamic limitation, contrary to ceria oxidation which is thermodynamically more favorable. In the previous chapter, LSMMg perovskite was highlighted as a suitable material for thermochemical cycling. The strong oxygen exchange capacity of CSM was also pointed out. Ceria foams were thus coated with LSMMg or CSM to enhance their reduction extent as well as their fuel production yields. Thermogravimetric analyses were performed with CeO_2/LSMMg and CeO_2/CSM powder mixtures (Figure SC-3), pointing out the promising redox behavior of these two compositions. In order to evaluate the beneficial impact of LSMMg coating on ceria, the performance of LSMMg-coated ceria foam (CF-LSMMg) was compared with those of a pure ceria foam with same cell density (20 ppi). First, a thermochemical cycle was performed in the solar reactor with the following "reference conditions": reduction at 1400 °C (T1) under atmospheric pressure, followed by an oxidation step starting at ~1000 °C (free cooling without solar power input) under 25mol% CO_2 as oxidant gas. Figure SC-7 presents the evolution of O_2 and CO production rates along with temperature profiles for the thermochemical cycle performed in these conditions. The O_2 production yield is twice higher for CF-LSMMg foam (166 µmol/g) than for pure CeO_2 foam (86 µmol/g). The LSMMg coating thus favors the reduction extent, which can be explained by the enhanced reduction extent of the perovskite material, as expected. Furthermore, a potential synergetic improvement of oxygen exchange in the composite material was revealed during the reduction step, in comparison with individual components. This was attributed to the thin LSMMg coating that boosts the oxygen exchange capacity of the composite material, in comparison with pure ceria. Accounting for the mass fraction of each material in the foam composite (10% LSMMg, 90% CeO_2), the expected theoretical O_2 yield would be ~119 µmol/g for CF-LSMMg (see Appendix for detailed calculation), which is lower than the value measured experimentally, thereby suggesting a synergistic effect of the composite layered structure. This demonstrates the promotional effect of LSMMg in the O_2 releasing step. However, the re-oxidation of CF-LSMMg foam is less favorable compared with pure CeO_2 foam. Indeed, the amount of CO produced (145 µmol/g), the peak CO production rate (0.8 mL/g/min) and the re-oxidation extent (44%) of CF-LSMMg foam are lower than those measured for a pure CeO_2 foam (186 µmol/g, 1.5 mL/g/min, 100%, respectively). Furthermore, the time required to reach 90% of the total CO amount produced (τ_{90}) is 7.4 min for CF-LSMMg foam (cycle #1), against only 5.7 min for pure CeO_2 foam. Contrary to the reduction step, the oxidation step is therefore hindered by the LSMMg coating which may act as a diffusion barrier limiting the access of oxidant species to the ceria bulk.

Figure SC-8 presents the two first thermochemical cycles of CF-LSMMg foam. Both the O_2 and CO production yields dropped between the first and second cycle. This can be explained by the low re-oxidation extent of the first cycle (44%) impeding full material re-oxidation. During the second cycle, the starting oxidation temperature was decreased down to 900 °C because a lower oxidation temperature thermodynamically favors the oxidation step. The CO

yield remained weak due to a lower reduction extent but the re-oxidation extent slightly increased up to 50%. It is thus necessary to further improve the re-oxidation extent to increase the thermochemical performance of the CF-LSMMg foam. The thin perovskite layer at the ceria surface hinders the access of oxidant gas to the reactive ceria, which mostly explains the partial re-oxidation observed during the two first cycles. Increasing the oxidant partial pressure can be a suitable option to favor both the reactant diffusion and reaction kinetics, and to promote the re-oxidation extent of the composite material.

3.3.4.2 Improvement of the fuel production capacity

In order to improve the re-oxidation extent of CF-LSMMg, some relevant operating conditions, highlighted in our previous study [205], were investigated during additional cycles. In total, the foam underwent 10 cycles, as presented in Figure 3-18. The operating conditions of each cycle along with O_2 and fuel production yields are reported in Table SC-3. The total amount of H_2 and CO produced reached 1.1 L (3 cycles) and 3.5 L (7 cycles), respectively. It is important to underline that the CF-LSMMg foam underwent these 10 cycles, corresponding to 26 h of on-sun operation, without any performance decline.

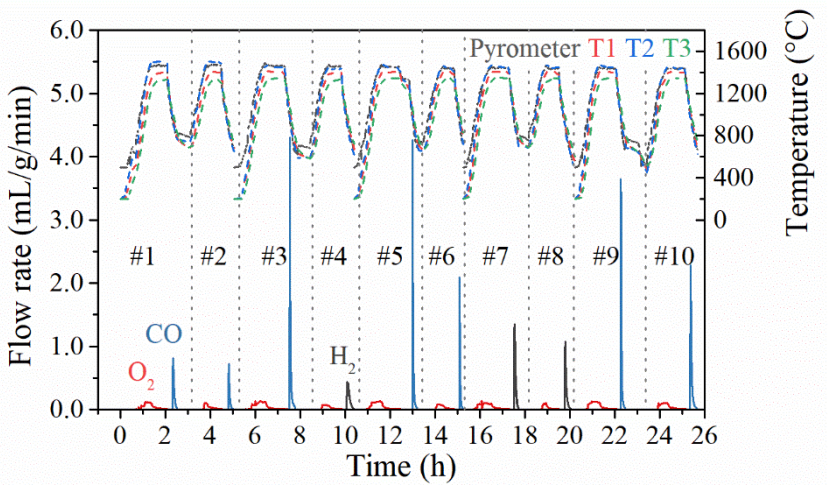

Figure 3-18: Evolution of O_2 and CO production rates during ten successive thermochemical cycles performed with CF-LSMMg.

Figure 3-19 presents the amounts of O_2 and CO or H_2 produced along with the re-oxidation extent, the reduction pressure and the oxidant molar fraction. A low pressure (~100 mbar) during the reduction step increases the reduction extent because oxygen release is thermodynamically favored by a low oxygen partial pressure. Moreover, the use of a low reduction pressure induces a higher fuel production yield, with for example an increase from 172 µmol/g (cycle #6) to 359 µmol/g (cycle #5) with a decrease of the reduction pressure from 0.873 bar to 0.098 bar. It seems that pressure reduction has a stronger effect on the performance of CF-LSMMg foam than on those of CeO_2 foam. Indeed, it leads to an improvement of 130% of the reduction extent for CF-LSMMg foam, while an increase of non-stoichiometry from δ=0.031 to 0.044 for pure ceria foam was previously reported [205] for a similar pressure reduction, corresponding only to 44% improvement. In addition, the pumping energy penalties only represent 0.27% of the total energy input, which is negligible accounting for the beneficial

increase of the reduction extent. Thus, using pumping to reduce the oxygen partial pressure during the reduction step is highly beneficial for system performance. Cycles #3 and #5 were performed practically under the same conditions (reduction at low pressure, re-oxidation in pure CO_2) and confirmed results repeatability since the O_2 and CO production yields were very similar.

Besides, the re-oxidation extent is directly correlated with the inlet oxidant molar fraction. A CO_2 molar fraction of 0.25 leads to an average re-oxidation extent of 47% versus 96% for a CO_2 molar fraction of 1.00. It should be noted that cycles #8 and #10 feature an apparent re-oxidation extent above 100%, which is due to incomplete re-oxidation during the previous cycle. The re-oxidation extent is also improved by increasing the H_2O molar fraction. The H_2O molar fraction cannot be increased as much as the CO_2 molar fraction due to technical limitations. However, a H_2O molar fraction of 0.50 is sufficient to reach complete re-oxidation extent, as shown in cycle #8.

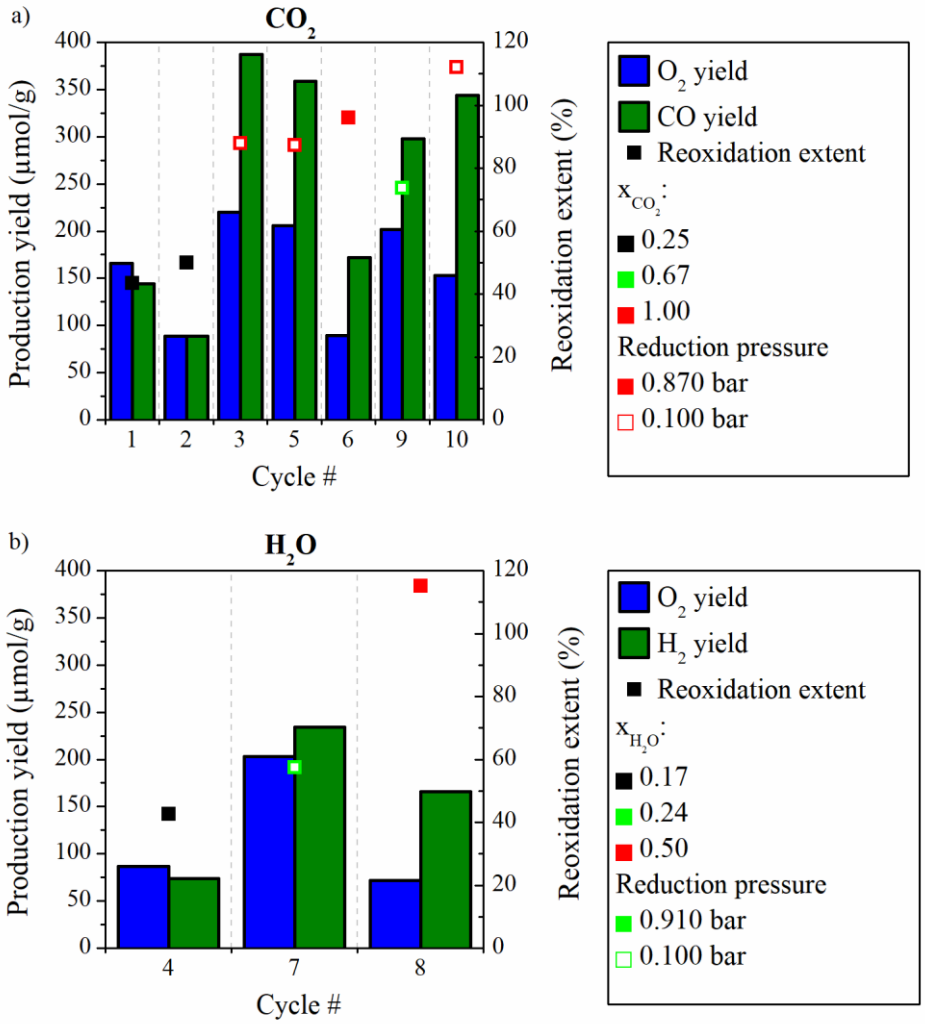

Figure 3-19: Fuel production yields and re-oxidation extents with different operating conditions for a) CO_2 oxidant gas and b) H_2O oxidant gas for CF-LSMMg; the bar color represents the gas produced, the square color shows the oxidant molar fraction and hollowed symbol indicates a low pressure during the reduction step

Similarly, different cycles were performed with a CeO_2-CSM foam in order to evaluate its thermochemical performance. In total, five CO_2 splitting cycles were carried out, corresponding to 10 h of continuous on-sun operation, and resulting in the production of 1.2 L of O_2 and 1.8 L of CO. All the performed cycles are represented in Figure SC-6 and the obtained O_2 and CO production yields are reported in Table SC-3. After the cycling, the CSM coated foams kept a very good mechanical integrity and no performance decline was observed.

3.3.4.3 Comparison of CO2 splitting activity for the coated and virgin ceria foams

As previously unveiled, fuel production by ceria foams is very sensitive to the operating conditions. Thus, the following parameters: reduction temperature at 1400 °C under 0.100 bar, oxidation step starting at 1050 °C with CO_2 molar fraction of 1.00 and total gas flow rate of 2.0 L/min were selected as "optimal conditions". The performance of coated ceria foams (CF-LSMMg and CF-CSM) with those of pure CeO_2 foam in these optimal conditions are compared in Figure 3-20. The CO cumulative production for the three foams is provided in Figure 3-21. As for the "reference conditions" (Figure SC-7), the CF-LSMMg foam reaches a higher reduction extent (222 µmol/g) than the pure CeO_2 foam (154 µmol/g). During the oxidation step, the CF-LSMMg foam exhibits a lower fuel production rate (4.6 mL/g/min) as well as a lower re-oxidation extent (87%) than the pure CeO_2 foam (7.5 mL/g/min and 100%, respectively). The time required to reach 90% of the maximum CO production yield is also significantly longer for CF-LSMMg (5.8 min) than for the pure CeO_2 foam (2.0 min), as evidenced in Figure 3-21. However, the CO production yield is significantly higher for CF-LSMMg foam (387 µmol/g) than for pure CeO_2 foam (341 µmol/g). The LSMMg coating thus permits to increase the amount of fuel produced, but it also tends to slower the production rate in comparison with uncoated ceria foam. Regarding CF-CSM, an enhancement of the reduction step is achieved with 235 µmol/g of O_2 produced in comparison with CF-LSMMg (222 µmol/g) and CeO_2 (154 µmol/g) foams. This can be attributed to the high oxygen release capacity of CSM. However, the CO production yield of CF-CSM foam is markedly lower (250 µmol/g) than for the CeO_2 foam. This is due to the low re-oxidation extent of CF-CSM (53%) in comparison with 87% and 100% for CF-LSMMg and CeO_2 foams, respectively. Furthermore, the oxidation kinetic is slower for CF-CSM than for CF-LSMMg and CeO_2 foams (peak CO production rate of 2.4 mL/g/min against 4.6 mL/g/min and 7.5 mL/g/min, respectively). Therefore, the CSM coating permits to enhance the reduction step but it has adverse impact on the oxidation step, probably because of the enhanced densification of the coated layer at the surface during the synthesis.

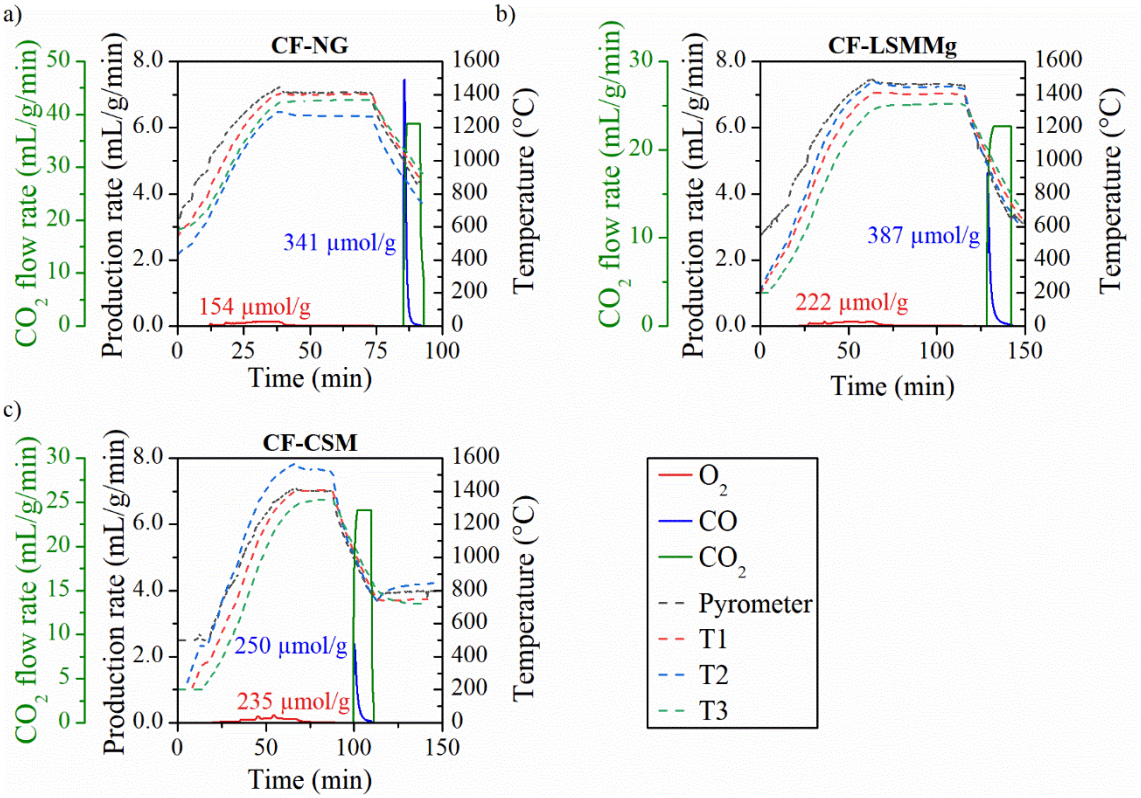

Figure 3-20: Comparison of performance for pure and coated ceria foams during thermochemical cycles performed with T1~1400 °C under 0.100 bar (reduction step), followed by oxidation starting at 1050 °C under 100% CO_2: a) CF-NG b) CF-LSMMg (Cycle #3) and c) CF-CSM (Cycle #1).

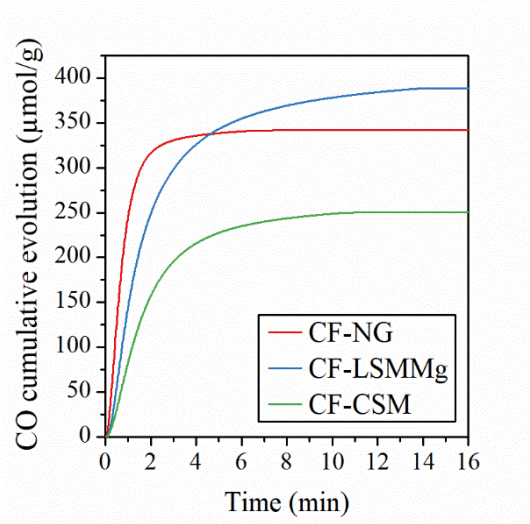

Figure 3-21: CO cumulative evolution for CF-NG, CF-LSMMg and CF-CSM foams during oxidation starting at 1050 °C under 100% CO_2 (after a reduction step performed with T1~1400 °C under 0.100 bar)

3.3.4.4 Dual-phase foam characterization

The ceria foam microstructure (before and after perovskite coating) has been characterized using Scanning Electron Microscopy (SEM) [206]. Millimetric scale open cells and fine granular microstructure were highlighted. For the fresh CF-LSMMg foam, the LSMMg coating was observable (A spot in Figure 3-22.a) on the ceria foam (B spot in Figure 3-22.a). The thickness of the LSMMg coating at the ceria surface was estimated to be ~10 µm [206]. The

distribution of elements was analyzed by EDS mapping (Figure SC-5), and confirmed the absence of interaction between LSMMg and ceria. The grain sizes of the LSMMg coating were in the range 3-10 µm. Regarding CF-CSM foam, the perovskite coating was also well identified (Figure 3-22.c), with grain sizes in the range 3-7 µm. A enhanced densification of the CSM coating was observed even before cycling (occurring during the composite synthesis), as opposed to the LSMMg-coating. This observation explains the better re-oxidation of CF-LSMMg, due to better access of the oxidant gas to ceria material. After cycling, only few residual particles of LSMMg (spot C) were found in CF-LSMMg, and instead different compositions were likely detected (CeO_2 in spot D, $CeMnO_3$ in spot E and $Ce_{0.5}Sr_{0.5}Mn_{0.9}Mg_{0.1}O_3$ in spot F). The LSMMg-coating on ceria did not sustain the investigated cycling conditions. However, no performance decline suggesting an adverse reaction between CeO_2 and LSMMg was observed. On the contrary, the perovskite phase in CF-CSM remained after cycling. The difference of stability between the perovskite coatings in CF-LSMMg and CF-CSM may be attributed to the oxidant gas used. Indeed CF-LSMMg was exposed to both H_2O and CO_2 while CF-CSM was only exposed to CO_2. An interaction between CeO_2 and LSMMg is suspected when the foam is exposed to H_2 or H_2O vapor, which could explain the observed instability of the LSMMg coating.

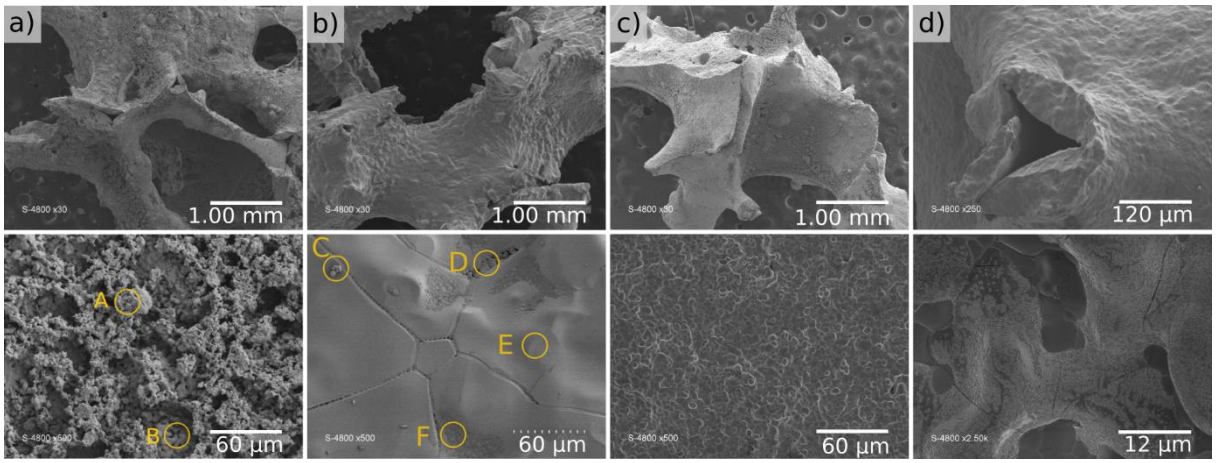

Figure 3-22: SEM images of perovskite-coated ceria foams: a) fresh and b) cycled CF-LSMMg, c) fresh and d) cycled CF-CSM

In spite of this, the LSMMg coating was shown to enhance the performance of ceria for thermochemical water splitting and CO_2 reduction cycles. In contrast, it was pointed out that the use of a CSM layer only enhanced the reduction extent of ceria but oxidation was not favored due to the densified microstructure of the layer, creating a barrier for gas access to the ceria surface. After the series of cycles performed, the foams shape and dimensions remained intact in the cavity and their thermomechanical integrity was not altered, although the CF-LSMMg structure was more brittle than the original one.

3.3.5 Investigation of ordered porous ceria structures

The thermochemical performance of ordered porous ceria structures prepared by additive manufacturing were investigated for comparison with reticulated porous ceria structures (non-ordered structures). In two-step thermochemical cycles, the temperature is a key parameter as

it impacts the non-stoichiometry extent achieved by the reactive material. To improve the solar-to-fuel conversion efficiency, the solar radiation absorption of the reactive material should be maximum in order to reach the reduction temperature with the minimal solar power input. Furthermore, the mass of reactive material should be maximized as it is directly related to the total amount of fuel produced. However, the solar absorption of the reactive material should not be enhanced at the expense of decreasing the mass of reactive material. Therefore, an approach to enhance the solar absorption was investigated by developing hierarchically ordered porous ceria structures with a tailored porosity gradient, with the goal of adjusting the optical thickness and achieving uniform heating without compromising the apparent density or the specific surface area. A first study pointed out the potential beneficial effect of hierarchically ordered geometries on thermal performance, by achieving a more uniform temperature distribution across the structure [216]. The microstructure of reactive foams was further optimized by addition of natural pore formers able to increase the micro-scale porosity of the foam within the struts, and thus the specific surface area. Series of ordered porous ceria structures were fabricated by the additive manufacturing technique.

The reactivity of CF-OG and CF-OGP samples was first investigated by thermogravimetric analysis, as shown in Figure 3-23 and the associated O_2 and CO yields along with the production rates are reported in Table 3-2. The amounts of O_2 and CO produced were similar for both CF-OG and CF-OGP. The reported values are in line with those previously obtained with ceria powders [99]. Regarding the reaction rate, reduction rates during both cycles were similar for both CF-OG and CF-OGP (in the range 0.09-0.10 mL/min/g). In contrast, the CO production rate achieved by CF-OGP was higher than that achieved by CF-OG (e.g., the CO production rate during the first cycle is 0.88 mL/g/min for CF-OGP against 0.64 mL/g/min for CF-OG), thus highlighting an enhancement of oxidation rate due to the pore former addition.

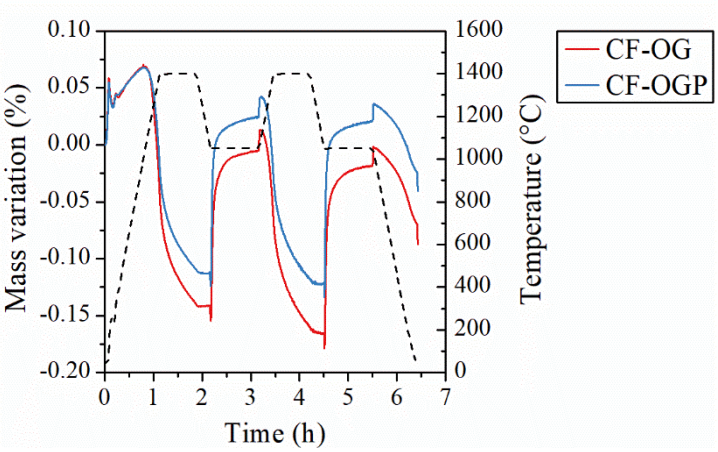

Figure 3-23: TGA of hierarchically ordered porous ceria structures: CF-OG and CF-OGP, during two thermochemical cycles

Table 3-2: O_2 and CO yields and production rates obtained during two thermochemical cycles in TGA with hierarchically ordered ceria structures

Foam	1st cycle				2nd cycle			
	O_2		CO		O_2		CO	
	yield (µmol/g)	production rate (mL/g/min)	yield (µmol/g)	production rate (mL/g/min)	yield (µmol/g)	production rate (mL/g/min)	yield (µmol/g)	production rate (mL/g/min)
CF-OG	66	0.10	93	0.64	56	0.09	100	0.72
CF-OGP	57	0.09	93	0.88	51	0.09	95	0.95

To study the impact of the pore forming addition and the hierarchically ordered geometry, different cycles were carried out with CF-OG and CF-OGP, as reported in Table SC-4. In total, 0.33 L and 0.63 L of H_2 (during 5 and 4 cycles, respectively) along with 0.87 L and 2.48 L of CO (during 8 and 11 cycles, respectively) were produced by CF-OG and CF-OGP, respectively. This corresponds to 17 h and 26 h of on-sun operation for the CF-OG and CF-OGP structures respectively.

A comparison of the performance of CF-OG foam with CF-10 as a reference, is provided in Figure 3-24a, for a reduction at 1400 °C under reduced (~110 mbar) pressure and oxidation starting at 1050 °C under 100% CO_2. Given that CF-OG is a full cylinder (4 stacked discs) whereas the CF-10 foam is centrally hollowed, the temperature gradient between T1 and the pyrometer is higher for CF-OG than for CF-10. Indeed, the pyrometer points the top surface of CF-OG instead of the bottom of central cavity for CF-10 (average foam temperature in this case). The reference control temperature was T1, located at the same place in both foams. The O_2 yield reached 150 µmol/g for CF-OG in comparison with 128 µmol/g for CF-10. The higher reduction extent of CF-OG could be explained by a better volumetric solar absorption in the structure volume thanks to the porosity gradient and a more uniform temperature distribution across the structure. Another possibility would be the high temperature reached on top of the foam, as indicated by the pyrometer, leading to higher O_2 yield than the CF-10 one. However, both the CO production yield and re-oxidation extent achieved by CF-OG (222 µmol/g and 74%, respectively) are lower than those measured for CF-10 (258 µmol/g and 100%, respectively). The different synthesis methods could affect the foam microstructure and consequently the oxidation reaction, but it seems unlikely that the ordered geometry affects the oxidation reaction. The uncomplete re-oxidation of CF-OG leads to a decrease of O_2 production from 150 µmol/g to 102 µmol/g between the first and second cycle. The non-stoichiometry extents reached after cycle #1 and #2 are similar (0.052 and 0.049, respectively), highlighting the incomplete re-oxidation during cycle #1.

The density of foams with ordered-geometry is ranging from 0.10 g/cm^3 (for 11 ppi discs) to 0.45 g/cm^3 (for 20 ppi discs) while CF-10 foam has a density of 1.03 g/cm^3. However, the density of ordered structures can be further increased by tuning both the strut thickness and the cell size, while maintaining the spatial distribution of the cells. Anyway, the ordered geometry is suitable to enhance the reduction step, even if further investigations are necessary in order to i) reduce the temperature gradient, ii) improve the synthesis method to reach complete re-oxidation, and iii) increase the foam density.

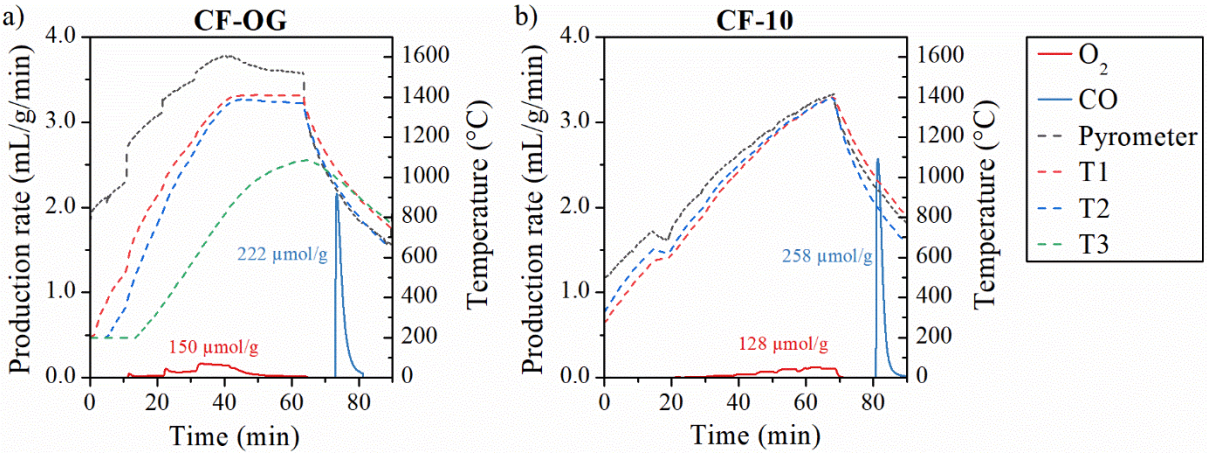

Figure 3-24: O_2 and CO evolution along with the temperature profiles during thermochemical cycling of ceria foams: a) CF-OG (cycle #1) and b) CF-10 (cycle #31), with a reduction at 1400 °C under reduced pressure followed by oxidation starting at 1050 °C under 100 %CO_2

As the specific surface area is a key parameter to promote the oxidation reaction, the addition of a pore former during material synthesis appears as an attractive option to enhance the oxidation step. Figure 3-25.a presents the evolution of CO production rate (x_{CO2}=1.00, $Q_{ox,tot}$=2 L/min) during the oxidation step starting at 900 °C, after a reduction step at 1400 °C under reduced pressure (~0.100 bar). The CO peak production rate reached 3.3 mL/g/min (cycle #5) and 4.9 mL/g/min (cycle #14) with CF-OG and CF-OGP foams, respectively. The CO production rate is thus higher for CF-OGP than for CF-OG. Furthermore, the CO yield produced by CF-OGP (248 µmol/g) is higher than that achieved by CF-OG (212 µmol/g). However, the CO peak production rate and yield remain lower than those attained by CF-NG foam (9.3 mL/min/g and 316 µmol/g, respectively) in similar operating conditions (T_{red}=1400 °C, p_{red}=0.110 bar, T_{ox}=900 °C, x_{CO_2}=1.00, $Q_{ox,tot}$=2 L/min).

Regarding the H_2 production rate, similar results were obtained, with an H_2 peak production rate higher for CF-OGP (1.1 mL/min/g) than for CF-OG (0.8 mL/min/g). Furthermore, the H_2 yield achieved by CF-OGP (243 µmol/g) is also higher than that achieved by CF-OG (166 µmol/g). The addition of a pore former in the synthesis positively impacts the oxidation rate as it enhances the reactive surface. The difference between the performance of non-ordered and ordered geometries can be explained by the different synthesis methods used to fabricate the ceria structures (the non-ordered RPC foams were made by ALSYS-CTI whereas the ordered ones were made by the replica method on 3D-printed polymer scaffolds at PROMES laboratory). Furthermore, the difference in cavity configurations between ordered and non-ordered structures can induce differences in temperature gradients inside the foam (especially the presence of the central cavity in RPC foams that favors temperature homogenization), leading to different thermochemical performance.

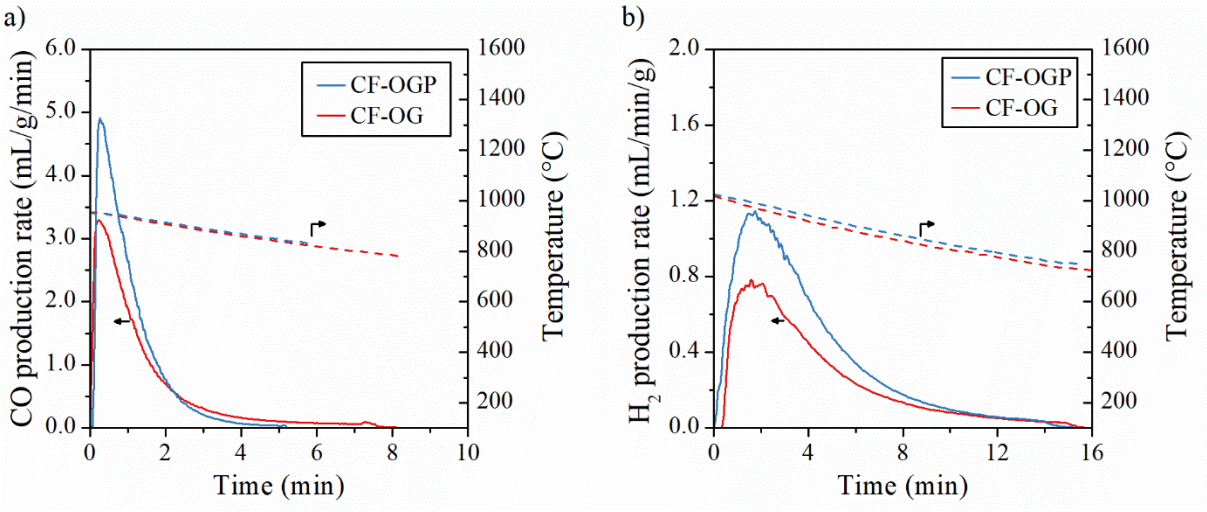

Figure 3-25: Comparison of performance for CF-OG and CF-OGP foams: a) CO production rate with oxidation starting at 950 °C (cycles #5 and #14) and b) H_2 production rate with oxidation starting at 1050 °C

The microstructure of ordered porous structures was investigated by SEM, as illustrated in Figure 3-26. The grain sizes, strut diameters and pore sizes were determined using image analysis (ImageJ software). Fresh CF-OG and CF-OGP foams showed grain sizes in the range 5-15 µm, while the strut diameter was estimated at ~250 µm. Micron-sized grains are observable, as well as hollows at the strut center (resulting from the firing of the polymeric template), thus forming an interconnected macroporous network. After cycling in the solar reactor, a densification/sintering of CF-OG foam is observable (grain sizes in the range 10-20 µm), with few remaining residual pores. In contrast, high porosity (pore sizes in the range 2-7 µm) can be observed in pristine CF-OGP (Figure 3-26c) in comparison with CF-OG, explaining enhanced fuel production rate for CF-OGP. As noticeable in Figure 3-26.d, a large amount of porosity remained after foam cycling, impeding drastic decrease of fuel production rate. This highlights the beneficial impact of pore formers on both foam microstructure and performance. In order to further investigate/compare the porous structures of CF-OGP and CF-10 foams, mercury porosimetry experiments (using AutoPore IV 9500) were carried out (Figure SC-9). The porosity within the struts was measured at 57% for CF-OGP and 36% for CF-10, confirming the very porous microstructure of CF-OGP. For both foams, the pore sizes distribution was bimodal. Small pore sizes (~0.5 µm) were measured for CF-OGP, in line with SEM observations, while the smallest pore sizes measured for CF-10 was ~3 µm. Furthermore, pore sizes ~132 µm were also measured for both CF-OGP and CF-10 foams, corresponding to central hollows in the strut, left by the fired polymer scaffold. Mercury porosimetry measurements usually provide smaller pore size than SEM measurements as the technique measured the size of pore entrance or constriction (for further explanations see Figure SC-10 and associated comments). This explains that mean strut diameters measured by Hg porosimetry was 132 µm whereas it was ~250 µm by SEM analysis.

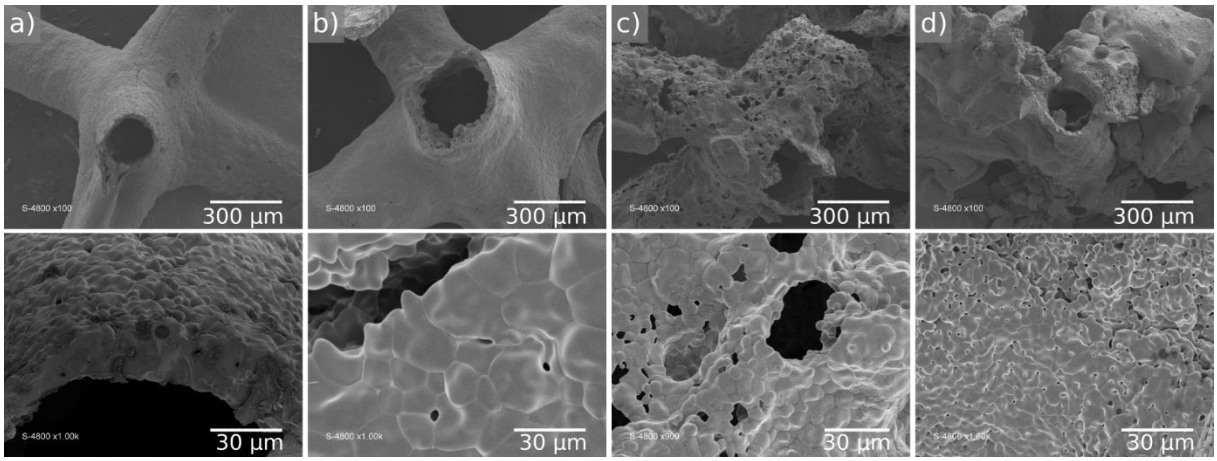

Figure 3-26: SEM images of a) fresh and b) cycled CF-OG, c) fresh and d) cycled CF-OGP

3.3.6 Energy conversion efficiencies

The solar-to-fuel conversion efficiency is an essential indicator to evaluate the thermochemical process performance. Indeed, thermochemical cycles should reach a solar-to-fuel conversion efficiency of 20% to be competitive with the combined electrolytic and photovoltaic technologies [47]. The instant solar-to-fuel energy conversion efficiency was calculated according to equation (45),

$$\eta_{solar-to-fuel} = \frac{\dot{n}_{fuel} HHV_{fuel}}{P_{solar}} \tag{45}$$

where $\dot{n}_{fuel}$ is the fuel production rate, HHV_{fuel} the high heating value of the fuel, and P_{solar} the solar power input during the reduction step. For the highest CO production rate (9.93 mL/g/min, cycle #32 with CF-10 foam), the solar-to-fuel conversion efficiency reached ~7.8% (considering maximal power input P_{solar} = 1.50 kW, and neglecting the power associated with pumping work and energy penalties arising from inert gas recycling). The order of magnitude of $\eta_{solar\text{-}to\text{-}fuel}$ was then estimated in a more realistic case, accounting for losses at the aperture and due to the presence of the window. Taking into account the incident radiation spillage around the cavity aperture due to concentration defects and attenuation by the window due to reflection and absorption (losses amounting to ~10% of P_{solar}), the effective solar power input was considered as 1.35 kW.

Another conversion efficiency was assessed by considering the cycle energy conversion efficiency (η_{cycle}), not linked to the solar power input but related to the actual mass of cycled ceria, as defined in equation (46),

$$\eta_{cycle} = \frac{n_{fuel} HHV_{fuel}}{\left(\Delta H_{red}(\delta_f) + Cp_{CeO_2} \Delta T\right) n_{CeO_2}} \tag{46}$$

where n_{fuel} is the total amount of produced fuel per cycle, $\Delta H_{red}(\delta_f)$ is the reduction enthalpy for the final non-stoichiometry reached (δ_f), Cp_{CeO_2} is the heat capacity of ceria, ΔT is the temperature swing between the reduction and oxidation steps, and n_{CeO_2} is the quantity of reacting ceria. The ceria heat capacity was taken at 80 J/(mol·K) [217] and the reduction

enthalpy was calculated according to the non-stoichiometry extent reached by the material from data in [196]. This efficiency is related to the actual energy consumed by the reaction (including both ceria heating with $\Delta T=T_{red}-T_{ox}$ and reduction enthalpy) and permits to skip the heat losses caused by the small reactor scale. For each material investigated in this chapter, the instant solar-to-fuel conversion efficiency and the cycle efficiency are reported in Table 3-3, while the data used to calculate efficiencies are reported in Table SC-6. The highest cycle efficiency was reached by CF-LSMMg (4.1%) due to its high CO production yield (387 µmol/g), while the highest instant solar-to-fuel conversion efficiency was achieved by CF-MG (8.7%). Increasing the amount of reacting ceria (using higher density foams with smaller cell sizes) or decreasing the solar power input (by reducing heat losses or improving radiation absorption efficiency of the foam) are possible strategies to improve the solar-to-fuel efficiency. In addition, the above calculated efficiencies should be further enhanced by up-scaling the solar reactor (lower surface-to-volume ratio) and using a sensible heat recovery system. Anyway, it is clear that the solar-to-fuel conversion efficiencies achieved in this study with reticulated microstructured ceria foams are among the highest obtained to date in a solar-heated reactor.

Table 3-3: Cycle efficiency and instant solar-to-fuel energy conversion efficiency for each investigated ceria structure

Foam	η_{cycle}	$\eta_{inst,solar\ to\ fuel}$
CF-20	2.6%	4.4%
CF-10	2.8%	8.6%
CF-NG	3.1%	7.9%
CF-MG	4.0%	8.7%
CF-HG	3.5%	6.7%
CF-LSMMg	4.1%	5.9%
CF-CSM	2.6%	3.1%
CF-OG	2.1%	1.5%
CF-OGP	3.3%	2.6%

3.4 Conclusion

In this chapter, the ability of the SUNFUEL monolithic reactor to perform two-step thermochemical cycles with highly-reactive ceria open-cell foams was demonstrated. An exhaustive investigation of the reactor operating parameters was performed to identify optimal reaction conditions for maximized fuel production. Reactor flexibility was assessed by testing various operating conditions. Robustness in solar processing was demonstrated by operating the system for extended periods at high temperatures under high-flux solar irradiation. Remarkable fuel production rates and yields as well as material performance stability were achieved during continuous on-sun operation with commercial-grade ceria foams exhibiting volumetric solar absorption via mm-scale open cells and relevant porous microstructure favoring solid-gas surface reactions.

Decreasing the pressure and/or increasing the temperature during the reduction step significantly improved the reduction extent reached by the reactive material. Regarding the oxidation step, increasing the oxidant molar fraction or the total gas flow rate and decreasing the oxidation temperature enhanced the fuel production rate. The highest CO production rate

of 9.9 mL/min/g was reached by optimizing the operating parameters, outperforming the maximum CO production rates reported to date.

Different reactive ceria open-cell foams were investigated. No significant differences in the thermochemical performance were observed with 20 ppi and 10 ppi foams while an axial cell size gradient intensified the thermal gradient in the foam but did not influence the fuel production yield. Perovskite-coated ceria foams were also investigated and the impact of perovskite coatings (LSMMg and CSM) on thermochemical cycle performance was probed. Both coatings enhanced the oxygen exchange in the dual phase composite during the reduction step compared to individual components. The LSMMg-coated ceria offered enhanced fuel production yield with suitable operating conditions in comparison with pristine ceria. On the contrary, the CSM-coating on ceria foam was found to negatively affect CO production yield. For both coated ceria foams, the fuel production rate was lower than for pure ceria, due to the barrier effect of the coatings hindering the diffusion of gaseous reactants. The re-oxidation of coated ceria foams was thus very sensitive to the oxidant molar fraction.

Ordered porous ceria structures prepared by additive manufacturing technique (replication using 3D-printed polymer scaffolds) were also tested in the solar reactor. The ordered geometry showed an increase of the reduction extent in comparison with non-ordered RPC foams in similar operating conditions. However, the oxidation step was not enhanced with ordered geometry foams due to their incomplete re-oxidation extent, which could be attributed to differences in synthesis method (different microstructures). Furthermore, the density of ordered structures was lower than for RPC foam, thereby decreasing the amount of reactive material loaded in the solar cavity. The addition of a natural porogen (wood particles) during the synthesis significantly improved the fuel production rate due to the increase of micro-scale porosity within the struts. The reactor performance should be further enhanced via scaling-up and optimization of ceria foam geometry, cell size and macrostructure for maximum solar radiation absorption and uniform heating. Furthermore, future work should address the geometric optimization of the 3D porous structures via thermal and fluid dynamics modelling for achieving uniform temperature distribution and complete reaction extent, as well as the shaping of porous reactive ceramics with controlled microstructure.

Chapitre 4 - Solar redox cycling of structured ceria particulate materials in direct and indirect heating solar reactors[3]

4.1 Introduction

During redox cycles, the reduction step is affected by the diffusion length for lattice oxygen transfer, while the oxidation reaction largely depends on the porous structure and specific surface area of the material, since it is a surface-controlled solid/gas reaction. These two properties are impacted by the reactive material microstructure [218], which is thus a key parameter for enhancing the thermochemical performance.

Among a variety of potential candidates, ceria fiber felt was first investigated to perform two-step thermochemical cycles in solar reactors, because the use of such designed 2D or 3D morphologies enhances fuel production rates. Furler et al. [67] reached a non-stoichiometry extent δ of 0.044 with a commercial ceria felt during the reduction step at 1650 °C. They obtained a syngas production of 5.88 mL/g with a solar-to-fuel energy conversion efficiency of 0.15%. The heat transfer limitation induced by low thermal conductivity of the ceria felt was the main reason for the low efficiency [67]. To overcome the poor thermal conductivity of the felt, reticulated porous ceramics (RPC), such as foams, have been explored to perform thermochemical cycles, as described in the chapter 3. The replication technique is one of the most commonly employed methods to prepare RPC foams [207]. Furler et al. [159] obtained non-stoichiometry extent up to 0.042 at a reduction temperature in the range of 1400-1600 °C with a ceria RPC foam. The achieved solar-to-fuel energy conversion efficiency reached 1.73%, namely a 4-fold increase compared with ceria felt. However, due to the low specific surface area, the peak fuel production rate was low. Dual-scale porosity RPC foams, combining mm-pore sizes with µm-pore sizes within the foam struts, were developed to favor the oxidation step, which provided faster fuel production rate with a higher fuel yield in comparison with more conventional foams with single-scale porosity [158]. Further advances were achieved in this thesis with coated RPC foams and the results obtained with such materials were reported in chapter 3.

Another type of morphology investigated in the literature consists of three-dimensionally ordered macroporous (3DOM) structures that enhance fuel production rates. Venstrom et al.

[3] Most of the results of this chapter have been published in two peer-reviewed articles:

- F.A.C. Oliveira, M.A. Barreiros, A. Haeussler, A. Caetano, A.I. Mouquinho, P.M.O. e Silva, R.M. Novais, R.C. Pullar and S. Abanades. *Sustainable Energy Fuels*, 2020, **4**, 3077–3089
- A. Haeussler, S. Abanades, F. Oliveira, M.A. Barreiros, A.P. Caetano, R. Novais and R.C. Pullar. *Energy & Fuels*, 2020, **34**, 9037–9049

[163, 164, 219] obtained an inverse replica of a face-centered cubic close-packed array, forming a 3DOM structure of ceria. The as synthesized 3DOM ceria structure exhibits a specific surface area (SSA) of 30 m²/g, which decreased to 10 m²/g after thermochemical cycling. With the 3DOM material, the peak production rate was enhanced (by 260%) in comparison with a more conventional low porosity ceria material (reticulated porous foam). The improvement of the oxidation kinetic was attributed to both the high SSA and the interconnected pore structure of the 3DOM material [163]. Recently, ecoceramics were developed for application in solar reactors for thermochemical cycles [165, 166]. Ecoceramics use natural sustainable materials as templates to produce biomimetic ceramics, offering the advantages of being both cost effective and eco-friendly [220]. They also create 3DOM structures, based on the natural cellular morphology of the template material, usually wood. Pine wood templated ceria permitted a 5-6 fold increase of the oxidation rate after a reduction at 1400 °C compared with non-porous ceria, but the microstructure was not retained after thermal treatment at 1500 °C [166]. Another study highlighted a 2-fold increase of CO production rate with cork-templated ceria in comparison with RPC ceria foam. The cell sizes in the biomimetic material were one order of magnitude smaller than those in the ceria foam, thus providing higher available surface area for the oxidation reaction [165]. Table 4-1 compares different key studies with the corresponding operating conditions and associated fuel production, highlighting the strong influence of the selected ceria structure on both fuel production rates and yields.

Table 4-1 : Comparison of key experiments using ceria materials in thermochemical cycles, with the corresponding operating conditions and associated fuel production (CO, H_2 or syngas)

References	**Materials**	**Facility used**	**Operating conditions**	**Oxidant**	**Fuel production rate & yield**
Furler et al. [67]	Ceria felt	Solar simulator	T_{red}= 1460-1647 °C T_{ox}< 927 °C	CO_2/H_2O	1.9 mL/min/g 262 µmol/g
Furler et al. [159]	Ceria foam	Solar simulator	T_{red}= 1420 °C T_{ox}< 1000 °C	CO_2	0.127 mL/min/g 65 µmol/g
Costa Olivera et al. [221]	Ceria foam	Solar furnace	T_{red}=1400 °C T_{ox}=1050 °C-850 °C	H_2O	0.6-0.8 mL/min/g 115 µmol/g
Costa Olivera et al. [221]	Cork templated ceria granules	Solar furnace	T_{red}=1400 °C T_{ox}=1050 °C-850 °C	H_2O	1-1.4 mL/min/g 133 µmol/g
Chueh et al. [68]	Porous monolithic ceria	Solar simulator	T_{red}=1420-1640 °C T_{ox}< 900 °C	CO_2	4.6 mL/min/g 192 µmol/g
Cho et al. [161]	Inert zirconia foam with CeO_2 coating	Solar furnace	T_{red}=1400-1600 °C T_{ox}=1100-900 °C	H_2O	116 µmol/g
Marxer et al. [46]	Dual-scale porosity ceria foam	Solar simulator	T_{red}=1450-1500 °C P_{red}=10 mbar T_{ox}=700-1000 °C	CO_2	1.2 mL/min/g 276 µmol/g
Haeussler et al. [205, 222]	Microstructured ceria foam	Solar furnace	T_{red}=1400 °C T_{ox}=1008-796 °C	CO_2/H_2O	8.36 mL/min/g 254 µmol/g
Gladen and Davidson[157]	Commercial fibrous ceria particles	Electric furnace	T_{red}=1500 °C T_{ox}=800 °C	CO_2	8.4 mL/min/g 51 µmol/g

This chapter aims to compare the thermochemical performance of various ceria porous materials in directly and indirectly-heated packed-bed solar reactors. Different ceria materials structured in divided form were thus investigated in order to study the impact of the material morphology on its redox activity. Accordingly, ceria-based materials with different morphologies have been selected to compare their ability for two-step thermochemical H_2O and CO_2 splitting, namely biomimetic cork-templated ceria, ceria RPC foam, ceria fibers, ceria pellets and ceria microstructured spheres. For each material, several consecutive cycles were performed with various operating conditions.

4.2 Method

4.2.1 Types of materials, synthesis methods and characterization

The considered materials were biomimetic cork-templated ceria, ceria foam, ceria fibers, ceria pellets and ceria miscrostructured spheres, abbreviated as CTCe, CeF, CeFB, CeP and CeMS respectively. Pictures of the reactive materials are presented in Figure SD-1 and Figure SD-2.

CeFB fiber boards (>99% purity) and CeP pellets (>99% purity) were supplied from Zircar Zirconia Inc. USA (density: 1153 kg/m^3 and 1842 kg/m^3 respectively). The ceria pellets were cylindrical, 4 mm in height and 4 mm in diameter.

Two types of ceria-based materials were synthesized at both the University of Aveiro and LNEG (Portugal), in the form of cork-derived ecoceramic granules, and polymer replicated foams.

Cork-derived ceria granules were synthesized following a procedure described in Figure 4-1, in which cork granules were heat-treated in a nitrogen atmosphere at 900 °C for 30 min to form carbon templates. The latter were then infiltrated with cerium nitrate solution ($Ce(NO_3)_3.6H_2O$, 99%, Sigma Aldrich) using a rotary evaporator under vacuum. Two routes (i and ii, Figure 4-1) were used in order to evaluate the influence of the solvent type and number of infiltration cycles on the microstructure of the produced ecoceramics:

i) Water was used to dissolve cerium nitrate and four infiltration/drying cycles were performed, considering previous works which showed that beyond the fourth cycle the weight gain is less relevant [223, 224] (hereafter denoted as CTCe17).

ii) Acetone was used to dissolve the cerium nitrate and only one infiltration/drying cycle was performed. Preliminary tests were performed (not shown for the sake of brevity) to evaluate the influence of the number of infiltration/drying cycles when using acetone. Results have shown that a higher number of cycles negatively affects the ecoceramic's microstructure, due to an increasing amount of cerium nitrate inside the cork-carbon template cells. After firing, this leads to a decrease in the ecoceramic's porosity, and could jeopardize its envisioned use in solar thermochemical energy production. Hereafter, this novel material is denoted CTCe19. It should be highlighted that with this route the goal was to decrease the time and energy consumption (e.g. rotary evaporator) required for the specimens' synthesis.

After a number of infiltration/drying steps (number depending on the synthesis protocol), the specimens were heated in air at 1600 °C for 30 min to remove carbon species, convert the cerium salt to a pure ceria, and consolidate the ceramic material while preserving the 3DOM cork structure.

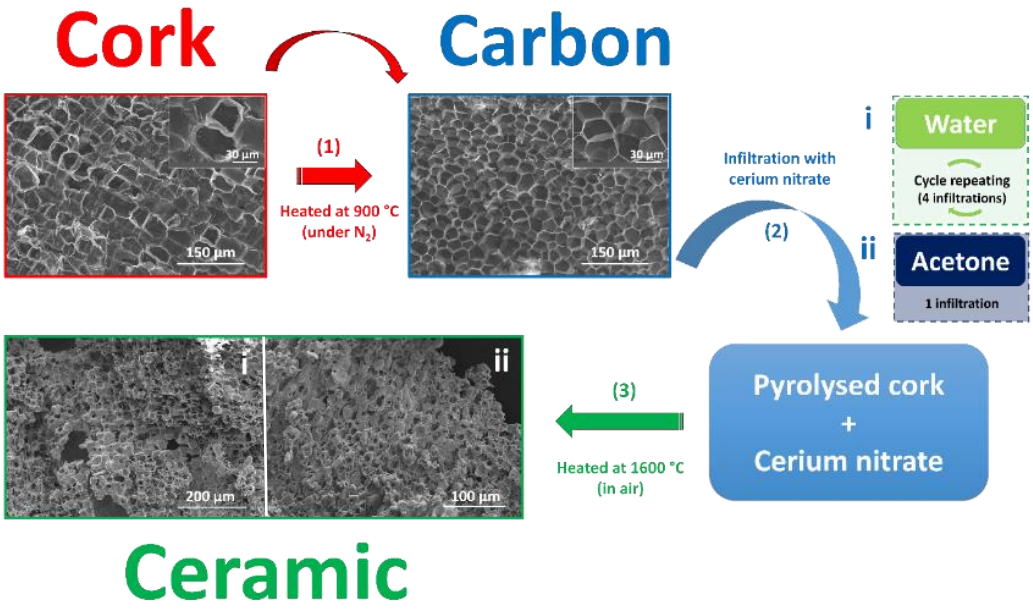

Figure 4-1: Schematic representation of the synthesis protocol for producing cork-derived ceria ecoceramics. Two different synthesis processes were compared, i) using water and ii) using acetone, and SEM images of the two resulting ceria ecoceramics are compared

Polymer-templated ceria foams (hereafter called CeF) with cylindrical shape (20 mm in diameter and 20 mm in height), were manufactured by the replication method reported in detail elsewhere [225]. Briefly, an aqueous slurry with a solid content of 40 vol.% was prepared from ceria powder (Aldrich Chemistry, ref. 211575, Austria, with average particle sizes (d_{50}) of 1 µm, 99.9% purity) together with 0.8 wt.% anionic polyelectrolyte dispersant (Dolapix CE64, Zschimmer & Schwarz, F.R. Germany). Addition of 5 wt. % polyvinyl alcohol (PVA, Riedel-de-Haën, F.R. Germany) was used to prevent the collapse of the foam structure during polymer burnout. Reagents were mixed together for 30 min in a Pyrex jar at 700 rpm. The resulting stock slurry was then used to impregnate an open-cell polyurethane (PU) foam (grade 20DB, manufactured by Flexipol – Espumas Sintéticas S.A., Portugal). The mean cell size of the PU foam was determined to be ~700 µm (36 ppi) by using image analysis, and its density was 21 kg m^{-3} [226]. After drying under controlled temperature and humidity conditions overnight, the samples were heated at 1 °C min^{-1} to 500 °C for 1 h, and subsequently sintered at 1450 °C for 30 min. These foams prepared by LNEG were strongly different from those supplied by CTI and used in the previous chapter (chapter 3). In particular, their cell size was much lower and they were used in a different reactor configuration (packed bed of foam pieces instead of a single monolith as in chapter 3).

Ceria microspheres (denoted as CeMS) were synthesized at IEM (Montpellier) using a process involving an ion-exchange resin [227, 228]. A polyacrylic resin constituted of microspheres

was washed successively with an aqueous nitic acid solution, an aqueous ammonia solution and then deionized water. This protocol was used both to remove all the exchangeable cations and chemical impurities from the resin and to convert it to its ammonium form. Then the resin was loaded in cerium by contacting it with an aqueous solution of Ce^{3+} ions, obtained by dissolution of cerium nitrate in pure water. The ionized or ionizable groups of the polyacrylic resin (carboxylate groups compensated by NH_4^+ cations) exhibit a strong affinity for the Ce^{3+} ions. Thus, the quantitative fixation of Ce^{3+} ions occurs at the atomic scale, providing good homogeneity and the possibility to control the final material porosity. After the cation exchange, the resin was first rinsed with pure water to remove the excess of non-fixed cations. Then, it was dried for 12 h at 100 °C to remove the water contained in the resin. Afterward, the resin underwent a first ceramization thermal treatment in air (4 h at 800 °C, heating ramp of 1 °C/min, free cooling) to remove the organic skeleton from the material. A second thermal treatment (4h at 1400 °C, heating ramp of 5 °C/min up to 800 °C and 1 °C/min up to 1400 °C, free cooling) was used to stabilize the ceria microstructure and morphology for high temperature applications. The final ceria particles were porous spheres (number average diameter of ~375 µm) with mainly open porosity (~36%) favoring an easy penetration/diffusion of gas species inside the particles. The specific surface area measured by the BET method was 0.3 m^2/g.

The redox activity of the reactive materials was determined by thermogravimetric analysis (TGA, Setaram Setsys Evo 1750) in controlled atmospheres. The sample (about 105 to 125 mg) was placed in a Pt crucible and submitted to two thermochemical cycles with the reduction step carried out at 1400 °C (heating rate of 20 °C min^{-1}), held for 45 min, in flowing Ar at 20 mL min^{-1} (99.999% purity), and the oxidation step at 1050 °C, held for 60 min, in flowing CO_2 stream mixed with Ar (total flow rate of 20 mL min^{-1}, 50% CO_2 in Ar). The sample mass loss during reduction (due to oxygen release) and gain during oxidation (due to oxygen replenishment from CO_2 gas to produce CO) were measured to determine the O_2 and CO production yields.

The morphology of the materials before and after cycling was studied by scanning electron microscopy (SEM). Samples were mounted on stubs with carbon tape, and then imaged on a Philips XL30 FEG microscope using an acceleration voltage of 3-10 kV. The true density of ceria was determined using AccuPyc 1330 Helium pycnometer (Micromeritics Int. Corp., USA). The specific surface area (S_{BET}) was determined by the BET method from N_2 adsorption experiments carried out at −196 °C using a Micromeritics ASAP 2020. Before these measurements, the samples were degassed at 4×10^{-3} mbar and 300 °C for 12 h.

4.2.2 Solar reactors for thermochemical H_2O- and CO_2- splitting cycles

Two solar reactors based on the packed-bed concept were used to perform thermochemical cycles in this chapter: an indirectly heated tubular solar reactor and a directly heated solar reactor.

4.2.2.1 Indirectly heated tubular solar reactor

The experimental setup was developed for investigating high-temperature solid−gas thermochemical reactions in controlled atmospheres. The solar tubular chemical reactor was mounted on a medium size solar furnace (MSSF) at CNRS-PROMES. It is described in detail elsewhere, and it is shown in Figure 4-2 [165]. Briefly, concentrated solar energy was used to drive the endothermic reduction of ceria, whilst the oxidation step was performed during free cooling without any solar energy supply. The high-temperature process heat was supplied by a horizontal axis solar furnace, consisting of a sun-tracking heliostat reflecting the incident solar irradiation towards a 2 m diameter parabolic dish concentrator. The solar reactor consisted of a cavity receiver with a 20 mm diameter aperture positioned at the focal point of the concentrator. The maximum incident thermal power absorbed by the cavity through the aperture is about 1.5 kW for a DNI[4] of 1 kW m^{-2} (only a fraction of this energy was necessary to reach the maximum operating temperature). The cavity made of graphite was lined with a surrounding insulation layer and shielded from the ambient atmosphere using a transparent Pyrex glass window. The samples (either cork-templated ceria granules or ceria foam, about 8−12 g) were placed as packed-beds inside an alumina tube (99.7% purity) with an internal diameter of 20 mm, vertically crossing the cavity. They were supported using a 3 mm thick ZrO_2 felt disc (Zircar Inc., USA) that is chemically inert under the operating conditions to avoid undesirable side reactions. The reaction temperature measurements were carried out using an alumina-shielded B-type thermocouple positioned directly within the reacting sample, inside the alumina tube. This cavity-type solar reactor configuration provides homogeneous temperature distribution within the reacting zone where the sample is placed (40 mm in height). Additional temperature measurements were performed by B-type thermocouples (at the cavity external walls and through the reactor insulation) and by a solar-blind pyrometer (pointing to the tube external wall). Purge gas (Ar, 99.999% purity, O_2 content below 2 ppm) and H_2O flowrates were regulated using electronic mass flow controllers and a peristaltic water pump, respectively. Liquid water was injected via a capillary directly into the tube, and vaporized before reaching the reactive material. The reduction flow rate was set at 0.25 NL min^{-1} of argon, whereas the oxidation step was performed with 0.21 NL min^{-1} H_2O and 0.25 NL min^{-1} Ar (i.e., 45v% H_2O in Ar), to keep the residence time of reacting gas constant during each cycle. These gases were fed from the top of the tube, and the product gases exiting from the reactor outlet at the bottom were monitored using devoted gas analyzers for O_2 and H_2.

Prior to each test, residual air in the reactor chamber was removed by successive vacuum pumping and refilling with Ar in order to ensure an inert atmosphere inside the tube. The reactor was first heated in Ar up to the target reduction temperature (~1400 °C). The reduction (endothermic) step consisted of heating the material up to 1400 °C, with a set heating rate (~30−40 °C/min), and maintaining a temperature plateau for ~15 min until the outlet O_2 concentration became low enough, meaning that the reduction was complete and the equilibrium state in the material oxygen stoichiometry was reached. The temperature was then decreased, and the O_2 concentration returned to almost zero before switching the gas

[4] Direct normal irradiance

atmosphere for the oxidation step. The temperature was controlled by adjusting the opening of a shutter placed between the heliostat and the concentrator, thereby adapting the solar energy input to the target temperature. The O_2 evolution was measured continually using an oxygen analyzer with zirconium oxide sensor (SETNAG™ JC48V, range: 10−10000 ppm, precision: 0.2%, calibrated with 5040 ppm O_2 in N_2). The temperature was lowered by closing the shutter for the reoxidation (exothermic) step, and H_2O (balanced with Ar) was injected into the reactor chamber to react with the oxygen-deficient material and thus produce H_2. The soaking time of the oxidation step during the temperature decrease was also roughly 15 min to reach reaction completion. H_2 concentration in the exhaust gas was measured on-line (concentration as a function of time profiles) by a specific analyzer (thermal conductivity detection, Emerson NGA2000; range: 0–10% H_2, precision: <1% of full-scale). The amounts of gas produced were then determined by time integration of the gas production rates. Each material was subjected to a minimum of 5 cycles (9 for CTCe19).

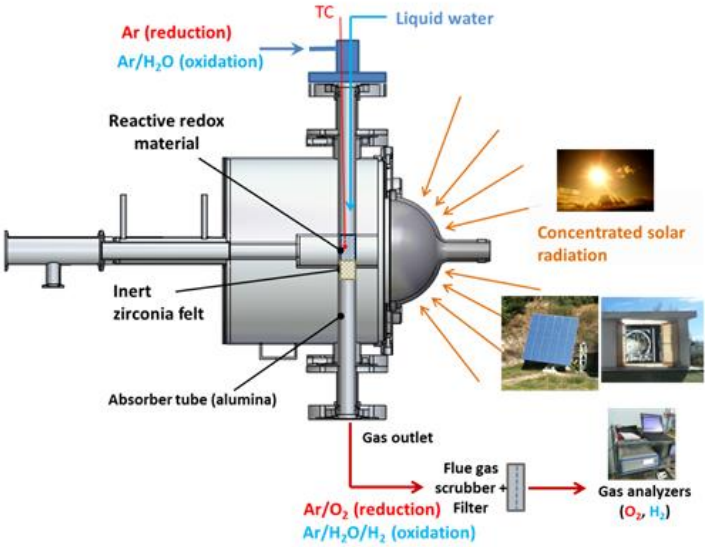

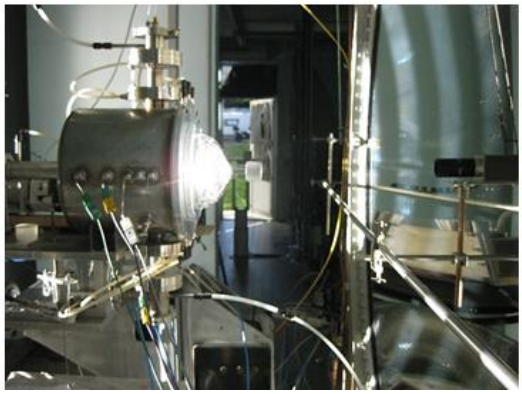

Figure 4-2: Schematic and side view of the tubular solar reactor at the focus of the solar concentrator

4.2.2.2 Directly heated solar reactor

The reactor with direct solar heating was the SUNFUEL reactor previously presented in the chapter 3. The only difference was the cavity configuration that was adapted to investigate the particulate materials in divided forms (Figure 4-3). For the cork-templated ceria granules, ceria

foams, ceria pellets and ceria microspheres materials, an alumina confiner tube was placed at the cavity center to position and maintain the main part of the reactive material around the tube in the annular region (as a packed-bed). Additionally, a portion of reactive material was placed at the tube bottom center, so as to permit a good and uniform heating of the whole material owing to radiation exchange inside the central tube cavity. In the case of ceria fibers boards, four boards were cut and placed vertically in the cavity without the alumina tube. Regarding CeMS, a cardboard insulation disk was placed at the bottom of the cavity to avoid particle escape. An alternative fluidized bed configuration was also considered in the case of CeMS particles, as presented in Figure SD-3. Unfortunately, this approach was not satisfactory because a part of the microspheres was blown out of the cavity in the window area by the upward gas flow. Two other configurations (Figure SD-4) were used to perform the cycles #1, #2 and #3 with the CeMS material.

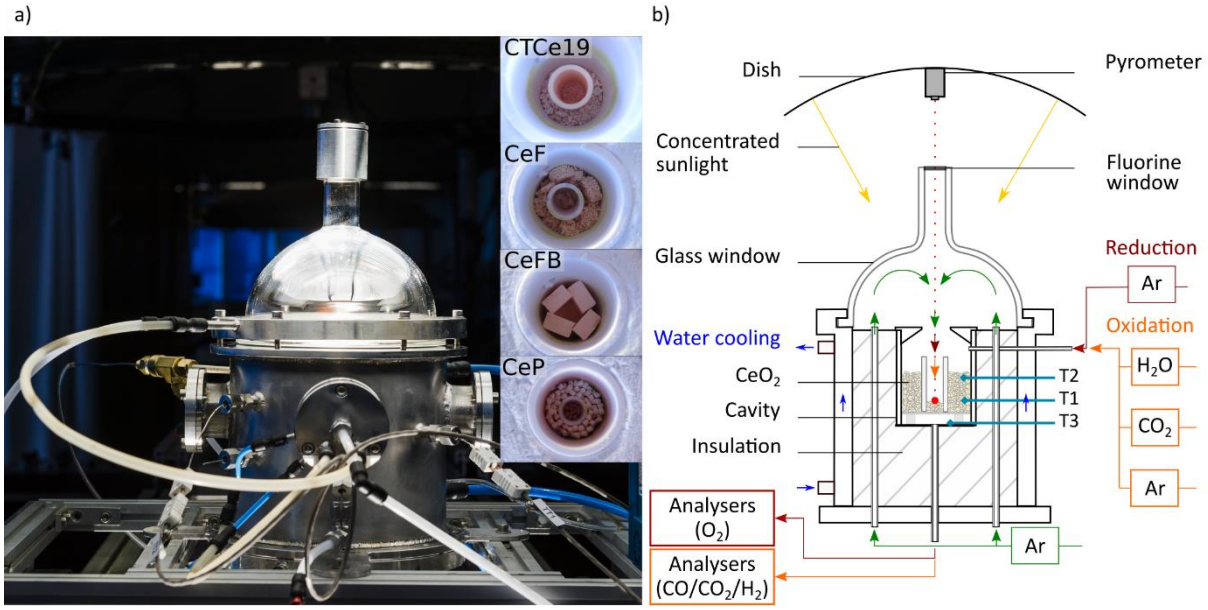

Figure 4-3: a) Photograph of the solar reactor, image inserts on the right show CTCe19, CeF, CeFB and CeP (from top to bottom) inside the alumina cavity and b) schematic illustration of the solar reactor, red arrows represent the gas flow during the reduction step, orange arrows the gas flow during the oxidation step, green arrows the Ar flow injected during both steps to protect the glass window and sweep the cavity, and blue arrows the water-cooling

4.3 Results and discussion

4.3.1 Redox activity characterization

Thermogravimetric analysis (TGA) was first performed to study the redox activity of the reactive materials before their integration and performance evaluation in the solar reactor. The amount of O_2 and CO produced in the TGA are in line with the typical values reported for ceria powders [36, 37]. The O_2 and CO amounts produced in the TGA are similar for all the investigated materials, in the range of 47-53 µmol/g and 83-99 µmol/g, respectively (Figure 4-4 and Table 4-2). The re-oxidation extent is above 84% in all cases (except for CeP). The first cycle of CeP is suspicious as the reduction is low and the mass uptake started even before the CO_2 injection. It suggests that part of the O_2 released during the reduction was trapped in the material structure, inducing a high local oxygen partial pressure at the reactive surface impeding

further reduction, and this oxygen was reincorporated just after the temperature decrease. Thus, the first cycle in TG analysis of CeP was not taken into account.

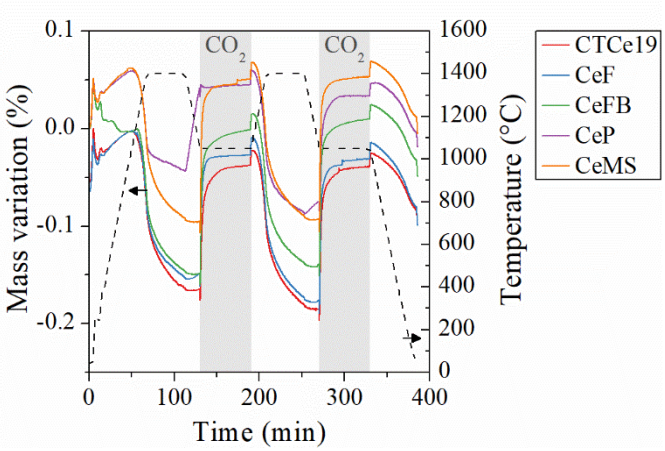

Figure 4-4: Reduction and re-oxidation profiles of CeFB, CeF, CTCe19, CeP and CeMS determined by TGA, along with the temperature profile (dashed line)

Table 4-2: O_2 and CO produced during TGA along with the non-stoichiometry extents (δ), re-oxidation yields and peak production rates

	Reduction step			Oxidation step		
Cycle #	**O_2 produced (µmol/g)**	**δ mol/mol**	**Peak O_2 production rate (ml/min/g)**	**CO produced (µmol/g)**	**Re-oxidation yield**	**Peak CO production rate (ml/min/g)**
CTCe19						
1	51	0.018	0.084	86	84%	0.652
2	51	0.018	0.079	98	96%	0.843
CeF						
1	47	0.016	0.087	83	88%	0.908
2	53	0.018	0.087	99	93%	1.042
CeFB						
1	47	0.016	0.086	99	100%	1.021
2	49	0.017	0.086	99	100%	1.044
CeP						
1	32	0.011	0.076	56	88%	0.069
2	46	0.016	0.084	74	80%	0.422
CeMS						
1	49	0.017	0.080	96	98%	0.782
2	50	0.017	0.080	99	99%	0.806

4.3.2 Materials tested in fixed bed tubular solar reactor

The reducibility and H_2O-splitting ability of CeO_2 samples were assessed via successive thermochemical cycles in the solar reactor under real solar irradiation conditions. Both the O_2 and H_2 rate evolutions, as well as the measured temperatures (inside the reactant $T_{material}$ and at the tube external wall T_{pyro}), are shown in Figure 4-5 to 4-7. The temperature of the reduction step was typically ~1400 °C, and was controlled by adjusting the shutter opening in response to the dynamic variations of the DNI owing to the diurnal transient evolution, or to instabilities resulting from the passage of clouds. The O_2 production rate depends on the heating rate, and is highly sensitive to small temperature changes, which thus denotes that it is controlled mainly

by the heat transfer rate. It features a broadened pattern (the total duration of O_2 release was ~30 min). The release of O_2 started at about 1000 °C, the O_2 concentration increased with temperature and a peak concentration was measured when approaching the temperature set-point. In contrast, the H_2 production rate exhibits a sharpened peak as soon as H_2O is injected and then the H_2 production decreases steadily (the total peak duration is typically ~10 min). This is related to the fact that the reoxidation reaction started promptly after steam was injected in the reactor at the desired temperature, while the O_2-releasing reaction occurred continually during sample heating and the reduction began at a low temperature (~1000 °C) with a slow kinetic rate. The other reason is associated with the different main governing mechanisms. The O_2-releasing reaction proceeds via diffusion of O^{2-} ions inside the solid structure and is heat transfer limited, whereas the H_2-generation reaction occurs by rapid surface reaction followed by internal gas diffusion through the porous structure. Two serial steps are involved: reaction at the surface, and diffusion of oxidant species within the bulk of the oxide.

Table SD-1 summarizes the calculated O_2 and H_2 yields obtained by integrating the production rate versus time profiles as well as thermochemical cycle conditions, including both the reduction and oxidation temperatures, the Ar and H_2O gas flow rates and mean DNI measured for each cycle.

In the case of CTCe17 (Figure 4-5), two sets of data were obtained using different sample amounts (day 1, 7.88 g; day 2, 8.94 g). During the first cycle, in day 1, the heating was stopped at ~ 1330 °C. The oxygen production of this initial cycle was only 27 µmol per g of ceria, and the corresponding H_2 peak rate was 0.6 mL min^{-1} g^{-1}. Once the cycle was repeated, the amount of oxygen released during the reduction step at 1400 °C was 75 µmol g^{-1}, corresponding to a reduction yield of 5%, which is in line with data reported previously for pure ceria synthesized by coprecipitation of hydroxides [99]. The reduction is a thermally activated process that proceeds with continuous oxygen disincorporation from the oxide lattice as the temperature is increased. The reduction rate (O_2 evolution) thus immediately decreased when the temperature dropped. Concerning the reoxidation step, the reduced CTCe17 material totally reacted with steam with a fast reaction rate. In addition, the temperature during oxidation step influenced the reoxidation rate, as expected. The lower the temperature, the higher the H_2 production rate (however, the H_2 production yield is not affected significantly, as shown in Table SD-1). This can be explained by thermodynamic limitations, i.e., the exothermic reaction is not favored by a temperature increase, in agreement with the results of chapter 3.

The theoretical maximum amount of oxygen released per gram of ceria (corresponding to the total reduction of Ce^{4+} to Ce^{3+}) is 1.45 mmol, and the maximum theoretical H_2 production is 2.9 mmol g^{-1}. During the reoxidation step at 1050 °C, the maximum H_2 production was 162.3 µmol g^{-1} (5.5% of the theoretical value). The increase in steam flow rate from 0.21 to 0.25 NL min^{-1} had no significant effect on the oxidation extent, as anticipated, since the H_2 yield is closely related to the reduction extent.

The thermochemical performance of CTCe19 (10.06 g, 9 cycles) follows a similar trend (Figure 4-6), although the material appears to be slightly less reactive than CTCe17. Indeed, the mean

oxygen production was merely 51 ± 5 µmol per g at 1400 °C, i.e., ~30% decrease, which corresponds to an average H_2 production yield of 116 ± 10 µmol g^{-1} (peak H_2 rate of 1.3 mL min^{-1} g^{-1}). When the reducing temperature was increased by merely 50 °C up to 1450 °C, the amount of oxygen released reached 89 µmol g^{-1} (~75% increase compared to the value obtained at 1400 °C). Without surprise, the H_2 peak rate reached a maximum of ~1.6 mL min^{-1} g^{-1} after oxidation at below 1050 °C. As also noticed for CTCe17, increasing the oxidation temperature from 950 °C to 1150 °C resulted in a decrease in H_2 yield from 114.1 to 101.2 µmol g^{-1} after reduction at 1400 °C (Table SD-1). This is because the peak rate of H_2 production increased when decreasing the oxidation temperature below 1150 °C, from 0.55 to 1.12 mL min^{-1} g^{-1} (Figure 4-6, day 2, cycles N° 4,5,6), while the oxidation duration was shortened (as evidenced by the sharpened H_2 production peak).

Regarding the polyurethane templated ceria CeF (12.07 g), five consecutive thermochemical redox cycles were carried out, and results are shown in Figure 4-7. After reduction at 1400 °C, the mean oxygen specific yield was 50 ± 4 µmol g^{-1}, i.e., similar to that obtained for CTCe19. In contrast, this value compares to 29 ± 5 µmol g^{-1} obtained for the foams produced and tested in [165]. This is related to microstructural features, as shall be discussed later. Again, the increase of reduction temperature from 1400 to 1450 °C had a significant effect on the oxygen yield, which rose from 50 to 72 µmol g^{-1} (44% increase), whereas the H_2 yield reached a maximum of 147 µmol g^{-1} (corresponding to a production rate of ~0.7 mL min^{-1} g^{-1}). The oxidation kinetics was also made faster by decreasing the temperature of steam injection from 1150 to 950 °C, in accordance with thermodynamic predictions. The superior reactivity of the cork-structured ceria when compared to ceria foam (CeF) is demonstrated by the significantly enhanced H_2 production rate (typically 1–1.4 mL min^{-1} g^{-1} for CTCe19 vs. 0.6–0.8 mL min^{-1} g^{-1} for CeF). Taking into account the peak H_2 production rate for CTCe19 (and high heating value of H_2 = 286 kJ mol^{-1}), the maximum $\eta_{solar\text{-}to\text{-}fuel}$ was estimated to be 0.34% (for 1 kW solar thermal power input absorbed in the solar reactor), while average efficiencies were ~0.28% for CTCe17 and ~0.21% for CeF materials. These values for a real lab-scale on-sun reactor system are quite low, given the low amount of processed ceria in the solar tubular reactor and could thus be enhanced by both increasing the oxide mass loading and up-scaling the reactor (inherently reducing heat losses). The estimated efficiencies derived from experimental studies are scarce to date, but of major importance to provide insights into the performance of real on-sun reactor systems. They usually differ from the projected ideal efficiencies obtained from thermodynamic analyses (in which kinetic limitation aspects are bypassed) that predict the maximum efficiencies theoretically achievable under various assumptions (operating conditions, heat recovery from gas and solid phases, …) [229]. The local pO_2 can also be higher around the sample at the particle surface due to the O_2 release, which hinders oxygen removal from the crystal lattice. This suggests that mass transfer limitations may play an important role on the rate of ceria reduction at this temperature. The evolved H_2/O_2 ratio is 2.1 ± 0.2, *i.e.* close to the stoichiometric value. In some cases, this ratio is higher than 2, because the reduced species that did not react during a previous oxidation at a higher temperature can be oxidized at a lower temperature. These results point out the superior reactivity of the cork-templated

ceria, suggesting that the material microstructure does indeed affect its redox performance. This is also shown by the average H_2 and O_2 yield values over three comparable cycles (2–4) for CTCe17, CTCe19 and CeF depicted in Figure 4-8.

These results are in line with those published previously for solar driven thermochemical splitting of CO_2 using cork-derived ceria ecoceramics and polymer replicated ceria foams [165]. For three comparable cycles at 1400–1050 °C, the total CO yield was 402.0 µmol g^{-1} for the cork ecoceramic (average = 134.0 µmol g^{-1} per cycle), and only 210.7 µmol g^{-1} for the replicated foam (average = 70.2 µmol g^{-1} per cycle) [165].

CTCe17 was produced by the same method as the samples previously tested for CO_2 splitting [165], i.e. using water as the solvent for cerium nitrate impregnation, and operating four impregnation cycles [223]. However, using so many cycles was found to negatively affect the final microstructure of the ecoceramic, as cerium nitrate began to fill the cork carbon template cells. This decreased the porosity of the sintered ecoceramic, a vital factor for solar thermochemical fuel production. Therefore, CTCe19 sample was prepared by reducing the number of impregnations cycles to just one, and by using acetone as a solvent. Acetone was found to better wet the hydrophobic carbon surface, and to quickly evaporate. Another motivation for using this route was to reduce the time and energy consumption during impregnation. Of course, acetone is a less sustainable/green solvent compared to water but it could be collected (condensed/captured in the rotary evaporator) and reused.

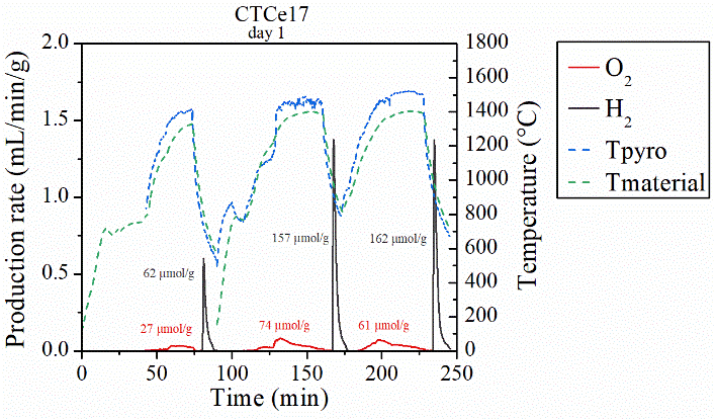

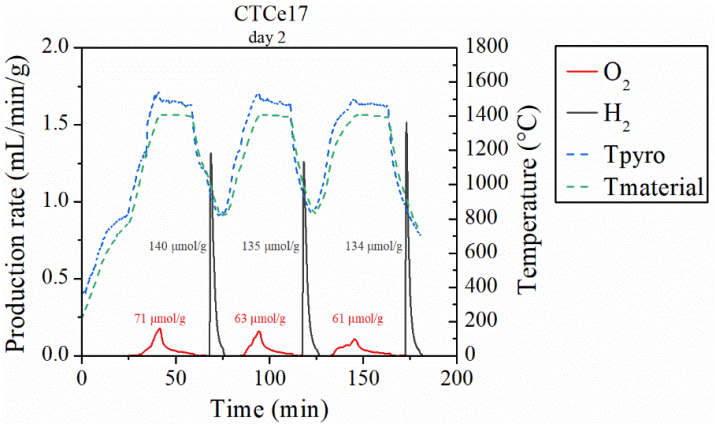

Figure 4-5: Time dependent solar thermochemical reduction and reoxidation profiles for CTCe17

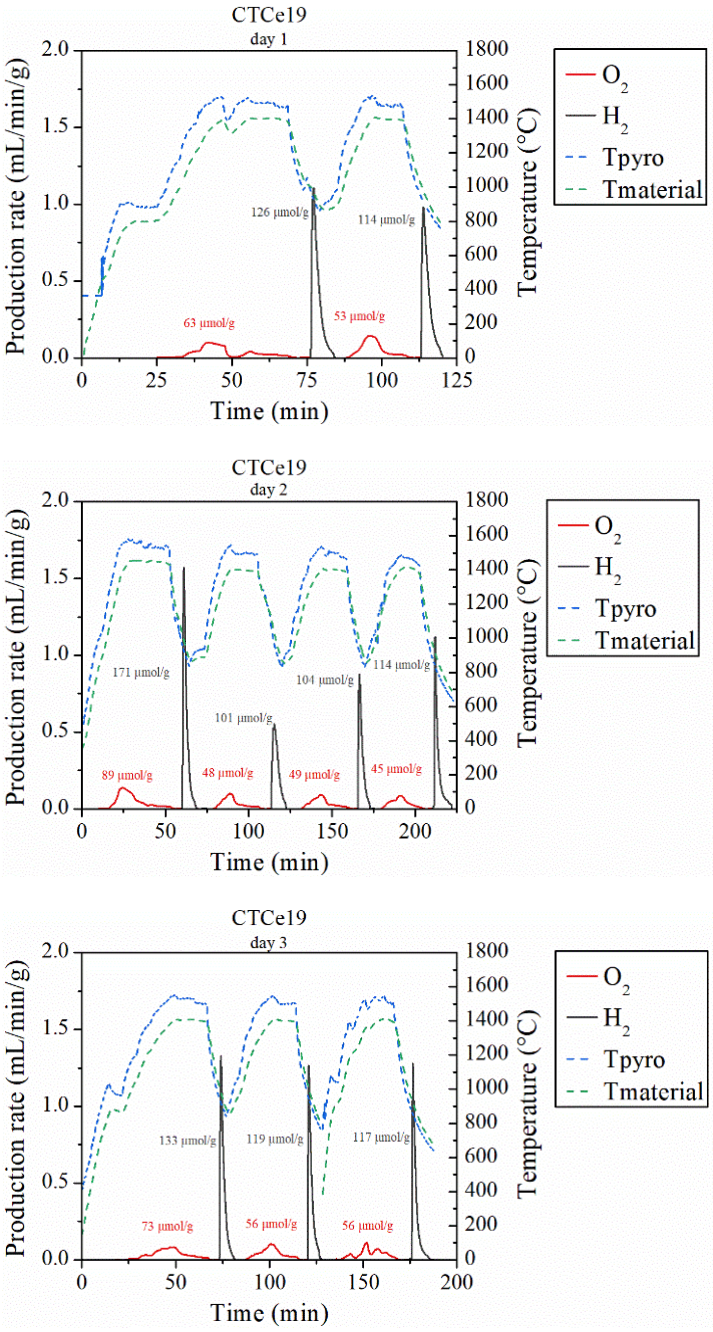

Figure 4-6: Time dependent solar thermochemical reduction and reoxidation profiles for CTCe19

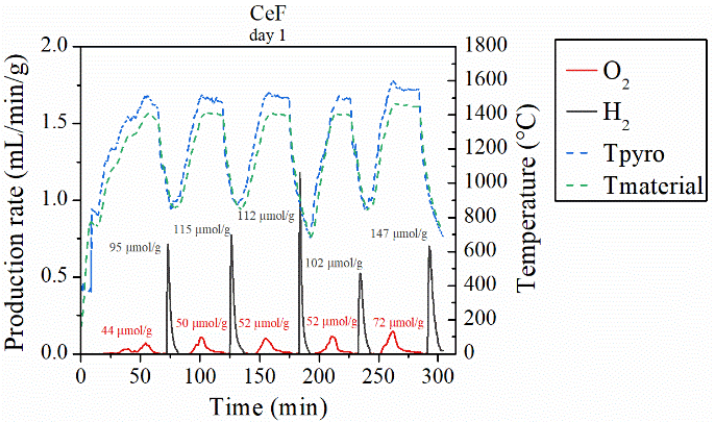

Figure 4-7: Time-dependent solar thermochemical reduction and reoxidation profile for CeF

A comparison of materials performance show that the "greener" synthesis route, using water as a solvent, produced a material (CTCe17) with superior performance in comparison with the quicker, but less sustainable, route using acetone (CTCe19). The results in Table SD-1 clearly demonstrate that CTCe17 was better at producing H_2 than CTCe19. For cycles #2–6, all at 1400–1050 °C, CTCe17 produced a total H_2 yield of 728.4 µmol g^{-1} (average = 145.7 µmol g^{-1}), compared to only 587.9 µmol g^{-1} for CTCe19 (average = 116.1 µmol g^{-1}). The first cycle for CTCe17 was ignored as ceria was not optimally reduced. The only cycle in which CTCe19 outperformed CTCe17 was cycle #3, in which CTCe17 produced 162.3 µmol g^{-1} at 1400 °C and CTCe19 produced 171.1 µmol g^{-1} at 1450 °C. As anticipated, the O_2 yield for this cycle was also higher for CTCe19 (88.9 µmol g^{-1} vs. 71.5 µmol g^{-1} for CTCe17), in view of the fact that raising the temperature by merely 50 °C (from 1400 to 1450 °C), has a noticeable effect on the reduction extent. Therefore, the highest H_2 yield was obtained for this particular cycle where CTCe19 was more reduced than in any other cycle (a similar trend was observed in cycle #5 for CeF). The average values of H_2 and O_2 production for CTCe17 and CTCe19 over cycles #2–4 are contrasted in Figure 4-8. The greener and more sustainable aqueous synthesis route should be clearly recommended for any future ceria ecoceramics production. It should be noted that despite the unavoidable variations between the cork powder batches (natural product from various trees of different ages and geographical locations) used in this work and for other CO_2 splitting investigations ([165, 224]), similar trends are observed. In all cases, cork ecoceramics offer significantly higher fuel and O_2 productions in comparison with replicated ceria foams.

Basically, the rationale for the increase in both CO and H_2 yields observed for the cork-templated ceria materials compared to the ceria foams counterparts, is related to the small cell size of the cork combined with its interconnected pore system. This result in larger geometric area being exposed to the gas stream, and facilitating the transport of gas phase species, thereby promoting a more effective oxidation of ceria under flowing CO_2 or steam.

Table 4-3 compares the data obtained in the present study (H_2O splitting by solar heating), with those reported in the literature under similar conditions. It is noteworthy that the comparative values in this table refer to studies performed by TG analysis and tests carried out using conventional heating sources (with one exception for Xe-arcs). Clearly, CTCe17 performs better than all other materials reduced at 1400 °C. A ceria felt made of compressed ceria fibers

offered superior H_2 yields when reduced at a higher temperature of 1450 °C and oxidized at a lower temperature of 900 °C [36]. This felt also overpassed the performance of a CTCe17-like cork-derived ceria for thermochemical CO_2 splitting [230]. However, as pointed out in a review discussing the effects of materials morphology in this process [218], such a dense 2D material made of compressed fibers could hardly be extended to 3D structures able to convert sizeable quantities of water to H_2. In addition, considerable degradation of the CeO_2 fibrous felt after exposure to high-flux radiation was also observed [67]. Furthermore, the low thermal conductivity of the ceria felt (1.3 W m^{-1} K^{-1}, at 1000 °C) resulted in undesired temperature gradient across the felt, so that a gradient in the extent of CeO_2 reduction should be assumed. This indicates that macroporous ceria structures (e.g. reticulated foams, cork-templated ecoceramics) enabling both penetration and volumetric absorption of concentrated solar radiation ought to be used in order to obtain a homogeneous temperature distribution.

The best results in Table 4-3 were obtained with a porous monolith derived from ceria powder and 30 wt% starch (monolith sintered at 1350 °C/5 h, then annealed at 1500 °C/3 h, offering 70% porosity and a specific surface area of ~0.1 m^2 g^{-1}) [51]. However, the cycling between 1500 °C and 800 °C corresponds to a very wide temperature swing of 700 °C, compared to the 350 °C used in the present study. The H_2 productivity was very high in the first cycle (8.5 mL g^{-1}) and decreased to ~6 mL g^{-1} after 100 cycles, and the H_2 production rate likewise fell from ~3.2 mL min^{-1} g^{-1} to ~1.5 mL min^{-1} g^{-1} after 100 cycles. Beyond H_2 production yields, material stability is an essential criterion for a viable thermochemical process. The decrease in reaction rate was related to an increase in grain sizes within the porous monolith, from ~5 µm to 15–20 µm after >100 cycles at 1500 °C [51]. This observation points out the need to decrease the ceria reduction temperature (e.g. at 1400 °C, as in this work) to avoid undesirable losses in fuel production.

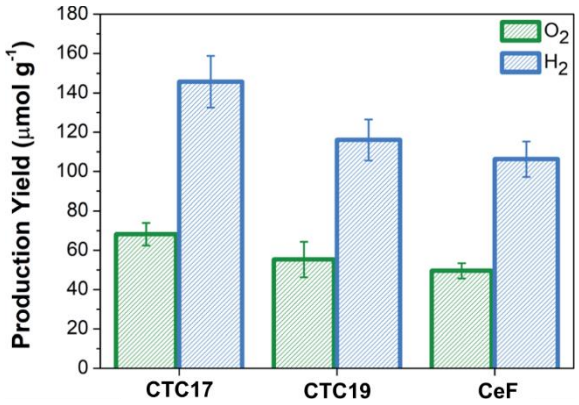

Figure 4-8: Comparison of average O_2 and H_2 production yields over cycles #2–4 for CG17 (cork ecoceramic with aqueous impregnation), CG19 (cork ecoceramic with acetone impregnation) and CeF (polymer replicated foam) after reduction at 1400 °C.

Table 4-3: Experimental H_2 yields for various materials used in thermochemical H_2O splitting cycles.

Materials	Structure	T_{red} (°C)	T_{ox} (°C)	Heating method	H_2 Yield (mL/g)	Ref.
$CeO_{2-x}Fe_2O_3$ (Ce:Fe = 8.9:1.1)	Powder	1400	1000	IR-image heating	1.9	[109]
$NiFeO_4$	Powder	1500	1000	IR-heating	3.4	[109]
CeO_2−Fe_2O_3	Powder	1400	1000	IR-heating	2.26	[75]
YSZ−Fe_3N_4	Powder	1500	1000	IR-heating	1.77	[75]
$Ce_{0.75}Zr_{0.25}O_{2-\delta}$	Powder	1450	1045	TGA	5.4	[36]
CeO_2	Powder	1400	1050	TGA	2.6	[96]
CeO_2	Powder	1400	1000	IR-heating	0.33	[75]
CeO_2	Porous Monolith	1500	800	TGA	8.5±0.6	[51]
CeO_2	Felt	1450	~900	Xe-arcs	4.18	[67]
CeO_2	Monolith	1500	500	IR-heating	3.19	[77]
CTCe17	3DOM	1400	1050	Solar-heating	3.3	This work
CTCe19	3DOM	1400	1050	Solar-heating	2.6	This work
CeF	Foam	1400	1050	Solar-heating	2.5	This work

4.3.3 Materials tested in direct heating solar reactor

In order to study the redox activity of the investigated materials in the solar reactor, each material was submitted to consecutive thermochemical cycles with different operating parameters (Figure 4-9). The goal of these redox cycling solar experiments was to demonstrate the solar process reliability, controllability and suitability for operation with the selected materials under realistic high flux solar irradiation, i.e. under conditions representative of a real process. The most relevant parameters were also investigated with the aim of optimizing the thermochemical redox performance. Changing the testing parameters such as inlet gas flow rates/compositions was also needed to show the performance sensitivity to the process conditions. Such experiments were also useful to demonstrate the stability of materials and to identify the most suitable ceria structures for operation in a solar reactor under real cycling conditions. The CTCe19 material was subjected to 16 cycles, corresponding to 20 h of successive cycles under continuous on-sun operation (tests performed during 4 consecutive days). Both CeF and CeFB materials underwent 7 cycles, equivalent to ~10 h (achieved during 2 consecutive days) of continuous on-sun operation (i.e. solar reactor continually heated with highly concentrated sunlight, except during night interruptions). Finally, 11 and 19 cycles were performed with CeP and CeMS materials respectively, which corresponded to 18 The operating conditions used for each cycle are summarized in Table SD-2. The highest peak fuel production rate obtained in this study reached 9.5 mL/g/min with CeP (with reduction at ~1400 °C under atmospheric pressure and oxidation under 100% CO_2 starting at 950 °C). In comparison, other studies [2, 46, 209] achieved a peak production rate of 1.2 mL/g/min using ceria foams cycled with more favorable operating conditions (reduction step at 1500 °C under 10 mbar). Moreover, the highest peak fuel production achieved with CTCe19 reached 3.1 mL/g/min whereas a previous study [165] using cork-templated ceria granules in a tubular packed-bed solar reactor reported a CO peak production rate of 1.9 mL/g/min under similar conditions (reduction step at ~1400 °C and atmospheric pressure). Clearly, an improvement of the peak fuel production rate was obtained in this work in comparison with previous reported

data, showing the relevance of the studied materials integrated within the developed solar reactor.

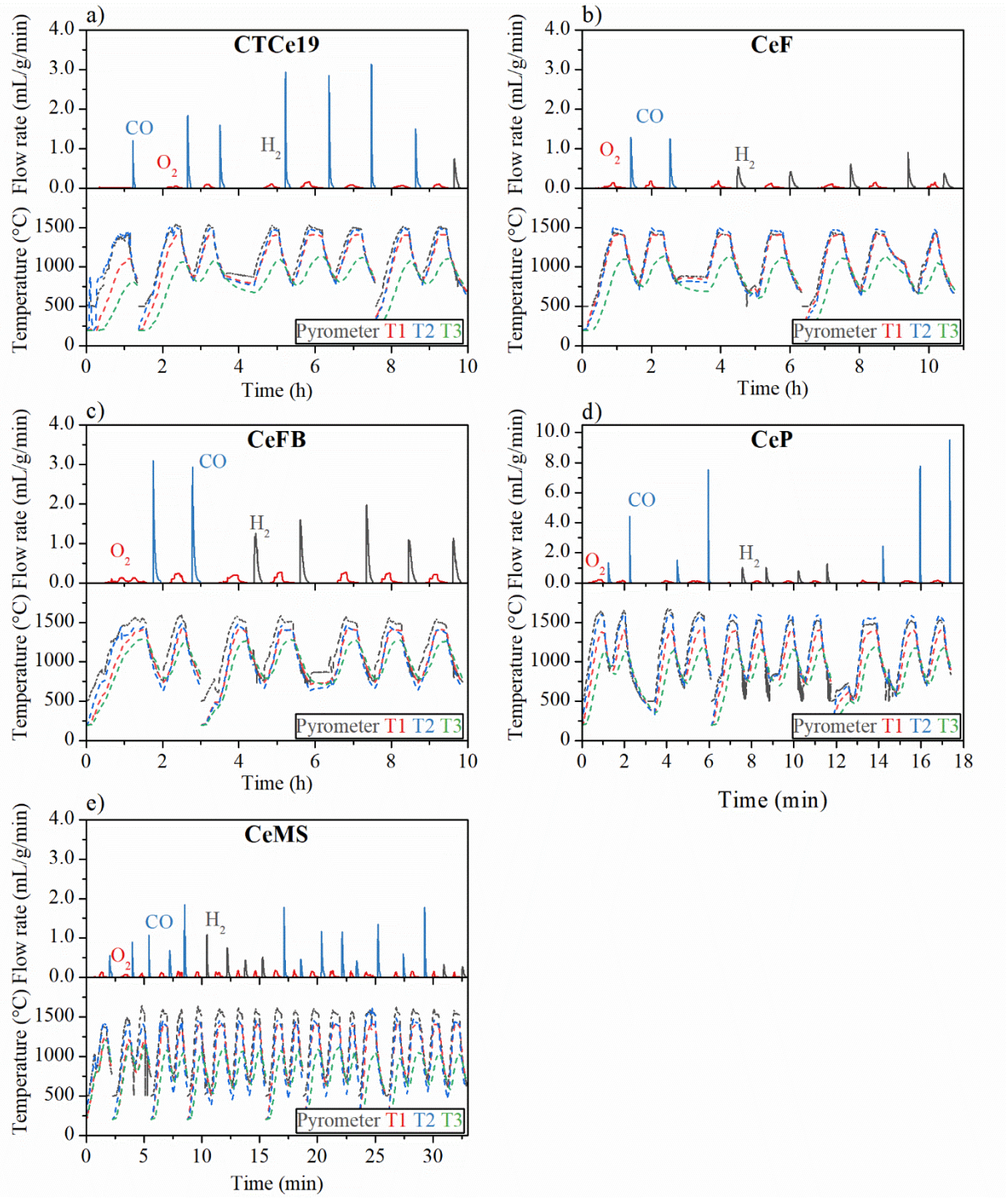

Figure 4-9: O_2 and fuel production rates during the performed cycles along with the temperature profiles for a) CTCe19 (16 cycles), b) CeF (7 cycles), c) CeFB (7 cycles), d) CeP (11 cycles) and e) CeMS (19 cycles). T1, T2 and T3 are the temperatures of the sample interior, sample surface and base of the reactor.

For CTCe19 and CeF, the O_2 and CO amounts produced in the solar reactor were 28% and 36% higher than those obtained in TGA, caused by the temperature gradient in the cavity (meaning higher temperatures in the upper part of the cavity, as suggested by T2 and $T_{pyrometer}$ being higher than T1). For CeFB, the O_2 and CO production yields obtained in the solar reactor were three

times higher than those obtained in TGA. The superior redox activity of CeFB over the other tested materials can be related to the important temperature gradient measured through this material in the reactor cavity (150°C gap between the pyrometer and T1). Although, the reference temperature was maintained at 1400 °C at T1, the part of the reactive material situated just above reached a much higher temperature due to the poor thermal conductivity of the fiber boards. Thus, the reactive material situated above T1 achieved larger reduction extent due to the higher temperature reached. The averaged oxygen non-stoichiometry reached by the whole material was thus higher (maximum δ~0.055). In addition, the fiber boards were directly exposed to the high flux solar radiation inside the cavity (no central confiner tube was used for CeFB, as shown in Figure 4-3), thus increasing dramatically the temperature of the material surface. Consequently, the O_2 and CO production yields of CeFB were higher than those of CTCe19 and CeF due to the higher reduction temperature reached by CeFB.

In order to compare the thermochemical performance of the reactive materials, a reference cycle (characterized by a reduction step at 1400 °C under Ar at atmospheric pressure, and an oxidation step with temperature decrease between 1050-850 °C in 25 mol% of CO_2) was performed for CTCe19 (cycle #12), CeF (cycle #1), CeFB (cycle #1), CeP (cycle #3) and CeMS (cycle #4) as presented in Figure 4-10. The oxygen and fuel production yields were much higher for CeFB, owing to the higher reduction temperature attained by this reactive material. For this cycling condition, the highest CO production rate (3.1 mL/g/min) was achieved for CeFB. All the materials presented a high re-oxidation yield (>87%).

As defined in the previous chapter, the instantaneous solar-to-fuel conversion efficiency can be calculated as follow:

$$\eta_{solar-to-fuel} = \frac{\dot{n}_{fuel} HHV_{fuel}}{P_{solar}} \tag{47}$$

where $\dot{n}_{fuel}$ represents the fuel production rate, HHV_{fuel} the high heating value of the fuel and P_{solar} the solar power input. The cycle efficiency (η_{cycle}) is defined in equation 48, to quantify the efficiency related to the actual amount of cycled ceria and to bypass the heat losses inherent to the prototype scale reactor:

$$\eta_{cycle} = \frac{n_{fuel} HHV_{fuel}}{\left(Cp_{\mathrm{CeO_2}} \Delta T + \Delta H(\delta_f)\right) n_{\mathrm{CeO_2}}} \tag{48}$$

where n_{fuel} represents the fuel production yield in the cycle, $Cp_{\mathrm{CeO_2}}$ the specific heating value of ceria, ΔT the temperature swing between the reduction and the oxidation steps, $\Delta H(\delta_f)$ the reduction enthalpy for final stoichiometry δ_f and $n_{\mathrm{CeO_2}}$ the amount of reacting ceria. The reduction enthalpy was calculated as a function of the non-stoichiometry extent, according to a procedure described elsewhere [196]. All the calculated efficiencies for the investigated materials are reported in Table 4-4. Due to its high fuel production rate, CeFB provided the highest instantaneous solar-to-fuel conversion efficiency. The low efficiency values are related to the low amount of processed reactive material that induced relatively small CO production

yields. Consequently, increasing the reactor scale associated with sensible heat recovery systems should drastically increase the overall efficiency to meet the requirements for an industrial implementation [47]. Regarding cycle efficiency, CeFB material also achieved the highest value (3.0 %) among the tested materials. The higher cycle efficiency of CeFB, compared with CTCe19, CeF, CeP and CeMS, is attributed to the high reduction extent reached by the reactive material arising from the higher thermal gradient (due to the poor thermal conductivity of this structure and the absence of confiner tube, thus changing the heating conditions along the height). The optimization of the solar-to-fuel efficiency is important for a future industrial process implementation as a high efficiency decreases the production cost of solar fuels [231].

Table 4-4: Cycle efficiency and instant solar-to-fuel energy conversion efficiency for each investigated ceria structure

Materials	η_{cycle}	$\eta_{inst,solar\ to\ fuel}$
CTCe19	1.18%	0.64%
CeF	1.28%	0.71%
CeFB	3.05%	1.45%
CeP	1.93%	1.36%
CeMS	1.71%	0.60%

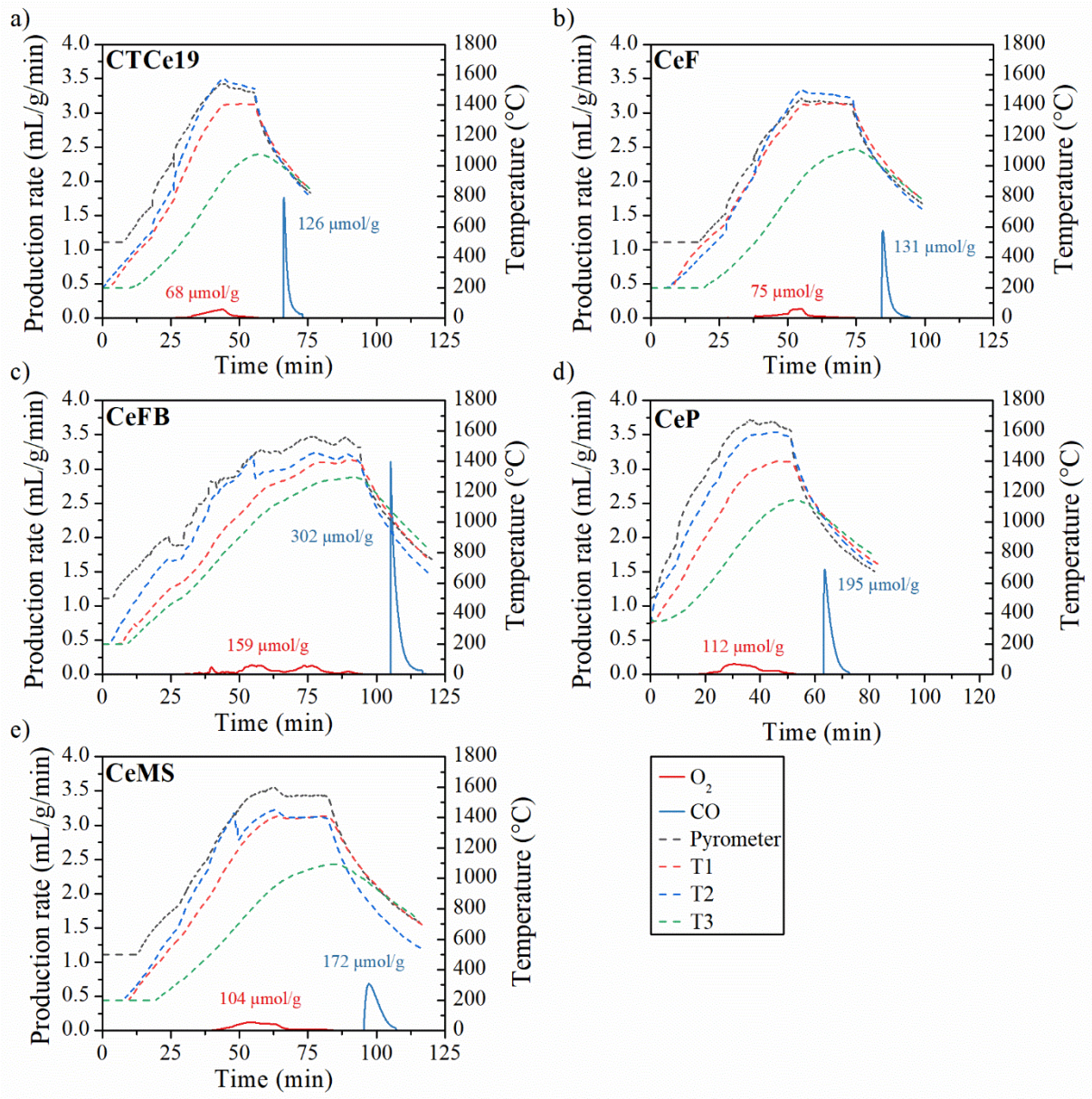

Figure 4-10 Thermochemical cycles at atmospheric pressure, $T1_{red}$=1400 °C and $T1_{ox}$=1050 °C-850 °C with 25mol% CO_2 during the oxidation step for a) CTCe19 (cycle #12), b) CeF (cycle #1), c) CeFB (cycle #1), d) CeP (cycle #3) and e) CeMS (cycle #4)

Table 4-5 summarizes the total mass of ceria loaded in the reactor, the number of cycles performed during the corresponding continuous on-sun operation along with the total gas amounts produced with the studied reactive materials. Figure 4-11 plots the oxygen production yields (squares) and the fuel production (bars) depending on the reduction temperature. The cycles performed under low pressure (e.g. 0.110 bar, cycle #5 for CTCe19) during the reduction step are also indicated (hollow squares). A low pressure during the reduction step improved both the reduction extent (δ up to 0.032) and the fuel production yield (190 µmol/g for CTCe19), as previously reported [76, 205]. In total, each of the five materials produced 4.30 L of H_2 and 7.25 L of CO, over 26 and 34 cycles, respectively. No significant performance decline with increasing the number of cycles (within the range investigated) was noticeable for CTCe19, CeF and CeP, revealing their promising thermochemical stability and resistance to

sintering under the harsh operating solar conditions. A long-term investigation of the materials stability and performance during extended on-sun testing periods for hundred cycles is still required to validate their suitability for real on-sun operations. In contrast, CeFB showed a strong performance decline with a drop in fuel production from 302 µmol/g to 230 µmol/g after 7 cycles. As stated before, the CeFB material reached a high temperature in its upper part leading to structure densification. The sharp decrease in fuel production can thus be explained by a densification of the reactive bulk fibers, which is also due to the thermal gradient arising from low thermal conductivity, and high optical thickness of the material. A similar decrease of reactivity due to sintering was previously observed with ceria felts [67]. Consequently, ceria fibers do not seem suitable for thermochemical cycles because of their poor thermal stability and low resistance to sintering, despite their ability for high fuel production. In addition, the radiative opacity of the fiber bulk might hinder its application when being directly irradiated by solar energy and, therefore, indirect heating may be more favorable.

Regarding CeMS material, a decline of its thermochemical performance was observed: for example, the CO yield dropped from 172 µmol/g to 114 µmol/g between cycles #4 and #14 for similar operating conditions (reduction at ~1400 °C under atmospheric pressure, oxidation with 25% CO_2 starting at ~1050 °C). Such performance decrease could result from either material sintering and/or a loss of reactive material in the solar cavity. SEM observations of the reactive particles after thermochemical cycles confirmed their sintering (see §3.4). In addition, as the microspheres are small (~300 µm) and spherical, their flowability is high and the particles tend to pass through the insulation interstices at the bottom of the cavity and thus cannot reach sufficient temperature to be reduced. Indeed, significant amounts of particles were found in interstices when the reactive material was removed from the reactor, providing credit to this hypothesis. Moreover, after cycle #14, a layer (~5 mm thick) of agglomerated particles was observed in the upper part of the cavity. Thus, the reactive CeMS material was removed and the agglomerated particles were crushed for being separated and reintroduced in the cavity (with a new global mass of 59.5388 g). An additional top-layer (~2 mm thick) of alumina particles was added to avoid direct exposure of CeMS to high-flux thermal radiation. After cycle #14, no variation of the production was observed, revealing that the redox activity of the microspheres was not significantly altered.

It can also be underlined that the few particles of CeP and CeMS which reacted with the alumina tube in the upper part of the cavity (directly irradiated by concentrated sunlight), led to the formation of $CeAlO_3$ (see Figure SD-5 and Figure SD-6 for further explanations). However, due to the small fraction of the reacted/modified material in both cases, no performance decline attributed to this reaction could be detected.

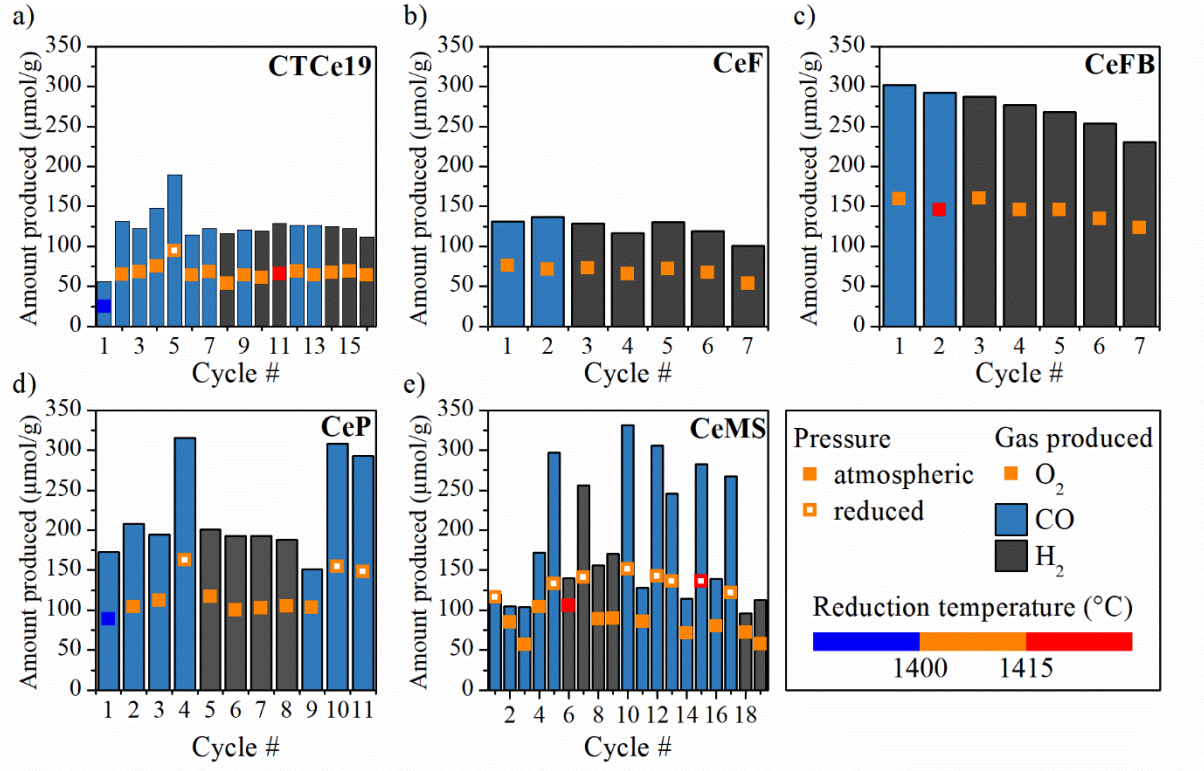

Figure 4-11: O_2 and fuel production yields over cycles for a) CTCe19, b) CeF, c) CeFB, d) CeP and e) CeMS; squares represent the O_2 production amount and bars refer to the fuel production. The reduction temperature is indicated by the color of the square.

Table 4-5: Ceria mass loaded in the reactor, number of cycles associated with continuous on-sun operation duration along with total O_2, H_2 and CO amounts produced with CTCe, CeF, CeFB, CeP and CeMS materials

	CTCe19	CeF	CeFB	CeP	CeMS
Material mass (g)	25.4096	39.5707	33.321	62.9846	62.2449
Number of cycles	16	7	7	11	19
Continuous on-sun operation (h)	20	11	10	18	32
Total O_2 amount produced (L)	0.50	0.42	0.76	1.40	2.67
Total H_2 amount produced (L)	0.41	0.53	0.98	1.09	1.29
Total CO amount produced (L)	0.72	0.24	0.44	2.32	3.54

4.3.4 Microstructural characterization

The morphology of the redox materials that were directly exposed to the high-flux solar irradiation plays a crucial role in their thermochemical performance. Bearing in mind that these materials were cycled at temperatures as high as 1400 °C, and subjected to steep temperature gradients, it is of upmost importance to analyze the microstructure of the samples before and after use in correlation with their relative performance and potential evolution.

The BET-specific surface area before cycling, measured by N_2 adsorption, was 0.31, 0.25, and 0.50 $m^2\ g^{-1}$ for CTCe19, CeF and CeP, respectively [221]. This would explain the slightly higher H_2 yields obtained for CTCe19 compared to its CeF counterpart. The specific surface

area of CeF and CeFB measured after cycling was 0.19 and 0.43 m^2 g^{-1}, respectively, in line with the high intrinsic reactivity of ceria fibers, despite low thermal stability [67, 157]. This can also explain the higher H_2 yield obtained for CeFB compared to its CeF counterpart.

The SEM images of CTCe17, CTCe19 and CeF after thermochemical cycles in the indirectly heated solar reactor are shown in Figure 4-12. Both CTCe17 and CTCe19 exhibit a cork-like microstructure, with cells of ~25 µm in diameter and a cell wall thickness of ~1 µm, despite the grain growth which occurred during their synthesis at 1600 °C (Figure 4-12). No significant differences were evidenced between CTCe17 and CTCe19 (Figure 4-12a–d), except that pore sizes in cell walls were larger for CTCe19 than for CTCe17, explaining the slightly lower reactivity of the former. In contrast, the microstructure of as-sintered CeF shows typical features of ceramic foams produced by the replication method, in particular the hollow nature of the struts seen in Figure 4-12e (indicated by arrows). No significant grain growth was observed for CeF after cycling.

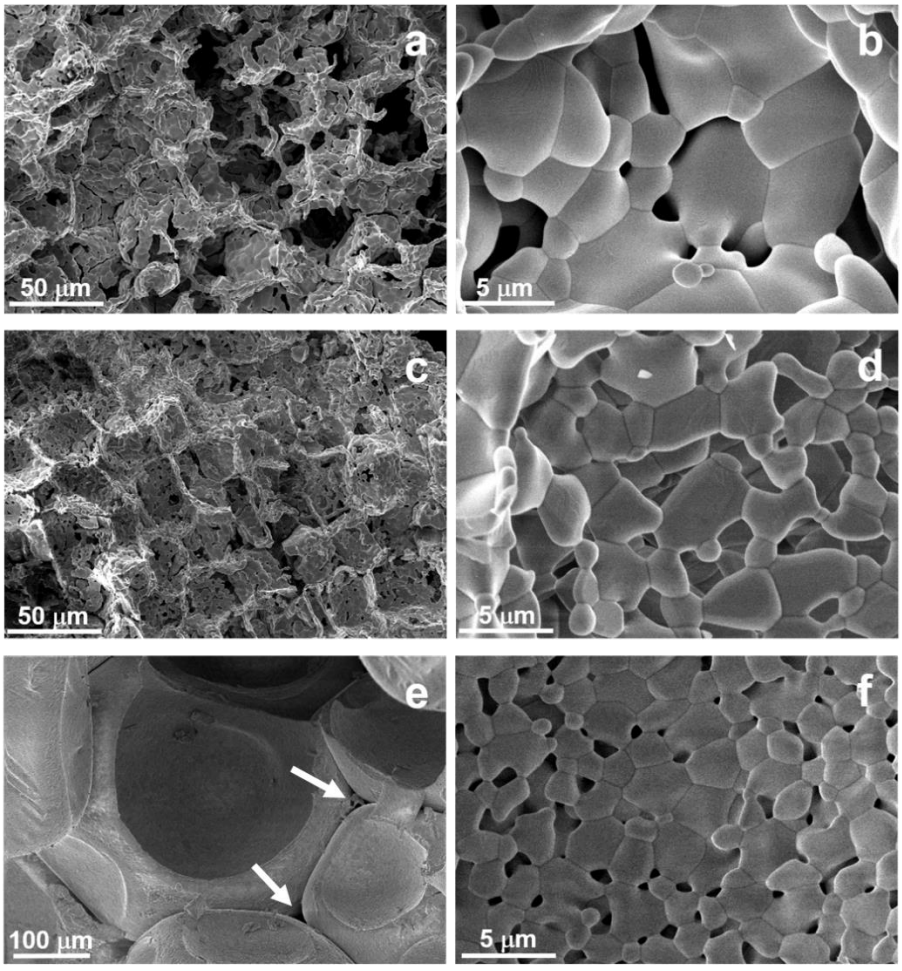

Figure 4-12: SEM micrographs showing the microstructure of CTCe17 (a and b), CTCe19 (c and d) and CeF (e and f) after thermochemical H_2O splitting cycles in indirect heating reactor

The SEM images of the investigated materials before and after thermochemical cycles in the directly heated solar reactor are compared in Figure 4-13. No noticeable change in morphology was observed for the cycled samples. The microstructure of CTCe19 consists of interconnected

closed cells with an average size of 25 µm. Residual pores (typically less than 1 µm), located at triple grain boundaries, remained unchanged after thermal cycling. The overall high stability and attractive fuel production rate of CTCe19 were attributed to the cork template derived microstructure which favors solid-gas oxidation reactions.

A similar microstructure was observed for CeF. However, in this case, the morphology consists of macropores with cell sizes of 575±55 µm, some of which have closed cell walls, and hollow struts with thickness around 50±5 µm containing micropores. These are typical features of ceramic foams produced by the replication technique [159]. The bulk density of the CeF material was 1.03±0.03 g cm^{-3}, which corresponds to an estimated porosity of ~87% when considering a value of 7.65 for the true density of ceria (measured by He pycnometry). Such macroporous cellular materials (such as foams, fiber mats) are defined as materials with high interconnected porosity (>70 vol%). The morphology of pores is mostly regular and the 3D architecture of cellular materials derives from the packing of polyhedral voids (cells) filling the space efficiently. The size of grains in CeF (~ 2 µm) was slightly smaller than in CTCe19, owing to the lower sintering temperature of the former (1450 °C for 30 min for CeF instead of 1600 °C for CTCe19), and hence its limited grain growth. These observations are in line with the recorded O_2 and fuel production yields. As for CeFB, no evidence of fiber degradation could be identified. However, partial shrinkage of the boards after cycling, together with a progressive decrease in H_2 yield over cycles, denoted a densification and loss of redox efficiency for H_2O splitting. The fibers (~ 5 µm in diameter) were arranged in a tangled web. The bulk density of the CeFB material was 0.89 g cm^{-3} and its estimated overall porosity was 88% (considering a value of 7.65 for the true density of ceria, measured by He pycnometry).

The fresh CeP material has grain sizes in the range 3-13 µm. SEM observations evidenced no variation of the material shape and morphology after cycling.

Regarding CeMS material, grain sizes were in the range 0.5-2 µm before cycling. After cycling, the few particles that reacted with the alumina part of the cavity showed a strong increase of their grain sizes in the range of 13-30 µm (Figure SD-7), while the others (the majority) showed a slight increase of their grain sizes (6-9 µm). However, this grain growth and sintering effect alone could hardly explain the progressive decrease of the production yield observed with CeMS over cycles. More consistently, the decline of CeMS performance could also result from the loss of a reactive material flowing out at the bottom of the cavity.

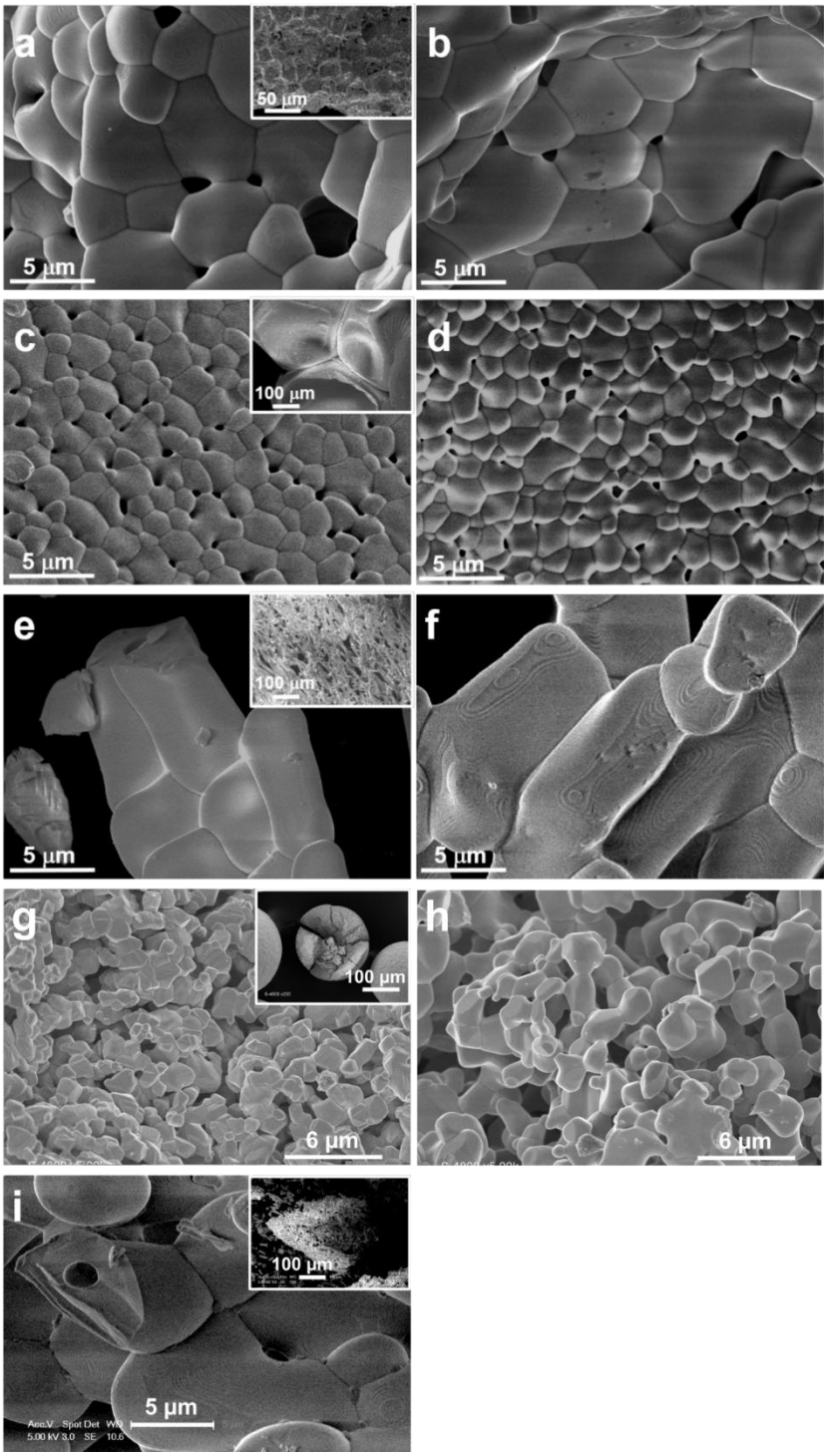

Figure 4-13 : Comparison of representative SEM images of CTCe, CeF, CeFB, CeMS and CeP prior (a, c, e, g, i) and after (b, d, f, h) thermal cycling. Inserts are images taken at lower magnification.

4.4 Conclusion

In this chapter, the thermochemical performance of different ceria structures was compared in indirectly and directly heated packed-bed solar reactors. The performance measured in both reactors were similar (e.g., 63 µmol/g of O_2 and 126 µmol/g of CO in indirectly heated reactor (cycle #1), against 67 µmol/g and 125 µmol/g in directly heated solar reactor (cycle #9) for CTCe19 under similar conditions). However, the solar-to-fuel conversion efficiency was

improved in the directly heated reactor thanks to the higher amount of reactive material being cycled for a similar solar power input. Nevertheless, the indirectly heated solar reactor allowed alleviating sintering issues caused by direct irradiation of the reactive material. In contrast, direct heating avoids inherent heat losses due to intermediate heating via the alumina tube. Therefore, the solar reactor design has to be adapted to the design of the reactive material (individual particles, 3D structures, monoliths…).

A series of reactive ceria materials with different macro/microstructures has been considered, including cork-templated ceria, RPC foam, commercial fiber boards, commercial pellets and microspheres. The ceria fibers yielded the highest reduction extent (averaged oxygen nonstoichiometry up to δ~0.055), thereby leading to superior fuel production yield (above 300 µmol/g in the first cycle, but decreasing in next cycles). This was attributed to the low thermal conductivity of the material and high thermal gradient across its height. It was demonstrated that, for these fibers, the surface directly irradiated by concentrated sunlight reached much higher temperatures than the target temperature (1400°C). This was also confirmed by a thermogravimetric analysis, highlighting that both O_2 and CO production yields were compliant with the other ceria materials under the same conditions. Furthermore, the fuel yield declined during cycling because of sintering, denoting that this material is not suitable for achieving stable cycling performance. Noticeably, the cork-templated ceria, the ceria foam and ceria pellets offered a good resistance to sintering, with no performance decline over cycles and a complete re-oxidation (fuel production of ~130 µmol/g, for a reduction step at 1400°C - atmospheric pressure, yielding δ~0.022-0.026). Biomimetic CTCe showed a higher fuel production rate compared to the other investigated materials, attributed to the favorable microstructure of the cork-derived ceramic. The morphology obtained from the cork structure led to improved redox activity, demonstrating the relevance of this material for thermochemical H_2O and CO_2 splitting cycles. Furthermore, two synthesis routes for ceria ecoceramic were investigated (multiple infiltration steps using water as solvent *vs* single infiltration step using acetone as solvent). The multiple infiltration route used water instead of acetone but required longer time and more energy than the single infiltration step route. The first method led to higher production yields (74 µmol/g of O_2 and 157 µmol/g H_2) with higher H_2 production rate (typically 1.4 mL/min/g) than the second method (63 µmol/g, 126 µmol/g and 1.1 mL/min/g, respectively). Due to the high flowability of CeMS microspheres that can escape from the cavity zone, the global fuel production rate based on the actual mass of CeMS material was somewhat low in comparison with other tested materials, despite its porous structure. The CeMS shape could be however adapted for fluidized bed reactors in order to favor the access of the oxidant gas to the reactive surface and thus favor the oxidation kinetic. Finally, it was demonstrated that commercial ceria pellets can be used as reactive material for thermochemical cycles since high fuel production rates were reached (up to 9.5 mL/min/g). This is advantageous for industrial implementation, as reactive materials should be commercially available at large scale in order to reduce fuel production costs.

Chapitre 5 - Solar membrane reactor for continuous and isothermal redox splitting of CO_2 and H_2O

5.1 Introduction

Two-step thermochemical cycles require large temperature swing and produce solar fuels sequentially in separate steps with temperature and/or pressure change. Temperature swing induces heat losses due to multiple cooling/heating stages, which negatively impact the solar-to-fuel conversion extent. Furthermore, it can also damage the reactor internal ceramic components and reactive material due to thermal stress. Thus, a process able to split CO_2 (or H_2O) by performing both steps (reduction and oxidation) simultaneously appears attractive as solar fuels will be produced continuously and isothermally. A membrane reactor is a relevant option for reaching this goal. In such a process, a reactive mixed ionic-electronic conducting membrane acts as an oxygen exchanger between both reaction zones and oxygen transfer medium to separate the produced O_2 and CO (or H_2), as shown in Figure 5-1. On the reduction side, maintained at low oxygen partial pressure, the membrane releases oxygen, thus creating oxygen vacancies, corresponding to reaction (49). According to Fick's law, the oxygen ions captured from CO_2 (or H_2O) on the oxidation side tend to migrate through the membranes toward the reduction side to re-equilibrate the oxygen vacancies created at the membrane surface. On the oxidation side, oxygen vacancies are refilled during CO_2 (or H_2O) splitting reaction, thereby leading to CO (or H_2) production, corresponding to reaction (50). These reactions occurring simultaneously produce solar fuels continuously. As O_2 and CO (H_2) are separated by the membrane, recombination cannot occur.

$$2Ce^{4+} + O^{2-} \rightarrow 2Ce^{3+} + V_O + \frac{1}{2}O_2 \quad (49)$$

$$2Ce^{3+} + V_O + CO_2 \rightarrow 2Ce^{4+} + CO + O^{2-} \quad (50)$$

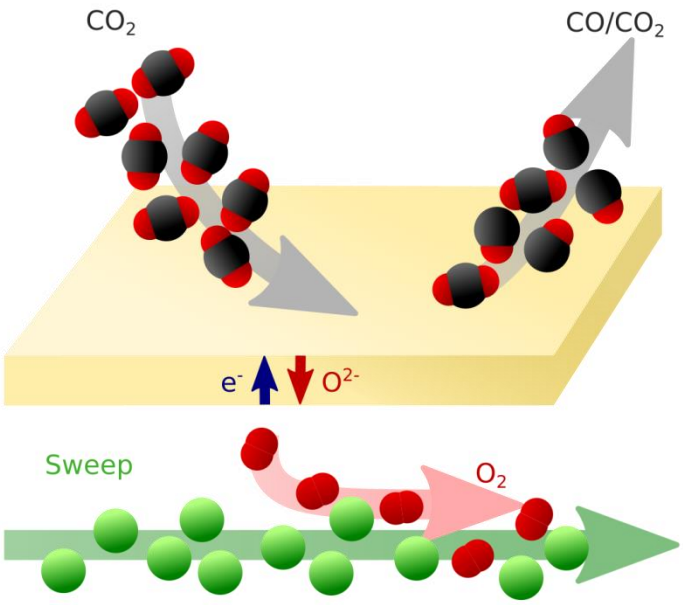

Figure 5-1: Schematic representation of the CO_2 dissociation process with a mixed ionic-electronic conducting membrane: the reduction side is maintained at low oxygen partial pressure thanks to inert gas flow (sweep) to favor a continuous transfer of oxygen ions and electrons across the membrane

In order to perform such solar-driven combined-step process, the reactive membrane should satisfy the following conditions:

- offer mixed ionic-electronic conduction properties and high selectivity for O_2 transport;
- be dense to separate the products with transport of oxygen ion through the membrane (no diffusion of molecular gas species through interconnected porosity and absence of defects allowing molecular diffusion);
- provide high oxygen ion diffusivity within the temperature range for CO_2 (or H_2O) splitting;
- maintain its crystallographic structure over a large range of conditions, especially at high temperatures (above 1400 °C).

The available surface area of the reactive membrane is also a key parameter for CO_2 dissociation [232, 233]. Ceramic membrane technologies were used for several applications, among them air separation [193, 234], air separation combined with methane partial oxidation [235], methane reforming [236] or nitrogen monoxide and nitrous oxide dissociation [237]. Gong et al. [238] developed a membrane reactor using a perovskite-disc membrane to perform air separation, as presented in Figure 5-2. The reactive membrane ($La_{0.4}Ba_{0.6}Fe_{0.8}Zn_{0.2}O_3$) was coupled with a commercial methane reforming catalyst. The He/CH_4 gas mixture was injected on the reduction side of the membrane, resulting in methane partial oxidation to CO without any NO_x production. On the membrane opposite side, synthetic air was continuously injected. The highest measured oxygen flux reached 0.9 $cm^3/cm^2/min$ at 950 °C for a 0.5 mm thick membrane.

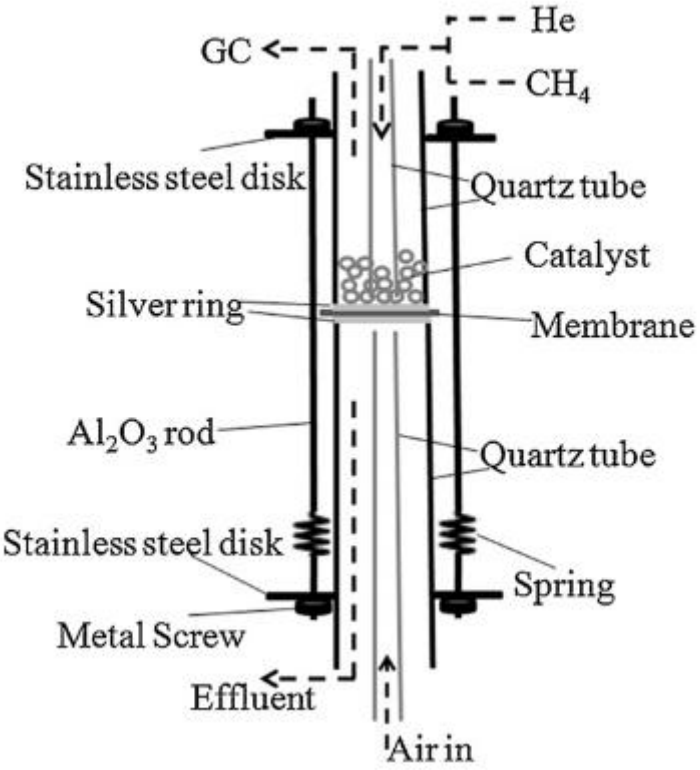

Figure 5-2: Membrane reactor for air separation and methane partial oxidation [238]

Perovskite based membranes were also studied to produce continuously H_2 and syngas (mixture of H_2/CO) by water splitting coupled with partial oxidation of methane, and the highest H_2 production rate measured was 3.4 µmol/cm^2/s with $BaCo_xFe_yZr_{1-x-y}O_3$ [239]. Other membranes such as $SrCo_{0.4}Fe_{0.5}Zr_{0.1}O_3$ [240], $SrCo_{0.8}Fe_{0.2}O_3$ [241] , $La_{0.6}Sr_{0.4}Co_{0.2}Fe_{0.8}O_3$ [236] or $La_{1-x}Sr_xFe_{1-y}M_yO_3$ (M=Ni, Co, Cr, Cu, Mn) [242, 243] have been investigated as well for carbon dioxide reforming to produce syngas. Jin et al.[240] developed a membrane reactor using a dense $BaCo_xFe_yZr_{1-x-y}O_3$ perovskite disk membrane coated with Nd/Al_2O_3 and $Pd/SrCo_{0.4}Fe_{0.5}Zr_{0.1}O_3$ catalysts (Figure 5-3). On the oxidation side, a CO_2/He mixture was injected, resulting in CO production, although a CH_4/Ar gas mixture was injected on the reduction side, resulting in syngas production. The experiment was run in the temperature range 850-950 °C and the oxygen flux through the membrane reached 1.36 mL/cm^2/min at 950 °C.

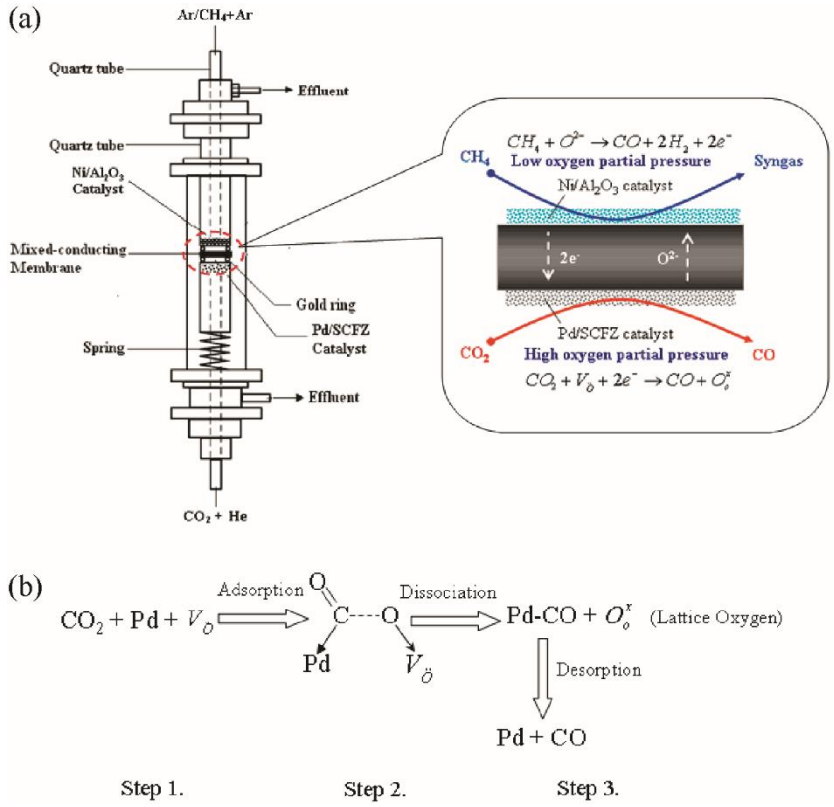

Figure 5-3: Membrane reactor developed by Jin et al. for CO_2 decomposition with methane [240]

Fluorite based membranes were proposed to directly dissociate CO_2 and H_2O using a membrane process. In 1993, Itoh et al. [244] proposed for the first time this concept to thermally decompose CO_2 using a reactive membrane. An yttria stabilized zirconia membrane in the temperature range of 1584-1782 K led to CO_2 conversion extent of 0.6%. Nigara et al. [245] highlighted the ability of ZrO_2-CeO_2-CaO membrane to dissociate H_2O at high temperature. Hydrogen was also produced by direct water splitting at high temperature using a reactive ZrO_2-TiO_2-Y_2O_3 membrane. An important oxygen partial pressure gradient is required in order to ensure a sufficiently low oxygen partial pressure for a mixed ionic and electronic conduction in the membrane [246].

More recently, Tou et al. [232, 247, 248] developed a ceria reactive membrane to produce CO from CO_2 dissociation (Figure 5-4). The reactor was composed of an inert alumina tube heated by artificial concentrated solar flux. The reactive membrane was placed inside the alumina tube and was indirectly heated. The membrane inside was swept with CO_2, leading to CO production, while Ar swept the membrane outside to remove the oxygen released by the membrane. A maximum CO production of 0.024 µmol/cm^2/s was achieved at 1600 °C.

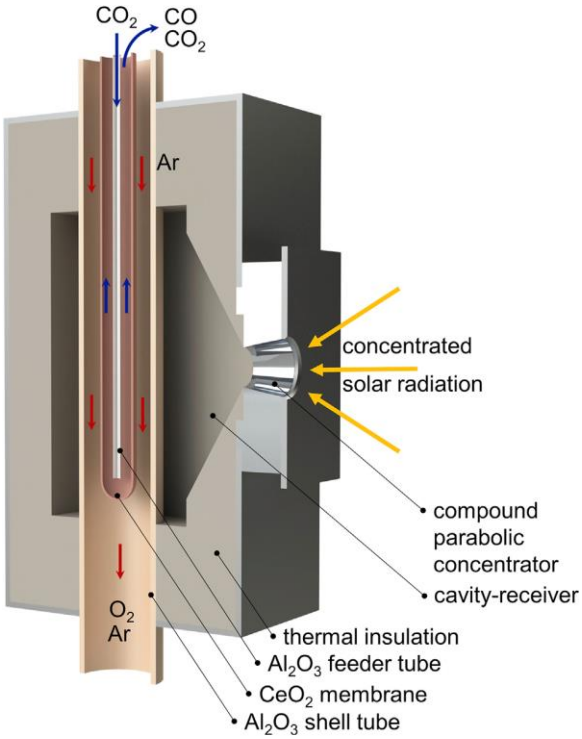

Figure 5-4: Solar membrane reactor developed by Tou et al. to produce CO by a continuous CO_2 splitting process [247]

5.2 Experimentation and method

5.2.1 Membrane synthesis and shaping

The ceria membranes were provided by Alsys-CTI. Commercial ceria powders (Marion Technologies) were used to prepare slurries. The membranes were synthesized by slip-casting, drying and sintering (1600 °C during 5 h). Three reactive membranes were provided and were used to produce solar fuels. The membranes include an uncoated ceria membrane (Figure 5-5.a) and two perovskite-coated ceria membranes (Figure 5-5.b and c), abbreviated in the following as UC, PCC1 and PCC2, respectively. The outer side of the PCC membranes was coated with $Ca_{0.5}Sr_{0.5}MnO_3$ (CSM) perovskite while the inner side was coated with $La_{0.5}Sr_{0.5}Mn_{0.9}Mg_{0.1}O_3$ (LSMMg). The UC and PCC2 membranes were 150 mm long whereas PCC1 membrane was only 135 mm long; the other dimensions are given in Figure 5-5.d. The perovskite coatings have been deposited by slip-casting (inside) and dip-coating (outside), using suitable optimized slurries. For both LSMMg and CSM perovskite formulations, the powder *(*synthesis with P2 Pechini method, see chapter 2*)* was dispersed in water (45 wt%) using a polymethacrylate dispersing agent (DARVAN C-N®) and polyvinyl alcohol (Rhodoviol, 2 wt%) as a binder/plasticizer. A SpeedMixer® (DAC 150.1 FVZ-K) was used to obtain a fluid, uniform, stable and smooth slurries, suitable for casting. For the inside LSMMg coating, the membrane was filled with the slurry, up to the membrane flange during 90 s. Then, the membrane was turned over to let the excess slurry flowing freely. For applying the external coating, the ceria tube was immersed in the CSM slurry during 90 s and then removed at a rate of 0.5 cm/min. In between the two deposition steps, the membranes were dried for 30 min at 100 °C and weighted. The mass uptake after the LSMMg coating was estimated at 0.5% while it was only ~0.2% for CSM coating. The membranes went through a multi-step thermal treatment with a final

sintering step at 1500 °C for 8 h (2 °C/min ramp). The membranes used in this study are shown in Figure 5-5. The membrane tubes are closed at one end (dead-end tubes or finger type) and fitted with a flange (collar shape) for tight fixation. The reactive surface area of membrane was considered as the area exposed to solar irradiation in the cavity, corresponding to 26 cm^2 for UC and PCC2 membranes and 22 cm^2 for PCC1 membrane.

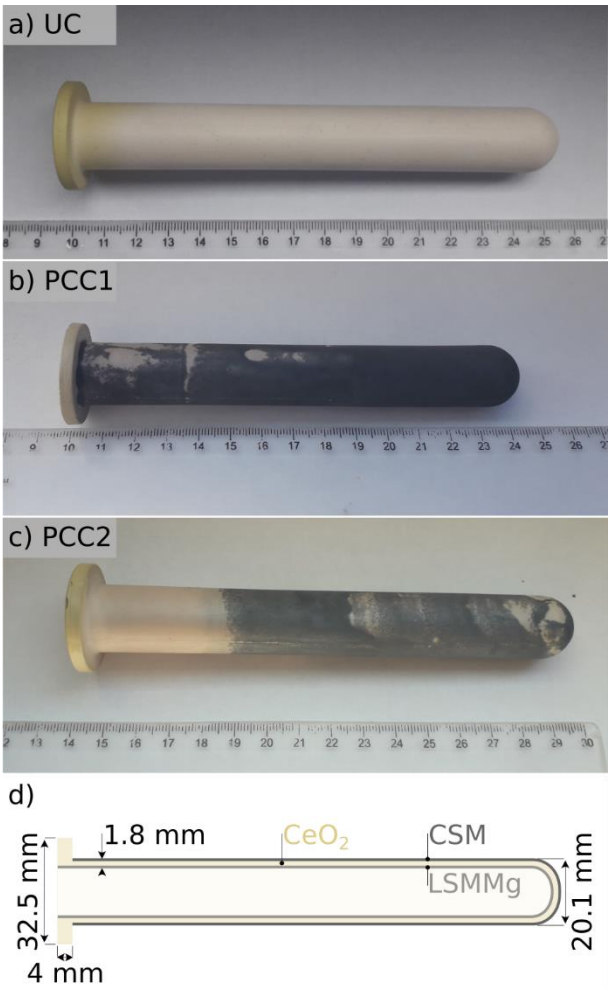

Figure 5-5: Reactive membranes used in the continuous thermochemical splitting process, a) pure uncoated ceria (UC) tube, b) and c) perovskite coated ceria (PCC1 and PCC2) tube, d) scheme of the membrane and dimensions

5.2.2 Reactor configuration

Isothermal experiments using ceria-based membranes to continuously produce solar fuels with *in-situ* extraction/pumping of the produced oxygen across the membrane, were performed in a vertical-axis medium-size solar facility of PROMES-CNRS laboratory (SUNFUEL reactor). As for the two-step process, the solar reactor was placed at the focus of a parabolic dish irradiated by a sun-tracking heliostat. The solar reactor was designed to produce continuously solar fuels with a separation of both the reaction steps and the gas products by a reactive membrane (Figure 5-6). The cavity was composed of an alumina cylinder (50 mm inner diameter and 80 mm height) with a lateral opening to let the membrane pass horizontally through it and it was closed by an alumina top cover with 19 mm diameter aperture. The cavity configuration permits both to maximize the absorbed concentrated solar radiation and to

minimize the solar re-radiation loss from the cavity to the surrounding environment. A hermetical transparent Pyrex window on top of the reactor allows the solar radiation to reach the cavity receiver/reaction chamber. A water-cooling system was used to cool the stainless-steel reactor shell and flanges in order to avoid sealing damages due to high temperatures. The reactive membrane was installed in the reactor thanks to a support fixed on the reactor side, resulting in ~25 cm^2 of the membrane surface being exposed to high-temperature solar heat inside the solar-cavity receiver. Seals on the membrane flange were used to prevent any gas transfer between the inner and outer sides of the membrane as well as any leak of the reactor to the outside. The reactive membrane was used as an oxygen transferring medium: its outside surface releases oxygen (reduction reaction) while its inner surface is re-oxidized with CO_2 (or H_2O). A CO_2/Ar mixture (or steam) was injected inside the membrane tube via an alumina pipe (6x4 mm) fixed to the membrane support. The extremity of the pipe reached the heated zone (extremity of the membrane tube), so that the oxidative gas swept the whole membrane length. In case water was used as an oxidant, liquid water was injected in an inox capillary inserted inside the alumina pipe, and then vaporized at the capillary exit (tip placed just before the cavity zone) and transported by Ar carrier gas flowing inside the alumina pipe.

At the tubular membrane reactor exit (inner side), the outlet gas was analyzed by an online gas analyzer (Emerson Xstream) equipped with IR (CO/CO_2, 0-40% for CO, 0-100% for CO_2) and thermal conductivity detector (H_2, 0-50%). Regarding the reduction side of the membrane, an Ar flow (99.9999% purity, $[O_2]<2$ ppm) was injected from the reactor bottom toward the Pyrex window via two stainless steel pipes in order to sweep the window area and then entered the cavity to flow in the downward direction. The O_2 released by the membrane was thus continuously evacuated from the cavity by the Ar carrier gas. The Ar/O_2 mixture was continuously analyzed by a trace O_2 electrochemical analyzer (Systech, range from 0.1 ppm to 1%, precision ±2% of reading). The gas flow rates were regulated with mass-flow controllers (MFC, Brooks Instruments model SLA5850S) while water was injected with a liquid mass flow controller (range 0−60 g/h, accuracy ±1% of full scale). In case of water injection, the outlet gas from the membrane reactor (inner side) flowed through a bubbler and a desiccant column to condense and remove excess steam in order to protect the gas analyzer. As the bubbler induced a pressure increase (~60 mbar) in the membrane tube, a second bubbler was placed at the cavity outlet (reduction side) to equilibrate the pressure. The reactor was heated by opening progressively the shutter system placed between the heliostat and the parabolic dish, to allow a slow and controlled heating of the membrane. When the target temperature was reached, the shutter was adjusted to maintain a constant temperature. The temperature was monitored thanks to B-type thermocouples (T1, T2, T3 and T4) along with a solar-blind pyrometer pointing on the membrane upper surface. T1 was placed below the membrane, in contact with its outer wall, T2 was in contact with the cavity outer wall, T3 was placed at the cavity bottom, and T4 was inserted into the membrane tube below the alumina pipe (Figure 5-6). The pressure in the reactor was measured by three pressure transmitters placed at both gas inlets and cavity. The pressures inside the membrane tube and within the cavity were maintained equal with a mechanical pressure regulator (metal diaphragm) to avoid undesired gas exchange between the

inner side of the membrane and the cavity in case the membrane was not completely densified (or not fully permeable to gas species in the course of the solar experiments due to cracks formation).

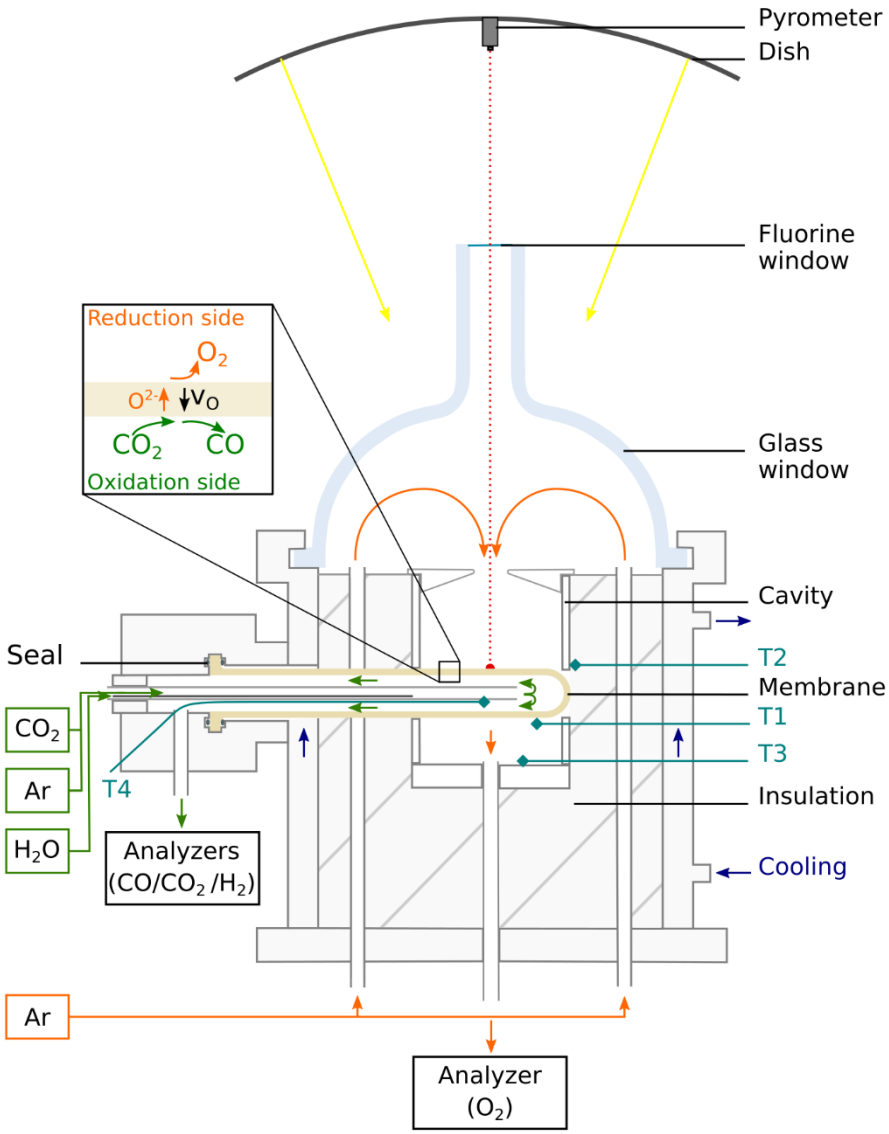

Figure 5-6: Schematic representation of the solar SUNFUEL reactor with dead-end tubular membrane configuration

5.3 Results and discussion

In order to assess the performance of the isothermal solar membrane reactor, different operating conditions have been studied. The impact of these conditions on both O_2 and fuel production rates has been investigated. Table 5-1 summarizes all the operating conditions along with the measured gas production rates (see also Figure SE-1) for the three reactive membranes. In total, 782 µmol/cm^2, 602 µmol/cm^2 and 1987 µmol/cm^2 of CO were produced with UC, PCC1 and PCC2 membranes after a total operation time under solar radiation of 7 h, 5 h and 8 h, respectively.

Table 5-1: Summary of the operating reactor parameters used for each membrane, along with the gas production rate achieved during the steady-state. $Q_{red,tot}$ and $Q_{ox,,tot}$ represent the total gas flow rate on the reduction and oxidation side, respectively

Condition #	Membrane	Temperature (°C)	$Q_{red, tot}$ (L/min)	Oxidant gas	$Q_{ox, tot}$ (L/min)	Oxidant molar fraction	O_2 production rate (±2%) (µmol/cm²/s)	CO production rate (±2%) (µmol/cm²/s)	H_2 production rate (±2%) (µmol/cm²/s)
1	UC	1496	1.0	CO_2	0.4	1.00	0.019	0.037	-
2	UC	1497	1.0	CO_2	0.4	0.50	0.013	0.027	-
3	UC	1496	1.0	CO_2	0.4	0.25	0.010	0.020	-
4	UC	1501	1.0	CO_2	0.4	1.00	0.020	0.041	-
5	UC	1499	1.0	CO_2	1.0	1.00	0.026	0.053	-
6	UC	1548	1.0	CO_2	1.0	1.00	0.035	0.071	-
7	UC	1547	1.0	CO_2	0.4	1.00	0.031	0.061	-
8	UC	1499	1.0	CO_2	0.4	1.00	0.019	0.038	-
9	UC	1448	1.0	CO_2	0.4	1.00	0.011	0.023	-
1	PCC1	1499	1.0	CO_2	0.4	0.50	0.018	0.036	-
2	PCC1	1508	1.0	CO_2	0.4	1.00	0.032	0.063	-
3	PCC1	1501	1.0	CO_2	1.0	1.00	0.045	0.090	-
4	PCC1	1553	1.0	CO_2	1.0	1.00	0.066	0.133	-
5	PCC1	1548	1.0	CO_2	0.4	1.00	0.039	0.078	-
6	PCC1	1548	1.0	CO_2/H_2O	0.4	0.5 CO_2/0.5 H_2O	0.033	0.049	0.017
7	PCC1	1550	1.0	H_2O	0.4	0.50	0.027	-	0.054
1	PCC2	1499	1.0	CO_2	0.4	0.50	0.018	0.035	-
2	PCC2	1499	1.0	CO_2	0.4	1.00	0.025	0.050	-
3	PCC2	1499	1.0	CO_2	0.4	0.50	0.017	0.035	-
4	PCC2	1501	1.0	CO_2	1.0	1.00	0.034	0.067	-
5	PCC2	1548	1.0	CO_2	1.0	1.00	0.048	0.096	-
6	PCC2	1547	1.0	CO_2	0.4	1.00	0.036	0.072	-
7	PCC2	1548	1.0	CO_2	0.4	0.50	0.018	0.037	-
8	PCC2	1545	1.0	H_2O	0.4	0.50	0.023	-	0.047

The membrane-driven continuous solar process for fuel production eliminates the need for the temperature swing used in two-step cycles. In the solar membrane-driven isothermal process, the gas flow production rate evolved until reaching steady-state values, meaning that the oxygen transfer from the oxidation to the reduction side was equilibrated. Figure 5-7 shows the evolution of both O_2 and CO production rates during the heating ramp and after temperature stabilization at 1550 °C (T4 inside the membrane) for CO_2 flow rate $Q_{ox,tot}$=1 L/min and CO_2 molar frraction x_{CO2}=1.00. Both O_2 and CO productions were already stabilized at 1500 °C, with similar $Q_{ox,tot}$ and x_{CO2} values. After temperature stabilization, the difference between the temperatures measured by T1 and T4 is small (< 20 °C), revealing a small radial temperature gradient in the membrane. Furthermore, the difference between the temperatures measured by T1 and Tpyrometer is also small. Although the cavity is similar to a black-body, an uncertainty of measurement remains for the temperature measured by the pyrometer due to the unknown membrane emissivity (an emissivity value of 1 was considered). The O_2 and CO production rates evolved during the transient period before reaching steady-state values. The O_2 production rose with temperature increase and the O_2 production peak occurred when the temperature reached the target temperature. After the O_2 peak production, the O_2 production rate decreased until reaching a stable value (0.048 µmol/s/cm^2). For each fixed operating condition, when the membrane reached the non-stoichiometry equilibrium in its thickness, the oxygen production was only attributed to the oxygen diffusivity through the membrane, which determined the oxygen flux for the considered temperature and oxygen partial pressure gradient. The time required to reach equilibrium likely depends on the membrane thickness and microstructure. Regarding the CO production rate, it started to decrease when the temperature increased due to thermodynamic limitation. Then, as further oxygen vacancies were created in the membrane thickness, the CO production increased up to 0.096 µmol/cm^2/s (while O_2 decreased) and reached equilibrium values. During a change in operating parameters, the O_2 and CO production rate evolved from a transient period towards steady-state stabilization at a ratio O_2:CO of 1:2. Once the steady-state established, the O_2 and CO production rates remained constant.

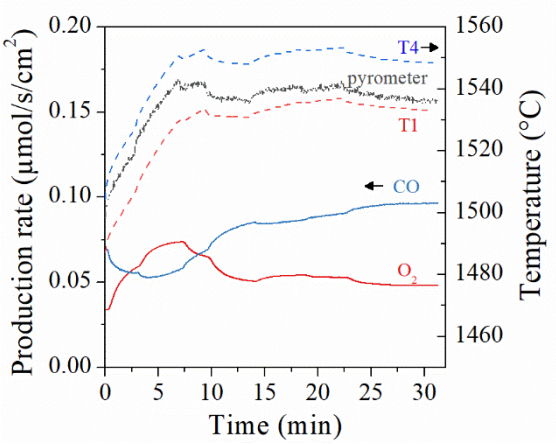

Figure 5-7: Evolution of the O_2 and CO production rates along with temperature, with $Q_{ox,tot}$=1.0 L/min and x_{CO2}=1.00, for the PCC2 membrane (condition #5)

An essential outcome for the membrane-driven solar process is a stable fuel production rate over time. The O_2 and CO production rates in steady-state under similar conditions have been

measured at different period of time after the beginning of the experiment. The results (Figure 5-8) confirmed that both O_2 and CO production rates were repeatable and stable for three similar conditions at different testing times, with values in the range 0.019-0.020 µmol/cm^2/s and 0.037-0.041 µmol/cm^2/s, respectively. Thus, the ceria membrane is clearly able to provide a stable CO production rate, with a mean value 0.039 µmol/cm^2/s and a standard deviation of 0.002.

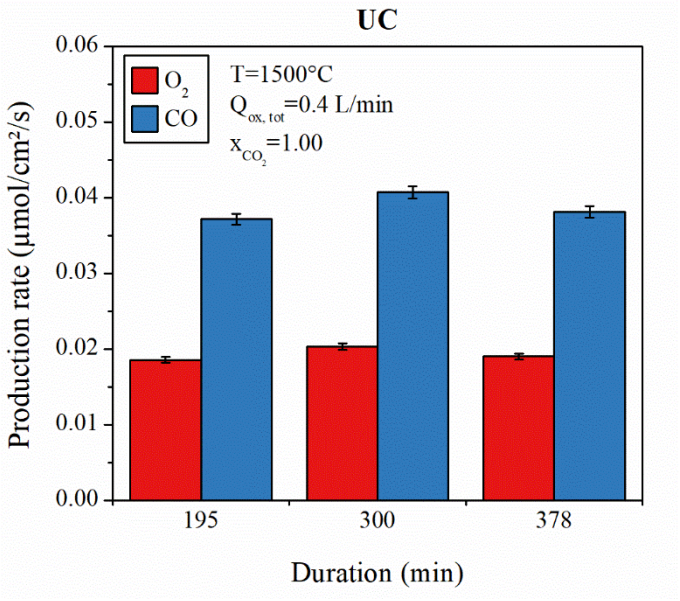

Figure 5-8: Evolution of O_2 and CO production rates as a function of the elapsed time since the experiment started, for UC ceria membrane (conditions #1, 4 and 8)

5.3.1 Influence of the operating parameters on CO production rate

5.3.1.1 Temperature

Temperature is a key parameter in the thermochemical production of solar fuels from redox materials. As exposed in the chapter 3 and as predicted by thermodynamics [51, 212], the temperature influences the reduction extent of reactive materials. Thus, it was relevant to study the influence of temperature on the production rate of reactive membranes. Figure 5-9.a presents the evolution of O_2 and CO production rates at steady state for different operating temperatures measured inside the membrane (T4). A temperature step was performed at 1400 °C, but no significant CO production was observed. The temperature was then further increased until observing a start of CO production above ~1400 °C. For a temperature of 1500 °C measured at T4, the temperature measured by T2 is lower than 1400 °C (Figure SE-2). As T2 thermocouple is in contact with the outside cavity wall, this means the temperature in the insulation layer is also below 1400 °C. Thus, the membrane surface situated outside of the reactor cavity in the insulation layer cannot react. Hence, the reactive surface of the membrane corresponds to the surface in the cavity. As expected, it appears that increasing the temperature leads to an increase of the production rates, it results in an increase of the reduction extent of the reactive material as well as a faster oxygen ionic conduction. Indeed, oxygen diffusivity through the membrane material requires lattice defects, specifically oxygen vacancies [247, 249], and the non-stoichiometry (δ) depends on both the temperature and the oxygen partial

pressure [51]. Thus, increasing the temperature enhances the non-stoichiometry extent achieved by the reactive oxide, which in turn promotes the CO_2 splitting capability. Although temperature increase cannot directly promote the CO_2 splitting step according to thermodynamics, results show that it still favors CO production by enhancing the oxygen transfer driving force, associated with oxygen vacancies gradient. Thus, O_2 and CO production rates in the redox membrane process were enhanced by a temperature rise, due to improved oxygen mobility. At 1547 °C, the O_2 and CO production rates reached maximum values of 0.031 µmol/cm^2/s and 0.061 µmol/cm^2/s, respectively, and the CO_2 conversion extent reached 0.5 mol%. Nevertheless, the maximum operating temperature is limited by the stability of the reactive material due to fastened ageing, strong thermal gradients along the membrane axis and possible risk of sublimation [65, 159]. The apparent activation energy of the reaction was determined by plotting the logarithm of the average production rate versus reverse temperatures (Figure 5-9.b) [232, 247]. The activation energy for the UC membrane was ~262 kJ/mol, while it was only ~114 kJ/mol and ~199 kJ/mol for PCC1 and PCC2 membranes, respectively.

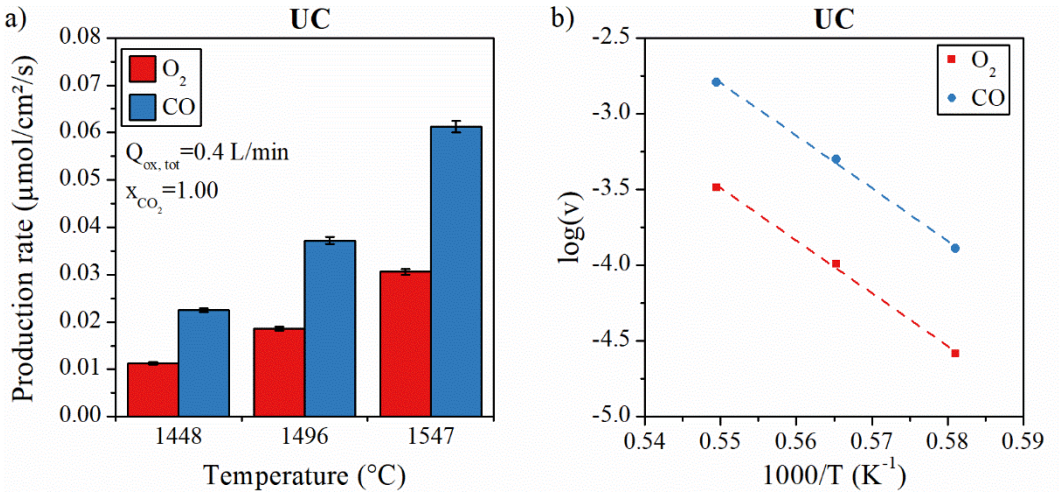

Figure 5-9: Influence of the reaction temperature on the performance of the UC membrane : a) Steady state production rates for three reaction temperatures (T4=1448 °C, 1496 °C and 1547 °C, corresponding to conditions #9, 1 and 7, respectively) with a total gas flow rate of 0.4 L/min on the oxidation side and a CO_2 molar fraction of 1.00, and b) logarithm plot of O_2 and CO production rates (v) versus reverse temperatures ($Q_{ox,\,tot}$=0.4 L/min, x_{CO2}=1.00)

5.3.1.2 Oxidant gas flow rate on the oxidation (inner) side of the membrane

In two-step thermochemical cycles, the importance of the total gas flow rate during the oxidation step was pointed out [206, 222]: an increase of the total gas flow rate enhanced the access of the oxidation gas to the reactive surface, thus improving the fuel production rate. Similarly, the influence of the oxidant gas flow rate on the inner side ($Q_{ox,tot}$) of the membrane was evaluated (Figure 5-10). A discussion about the evolution of O_2 and CO production during the transient period corresponding to the variation of $Q_{ox,tot}$ is provided in appendix (Figure SE-4). Increasing $Q_{ox,tot}$ from 0.4 L/min to 1.0 L/min improved the steady-state O_2 and CO production rates from 0.019 µmol/cm^2/s to 0.026 µmol/cm^2/s and from 0.038 µmol/cm^2/s to 0.052 µmol/cm^2/s, respectively. Furthermore, the CO:CO_2 ratio decreased from 0.52% to 0.33% with an increase of Q_{ox}, which favored the thermodynamic driving force toward CO production. Moreover, a high total gas flow rate on the oxidation side improves mass transfer and promotes the access of the oxidant gas to the reactive surface, which favors the oxidation

reaction (surface-controlled reaction). Meanwhile, dilution of products is enhanced and their continuous removal from the reaction site shifts the equilibrium towards CO production. However, the increase of $Q_{ox,tot}$ led to a decrease of the CO_2 conversion extent (0.5% at $Q_{ox,tot}$= 0.4 L/min versus 0.3% at $Q_{ox,tot}$= 1 L/min). The CO_2 conversion extent tends to follow the same behavior as the CO:CO_2 ratio. In fact, the latter corresponds to the CO production rate divided by the CO_2 flow rate at the reactor exit, while the CO_2 conversion extent corresponds to the ratio (CO production rate) / (CO_2 flow rate injected). The CO_2 flow rate at the reactor exit is very similar to the injected CO_2 flow rate, since only a small fraction of the CO_2 is consumed, making the CO:CO_2 ratio and the CO_2 conversion extent very close. Thus, decreasing the CO:CO_2 ratio to favor the oxidation reaction is achieved at the expense of a lower CO_2 conversion extent. Therefore, increasing the total gas flow rate on the oxidation (inner) side of the membrane has a beneficial impact on both CO and associated O_2 production rates, in spite of a negative effect on the CO_2 conversion extent.

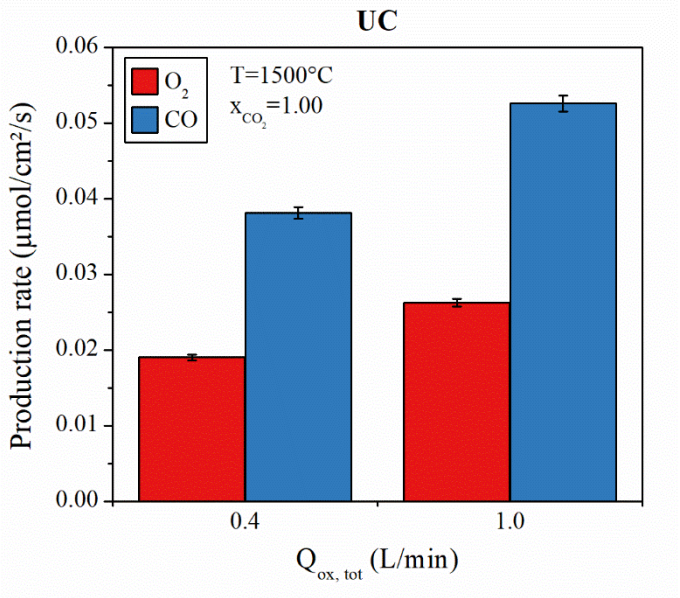

Figure 5-10: O_2 and CO production rates with total flow rates of 0.4 L/min and 1.0 L/min on the oxidation side, at 1500 °C and with a CO_2 molar fraction of 1.00, for UC membrane (conditions #8 and 5, respectively)

5.3.1.3 Oxidant molar fraction

The CO_2 oxidant molar fraction was highlighted as a key parameter for the CO production rate in two-step thermochemical cycles [205, 206, 222]. The influence of the CO_2 molar fraction on the O_2 and CO production rates at steady-state was investigated as presented in Figure 5-11. The evolution of O_2 and CO production rates in transient conditions due to the variation of x_{CO2} is discussed in appendix (Figure SE-5). The CO_2 molar fraction was investigated by adjusting the CO_2 and Ar inlet gas flow rates to obtain the desired oxidant molar fraction while the total gas flow rate was maintained constant (at 0.4 NL/min). Increasing the CO_2 oxidant molar fraction from 0.25 to 1.00 induced a rise of the O_2 production rate (from 0.010 µmol/cm^2/s to 0.019 µmol/cm^2/s) as well as the CO production rate (from 0.020 µmol/cm^2/s to 0.037 µmol/cm^2/s). The low CO:CO_2 ratio (0.32%) obtained with x_{CO2}=1 in comparison with 0.73% for x_{CO2}=0.25 could explain the higher membrane oxidation since the oxidation reaction

is thermodynamically favored by a low CO:CO_2 ratio. Thus, the O_2 and CO production rates are enhanced by increasing the CO_2 oxidant molar fraction because the membrane oxidation on the inner side is favored.

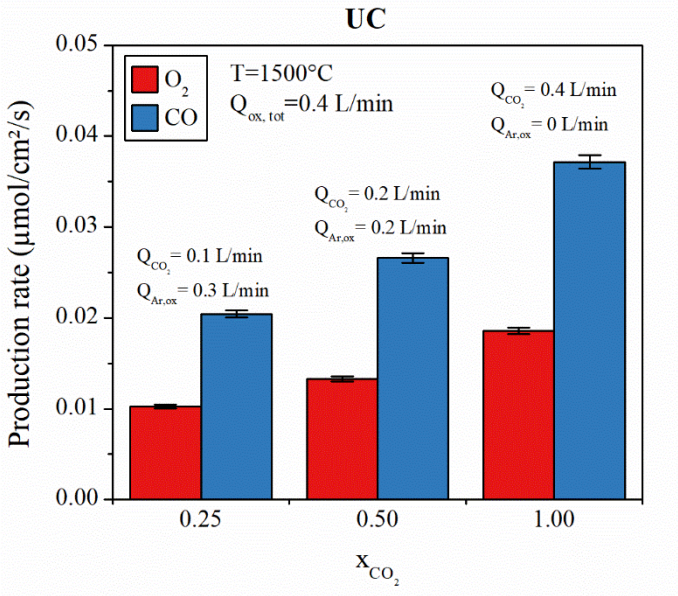

Figure 5-11: O_2 and CO production rates in steady state obtained with different CO_2 molar fractions (0.25, 0.50 and 1.00, corresponding to conditions #3, 2 and 1, respectively) for UC membrane

5.3.1.4 Type of oxidant gas

Water and CO_2 are usually used as oxidant gas to produce either CO, H_2 or syngas. However, the oxidant gas behaves differently as a function of temperature due to the different thermodynamic constants. Actually, the dissociation temperature of H_2O is higher than the CO_2 one, as experimentally evidenced in this study with the isothermal membrane reactor. The influence of the oxidant gas on fuel production was investigated with four oxidant gas compositions, as depicted in Figure 5-12. It should be noted that the water molar concentration could not be fixed at a value of 1.00 due to the necessity of using a carrier gas. With a mixture of CO_2 and H_2O, the CO production rate (0.049 µmol/cm^2/s) was higher than the H_2 production rate (0.017 µmol/cm^2/s), due to a more favorable CO_2 dissociation reaction. This fits our previous results with ceria-based foams, showing that H_2O is less favorable than CO_2 as oxidant gas [205]. However, shortly after the water injection, the reactive membrane was cracked. For this reason, reaching steady-state H_2 production was not possible. This event could potentially result from the occurrence of cold points created by water condensation and inducing sharp temperature gradients in the membrane. Unexpectedly, the measured H_2 production rate (0.052 µmol/cm^2/s) with 50% H_2O/Ar mixture was higher than the CO production rate (0.036 µmol/cm^2/s) obtained with 50% CO_2/Ar mixture. This result could however be attributed to the membrane rupture during water injection, impeding to reach a complete established steady-state H_2 production rate. Thus, CO_2 splitting appears to be more propitious than H_2O splitting as it does not induce any condensation issue and its dissociation is more favorable. However, CO production requires additional energy to separate CO from unreacted CO_2 while H_2 can be very easily purified by steam condensation.

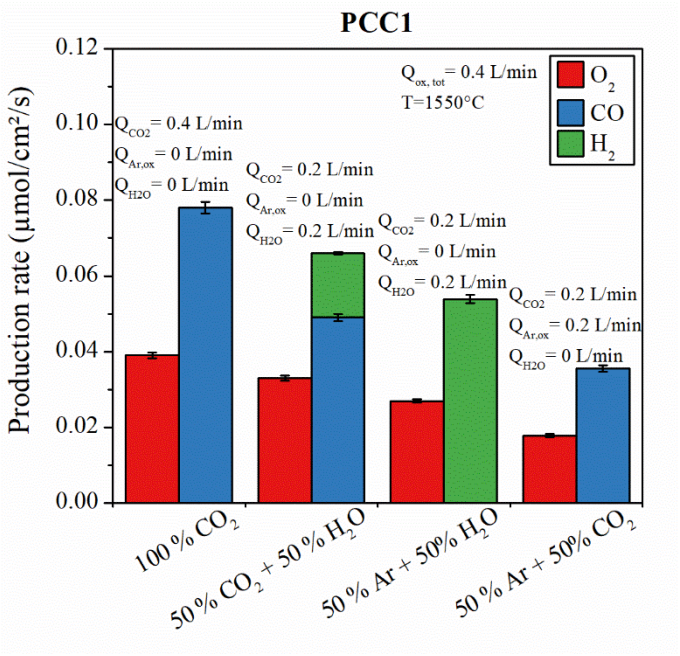

Figure 5-12: O_2 and CO production rates with different compositions of oxidant gas, for PPC1 membrane (conditions #2, 6, 7 and 1)

5.3.2 Impact of the reactive perovskite coatings

Dual phase perovskite-ceria composites were previously highlighted for their enhanced thermochemical performance in comparison with pristine ceria [206, 250]. In the present work, the thermochemical performance of perovskite-coated ceria membranes was compared with those of a pristine ceria membrane. The inner ceria membrane surface was coated with LSMMg with a fine microstructure able to increase the available surface area for the oxidation reaction. The outer membrane surface was coated with CSM to favor the reduction extent of the ceria material and enhance the oxygen gradient across the membrane thickness. Two coated membranes were tested, differing mainly by the length of the tube inserted in the cavity (shorter for PCC1). Figure 5-13 compares the O_2 and CO production rates at steady state for uncoated and coated ceria membranes. Enhanced O_2 and CO production rates were clearly obtained for both coated membranes, although limited improvement was measured for the longer PCC2 one. This result was attributed to a less uniform coating on the PCC2 membrane (Figure 5-5), highlighting the key-role of a continuous and uniform reactive perovskite coating on the ceria membrane. At 1550 °C with Q_{ox}=1.0 L/min and x_{CO2}=1.00, higher O_2 and CO production rates were obtained for both PCC1 (0.066 µmol/cm^2/s and 0.133 µmol/cm^2/s, respectively) and PCC2 membranes (0.048 µmol/cm^2/s and 0.096 µmol/cm^2/s, respectively) in comparison with the UC membrane (0.035 µmol/cm^2/s and 0.071 µmol/cm^2/s, respectively). Moreover, for all the investigated operating conditions, the CO production rates were enhanced in the range 27-72% and 18-36% for PCC1 and PCC2 membranes respectively, in comparison with the UC membrane. This clearly demonstrates the beneficial role of the perovskite coatings. The improvement of the production capacity with the reactive thin coatings can be attributed to the better reduction of the membrane material, enhancing the oxygen mobility. Therefore, appropriate

perovskite coatings appear as an interesting lever to improve the continuous solar fuel production with ceria membranes.

In the study of Tou et al. [247] using a ceria membrane reactor, a maximum CO production rate of 0.024 µmol/cm^2/s was reached with the following operating conditions: $p_{O2}=10^{-6}$ bar, T=1600 °C, Q_{ox}= 0.2 L/min and x_{CO2}= 1.00. In the present work, at 1500 °C with a total flow rate of 0.4 L/min on the oxidation side and a CO_2 molar fraction of 1.00, the CO production rate achieved at steady state was 0.038 µmol/cm^2/s, 0.063 µmol/cm^2/s and 0.050 µmol/cm^2/s with UC, PCC1 and PCC2 membranes, respectively. Despite a lower operating temperature, these values are much higher than those measured by Tou et al. [232, 247]. This attractive performance could be explained by more favorable operating conditions, in particular a higher total gas flow rate on the oxidation side, favoring the membrane material re-oxidation, as previously highlighted. Therefore, an optimization of the operating parameters is a key aspect to achieve high fuel production. For all the investigated membranes, the maximum CO production rates (0.071 µmol/cm^2/s, 0.133 µmol/cm^2/s and 0.096 µmol/cm^2/s for UC, PCC1 and PCC2, respectively) were achieved for the following optimized operating conditions: T=1550 °C, Q_{ox}=1 L/min and x_{CO2}=1.00 (Figure 5-13). Other parameters are likely to impact the gas production rates, such as the Ar flow rate on the reduction side (influencing both mass transfer of gaseous oxygen and oxygen partial pressure). Decreasing the oxygen partial pressure on the reduction side via dilution or with mechanical or thermochemical pumping [251] should further promote the oxygen transfer through the membrane.

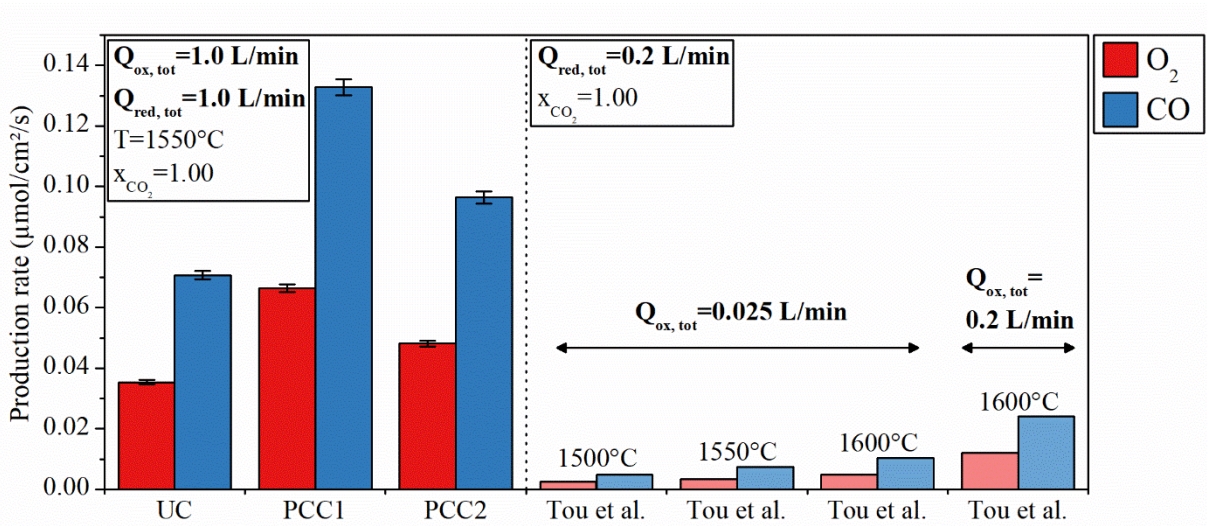

Figure 5-13: Comparison of O_2 and CO production rates obtained in this work and by Tou et al. [247]

5.3.3 Microstructural analysis of the reactive membranes

The membrane surface microstructure is an important characteristic as the oxidation reaction is surface-controlled. The microstructure of the ceria membrane surface and its perovskite layers were investigated by SEM (Figure 5-14). The fresh UC membrane features grain sizes in the range 3-12 µm, while the grain sizes of the fresh CSM and LSMMg coatings are in the range 10-25 µm and 1-5 µm, respectively. The CSM coating (reduction side) thus offers large grain sizes, whereas the LSMMg coating provides smaller grain sizes in comparison with the

uncoated UC membrane. Lowering the grain sizes on the oxidation side with the LSMMg coating can enhance the reactive membrane oxidation by favoring surface exchanges. However, as shown in Figure 5-14, strong sintering was evidenced after membrane utilization in the solar reactor. Ceria grain sizes increased in the range 8-30 µm, while those of LSMMg and CSM coatings grew in the range 5-40 µm. This strong sintering may be attributed to long term testing at a temperature similar to (or slightly above) the initial membrane sintering temperature in air.

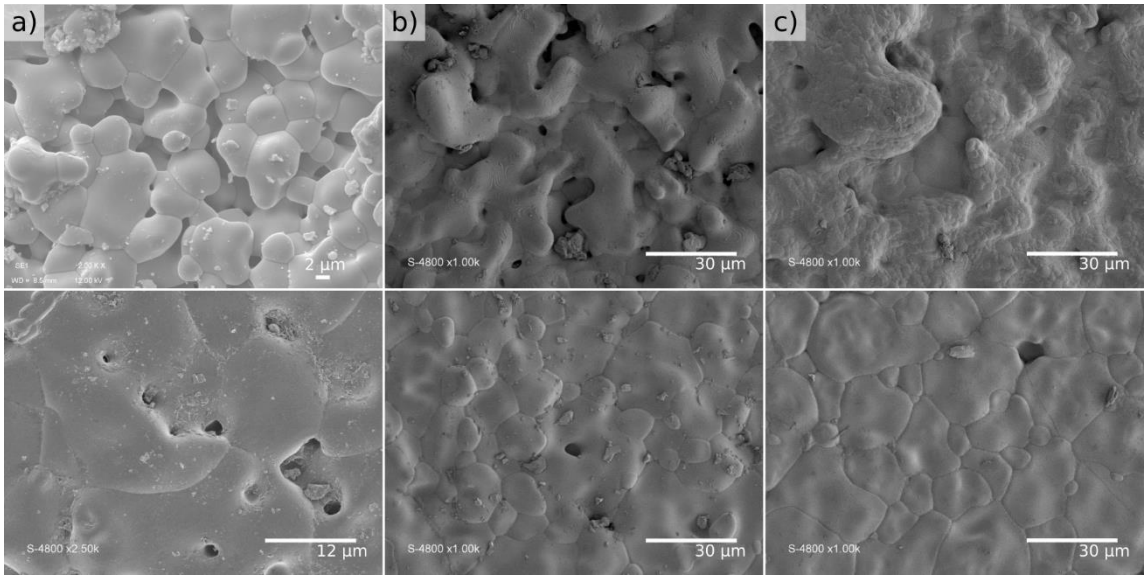

Figure 5-14: SEM images of the surface of: a) pristine UC ceria membrane, b) CSM coating and c) LSMMg coating before (top) and after (below) their utilization in the solar reactor

5.3.4 Comparison between a two-step process and a continuous membrane process

In two-step thermochemical cycles, temperature and pressure swings impose severe thermo-mechanical stress to the material as well as energy losses. Moreover, O_2 and the fuel are temporally separated in different alternating steps and thus are not produced continuously. In contrast, the membrane process occurs at high temperature but in isothermal conditions (no thermal shocks in steady state), while the fuel and O_2 are spatially separated during the reactions, enabling continuous production. In both isothermal and two-steps processes, the products are produced separately, thus avoiding unwanted recombination.

A direct comparison of the amount of fuel produced by the isothermal membrane and the two-step redox process is not straightforward. Indeed, the amount of fuel produced with two-step cycles depends on the mass of reactive material loaded in the reactor, whereas for the single-step membrane process, the amount of fuel produced is linked to the membrane active surface. A simple attempt to compare the performance of both processes with the solar-to-fuel conversion efficiency is presented hereafter. Due to the discontinuous fuel production in a two-step thermochemical cycle, the solar-to-fuel efficiency should be calculated for the whole cycle, according to equation (51)

$$\eta_{two\ step} = \frac{n_{fuel} HHV_{fuel}}{E_{solar}} \tag{51}$$

where n_{fuel} is the total fuel amount produced during the whole cycle, HHV_{fuel} the high heating value of the fuel and E_{solar} is the total solar energy input during the cycle. Whereas for a single-step process, the solar-to-fuel conversion efficiency is determined according to equation (52)

$$\eta_{single\ step} = \frac{\dot{n}_{fuel} HHV_{fuel}}{P_{solar}} \quad (52)$$

where $\dot{n}_{fuel}$ represents the fuel production rate at steady state and P_{solar} the solar power input at steady state. Considering the two-step cycles reported in [206]: 0.030 mol of CO were produced by a LSMMg-coated ceria foam, with a reduction step at 1400 °C under Ar, followed by an oxidation step with CO_2 (x_{CO2}=1 and total flow rate of 1 L/min) in the range 1041 °C-680 °C, for a total cycle duration of 135 min, leading to a solar-to-fuel conversion efficiency of 0.13% for the whole cycle. In the present work the PCC1 membrane produced 0.133 µmol/cm^2/s of CO (at 1550 °C with x_{CO2}=1 and $Q_{ox,\ tot}$=1 L/min), corresponding to a production of 0.011 mol of CO during 135 min. The associated solar-to-fuel conversion efficiency is 0.08%, thus slightly lower than for the two-step process. At this reactor scale, the amount of reactive material and available surface strongly impacts the solar-to-fuel conversion efficiency. However, no attempt was done to optimize the solar-to-fuel conversion efficiency in the reactor; decreasing heat loss and using a heat recuperation system might be suitable options. Therefore, further optimizations on both processes are still required to extrapolate the process at larger scale. The two-step process (with temperature swing) globally favors fuel production due to high Δδ, but heat recovery systems are required and reaction kinetics need to be optimized to reduce cycling times. In contrast, the direct isothermal thermolysis via redox membrane (with oxygen partial pressure gradient) spatially separates the gas products while alleviating heat losses and thermal shocks, and achieves continuous and simultaneous production of O_2 and H_2/CO, but high Δδ and membrane stability need to be searched.

5.3.5 Thermo-mechanical stability of the reactive membrane

In view of future large-scale implementation, the reactive membranes should be able to undergo long term on-sun operation as well as heating/cooling inherent with daily-sun cycling. During this first lab-scale study, the UC, PCC1 and PCC2 membranes broke (Figure 5-15) after 7 h, 5 h and 8.5 h of on-sun operation respectively. The UC membrane broke during the cooling step after one full day operation whereas the two coated PCC membranes broke during water injection. The breaking areas correspond to zones submitted to high thermal gradients: located either between the cavity and the insulation, or close to the water-cooling parts of the reactor. It should be underlined that the PCC2 membrane underwent a cooling and re-heating test without any failure, thus highlighting the possibility to preserve its mechanical integrity with "slow" cooling ramp (13 °C/min) and using only CO_2 as oxidant gas. An alteration of the reactive coating on the PCC2 membrane was observed (Figure 5-15c), in comparison with the original one (Figure 5-15.c), although no significant decline of the thermochemical performance was evidenced. Further improvement of the membrane mechanical resistance to thermal stress would be required to validate the process sustainability.

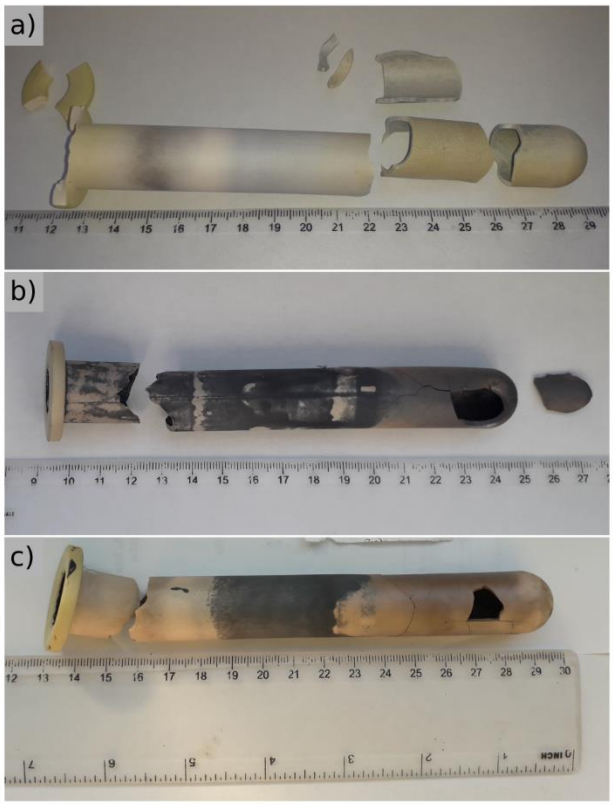

Figure 5-15: Pictures of a) UC, b) PCC1 and c) PCC2 membranes after utilization in the solar reactor

5.4 Conclusion

In this chapter, solar fuels were produced isothermally (at 1450-1550 °C) with a solar-driven single step thermolysis process using a reactive tubular membrane. In total, 1.91 L of CO and 0.02 L of H_2 were produced, highlighting the ability of the SUNFUEL reactor to provide solar fuels in a continuous redox membrane process with *in-situ* separation of reaction products. All the tested reactive membranes were able to produce continuously solar fuels, during up to 8.5 h. The reuse of membrane during different operating days also revealed possible, provided the cooling step down to room temperature was slow enough and controlled. The influence of the main operating parameters was investigated. The temperature increase improved the CO production rate as it enhanced the oxygen mobility through the membrane due to the creation of oxygen vacancies. Increasing the total gas flow rate on the membrane oxidation side or the oxidant molar fraction, favored CO production as the membrane re-oxidation was boosted. Consequently, the fuel production rate was favored at high temperature, with high gas flow rate and high oxidant molar fraction on the oxidation side. The fuel production rate could be further enhanced by lowering the oxygen partial pressure on the reduction side using either mechanical pumping or thermochemical oxygen pumping.

Regarding the oxidant gas influence, CO_2 dissociation was more favorable than H_2O dissociation. Furthermore, H_2O causes thermal stress due to undesired steam condensation in the cold part of the membrane, probably responsible for membrane breakage. H_2 production in the solar membrane reactor will deserve further investigation as it offers capital interest for industry. Moreover, an innovative composite ceria-based membrane, coated with perovskite

materials, was implemented in the reactor. The perovskite coatings improved both O_2 and CO production rates as it boosted the creation of oxygen vacancies in the membrane materials. Both CSM and LSMMg coatings appeared to be promising to enhance the thermochemical performance of the pristine ceria membrane. The maximum CO production rate achieved 0.13 µmol/cm^2/s with PCC1 membrane at 1550 °C with a CO_2 molar fraction of 1.00 and a total flow rate on the oxidation side of 1.00 NL/min. These results outperformed by a factor of about x5, the data reported in the literature for a ceria membrane reactor. Such attractive performance could possibly result from more favorable oxidation conditions (higher inlet gas flow rates). Nevertheless, all the tested membranes were broken after few hours of utilization, mainly because of thermal stress and predominantly when injecting steam. This underlines the necessity to further enhance the thermo-mechanical resistance of the reactive membranes, in order to allow for longer time utilization with both CO_2 and H_2O, with day/night cycling. In future study, the ability of the reactive membrane to produce solar fuels over long duration during successive days should be demonstrated.

General conclusion and perspectives

Thermochemical H_2O and CO_2 splitting processes are a promising solution to free the worldwide energy production from fossil fuels and reach a carbon neutral economy. Indeed, two-step thermochemical cycles produce CO and H_2 with H_2O, CO_2 and heat as sole inputs, whereas a reactive metal oxide is regenerated. Thus the process can be considered as carbon neutral provided that the required energy input is renewable such as concentrated solar heat. The produced hydrogen can be directly used (*e.g.* in fuel cells) whereas syngas can be converted into valuable products such as liquid hydrocarbons with Fischer-Tropsch synthesis, or methanol. Furthermore, the oxygen produced during the reduction step can be stored and used for other applications.

This work focused on the experimental investigation of solar fuel production by CO_2 and H_2O splitting using non-stoichiometric oxides. A literature survey was performed to highlight the key parameters that can be used to improve thermochemical efficiency. Among them: the chemical composition and microstructure/morphology of the oxygen carrier, the reactor design and the operating parameters.

The approach used during this thesis to investigate the solar process is structured around the following points:

- Investigation of suitable chemical compositions for the redox materials involved in thermochemical cycles using experimental screening tests.
- Development and parametric study of the monolithic configuration of the SUNFUEL solar reactor to highlight relevant parameters enhancing the thermochemical performance.
- Experimental study of the impact of the reactive materials and their microstructure with respect to their shape (3D structures or particulate media) on the thermochemical performance.
- Design and parametric study of the membrane configuration of the SUNFUEL reactor with the use of two different types of membranes.

Perovskite oxides arose as a promising class of materials for thermochemical cycles, due to the large range of non-stoichiometry reachable along with their stability over a large range of operating conditions. Unlike ceria, thermodynamics is not favorable for the complete re-oxidation of perovskite materials and a large temperature swing between reduction and oxidation steps or an oxidant excess are usually required to increase the fuel production rate. However, the large amount of doping possibilities in perovskite materials offers great potential for tuning their thermodynamic properties. In light of the available data on the redox materials investigated so far, the most promising compositions were selected to experimentally study their redox activity. The reactive powders were synthesized with the Pechini method which provides a porous microstructure, especially suitable for thermochemical cycles, while their redox activity was first evaluated with thermogravimetric analysis. This experimental screening highlighted the difficulty to combine high reduction extent achievable by the reactive material with complete re-oxidation extent and fast reaction rates. From the redox activity study, $La_{0.5}Sr_{0.5}Mn_{0.9}Mg_{0.1}O_3$ (LSMMg) was pointed

out as a good compromise between redox activity for CO_2 splitting and thermal stability, appearing as a promising material for two-step thermochemical cycles.

Afterward, kinetic and thermodynamic characteristics of LSMMg redox reactions were extensively probed. The kinetic study of LSMMg revaled an evolution of the activation energy as a function of the reduction extent during the reduction reaction, which was never investigated before. The thermodynamic analysis was used to predict the theoretical performance of the oxygen carrier material and can be wisely applied to pre-select potential reactive materials. However, a thermodynamic study alone is not sufficient, as it does not consider practical considerations such as kinetic limitations or sintering effects. To alleviate this drawback, a kinetic study is necessary as it provides essential information and better understanding about reaction mechanisms and durations, which are key parameters for reactor design and large-scale implementation. Other tools such as density functional theory can be used to enlighten the choice of oxygen carriers. A detailed experimental study is also required to select a reactive material and validate its application for thermochemical cycles. Doping strategies in perovskite materials represent a pathway to overpass the thermochemical performance of ceria, the current state of the art material. Another class of emerging materials potentially suitable for thermochemical cycles is entropy-stabilized oxides, promoting configurational disorder into mixed oxide by populating a single sublattice with many distinct cations. Indeed, entropy-stabilized oxides were recently pointed out for their oxygen exchange capacity via reversible solid-solid phase transition. The suitability of this new material class for thermochemical cycles should be further investigated. Broadly speaking, the investigation of the reactive materials should aim to decrease the reduction temperature and the temperature swing between steps, and increase the reduction extent, while optimizing the re-oxidation extent and enhancing the kinetics. Furthermore, other criteria such as non-toxicity, availability of the material resource and environmental impact of material production and shaping should also orient the selection of a reactive material.

In this thesis, in addition to materials-related studies, a novel solar reactor was designed and developed at PROMES laboratory to produce solar fuels from CO_2 and H_2O splitting reactions. The reactor was designed to be scalable and flexible in order to perform either two-step thermochemical cycles (monolithic configuration) or continuous production of CO or H_2 by CO_2 or H_2O-splitting, with a reactive and oxygen permeable membrane (membrane configuration).

Firstly, an extensive parametric study of the monolithic reactor configuration during two-step redox cycles was performed. The strong impact of the operating parameters on the thermochemical performance was highlighted, especially on the reduction extent as well as the oxidation rate. The study of process performance sensitivity to operating parameters pointed out the beneficial effect of a high reduction temperature, low reduction pressure, high oxidant molar fraction and high gas flow rate during the oxidation step to enhance the thermochemical performance. Industrial reticulated porous ceramic (RPC) foams made of ceria and provided by ALSYS-CTI were used as reactive materials in the solar reactor. With such foams, the highest CO production rate (9.9 mL/min/g) was achieved with suitable operating conditions (reduction step at 1400°C with a reduced pressure ~100 mbar, and oxidation step under pure CO_2 and free cooling at temperature below 1050°C). The highest value reported so far in the literature reached 1.2 mL/min/g, with

more stringent conditions (reduction at 1500°C and 10 mbar). These first results highlighted the possibility to use industrial foams prepared via standard techniques directly in a solar reactor to produce solar fuels.

Another set of RPC foams made of ceria were coated with perovskite layer by IEM to investigate the performance of dual-phase composites. Given that LSMMg-coated ceria foam led to enhanced fuel production yield in comparison with pristine ceria, such an approach could be relevant to improve the overall system productivity. However, the production rate was decreased due to reactant diffusion limitations through the perovskite layer covering the reactive ceria surface. The re-oxidation extent reached by the perovskite-coated foam was directly linked to the oxidant molar fraction used during the oxidation step. The potential to improve the thermochemical performance by coupling ceria with adapted perovskite was highlighted. After cycling, although no performance decline was observed, an interaction between ceria and perovskite phases was evidenced (probably occurring in the presence of steam) and will require further investigation for unraveling the perovskite/ceria interaction mechanisms. The perovskite/ceria ratio, the perovskite coating formulation or the morphology and structure of the phase interface deserve investigation to further enhance the thermochemical performance. Besides, improving the volumetric solar absorption efficiency of the reactive material enhances the global process efficiency as it decreases the required solar power input to reach the target reduction temperature. The recent emergence of additive manufacturing processes allows to develop reactive structured materials with ordered geometry and hierarchical structure, able to enhance the volumetric solar absorptivity and providing homogeneous heating of the oxygen carrier. The first investigation of additive-manufactured ordered porous ceria monoliths made from 3D printed polymer scaffolds was done during this thesis. The developed materials reached decent fuel production during the thermochemical cycles performed in the solar reactor, demonstrating the interest of such an approach for concentrated solar applications.

Furthermore, different structured ceria materials in divided forms were also tested as packed beds in the solar reactor in order to compare their ability to split H_2O and CO_2. The investigated commercial-grade ceria pellets (prepared by sintering ceria fibers in the form of cylindrical pellets) showed very high fuel production rates (9.5 mL/min/g), pointing out the very good performance of commercially available reactive materials. Other alternative microstructures such as ceria porous microspheres and cork-templated biomimetic ceria ceramic structures were investigated as reactive materials in the solar reactor. Although the reactor design was not perfectly adapted for ceria microspheres, the potential application of such materials (prepared by IEM) to perform thermochemical cycles was demonstrated.

In addition, within a European project collaboration involving LNEG and the University of Aveiro (Portugal), cork-templated ceria particles also demonstrated good thermochemical performance, given that the highest fuel production rate achieved by this material was 3.1 mL/min/g, with good thermal stability during redox cycling. Furthermore, biomimetic ceramics were prepared with a "green" chemistry pathway and the resulting materials were successfully tested to split H_2O and CO_2. Using an indirectly-heated solar tubular reactor, the ceria granules prepared from green synthesis route offered average H_2 production yield which are 25% and 32% higher than those of

acetone-derived ecoceramic and replicated ceria foam, respectively. This demonstrates the possibility to produce efficient reactive ecoceramics using “green” chemistry. In the future, the material microstructure optimization should continue through application of shaping methods yielding materials microstructure with high specific surface and good stability under harsh environmental conditions. In this work, the reactive materials underwent up to 50 cycles, while no significant performance decline was observed, but the number of cycles still remains low in comparison with the number of cycles required for validating a process up-scale. Next studies should demonstrate the long-term stability of redox materials for industrial fuel production.

Finally, the membrane configuration of the SUNFUEL reactor was investigated with a detailed parametric study and different membrane structures (pure ceria or perovskite-coated ceria) in the form of dead-end tubes inserted inside the reactor cavity and directly irradiated. The pristine ceria supports were specially developed by ALSYS-CTI for the SUNFUEL project. For the first time, continuous and isothermal redox splitting of CO_2 (and H_2O) using an oxygen conducting membrane was demonstrated in a solar reactor using real concentrated solar flux. The reactive membranes underwent full day lasting few hours of on-sun operation, highlighting their resistance to high temperatures (over 1500°C) maintained in dwell. However, temperature gradients existing along the membrane length (from the fixing side on the support to the zone located in the irradiated cavity) caused strong thermal stresses and weaknesses. After their utilization, the membranes turned out to be fragile and required specific attention during heating and cooling steps. For solar process implementation, the membrane should resist to long on-sun operation duration and to heating/cooling cycles due to daily sun-cycling. In this respect, future research should focus on the improvement of the thermomechanical resistance of membranes, especially by minimizing thermal gradients. In addition, for future reactor design, cold point should be avoided to limit steam condensation which may be responsible for membrane failure.

Regarding membrane composition, perovskite-coated ceria membranes were found to outperform pure ceria membrane, pointing out the interest to boost the oxygen transfer rate by developing dual-phase membranes. Membranes made entirely of perovskites could also be investigated to offer higher oxygen conductivity at lower temperatures (below 1400°C). In addition, coating of perfectly dense thin layers on a porous support could provide an ideal microstructure with high available specific surface area on the oxidation side, able to further enhance the thermochemical performance. In this work, densified perovskite layers were deposited on both sides of ceria tubular supports and investigated in the solar reactor. Single coatings on each side of the support (not tested due to the lack of available supports) will need be studied to distinguish their individual effects. Moreover, the isothermal continuous solar fuel production could be further enhanced by lowering the oxygen partial pressure on the reduction side of the membrane. A first option would be to increase the inert gas flow, sweeping the released oxygen at the membrane surface, which induces energy penalty for inert gas recycling. The oxygen partial pressure can also be decreased by mechanical pumping. In this case, the reactive membrane should be perfectly sealed and completely dense to avoid any transfer of molecular gas species from the oxidation to the reduction side due to the pressure gradient. An alternative to mechanical pumping is thermochemical pumping for consuming only the released oxygen. For this option, a different reactor design including thermochemical pumping should be used.

The process scale-up is now an important step to consider large-scale development of solar fuel production. The feasibility of a solar reactor at lab-scale using ceria-based materials to split H_2O and CO_2 was evidenced. A demonstration at pilot-scale is required to probe the utilization of CO_2- and H_2O-splitting thermochemical process for the industrial production of solar fuels. Concurrently, an estimation of solar fuel production costs using experimental data including the entire process chain, from the reactive material fabrication to the solar installation costs should be carried out. A comparison of the economics related to both the investigated processes (two-step redox cycles vs. isothermal thermolysis via oxygen-conducting membranes) will provide realistic production costs, and will help to evaluate the economic competitiveness of solar fuel production by CO_2 and H_2O splitting reactions at high temperatures.

Regarding membrane composition, perovskite-coated ceria membranes were found to outperform pure ceria membrane, pointing out the interest to boost the oxygen transfer rate by developing dual-phase membranes. Membranes made entirely of perovskites could also be investigated to offer higher oxygen conductivity at lower temperatures (below 1400 °C). In addition, coating of perfectly dense thin layers on a porous support could provide an ideal microstructure with high available specific surface area on the oxidation side, able to further enhance the thermochemical performance. In this work, densified perovskite layers were deposited on both sides of ceria tubular supports and investigated in the solar reactor. Single coatings on each side of the support (not tested due to the lack of available supports) will need to be studied to distinguish their individual effects. Moreover, the isothermal continuous solar fuel production could be further enhanced by lowering the oxygen partial pressure on the reduction side of the membrane. A first option would be to increase the inert gas flow, sweeping the released oxygen at the membrane surface, which induces energy penalty for inert gas recycling. The oxygen partial pressure can also be decreased by mechanical pumping. In this case, the reactive membrane should be perfectly sealed and completely dense to avoid any transfer of molecular gas species from the oxidation to the reduction side due to the pressure gradient. An alternative to mechanical pumping is thermochemical pumping for consuming only the released oxygen. For this option, a different reactor design including thermochemical pumping should be used.

References

[1] "CO_2 Emissions from Fuel Combustion 2017 - Highlights," *International Energy Agency*, p. 162, 2017.

[2] D. Marxer, P. Furler, J. Scheffe, H. Geerlings, C. Falter, V. Batteiger, A. Sizmann, and A. Steinfeld, "Demonstration of the Entire Production Chain to Renewable Kerosene via Solar Thermochemical Splitting of H_2O and CO_2," *Energ. Fuel*, vol. 29, no. 5, pp. 3241–3250, 2015, doi: 10.1021/acs.energyfuels.5b00351.

[3] A. Farooqui, M. Boaro, J. Llorca, and M. Santarelli, "Solar Fuels via Two-Step Thermochemical Redox Cycles," in *Advances in Greener Energy Technologies*, A. K. Bhoi, K. S. Sherpa, A. Kalam, and G.-S. Chae, Eds. Singapore: Springer Singapore, 2020, pp. 31–84.

[4] D. A. Dimitrakis, "Thermochemical Water and Carbon Dioxide Redox Splitting for Neutral Carbon Footprint Solar Fuels: From Material to Reactor," Doctoral dissertation, Aristotle University of Thessaloniki, (Greece), 2017.

[5] M. Wang, Z. Wang, X. Gong, and Z. Guo, "The intensification technologies to water electrolysis for hydrogen production – A review," *Renewable and Sustainable Energy Reviews*, vol. 29, pp. 573–588, 2014, doi: 10.1016/j.rser.2013.08.090.

[6] K. Surla, "Hydrogène," *Techniques de l'ingénieur Fabrication des grands produits industriels en chimie et pétrochimie*, vol. base documentaire : TIB319DUO, no. ref. article : j6368, 2019.

[7] M. M. Rashid, M. K. Al Mesfer, H. Naseem, and M. Danish, "Hydrogen production by water electrolysis: a review of alkaline water electrolysis, PEM water electrolysis and high temperature water electrolysis," *Int. J. Eng. Adv. Technol*, vol. 4, no. 3, pp. 2249–8958, 2015.

[8] K. Zeng and D. Zhang, "Recent progress in alkaline water electrolysis for hydrogen production and applications," *Progress in Energy and Combustion Science*, vol. 36, no. 3, pp. 307–326, 2010, doi: 10.1016/j.pecs.2009.11.002.

[9] P. Millet, N. Mbemba, S. A. Grigoriev, V. N. Fateev, A. Aukauloo, and C. Etiévant, "Electrochemical performances of PEM water electrolysis cells and perspectives," *International Journal of Hydrogen Energy*, vol. 36, no. 6, pp. 4134–4142, 2011, doi: 10.1016/j.ijhydene.2010.06.105.

[10] I. Vincent and D. Bessarabov, "Low cost hydrogen production by anion exchange membrane electrolysis: A review," *Renewable and Sustainable Energy Reviews*, vol. 81, pp. 1690–1704, 2018, doi: 10.1016/j.rser.2017.05.258.

[11] M. Dehghanimadvar, R. Shirmohammadi, M. Sadeghzadeh, A. Aslani, and R. Ghasempour, "Hydrogen production technologies: Attractiveness and future perspective," *Int. J. Energy Res.*, 2020, doi: 10.1002/er.5508.

[12] A. Pareek, R. Dom, J. Gupta, J. Chandran, A. Vivek, and P. H. Borse, "Insights into renewable hydrogen energy: Recent advances and prospects," *Mater. Sci. Energy Technol.*, 2020, doi: 10.1016/j.mset.2019.12.002.

[13] T. Smolinka, E. T. Ojong, and J. Garche, "Hydrogen Production from Renewable Energies—Electrolyzer Technologies," in *Electrochemical Energy Storage for Renewable Sources and Grid Balancing*, Elsevier, 2015, pp. 103–128.

[14] S. D. Ebbesen and M. Mogensen, "Electrolysis of carbon dioxide in Solid Oxide Electrolysis Cells," *Journal of Power Sources*, vol. 193, no. 1, pp. 349–358, 2009, doi: 10.1016/j.jpowsour.2009.02.093.

[15] M. Lin and S. Haussener, "Techno-economic modeling and optimization of solar-driven high-temperature electrolysis systems," *Solar Energy*, vol. 155, pp. 1389–1402, 2017, doi: 10.1016/j.solener.2017.07.077.

[16] E. Touloupakis and G. Torzillo, "Photobiological hydrogen production," in *Solar Hydrogen Production*, Elsevier, 2019, pp. 511–525.

[17] G. Torzillo, A. Scoma, C. Faraloni, and L. Giannelli, "Advances in the biotechnology of hydrogen production with the microalga *Chlamydomonas reinhardtii*," *Critical Reviews in Biotechnology*, vol. 35, no. 4, pp. 485–496, 2015, doi: 10.3109/07388551.2014.900734.

[18] U. Albrecht, M. Altmann, F. Barth, U. Bünger, D. Fraile, J.-C. Lanoix, Pschorr-Schoberer, W. Vanhoudt, W. Weindorf, M. Zerta, and W. Zittel, "Study on hydrogen from renewable resources in the EU Final Report," Ludwig-Bölkow-SystemtechnikGmbH(LBST), 2015.

[19] B. Zhang and L. Sun, "Artificial photosynthesis: opportunities and challenges of molecular catalysts," *Chemical Society Reviews*, vol. 48, no. 7, pp. 2216–2264, 2019, doi: 10.1039/C8CS00897C.

[20] X. Meng, B. Eluagwule, M. Wang, L. Wang, and Jason, "Solar photocatalysis for environmental remediation," in *Handbook of Smart Photocatalytic Materials*, A. K. Mishra and C. M. Hussain, Eds. Elsevier, 2020.

[21] S.-H. Liu and H.-R. Syu, “One-step fabrication of N-doped mesoporous TiO_2 nanoparticles by self-assembly for photocatalytic water splitting under visible light,” *Applied Energy*, vol. 100, pp. 148–154, 2012, doi: 10.1016/j.apenergy.2012.03.063.

[22] M. Romero and A. Steinfeld, “Concentrating solar thermal power and thermochemical fuels,” *Energ. Environ. Sci.*, vol. 5, no. 11, p. 9234, 2012, doi: 10.1039/c2ee21275g.

[23] A. Ferrière, “Centrales solaires thermodynamiques,” *Techniques de l’ingénieur Énergies renouvelables*, vol. base documentaire : TIB594DUO., no. ref. article : be8903, 2008.

[24] H. Müller-Steinhagen and F. Trieb, “Concentrating solar power,” *A review of the technology. Ingenia Inform QR Acad Eng*, vol. 18, pp. 43–50, 2004.

[25] A. Steinfeld, “Solar thermochemical production of hydrogen—a review,” *Sol. Energy*, vol. 78, no. 5, pp. 603–615, 2005, doi: 10.1016/j.solener.2003.12.012.

[26] S. Abanades and G. Flamant, “Hydrogen production from solar thermal dissociation of methane in a high-temperature fluid-wall chemical reactor,” *Chemical Engineering and Processing: Process Intensification*, vol. 47, no. 3, pp. 490–498, 2008, doi: 10.1016/j.cep.2007.01.006.

[27] P. v. Zedtwitz, J. Petrasch, D. Trommer, and A. Steinfeld, “Hydrogen production via the solar thermal decarbonization of fossil fuels,” *Solar Energy*, vol. 80, no. 10, pp. 1333–1337, 2006, doi: 10.1016/j.solener.2005.06.007.

[28] C. Agrafiotis, H. von Storch, M. Roeb, and C. Sattler, “Solar thermal reforming of methane feedstocks for hydrogen and syngas production—A review,” *Renew. Sustain. Energ. Rev.*, vol. 29, pp. 656–682, 2014, doi: 10.1016/j.rser.2013.08.050.

[29] S. Chuayboon, S. Abanades, and S. Rodat, “Syngas production via solar-driven chemical looping methane reforming from redox cycling of ceria porous foam in a volumetric solar reactor,” *Chem. Eng. J.*, vol. 356, pp. 756–770, 2019, doi: 10.1016/j.cej.2018.09.072.

[30] N. Piatkowski, C. Wieckert, A. W. Weimer, and A. Steinfeld, “Solar-driven gasification of carbonaceous feedstock—a review,” *Energy & Environmental Science*, vol. 4, no. 1, pp. 73–82, 2011, doi: 10.1039/C0EE00312C.

[31] P. Lichty, C. Perkins, B. Woodruff, C. Bingham, and A. Weimer, “Rapid High Temperature Solar Thermal Biomass Gasification in a Prototype Cavity Reactor,” *J. Sol. Energy Eng*, vol. 132, no. 1, 2010, doi: 10.1115/1.4000356.

[32] R. F. Service, “Biomass Fuel Starts to See the Light,” *Science*, vol. 326, no. 5959, pp. 1474–1474, 2009, doi: 10.1126/science.326.5959.1474.

[33] S. Z. Baykara, “Experimental solar water thermolysis,” *Int. J. Hydrogen Energy*, vol. 29, no. 14, pp. 1459–1469, 2004, doi: 10.1016/j.ijhydene.2004.02.011.

[34] M. Lange, M. Roeb, C. Sattler, and R. Pitz-Paal, “T–S diagram efficiency analysis of two-step thermochemical cycles for solar water splitting under various process conditions,” *Energy*, vol. 67, pp. 298–308, 2014, doi: 10.1016/j.energy.2014.01.112.

[35] S. Abanades and M. Chambon, “CO_2 Dissociation and Upgrading from Two-Step Solar Thermochemical Processes Based on ZnO/Zn and SnO_2 /SnO Redox Pairs,” *Energ. Fuel*, vol. 24, no. 12, pp. 6667–6674, 2010, doi: 10.1021/ef101092u.

[36] S. Abanades, A. Legal, A. Cordier, G. Peraudeau, G. Flamant, and A. Julbe, “Investigation of reactive cerium-based oxides for H_2 production by thermochemical two-step water-splitting,” *J. Mater. Sci.*, vol. 45, no. 15, pp. 4163–4173, 2010, doi: 10.1007/s10853-010-4506-4.

[37] F. Call, M. Roeb, M. Schmücker, C. Sattler, and R. Pitz-Paal, “Ceria Doped with Zirconium and Lanthanide Oxides to Enhance Solar Thermochemical Production of Fuels,” *J. Phys. Chem. C*, vol. 119, no. 13, pp. 6929–6938, 2015, doi: 10.1021/jp508959y.

[38] T. Kodama, Y. Kondoh, R. Yamamoto, H. Andou, and N. Satou, “Thermochemical hydrogen production by a redox system of ZrO_2-supported Co(II)-ferrite,” *Sol. Energy*, vol. 78, no. 5, pp. 623–631, 2005, doi: 10.1016/j.solener.2004.04.008.

[39] J. E. Miller, M. D. Allendorf, R. B. Diver, L. R. Evans, N. P. Siegel, and J. N. Stuecker, “Metal oxide composites and structures for ultra-high temperature solar thermochemical cycles,” *J. Mater. Sci.*, vol. 43, no. 14, pp. 4714–4728, 2008, doi: 10.1007/s10853-007-2354-7.

[40] P. G. Loutzenhiser, M. E. Gálvez, I. Hischier, A. Stamatiou, A. Frei, and A. Steinfeld, “CO_2 Splitting via Two-Step Solar Thermochemical Cycles with Zn/ZnO and FeO/Fe_3O_4 Redox Reactions II: Kinetic Analysis,” *Energ. Fuel*, vol. 23, no. 5, pp. 2832–2839, 2009, doi: 10.1021/ef801142b.

[41] C. Agrafiotis, A. Zygogianni, C. Pagkoura, M. Kostoglou, and A. G. Konstandopoulos, “Hydrogen production via solar-aided water splitting thermochemical cycles with nickel ferrite: Experiments and modeling,” *AlChE J.*, vol. 59, no. 4, pp. 1213–1225, 2013, doi: 10.1002/aic.13882.

[42] M. Takacs, M. Hoes, M. Caduff, T. Cooper, J. R. Scheffe, and A. Steinfeld, “Oxygen nonstoichiometry, defect equilibria, and thermodynamic characterization of $LaMnO_3$ perovskites with Ca/Sr A-site and Al B-site doping,” *Acta Mater.*, vol. 103, pp. 700–710, 2016, doi: 10.1016/j.actamat.2015.10.026.

[43] Q. Jiang, J. Tong, G. Zhou, Z. Jiang, Z. Li, and C. Li, "Thermochemical CO_2 splitting reaction with supported $La_xA_{1-x}Fe_yB_{1-y}O_3$ (A=Sr, Ce, B=Co, Mn; $0 \leqslant x, y \leqslant 1$) perovskite oxides," *Sol. Energy*, vol. 103, pp. 425–437, 2014, doi: 10.1016/j.solener.2014.02.033.

[44] A. H. McDaniel, A. Ambrosini, E. N. Coker, J. E. Miller, W. C. Chueh, R. O'Hayre, and J. Tong, "Nonstoichiometric Perovskite Oxides for Solar Thermochemical H_2 and CO Production," *Energy Procedia*, vol. 49, pp. 2009–2018, 2014, doi: 10.1016/j.egypro.2014.03.213.

[45] R. J. Carrillo and J. R. Scheffe, "Advances and trends in redox materials for solar thermochemical fuel production," *Sol. Energy*, vol. 156, pp. 3–20, 2017, doi: 10.1016/j.solener.2017.05.032.

[46] D. Marxer, P. Furler, M. Takacs, and A. Steinfeld, "Solar thermochemical splitting of CO_2 into separate streams of CO and O_2 with high selectivity, stability, conversion, and efficiency," *Energ. Environ. Sci.*, vol. 10, no. 5, pp. 1142–1149, 2017, doi: 10.1039/C6EE03776C.

[47] N. P. Siegel, J. E. Miller, I. Ermanoski, R. B. Diver, and E. B. Stechel, "Factors Affecting the Efficiency of Solar Driven Metal Oxide Thermochemical Cycles," *Ind. Eng. Chem. Res.*, vol. 52, no. 9, pp. 3276–3286, 2013, doi: 10.1021/ie400193q.

[48] I. Dincer and C. Acar, "Review and evaluation of hydrogen production methods for better sustainability," *International Journal of Hydrogen Energy*, vol. 40, no. 34, pp. 11094–11111, 2015, doi: 10.1016/j.ijhydene.2014.12.035.

[49] F. Safari and I. Dincer, "A review and comparative evaluation of thermochemical water splitting cycles for hydrogen production," *Energy Convers. Manage.*, vol. 205, p. 112182, 2020, doi: 10.1016/j.enconman.2019.112182.

[50] M. Kubicek, A. H. Bork, and J. L. M. Rupp, "Perovskite oxides – a review on a versatile material class for solar-to-fuel conversion processes," *J. Mater. Chem. A*, vol. 5, no. 24, pp. 11983–12000, 2017, doi: 10.1039/C7TA00987A.

[51] W. C. Chueh and S. M. Haile, "A thermochemical study of ceria: exploiting an old material for new modes of energy conversion and CO_2 mitigation," *Phil. Trans. R. Soc. A*, vol. 368, no. 1923, pp. 3269–3294, 2010, doi: 10.1098/rsta.2010.0114.

[52] B. Meredig and C. Wolverton, "First-principles thermodynamic framework for the evaluation of thermochemical H_2O - or CO_2 - splitting materials," *Phys. Rev. B*, vol. 80, no. 24, pp. 245119–245126, 2009, doi: 10.1103/PhysRevB.80.245119.

[53] M. Takacs, J. R. Scheffe, and A. Steinfeld, "Oxygen nonstoichiometry and thermodynamic characterization of Zr doped ceria in the 1573–1773 K temperature range," *Phys. Chem. Chem. Phys.*, vol. 17, no. 12, pp. 7813–7822, 2015, doi: 10.1039/C4CP04916K.

[54] I. Al-Shankiti, B. D. Ehrhart, and A. W. Weimer, "Isothermal redox for H_2O and CO_2 splitting – A review and perspective," *Sol. Energy*, vol. 156, pp. 21–29, 2017, doi: 10.1016/j.solener.2017.05.028.

[55] B. Bulfin, J. Vieten, C. Agrafiotis, M. Roeb, and C. Sattler, "Applications and limitations of two step metal oxide thermochemical redox cycles; a review," *J. Mater. Chem. A*, vol. 5, no. 36, pp. 18951–18966, 2017, doi: 10.1039/C7TA05025A.

[56] J. R. Scheffe, D. Weibel, and A. Steinfeld, "Lanthanum–Strontium–Manganese perovskites as redox materials for solar thermochemical splitting of H_2O and CO_2," *Energ. Fuel*, vol. 27, no. 8, pp. 4250–4257, 2013, doi: 10.1021/ef301923h.

[57] T. C. Davenport, M. Kemei, M. J. Ignatowich, and S. M. Haile, "Interplay of material thermodynamics and surface reaction rate on the kinetics of thermochemical hydrogen production," *Int. J. Hydrogen Energy*, vol. 42, no. 27, pp. 16932–16945, 2017, doi: 10.1016/j.ijhydene.2017.05.184.

[58] T. Alessandro and F. Paolo, *Catalysis By Ceria And Related Materials (2nd Edition)*. World Scientific Publishing Company, 2013.

[59] H. Inaba and H. Tagawa, "Ceria-based solid electrolytes," *Solid State Ionics*, vol. 83, no. 1, pp. 1–16, 1996, doi: 10.1016/0167-2738(95)00229-4.

[60] N. Mahato, A. Gupta, and K. Balani, "Doped zirconia and ceria-based electrolytes for solid oxide fuel cells: a review," *Nanomaterials and Energy*, vol. 1, no. 1, pp. 27–45, 2012, doi: 10.1680/nme.11.00004.

[61] T. Montini, M. Melchionna, M. Monai, and P. Fornasiero, "Fundamentals and Catalytic Applications of CeO_2 -Based Materials," *Chem. Rev.*, vol. 116, no. 10, pp. 5987–6041, 2016, doi: 10.1021/acs.chemrev.5b00603.

[62] A. Trovarelli, "Catalytic Properties of Ceria and CeO_2 -Containing Materials," *Catal. Rev.*, vol. 38, no. 4, pp. 439–520, 1996, doi: 10.1080/01614949608006464.

[63] B. Bulfin, A. J. Lowe, K. A. Keogh, B. E. Murphy, O. Lübben, S. A. Krasnikov, and I. V. Shvets, "Analytical Model of CeO_2 Oxidation and Reduction," *J. Phys. Chem. C*, vol. 117, no. 46, pp. 24129–24137, 2013, doi: 10.1021/jp406578z.

[64] J. E. Miller, A. H. McDaniel, and M. D. Allendorf, "Considerations in the Design of Materials for Solar-Driven Fuel Production Using Metal-Oxide Thermochemical Cycles," *Adv. Energy Mater.*, vol. 4, no. 2, p. 1300469, 2014, doi: 10.1002/aenm.201300469.

[65] S. Abanades and G. Flamant, “Thermochemical hydrogen production from a two-step solar-driven water-splitting cycle based on cerium oxides,” *Sol. Energy*, vol. 80, no. 12, pp. 1611–1623, 2006, doi: 10.1016/j.solener.2005.12.005.

[66] W. C. Chueh and S. M. Haile, “Ceria as a Thermochemical Reaction Medium for Selectively Generating Syngas or Methane from H_2O and CO_2,” *ChemSusChem*, vol. 2, no. 8, pp. 735–739, 2009, doi: 10.1002/cssc.200900138.

[67] P. Furler, J. R. Scheffe, and A. Steinfeld, “Syngas production by simultaneous splitting of H_2O and CO_2 via ceria redox reactions in a high-temperature solar reactor,” *Energ. Environ. Sci.*, vol. 5, no. 3, pp. 6098–6103, 2012, doi: 10.1039/C1EE02620H.

[68] W. C. Chueh, C. Falter, M. Abbott, D. Scipio, P. Furler, S. M. Haile, and A. Steinfeld, “High-Flux Solar-Driven Thermochemical Dissociation of CO_2 and H_2O Using Nonstoichiometric Ceria,” *Science*, vol. 330, no. 6012, pp. 1797–1801, 2010, doi: 10.1126/science.1197834.

[69] J. R. Scheffe and A. Steinfeld, “Oxygen exchange materials for solar thermochemical splitting of H_2O and CO_2: a review,” *Mater. Today*, vol. 17, no. 7, pp. 341–348, 2014, doi: 10.1016/j.mattod.2014.04.025.

[70] N. R. Rhodes, M. M. Bobek, K. M. Allen, and D. W. Hahn, “Investigation of long term reactive stability of ceria for use in solar thermochemical cycles,” *Energy*, vol. 89, pp. 924–931, 2015, doi: 10.1016/j.energy.2015.06.041.

[71] A. H. McDaniel, “Renewable energy carriers derived from concentrating solar power and nonstoichiometric oxides,” *Curr. Opin. Green Sustainable Chem.*, vol. 4, pp. 37–43, 2017, doi: 10.1016/j.cogsc.2017.02.004.

[72] A. Haeussler, S. Abanades, J. Jouannaux, M. Drobek, A. Ayral, and A. Julbe, “Recent progress on ceria doping and shaping strategies for solar thermochemical water and CO_2 splitting cycles,” *AIMS Mater. Sci.*, vol. 6, no. 5, pp. 657–684, 2019, doi: 10.3934/matersci.2019.5.657.

[73] T. C. Davenport, C.-K. Yang, C. J. Kucharczyk, M. J. Ignatowich, and S. M. Haile, “Maximizing fuel production rates in isothermal solar thermochemical fuel production,” *Appl. Energy*, vol. 183, pp. 1098–1111, 2016, doi: 10.1016/j.apenergy.2016.09.012.

[74] Q.-L. Meng, C. Lee, S. Shigeta, H. Kaneko, and Y. Tamaura, “Solar hydrogen production using $Ce_{1-x}Li_xO_{2-\delta}$ solid solutions via a thermochemical, two-step water-splitting cycle,” *J. Solid State Chem.*, vol. 194, pp. 343–351, 2012, doi: 10.1016/j.jssc.2012.05.024.

[75] H. Kaneko, T. Miura, H. Ishihara, S. Taku, T. Yokoyama, H. Nakajima, and Y. Tamaura, “Reactive ceramics of CeO_2–MO_x (M=Mn, Fe, Ni, Cu) for H_2 generation by two-step water splitting using concentrated solar thermal energy,” *Energy*, vol. 32, no. 5, pp. 656–663, 2007, doi: 10.1016/j.energy.2006.05.002.

[76] J. R. Scheffe and A. Steinfeld, “Thermodynamic Analysis of Cerium-Based Oxides for Solar Thermochemical Fuel Production,” *Energ. Fuel*, vol. 26, no. 3, pp. 1928–1936, 2012, doi: 10.1021/ef201875v.

[77] Q.-L. Meng, C. Lee, T. Ishihara, H. Kaneko, and Y. Tamaura, “Reactivity of CeO_2-based ceramics for solar hydrogen production via a two-step water-splitting cycle with concentrated solar energy,” *Int. J. Hydrogen Energy*, vol. 36, no. 21, pp. 13435–13441, 2011, doi: 10.1016/j.ijhydene.2011.07.089.

[78] N. Jaiswal, D. Kumar, S. Upadhyay, and O. Parkash, “Effect of Mg and Sr co-doping on the electrical properties of ceria-based electrolyte materials for intermediate temperature solid oxide fuel cells,” *J. Alloy Comp.*, vol. 577, pp. 456–462, 2013, doi: 10.1016/j.jallcom.2013.06.094.

[79] C. Lee, Q.-L. Meng, H. Kaneko, and Y. Tamaura, “Solar Hydrogen Productivity of Ceria–Scandia Solid Solution Using Two-Step Water-Splitting Cycle,” *J. Sol. Energy Eng.*, vol. 135, no. 1, pp. 011002–011008, 2012, doi: 10.1115/1.4006876.

[80] J. R. Scheffe, R. Jacot, G. R. Patzke, and A. Steinfeld, “Synthesis, Characterization, and Thermochemical Redox Performance of Hf^{4+}, Zr^{4+}, and Sc^{3+} Doped Ceria for Splitting CO_2,” *J. Phys. Chem. C*, vol. 117, no. 46, pp. 24104–24114, 2013, doi: 10.1021/jp4050572.

[81] Q. Jiang, G. Zhou, Z. Jiang, and C. Li, “Thermochemical CO_2 splitting reaction with $Ce_xM_{1-x}O_{2-\delta}$ (M=Ti^{4+}, Sn^{4+}, Hf^{4+}, Zr^{4+}, La^{3+}, Y^{3+} and Sm^{3+}) solid solutions,” *Sol. Energy*, vol. 99, pp. 55–66, 2014, doi: 10.1016/j.solener.2013.10.021.

[82] E. V. Ramos-Fernandez, N. R. Shiju, and G. Rothenberg, “Understanding the solar-driven reduction of CO_2 on doped ceria,” *RSC Adv.*, vol. 4, no. 32, pp. 16456–16463, 2014, doi: 10.1039/C4RA01242A.

[83] N. Gokon, T. Suda, and T. Kodama, “Oxygen and hydrogen productivities and repeatable reactivity of 30-mol%-Fe-, Co-, Ni-, Mn-doped $CeO_{2-\delta}$ for thermochemical two-step water-splitting cycle,” *Energy*, vol. 90, pp. 1280–1289, 2015, doi: 10.1016/j.energy.2015.06.085.

[84] R. R. Bhosale and G. D. Takalkar, “Nanostructured co-precipitated $Ce_{0.9}Ln_{0.1}O_2$ (Ln = La, Pr, Sm, Nd, Gd, Tb, Dy, or Er) for thermochemical conversion of CO_2,” *Ceram. Int.*, vol. 44, no. 14, pp. 16688–16697, 2018, doi: 10.1016/j.ceramint.2018.06.096.

[85] Q.-L. Meng, C. Lee, H. Kaneko, and Y. Tamaura, "Solar thermochemical process for hydrogen production via two-step water splitting cycle based on $Ce_{1-x}Pr_xO_{2-\delta}$ redox reaction," *Thermochim. Acta*, vol. 532, pp. 134–138, 2012, doi: 10.1016/j.tca.2011.01.028.

[86] A. Bonk, A. C. Maier, M. V. F. Schlupp, D. Burnat, A. Remhof, R. Delmelle, A. Steinfeld, and U. F. Vogt, "The effect of dopants on the redox performance, microstructure and phase formation of ceria," *J. Power Sources*, vol. 300, pp. 261–271, 2015, doi: 10.1016/j.jpowsour.2015.09.073.

[87] R. Jacot, R. Moré, R. Michalsky, A. Steinfeld, and G. R. Patzke, "Trends in the phase stability and thermochemical oxygen exchange of ceria doped with potentially tetravalent metals," *J. Mater. Chem. A*, vol. 5, no. 37, pp. 19901–19913, 2017, doi: 10.1039/C7TA04063F.

[88] A. Le Gal and S. Abanades, "Dopant Incorporation in Ceria for Enhanced Water-Splitting Activity during Solar Thermochemical Hydrogen Generation," *J. Phys. Chem. C*, vol. 116, no. 25, pp. 13516–13523, 2012, doi: 10.1021/jp302146c.

[89] C. Muhich and A. Steinfeld, "Principles of doping ceria for the solar thermochemical redox splitting of H_2O and CO_2," *J. Mater. Chem. A*, vol. 5, no. 30, pp. 15578–15590, 2017, doi: 10.1039/C7TA04000H.

[90] D. A. Andersson, S. I. Simak, N. V. Skorodumova, I. A. Abrikosov, and B. Johansson, "Theoretical study of CeO_2 doped with tetravalent ions," *Phys. Rev. B*, vol. 76, no. 17, pp. 174119–174129, 2007, doi: 10.1103/PhysRevB.76.174119.

[91] S. Abanades and A. Le Gal, "CO_2 splitting by thermo-chemical looping based on $Zr_xCe_{1-x}O_2$ oxygen carriers for synthetic fuel generation," *Fuel*, vol. 102, pp. 180–186, 2012, doi: 10.1016/j.fuel.2012.06.068.

[92] P. Fornasiero, R. Dimonte, G. R. Rao, J. Kaspar, S. Meriani, A. Trovarelli, and M. Graziani, "Rh-Loaded CeO_2-ZrO_2 Solid-Solutions as Highly Efficient Oxygen Exchangers: Dependence of the Reduction Behavior and the Oxygen Storage Capacity on the Structural-Properties," *J. Catal.*, vol. 151, no. 1, pp. 168–177, 1995, doi: 10.1006/jcat.1995.1019.

[93] A. Le Gal and S. Abanades, "Catalytic investigation of ceria-zirconia solid solutions for solar hydrogen production," *Int. J. Hydrogen Energy*, vol. 36, no. 8, pp. 4739–4748, 2011, doi: 10.1016/j.ijhydene.2011.01.078.

[94] G. Vlaic, P. Fornasiero, S. Geremia, J. Kašpar, and M. Graziani, "Relationship between the Zirconia-Promoted Reduction in the Rh-Loaded $Ce_{0.5}Zr_{0.5}O_2$ Mixed Oxide and the Zr–O Local Structure," *J. Catal.*, vol. 168, no. 2, pp. 386–392, 1997, doi: 10.1006/jcat.1997.1644.

[95] C. Muhich, M. Hoes, and A. Steinfeld, "Mimicking tetravalent dopant behavior using paired charge compensating dopants to improve the redox performance of ceria for thermochemically splitting H2O and CO2," *Acta Mater.*, vol. 144, pp. 728–737, 2018, doi: 10.1016/j.actamat.2017.11.022.

[96] A. Le Gal, S. Abanades, N. Bion, T. Le Mercier, and V. Harlé, "Reactivity of Doped Ceria-Based Mixed Oxides for Solar Thermochemical Hydrogen Generation via Two-Step Water-Splitting Cycles," *Energ. Fuel*, vol. 27, no. 10, pp. 6068–6078, 2013, doi: 10.1021/ef4014373.

[97] B. Bulfin, M. Lange, L. de Oliveira, M. Roeb, and C. Sattler, "Solar thermochemical hydrogen production using ceria zirconia solid solutions: Efficiency analysis," *Int. J. Hydrogen Energy*, vol. 41, no. 42, pp. 19320–19328, 2016, doi: 10.1016/j.ijhydene.2016.05.211.

[98] M. A. Ganzoury, S.-E. K. Fateen, S. T. El Sheltawy, A. M. Radwan, and N. K. Allam, "Thermodynamic and efficiency analysis of solar thermochemical water splitting using Ce–Zr mixtures," *Sol. Energy*, vol. 135, pp. 154–162, 2016, doi: 10.1016/j.solener.2016.05.053.

[99] A. Le Gal, S. Abanades, and G. Flamant, "CO_2 and H_2O Splitting for Thermochemical Production of Solar Fuels Using Nonstoichiometric Ceria and Ceria/Zirconia Solid Solutions," *Energ. Fuel*, vol. 25, no. 10, pp. 4836–4845, 2011, doi: 10.1021/ef200972r.

[100] C. L. Muhich, S. Blaser, M. C. Hoes, and A. Steinfeld, "Comparing the solar-to-fuel energy conversion efficiency of ceria and perovskite based thermochemical redox cycles for splitting H_2O and CO_2," *Int. J. Hydrogen Energy*, vol. 43, no. 41, pp. 18814–18831, 2018, doi: 10.1016/j.ijhydene.2018.08.137.

[101] M. Kang, J. Zhang, C. Wang, F. Wang, N. Zhao, F. Xiao, W. Wei, and Y. Sun, "CO_2 splitting via two step thermochemical reactions over doped ceria/zirconia solid solutions," *RSC Adv.*, vol. 3, no. 41, pp. 18878–18885, 2013, doi: 10.1039/c3ra43742f.

[102] M. Kang, X. Wu, J. Zhang, N. Zhao, W. Wei, and Y. Sun, "Enhanced thermochemical CO_2 splitting over Mg- and Ca-doped ceria/zirconia solid solutions," *RSC Adv.*, vol. 4, no. 11, pp. 5583–5590, 2014, doi: 10.1039/c3ra45595e.

[103] R. R. Bhosale, A. Kumar, F. AlMomani, U. Ghosh, S. Al-Muhtaseb, R. Gupta, and I. Alxneit, "Assessment of $Ce_xZr_yHf_zO_2$ based oxides as potential solar thermochemical CO_2 splitting materials," *Ceram. Int.*, vol. 42, no. 8, pp. 9354–9362, 2016, doi: 10.1016/j.ceramint.2016.02.100.

[104] R. Jacot, J. M. Naik, R. Moré, R. Michalsky, A. Steinfeld, and G. R. Patzke, "Reactive stability of promising scalable doped ceria materials for thermochemical two-step CO_2 dissociation," *J. Mater. Chem. A*, vol. 6, no. 14, pp. 5807–5816, 2018, doi: 10.1039/C7TA10966K.

[105] Q.-L. Meng and Y. Tamaura, "Enhanced hydrogen production by doping Pr into $Ce_{0.9}Hf_{0.1}O_2$ for thermochemical two-step water-splitting cycle," *J. Phys. Chem. Solids*, vol. 75, no. 3, pp. 328–333, 2014, doi: 10.1016/j.jpcs.2013.07.023.

[106] F. Lin, A. Wokaun, and I. Alxneit, "Rh-doped Ceria: Solar Organics From H_2O, CO_2 and Sunlight?," *Energy Procedia*, vol. 69, pp. 1790–1799, 2015, doi: 10.1016/j.egypro.2015.03.151.

[107] S. Mostrou, R. Büchel, S. E. Pratsinis, and J. A. van Bokhoven, "Improving the ceria-mediated water and carbon dioxide splitting through the addition of chromium," *Appl. Catal. A.*, vol. 537, pp. 40–49, 2017, doi: 10.1016/j.apcata.2017.03.001.

[108] M. Hoes, C. L. Muhich, R. Jacot, G. R. Patzke, and A. Steinfeld, "Thermodynamics of paired charge-compensating doped ceria with superior redox performance for solar thermochemical splitting of H_2O and CO_2," *J. Mater. Chem. A*, vol. 5, no. 36, pp. 19476–19484, 2017, doi: 10.1039/C7TA05824A.

[109] H. Kaneko, H. Ishihara, S. Taku, Y. Naganuma, N. Hasegawa, and Y. Tamaura, "Cerium ion redox system in $CeO_{2-x}Fe_2O_3$ solid solution at high temperatures (1273–1673 K) in the two-step water-splitting reaction for solar H_2 generation," *J. Mater. Sci.*, vol. 43, no. 9, pp. 3153–3161, 2008, doi: 10.1007/s10853-008-2499-z.

[110] H. Kaneko and Y. Tamaura, "Reactivity and XAFS study on $(1-x)CeO_2$–xNiO (x=0.025–0.3) system in the two-step water-splitting reaction for solar H_2 production," *J. Phys. Chem. Solids*, vol. 70, no. 6, pp. 1008–1014, 2009, doi: 10.1016/j.jpcs.2009.05.015.

[111] F. Lin, V. A. Samson, A. O. Wismer, D. Grolimund, I. Alxneit, and A. Wokaun, "Zn-modified ceria as a redox material for thermochemical H_2O and CO_2 splitting: effect of a secondary ZnO phase on its thermochemical activity," *CrystEngComm*, vol. 18, no. 14, pp. 2559–2569, 2016, doi: 10.1039/C6CE00430J.

[112] A. Evdou, V. Zaspalis, and L. Nalbandian, "$La_{(1-x)}Sr_xMnO_{3-\delta}$ perovskites as redox materials for the production of high purity hydrogen," *Int. J. Hydrogen Energy*, vol. 33, no. 20, pp. 5554–5562, 2008, doi: 10.1016/j.ijhydene.2008.06.036.

[113] M. A. Peña and J. L. G. Fierro, "Chemical structures and performance of perovskite oxides," *Chem. Rev.*, vol. 101, no. 7, pp. 1981–2018, 2001, doi: 10.1021/cr980129f.

[114] J. Sunarso, S. S. Hashim, N. Zhu, and W. Zhou, "Perovskite oxides applications in high temperature oxygen separation, solid oxide fuel cell and membrane reactor: A review," *Prog. Energy Combust. Sci.*, vol. 61, pp. 57–77, 2017, doi: 10.1016/j.pecs.2017.03.003.

[115] K. J. Albrecht, G. S. Jackson, and R. J. Braun, "Thermodynamically consistent modeling of redox-stable perovskite oxides for thermochemical energy conversion and storage," *Appl. Energy*, vol. 165, pp. 285–296, 2016, doi: 10.1016/j.apenergy.2015.11.098.

[116] T. Ishihara, Ed., *Perovskite oxide for solid oxide fuel cells*. Boston, MA: Springer US, 2009.

[117] A. A. Emery, J. E. Saal, S. Kirklin, V. I. Hegde, and C. Wolverton, "High-throughput computational screening of perovskites for thermochemical water splitting applications," *Chem. Mater.*, vol. 28, no. 16, pp. 5621–5634, 2016, doi: 10.1021/acs.chemmater.6b01182.

[118] A. Haeussler, S. Abanades, J. Jouannaux, and A. Julbe, "Non-Stoichiometric Redox Active Perovskite Materials for Solar Thermochemical Fuel Production: A Review," *Catalysts*, vol. 8, no. 12, pp. 611–631, 2018, doi: 10.3390/catal8120611.

[119] C.-K. Yang, Y. Yamazaki, A. Aydin, and S. M. Haile, "Thermodynamic and kinetic assessments of strontium-doped lanthanum manganite perovskites for two-step thermochemical water splitting," *J. Mater. Chem. A*, vol. 2, no. 33, pp. 13612–13623, 2014, doi: 10.1039/C4TA02694B.

[120] C. Agrafiotis, M. Roeb, and C. Sattler, "A review on solar thermal syngas production via redox pair-based water/carbon dioxide splitting thermochemical cycles," *Renew. Sustain. Energ. Rev.*, vol. 42, pp. 254–285, 2015, doi: 10.1016/j.rser.2014.09.039.

[121] A. Demont, S. Abanades, and E. Beche, "Investigation of Perovskite Structures as Oxygen-Exchange Redox Materials for Hydrogen Production from Thermochemical Two-Step Water-Splitting Cycles," *J. Phys. Chem. C*, vol. 118, no. 24, pp. 12682–12692, 2014, doi: 10.1021/jp5034849.

[122] J. H. Kuo, H. U. Anderson, and D. M. Sparlin, "Oxidation-reduction behavior of undoped and Sr-doped $LaMnO_3$ nonstoichiometry and defect structure," *J. Solid State Chem.*, vol. 83, no. 1, pp. 52–60, 1989, doi: 10.1016/0022-4596(89)90053-4.

[123] J. Mizusaki, "Oxygen nonstoichiometry and defect equilibrium in the perovskite-type oxides $La_{1-x}Sr_xMnO_{3+d}$," *Solid State Ionics*, vol. 129, no. 1–4, pp. 163–177, 2000, doi: 10.1016/S0167-2738(99)00323-9.

[124] S. Dey and C. N. R. Rao, "Splitting of CO_2 by Manganite Perovskites to Generate CO by Solar Isothermal Redox Cycling," *ACS Energy Lett.*, vol. 1, no. 1, pp. 237–243, 2016, doi: 10.1021/acsenergylett.6b00122.

[125] A. Demont and S. Abanades, "Solar thermochemical conversion of CO_2 into fuel via two-step redox cycling of non-stoichiometric Mn-containing perovskite oxides," *J. Mater. Chem. A*, vol. 3, no. 7, pp. 3536–3546, 2015, doi: 10.1039/C4TA06655C.

[126] D. Maiti, B. J. Hare, Y. A. Daza, A. E. Ramos, J. N. Kuhn, and V. R. Bhethanabotla, "Earth abundant perovskite oxides for low temperature CO_2 conversion," *Energy Environ. Sci.*, vol. 11, no. 3, pp. 648–659, 2018, doi: 10.1039/C7EE03383D.

[127] L. Wang, M. Al-Mamun, P. Liu, Y. L. Zhong, Y. Wang, H. G. Yang, and H. Zhao, "Enhanced Thermochemical H_2 Production on Ca-Doped Lanthanum Manganite Perovskites Through Optimizing the Dopant Level and Re-oxidation Temperature," *Acta Metall. Sinica*, vol. 31, no. 4, pp. 431–439, 2018, doi: 10.1007/s40195-018-0715-7.

[128] C. N. R. Rao and S. Dey, "Generation of H_2 and CO by solar thermochemical splitting of H_2O and CO_2 by employing metal oxides," *J. Solid State Chem.*, vol. 242, pp. 107–115, 2016, doi: 10.1016/j.jssc.2015.12.018.

[129] M. Ezbiri, "Design of perovskite redox materials for the thermochemical splitting of H_2O and CO_2 and for O_2 separation," Doctoral dissertation, ETH Zurich, (Switzerland), 2017.

[130] S. Dey, B. S. Naidu, and C. N. R. Rao, "$Ln_{0.5}A_{0.5}MnO_3$ (Ln=Lanthanide, A= Ca, Sr) Perovskites Exhibiting Remarkable Performance in the Thermochemical Generation of CO and H_2 from CO_2 and H_2 O," *Chem. Eur. J.*, vol. 21, no. 19, pp. 7077–7081, 2015, doi: 10.1002/chem.201500442.

[131] S. Dey, B. S. Naidu, A. Govindaraj, and C. N. R. Rao, "Noteworthy performance of $La_{1-x}Ca_xMnO_3$ perovskites in generating H_2 and CO by the thermochemical splitting of H_2O and CO_2," *Phys. Chem. Chem. Phys.*, vol. 17, no. 1, pp. 122–125, 2015, doi: 10.1039/C4CP04578E.

[132] C. N. R. Rao and S. Dey, "Solar thermochemical splitting of water to generate hydrogen," *PNAS*, p. 201700104, 2017, doi: 10.1073/pnas.1700104114.

[133] A. Demont and S. Abanades, "High redox activity of Sr-substituted lanthanum manganite perovskites for two-step thermochemical dissociation of CO_2," *RSC Adv.*, vol. 4, no. 97, pp. 54885–54891, 2014, doi: 10.1039/C4RA10578H.

[134] M. M. Nair and S. Abanades, "Experimental screening of perovskite oxides as efficient redox materials for solar thermochemical CO_2 conversion," *Sustainable Energy Fuels*, vol. 2, no. 4, pp. 843–854, 2018, doi: 10.1039/C7SE00516D.

[135] T. Cooper, J. R. Scheffe, M. E. Galvez, R. Jacot, G. Patzke, and A. Steinfeld, "Lanthanum Manganite Perovskites with Ca/Sr A-site and Al B-site Doping as Effective Oxygen Exchange Materials for Solar Thermochemical Fuel Production," *Energy Technol.*, vol. 3, no. 11, pp. 1130–1142, 2015, doi: 10.1002/ente.201500226.

[136] A. H. McDaniel, E. C. Miller, D. Arifin, A. Ambrosini, E. N. Coker, R. O'Hayre, W. C. Chueh, and J. Tong, "Sr- and Mn-doped $LaAlO_{3-\delta}$ for solar thermochemical H_2 and CO production," *Energ. Environ. Sci.*, vol. 6, no. 8, pp. 2424–2428, 2013, doi: 10.1039/c3ee41372a.

[137] J. E. Miller, A. Ambrosini, E. N. Coker, M. D. Allendorf, and A. H. McDaniel, "Advancing Oxide Materials for Thermochemical Production of Solar Fuels," *Energy Procedia*, vol. 49, pp. 2019–2026, 2014, doi: 10.1016/j.egypro.2014.03.214.

[138] D. Sastre, A. J. Carrillo, D. P. Serrano, P. Pizarro, and J. M. Coronado, "Exploring the Redox Behavior of $La_{0.6}Sr_{0.4}Mn_{1-x}Al_xO_3$ Perovskites for CO_2-Splitting in Thermochemical Cycles," *Top. Catal.*, vol. 60, no. 15–16, pp. 1108–1118, 2017, doi: 10.1007/s11244-017-0790-4.

[139] S. Cimino, L. Lisi, S. De Rossi, M. Faticanti, and P. Porta, "Methane combustion and CO oxidation on $LaAl_{1-x}Mn_xO_3$ perovskite-type oxide solid solutions," *Appl. Catal. B Environ.*, vol. 43, no. 4, pp. 397–406, 2003, doi: 10.1016/S0926-3373(03)00023-7.

[140] A. M. Deml, V. Stevanović, A. M. Holder, M. Sanders, R. O'Hayre, and C. B. Musgrave, "Tunable Oxygen Vacancy Formation Energetics in the Complex Perovskite Oxide $Sr_xLa_{1-x}Mn_yAl_{1-y}O_3$," *Chem. Mater.*, vol. 26, no. 22, pp. 6595–6602, 2014, doi: 10.1021/cm5033755.

[141] Yuta Sugiyama, Nobuyuki Gokon, Hyun-Seok Cho, Selvan Bellan, Tsuyoshi Hatamachi, and Tatsuya Kodama, "Thermochemical two-step water-splitting using perovskite oxide for solar hydrogen production," in *ACTS-P00577*, Jeju Island, Korea, 2017.

[142] M. M. Nair and S. Abanades, "Insights into the Redox Performance of Non-stoichiometric Lanthanum Manganite Perovskites for Solar Thermochemical CO_2 Splitting," *ChemistrySelect*, vol. 1, no. 15, pp. 4449–4457, 2016, doi: 10.1002/slct.201601171.

[143] L. Wang, M. Al-Mamun, P. Liu, Y. Wang, H. Gui Yang, and H. Zhao, "$La_{1-x}Ca_xMn_{1-y}Al_yO_3$ perovskites as efficient catalysts for two-step thermochemical water splitting in conjunction with exceptional hydrogen yields," *Chin. J. Catal.*, vol. 38, no. 6, pp. 1079–1086, 2017, doi: 10.1016/S1872-2067(17)62820-1.

[144] M. E. Gálvez, R. Jacot, J. Scheffe, T. Cooper, G. Patzke, and A. Steinfeld, "Physico-chemical changes in Ca, Sr and Al-doped La–Mn–O perovskites upon thermochemical splitting of CO_2 via redox cycling," *Phys. Chem. Chem. Phys.*, vol. 17, no. 9, pp. 6629–6634, 2015, doi: 10.1039/C4CP05898D.

[145] L. Wang, M. Al-Mamun, Y. L. Zhong, L. Jiang, P. Liu, Y. Wang, H. G. Yang, and H. Zhao, "Ca^{2+} and Ga^{3+} doped $LaMnO_3$ perovskite as a highly efficient and stable catalyst for two-step thermochemical water splitting," *Sustainable Energy Fuels*, vol. 1, no. 5, pp. 1013–1017, 2017, doi: 10.1039/C6SE00097E.

[146] S. Dey, B. S. Naidu, and C. N. R. Rao, "Beneficial effects of substituting trivalent ions in the B-site of $La_{0.5}Sr_{0.5}Mn_{1-x}A_xO_3$ (A = Al, Ga, Sc) on the thermochemical generation of CO and H_2 from CO_2 and H_2O," *Dalton Trans.*, vol. 45, no. 6, pp. 2430–2435, 2016, doi: 10.1039/C5DT04822B.

[147] G. Luciani, G. Landi, A. Aronne, and A. Di Benedetto, "Partial substitution of B cation in $La_{0.6}Sr_{0.4}MnO_3$ perovskites: A promising strategy to improve the redox properties useful for solar thermochemical water and carbon dioxide splitting," *Sol. Energy*, vol. 171, pp. 1–7, 2018, doi: 10.1016/j.solener.2018.06.058.

[148] L. Wang, M. Al-Mamun, P. Liu, Y. Wang, H. G. Yang, and H. Zhao, "Notable hydrogen production on $La_xCa_{1-x}CoO_3$ perovskites via two-step thermochemical water splitting," *J. Mater. Sci.*, vol. 53, no. 9, pp. 6796–6806, 2018, doi: 10.1007/s10853-018-2004-2.

[149] M. Orfila, M. Linares, R. Molina, J. Á. Botas, R. Sanz, and J. Marugán, "Perovskite materials for hydrogen production by thermochemical water splitting," *Int. J. Hydrogen Energy*, vol. 41, no. 42, pp. 19329–19338, 2016, doi: 10.1016/j.ijhydene.2016.07.041.

[150] L. Wang, M. Al-Mamun, Y. L. Zhong, P. Liu, Y. Wang, H. G. Yang, and H. Zhao, "Enhanced Thermochemical Water Splitting through Formation of Oxygen Vacancy in $La_{0.6}Sr_{0.4}BO_{3-\delta}$ (B=Cr, Mn, Fe, Co, and Ni) Perovskites," *ChemPlusChem*, vol. 83, no. 10, pp. 924–928, 2018, doi: 10.1002/cplu.201800178.

[151] A. H. Bork, M. Kubicek, M. Struzik, and J. L. M. Rupp, "Perovskite $La_{0.6}Sr_{0.4}Cr_{1-x}Co_xO_{3-\delta}$ solid solutions for solar-thermochemical fuel production: strategies to lower the operation temperature," *J. Mater. Chem. A*, vol. 3, no. 30, pp. 15546–15557, 2015, doi: 10.1039/C5TA02519B.

[152] R. D. Shannon, "Revised effective ionic radii and systematic studies of interatomic distances in halides and chalcogenides," *Acta Crystallogr., Sect. A: Found. Crystallogr.*, vol. 32, no. 5, pp. 751–767, 1976, doi: 10.1107/S0567739476001551.

[153] P. P. Rodenbough and S.-W. Chan, "Thermal oxygen exchange cycles in mixed manganese perovskites," *Ceram. Int.*, vol. 44, no. 2, pp. 1343–1347, 2018, doi: 10.1016/j.ceramint.2017.08.168.

[154] D. R. Barcellos, M. D. Sanders, J. Tong, A. H. McDaniel, and R. P. O'Hayre, "$BaCe_{0.25}Mn_{0.75}O_{3-\delta}$ —a promising perovskite-type oxide for solar thermochemical hydrogen production," *Energ. Environ. Sci.*, vol. 11, pp. 3256–3265, 2018, doi: 10.1039/C8EE01989D.

[155] D. Yadav and R. Banerjee, "A review of solar thermochemical processes," *Renew. Sustain. Energ. Rev.*, vol. 54, pp. 497–532, 2016, doi: 10.1016/j.rser.2015.10.026.

[156] W. T. Gibbons, L. J. Venstrom, R. M. De Smith, J. H. Davidson, and G. S. Jackson, "Ceria-based electrospun fibers for renewable fuel production via two-step thermal redox cycles for carbon dioxide splitting," *Phys. Chem. Chem. Phys.*, vol. 16, no. 27, pp. 14271–14280, 2014, doi: 10.1039/C4CP01974A.

[157] A. C. Gladen and J. H. Davidson, "The morphological stability and fuel production of commercial fibrous ceria particles for solar thermochemical redox cycling," *Sol. Energy*, vol. 139, pp. 524–532, 2016, doi: 10.1016/j.solener.2016.10.029.

[158] P. Furler, J. Scheffe, D. Marxer, M. Gorbar, A. Bonk, U. Vogt, and A. Steinfeld, "Thermochemical CO_2 splitting *via* redox cycling of ceria reticulated foam structures with dual-scale porosities," *Phys. Chem. Chem. Phys.*, vol. 16, no. 22, pp. 10503–10511, 2014, doi: 10.1039/C4CP01172D.

[159] P. Furler, J. Scheffe, M. Gorbar, L. Moes, U. Vogt, and A. Steinfeld, "Solar Thermochemical CO_2 Splitting Utilizing a Reticulated Porous Ceria Redox System," *Energ. Fuel*, vol. 26, no. 11, pp. 7051–7059, 2012, doi: 10.1021/ef3013757.

[160] M. Takacs, S. Ackermann, A. Bonk, M. Neises-von Puttkamer, Ph. Haueter, J. R. Scheffe, U. F. Vogt, and A. Steinfeld, "Splitting CO_2 with a ceria-based redox cycle in a solar-driven thermogravimetric analyzer," *AIChE J.*, vol. 63, no. 4, pp. 1263–1271, 2017, doi: 10.1002/aic.15501.

[161] H. S. Cho, T. Myojin, S. Kawakami, N. Gokon, T. Kodama, Y. H. Kang, S. N. Lee, K. K. Chai, H. K. Yoon, and H. J. Lee, "Solar Demonstration of Thermochemical Two-step Water Splitting Cycle Using CeO_2/MPSZ Ceramic foam Device by $45kW_{th}$ KIER Solar Furnace," *Energy Procedia*, vol. 49, pp. 1922–1931, 2014, doi: 10.1016/j.egypro.2014.03.204.

[162] S. Ackermann, J. Scheffe, J. Duss, and A. Steinfeld, "Morphological Characterization and Effective Thermal Conductivity of Dual-Scale Reticulated Porous Structures," *Materials*, vol. 7, no. 12, pp. 7173–7195, 2014, doi: 10.3390/ma7117173.

[163] L. J. Venstrom, N. Petkovich, S. Rudisill, A. Stein, and J. H. Davidson, "The Effects of Morphology on the Oxidation of Ceria by Water and Carbon Dioxide," *J. Sol. Energ. Eng.*, vol. 134, no. 1, pp. 011005–011012, 2012, doi: 10.1115/1.4005119.

[164] N. D. Petkovich, S. G. Rudisill, L. J. Venstrom, D. B. Boman, J. H. Davidson, and A. Stein, "Control of Heterogeneity in Nanostructured $Ce_{1-x}Zr_xO_2$ Binary Oxides for Enhanced Thermal Stability and Water Splitting Activity," *J. Phys. Chem. C*, vol. 115, no. 43, pp. 21022–21033, 2011, doi: 10.1021/jp2071315.

[165] F. A. Costa Oliveira, M. A. Barreiros, S. Abanades, A. P. F. Caetano, R. M. Novais, and R. C. Pullar, "Solar thermochemical CO_2 splitting using cork-templated ceria ecoceramics," *J. CO_2 Util.*, vol. 26, pp. 552–563, 2018, doi: 10.1016/j.jcou.2018.06.015.

[166] C. D. Malonzo, R. M. De Smith, S. G. Rudisill, N. D. Petkovich, J. H. Davidson, and A. Stein, "Wood-Templated CeO_2 as Active Material for Thermochemical CO Production," *J. Phys. Chem. C*, vol. 118, no. 45, pp. 26172–26181, 2014, doi: 10.1021/jp5083449.

[167] B. J. Hathaway, R. Bala Chandran, A. C. Gladen, T. R. Chase, and J. H. Davidson, "Demonstration of a Solar Reactor for Carbon Dioxide Splitting via the Isothermal Ceria Redox Cycle and Practical Implications," *Energ. Fuel*, vol. 30, no. 8, pp. 6654–6661, 2016, doi: 10.1021/acs.energyfuels.6b01265.

[168] B. J. Hathaway, R. Bala Chandran, S. Sedler, D. Thomas, A. Gladen, T. Chase, and J. H. Davidson, "Effect of Flow Rates on Operation of a Solar Thermochemical Reactor for Splitting CO_2 Via the Isothermal Ceria Redox Cycle," *J. Sol. Energy Eng.*, vol. 138, no. 1, p. 011007, 2015, doi: 10.1115/1.4032019.

[169] R. B. Diver, J. E. Miller, N. P. Siegel, and T. A. Moss, "Testing of a CR5 Solar Thermochemical Heat Engine Prototype," in *ASME 2010 4th International Conference on Energy Sustainability, Volume 2*, Phoenix, Arizona, USA, 2010, pp. 97–104, doi: 10.1115/ES2010-90093.

[170] R. B. Diver, J. E. Miller, M. D. Allendorf, N. P. Siegel, and R. E. Hogan, "Solar Thermochemical Water-Splitting Ferrite-Cycle Heat Engines," *J. Sol. Energy Eng.*, vol. 130, no. 4, p. 041001, 2008, doi: 10.1115/1.2969781.

[171] E. Koepf, S. G. Advani, A. Steinfeld, and A. K. Prasad, "A novel beam-down, gravity-fed, solar thermochemical receiver/reactor for direct solid particle decomposition: Design, modeling, and experimentation," *Int. J. Hydrogen Energy*, vol. 37, no. 22, pp. 16871–16887, 2012, doi: 10.1016/j.ijhydene.2012.08.086.

[172] N. Gokon, T. Mataga, N. Kondo, and T. Kodama, "Thermochemical two-step water splitting by internally circulating fluidized bed of $NiFe_2O_4$ particles: Successive reaction of thermal-reduction and water-decomposition steps," *Int. J. Hydrogen Energy*, vol. 36, no. 8, pp. 4757–4767, 2011, doi: 10.1016/j.ijhydene.2011.01.076.

[173] I. Ermanoski, N. P. Siegel, and E. B. Stechel, "A New Reactor Concept for Efficient Solar-Thermochemical Fuel Production," *J. Sol. Energy Eng.*, vol. 135, no. 3, p. 031002, 2013, doi: 10.1115/1.4023356.

[174] C. L. Muhich, B. D. Ehrhart, I. Al-Shankiti, B. J. Ward, C. B. Musgrave, and A. W. Weimer, "A review and perspective of efficient hydrogen generation via solar thermal water splitting," *WIREs Energy Environ.*, vol. 5, no. 3, pp. 261–287, 2015, doi: 10.1002/wene.174.

[175] M. Chambon, S. Abanades, and G. Flamant, "Thermal dissociation of compressed ZnO and SnO_2 powders in a moving-front solar thermochemical reactor," *AlChE J.*, vol. 57, no. 8, pp. 2264–2273, 2011, doi: 10.1002/aic.12432.

[176] G. Centi and S. Perathoner, "Opportunities and prospects in the chemical recycling of carbon dioxide to fuels," *Catal. Today*, vol. 148, no. 3–4, pp. 191–205, 2009, doi: 10.1016/j.cattod.2009.07.075.

[177] C. Milone, Y. Kato, and E. Mastronardo, "Thermal Energy Storage with Chemical Reactions," in *Recent Advancements in Materials and Systems for Thermal Energy Storage*, A. Frazzica and L. F. Cabeza, Eds. Cham: Springer International Publishing, 2019, pp. 15–32.

[178] T. O. L. Sunde, T. Grande, and M.-A. Einarsrud, "Modified Pechini synthesis of oxide powders and thin films," in *Handbook of sol-gel science and technology*, Springer, 2016.

[179] M. P. Pechini, "Method of preparing lead and alkaline earth titanates and niobates and coating method using the same to form a capacitor," US3330697A, 11-Jul-1967.

[180] S. Brunauer, P. H. Emmett, and E. Teller, "Adsorption of Gases in Multimolecular Layers," *J. Am. Ceram. Soc.*, vol. 60, no. 2, pp. 309–319, 1938, doi: 10.1021/ja01269a023.

[181] G. B. J. de Boer, C. de Weerd, D. Thoenes, and H. W. J. Goossens, "Laser Diffraction Spectrometry: Fraunhofer Diffraction Versus Mie Scattering," *Particle & Particle Systems Characterization*, vol. 4, no. 1–4, pp. 14–19, 1987, doi: 10.1002/ppsc.19870040104.

[182] J. Jouannaux, A. Haeussler, M. Drobek, A. Ayral, S. Abanades, and A. Julbe, "Lanthanum manganite perovskite ceramic powders for CO_2 splitting: Influence of Pechini synthesis parameters on sinterability and reactivity," *Ceram. Int.*, vol. 45, no. 12, pp. 15636–15648, 2019, doi: 10.1016/j.ceramint.2019.05.075.

[183] A. L. A. da Silva, L. da Conceição, A. M. Rocco, and M. M. V. M. Souza, "Synthesis of Sr-doped $LaMnO_3$ and $LaCrO_3$ powders by combustion method: structural characterization and thermodynamic evaluation," *Cerâmica*, vol. 58, no. 348, pp. 521–528, 2012, doi: 10.1590/S0366-69132012000400018.

[184] S. P. Jiang, "Development of lanthanum strontium manganite perovskite cathode materials of solid oxide fuel cells: a review," *J. Mater. Sci.*, vol. 43, no. 21, pp. 6799–6833, 2008, doi: 10.1007/s10853-008-2966-6.

[185] Y. Xue, H. Miao, S. Sun, Q. Wang, S. Li, and Z. Liu, "$(La_{1-x}Sr_x)_{0.98}MnO_3$ perovskite with A-site deficiencies toward oxygen reduction reaction in aluminum-air batteries," *J. Power Sources*, vol. 342, pp. 192–201, 2017, doi: 10.1016/j.jpowsour.2016.12.065.

[186] H.-C. Cho, S. Kuramoto, S. Takase, J.-H. Song, and Y. Shimizu, "Sensing Properties of Impedancemetric Solid-Electrolyte NO_x Sensor Using Perovskite-Type Lanthanum Manganite-Based Receptor," *Sens. Mater.*, vol. 24, no. 1, p. 31, 2012, doi: 10.18494/SAM.2012.763.

[187] M. R. Mullen, J. V. Spirig, J. Hoy, J. L. Routbort, D. Singh, and P. K. Dutta, "Development of nanosized lanthanum strontium aluminum manganite as electrodes for potentiometric oxygen sensor," *Sensors and Actuators B: Chemical*, vol. 203, pp. 670–676, 2014, doi: 10.1016/j.snb.2014.07.027.

[188] S. Ponce, M. A. Peña, and J. L. G. Fierro, "Surface properties and catalytic performance in methane combustion of Sr-substituted lanthanum manganites," *Appl. Catal. B Environ.*, vol. 24, no. 3, pp. 193–205, 2000, doi: 10.1016/S0926-3373(99)00111-3.

[189] G. J. la O' and Y. Shao-Horn, "Thickness Dependence of Oxygen Reduction Reaction Kinetics on Strontium-Substituted Lanthanum Manganese Perovskite Thin-Film Microelectrodes," *Electrochem. Solid-State Lett.*, vol. 12, no. 5, p. B82, 2009, doi: 10.1149/1.3095681.

[190] A. H. Bork, E. Povoden-Karadeniz, and J. L. M. Rupp, "Modeling Thermochemical Solar-to-Fuel Conversion: CALPHAD for Thermodynamic Assessment Studies of Perovskites, Exemplified for (La,Sr)MnO_3," *Adv. Energy Mater.*, vol. 7, no. 1, p. 1601086, 2017, doi: 10.1002/aenm.201601086.

[191] O. Toulemonde, N. N'Guyen, F. Studer, and A. Traverse, "Spin State Transition in $LaCoO_3$ with Temperature or Strontium Doping as Seen by XAS," *J. Solid State Chem.*, vol. 158, no. 2, pp. 208–217, 2001, doi: 10.1006/jssc.2001.9094.

[192] O. Haas, R. P. W. J. Struis, and J. M. McBreen, "Synchrotron X-ray absorption of $LaCoO_3$ perovskite," *J. Solid State Chem.*, vol. 177, no. 3, pp. 1000–1010, 2004, doi: 10.1016/j.jssc.2003.10.004.

[193] C. Abughayada, "Air separation and oxygen storage properties of hexagonal rare-earth manganites.," Doctoral dissertation, Northern Illinois University, (USA), 2015.

[194] H. Kong, X. Kong, H. Wang, and J. Wang, "A strategy for optimizing efficiencies of solar thermochemical fuel production based on nonstoichiometric oxides," *Int. J. Hydrogen Energy*, 2019, doi: 10.1016/j.ijhydene.2019.05.197.

[195] G. Takalkar, R. R. Bhosale, S. Rashid, F. AlMomani, R. A. Shakoor, and A. Al Ashraf, "Application of Li-, Mg-, Ba-, Sr-, Ca-, and Sn-doped ceria for solar-driven thermochemical conversion of carbon dioxide," *J. Mater. Sci.*, 2020, doi: 10.1007/s10853-020-04875-1.

[196] R. J. Panlener, R. N. Blumenthal, and J. E. Garnier, "A thermodynamic study of nonstoichiometric cerium dioxide," *J. Phys. Chem. Solids*, vol. 36, no. 11, pp. 1213–1222, 1975, doi: 10.1016/0022-3697(75)90192-4.

[197] A. Khawam and D. R. Flanagan, "Solid-State Kinetic Models: Basics and Mathematical Fundamentals," *J. Phys. Chem. B*, vol. 110, no. 35, pp. 17315–17328, 2006, doi: 10.1021/jp062746a.

[198] S. Vyazovkin, A. K. Burnham, J. M. Criado, L. A. Pérez-Maqueda, C. Popescu, and N. Sbirrazzuoli, "ICTAC Kinetics Committee recommendations for performing kinetic computations on thermal analysis data," *Thermochim. Acta*, vol. 520, no. 1–2, pp. 1–19, 2011, doi: 10.1016/j.tca.2011.03.034.

[199] O. Levenspiel, *Chemical reaction engineering*, 3. ed. Hoboken, NJ: Wiley, 1999.

[200] H. L. Friedman, "Kinetics of thermal degradation of char-forming plastics from thermogravimetry. Application to a phenolic plastic," *J. Polym. Sci., Part C: Polym. Symp.*, vol. 6, no. 1, pp. 183–195, 1964, doi: 10.1002/polc.5070060121.

[201] H. S. Cho, N. Gokon, T. Kodama, Y. H. Kang, and H. J. Lee, "Improved operation of solar reactor for two-step water-splitting H_2 production by ceria-coated ceramic foam device," *Int. J. Hydrogen Energy*, vol. 40, no. 1, pp. 114–124, 2015, doi: 10.1016/j.ijhydene.2014.10.084.

[202] P. Furler, D. Marxer, J. Scheffe, D. Reinalda, H. Geerlings, C. Falter, V. Batteiger, A. Sizmann, and A. Steinfeld, "Solar kerosene from H_2O and CO_2," *AIP Conference Proceedings*, vol. 1850, no. 1, p. 100006, 2017, doi: 10.1063/1.4984463.

[203] J. E. Miller, M. D. Allendorf, A. Ambrosini, K. . S. Chen, E. N. Coker, D. E. Dedrick, R. Diver, R. E. Hogan, I. Ermanosk, T. A. Johansson, G. L. Kellogg, A. H. McDaniel, N. Siegel, C. L. Staiger, and E. B. Stechel, "Reimagining Liquid Transportation Fuels: Sunshine to Petrol," Sandia National Laboratories, USA, SAND2012-0307, 2012.

[204] H. I. Villafán-Vidales, C. A. Arancibia-Bulnes, D. Riveros-Rosas, H. Romero-Paredes, and C. A. Estrada, "An overview of the solar thermochemical processes for hydrogen and syngas production: Reactors, and facilities," *Renew. Sustain. Energ. Rev.*, vol. 75, pp. 894–908, 2017, doi: 10.1016/j.rser.2016.11.070.

[205] A. Haeussler, S. Abanades, A. Julbe, J. Jouannaux, M. Drobek, A. Ayral, and B. Cartoixa, "Remarkable performance of microstructured ceria foams for thermochemical splitting of H_2O and CO_2 in a novel high-temperature solar reactor," *Chem. Eng. Res. Des.*, vol. 156, pp. 311–323, 2020, doi: 10.1016/j.cherd.2020.02.008.

[206] A. Haeussler, S. Abanades, A. Julbe, J. Jouannaux, and B. Cartoixa, "Two-step CO_2 and H_2O splitting using perovskite-coated ceria foam for enhanced green fuel production in a porous volumetric solar reactor," *Journal of CO_2 Utilization*, vol. 41, p. 101257, 2020, doi: 10.1016/j.jcou.2020.101257.

[207] S. Karl and A. V. Somers, “Method of making porous ceramic articles,” US3090094A, 21-May-1963.
[208] S. Ackermann, L. Sauvin, R. Castiglioni, J. L. M. Rupp, J. R. Scheffe, and A. Steinfeld, “Kinetics of CO_2 Reduction over Nonstoichiometric Ceria,” *J. Phys. Chem. C*, vol. 119, no. 29, pp. 16452–16461, 2015, doi: 10.1021/acs.jpcc.5b03464.
[209] P. Furler, D. Marxer, M. Takacs, and A. Steinfeld, “Solar thermochemical reactor technology for splitting CO_2,” *AIP Conference Proceedings*, vol. 2033, no. 1, p. 130005, 2018, doi: 10.1063/1.5067139.
[210] R. Carrillo and J. R. Scheffe, “Beyond Ceria: Theoretical Investigation of Isothermal and Near-Isothermal Redox Cycling of Perovskites for Solar Thermochemical Fuel Production,” *Energ. Fuel*, vol. 33, no. 12, pp. 12871–12884, 2019, doi: 10.1021/acs.energyfuels.9b02714.
[211] R. Bader, L. J. Venstrom, J. H. Davidson, and W. Lipiński, “Thermodynamic Analysis of Isothermal Redox Cycling of Ceria for Solar Fuel Production,” *Energ. Fuel*, vol. 27, no. 9, pp. 5533–5544, 2013, doi: 10.1021/ef400132d.
[212] B. Bulfin, F. Call, M. Lange, O. Lübben, C. Sattler, R. Pitz-Paal, and I. V. Shvets, “Thermodynamics of CeO_2 Thermochemical Fuel Production,” *Energ. Fuel*, vol. 29, no. 2, pp. 1001–1009, 2015, doi: 10.1021/ef5019912.
[213] A. De la Calle and A. Bayon, “Annual performance of a thermochemical solar syngas production plant based on non-stoichiometric CeO_2,” *Int. J. Hydrogen Energy*, vol. 44, no. 3, pp. 1409–1424, 2019, doi: 10.1016/j.ijhydene.2018.11.076.
[214] B. D. Ehrhart, C. L. Muhich, I. Al-Shankiti, and A. W. Weimer, “System efficiency for two-step metal oxide solar thermochemical hydrogen production – Part 2: Impact of gas heat recuperation and separation temperatures,” *Int. J. Hydrogen Energy*, vol. 41, no. 44, pp. 19894–19903, 2016, doi: 10.1016/j.ijhydene.2016.07.110.
[215] P. Nikolaidis and A. Poullikkas, “A comparative overview of hydrogen production processes,” *Renew. Sustain. Energ. Rev.*, vol. 67, pp. 597–611, 2017, doi: 10.1016/j.rser.2016.09.044.
[216] M. Hoes, S. Ackermann, D. Theiler, P. Furler, and A. Steinfeld, “Additive-manufactured ordered porous structures made of ceria for concentrating solar applications,” *Energy Technol.*, 2019, doi: 10.1002/ente.201900484.
[217] M. Ricken, J. Nölting, and I. Riess, “Specific heat and phase diagram of nonstoichiometric ceria (CeO_{2-x}),” *J. Solid State Chem.*, vol. 54, no. 1, pp. 89–99, 1984, doi: 10.1016/0022-4596(84)90135-X.
[218] R. Pullar, R. Novais, A. Caetano, A. Barreiros, S. Abanades, and F. Oliveira, “A review of solar thermochemical CO_2 splitting using ceria-based ceramics with designed morphologies and microstructures,” *Front. Chem.*, vol. 7, p. 601, 2019, doi: 10.3389/fchem.2019.00601.
[219] L. J. Venstrom, N. Petkovich, S. Rudisill, A. Stein, and J. H. Davidson, “The Oxidation of Macroporous Cerium and Cerium-Zirconium Oxide for the Solar Thermochemical Production of Fuels,” in *ASME 2011 5th International Conference on Energy Sustainability, Parts A, B, and C*, Washington, DC, USA, 2011, pp. 1585–1593, doi: 10.1115/ES2011-54160.
[220] M. Singh, “Environmentally conscious ceramics (ecoceramics) from natural wood precursors,” *Curr. Opin. Solid State Mater. Sci.*, vol. 7, no. 3, pp. 247–254, 2003, doi: 10.1016/j.cossms.2003.09.004.
[221] F. A. C. Oliveira, M. A. Barreiros, A. Haeussler, A. Caetano, A. I. Mouquinho, P. M. O. e Silva, R. M. Novais, R. C. Pullar, and S. Abanades, “High performance cork-templated ceria for solar thermochemical hydrogen production via two-step water-splitting cycles,” *Sustainable Energy Fuels*, vol. 4, pp. 3077–3089, 2020, doi: 10.1039/D0SE00318B.
[222] A. Haeussler, S. Abanades, A. Julbe, J. Jouannaux, and B. Cartoixa, “Solar thermochemical fuel production from H_2O and CO_2 splitting via two-step redox cycling of reticulated porous ceria structures integrated in a monolithic cavity-type reactor,” *Energy*, vol. 201, p. 117649, 2020, doi: 10.1016/j.energy.2020.117649.
[223] R. M. Novais and R. C. Pullar, “Comparison of low and high pressure infiltration regimes on the density and highly porous microstructure of ceria ecoceramics made from sustainable cork templates,” *J. Eur. Ceram. Soc.*, vol. 39, no. 4, pp. 1287–1296, 2019, doi: 10.1016/j.jeurceramsoc.2018.11.050.
[224] R. C. Pullar, L. Gil, and F. A. C. Oliveira, “Biomimetic cork-based CeO_2 ecoceramics for hydrogen generation using concentrated solar energy,” *Ciência & Tecnologia dos Materiais*, vol. 28, no. 1, pp. 23–28, 2016, doi: 10.1016/j.ctmat.2016.04.002.
[225] F. A. C. Oliveira, S. Dias, J. M. G. Mascarenhas, J. M. F. Ferreira, S. Olhero, and D. P. Dias, “Fabrication of Cellular Cordierite Foams,” *Materials Science Forum*, vol. 455–456, pp. 177–181, 2004, doi: 10.4028/www.scientific.net/MSF.455-456.177.
[226] M. J. Matos, M. Fátima Vaz, J. C. Fernandes, and F. A. C. Oliveira, “Structure of Cellular Cordierite Foams,” *Materials Science Forum*, vol. 455–456, pp. 163–167, 2004, doi: 10.4028/www.scientific.net/MSF.455-456.163.
[227] T. Delahaye, M. Caisso, and S. Picart, “Procédé de préparation d’un substrat en céramique oxyde mettant en oeuvre une résine échangeuse d’ions,” European Patent EP15200498.2, 22-Jun-2016.

[228] M. Caisso, F. Lebreton, D. Horlait, S. Picart, P. M. Martin, R. Bès, C. Renard, P. Roussel, D. R. Neuville, K. Dardenne, J. Rothe, T. Delahaye, and A. Ayral, "Nanostructured gadolinium-doped ceria microsphere synthesis from ion exchange resin: Multi-scale in-situ studies of solid solution formation," *Journal of Solid State Chemistry*, vol. 218, pp. 155–163, 2014, doi: 10.1016/j.jssc.2014.06.028.

[229] S. Li, V. M. Wheeler, P. B. Kreider, R. Bader, and W. Lipiński, "Thermodynamic Analyses of Fuel Production via Solar-Driven Non-stoichiometric Metal Oxide Redox Cycling. Part 2. Impact of Solid–Gas Flow Configurations and Active Material Composition on System-Level Efficiency," *Energy & Fuels*, vol. 32, no. 10, pp. 10848–10863, 2018, doi: 10.1021/acs.energyfuels.8b02082.

[230] D. Arifin and A. W. Weimer, "Kinetics and mechanism of solar-thermochemical H_2 and CO production by oxidation of reduced CeO_2," *Sol. Energy*, vol. 160, pp. 178–185, 2018, doi: 10.1016/j.solener.2017.11.075.

[231] C. Falter, N. Scharfenberg, and A. Habersetzer, "Geographical Potential of Solar Thermochemical Jet Fuel Production," *Energies*, vol. 13, no. 4, p. 802, 2020, doi: 10.3390/en13040802.

[232] M. Tou, "A Membrane Reactor for the Solar Thermolysis of CO_2 and H_2O: A Thermodynamic and Experimental Analysis," Doctoral dissertation, ETH Zurich, (Switzerland), 2019.

[233] X.-Y. Wu and A. F. Ghoniem, "Mixed ionic-electronic conducting (MIEC) membranes for thermochemical reduction of CO_2: A review," *Prog. Energy Combust. Sci.*, vol. 74, pp. 1–30, 2019, doi: 10.1016/j.pecs.2019.04.003.

[234] E. M. Pfaff, A. Kaletsch, and C. Broeckmann, "Design of a Mixed Ionic/Electronic Conducting Oxygen Transport Membrane Pilot Module," *Chem. Eng. Technol.*, vol. 35, no. 3, pp. 455–463, 2012, doi: 10.1002/ceat.201100447.

[235] U. Balachandran, J. T. Dusek, and S. M. Sweeney, "Methane to syngas via ceramic membranes," *Am. Ceram. Soc. Bull.*, vol. 74, pp. 71–75, 1995.

[236] R. Michalsky, D. Neuhaus, and A. Steinfeld, "Carbon Dioxide Reforming of Methane using an Isothermal Redox Membrane Reactor," *Energy Technol.*, vol. 3, no. 7, pp. 784–789, 2015, doi: 10.1002/ente.201500065.

[237] H. Jiang, L. Xing, O. Czuprat, H. Wang, S. Schirrmeister, T. Schiestel, and J. Caro, "Highly effective NO decomposition by in situ removal of inhibitor oxygen using an oxygen transporting membrane," *Chem. Commun.*, no. 44, p. 6738, 2009, doi: 10.1039/b912269a.

[238] Z. Gong and L. Hong, "Integration of air separation and partial oxidation of methane in the $La_{0.4}Ba_{0.6}Fe_{0.8}Zn_{0.2}O_{3-\delta}$ membrane reactor," *J. Membr. Sci.*, vol. 380, no. 1–2, pp. 81–86, 2011, doi: 10.1016/j.memsci.2011.06.033.

[239] H. Jiang, H. Wang, S. Werth, T. Schiestel, and J. Caro, "Simultaneous Production of Hydrogen and Synthesis Gas by Combining Water Splitting with Partial Oxidation of Methane in a Hollow-Fiber Membrane Reactor," *Angew. Chem. Int. Ed.*, vol. 47, no. 48, pp. 9341–9344, 2008, doi: 10.1002/anie.200803899.

[240] W. Jin, C. Zhang, X. Chang, Y. Fan, W. Xing, and N. Xu, "Efficient Catalytic Decomposition of CO_2 to CO and O_2 over Pd/Mixed-Conducting Oxide Catalyst in an Oxygen-Permeable Membrane Reactor," *Environ. Sci. Technol.*, vol. 42, no. 8, pp. 3064–3068, 2008, doi: 10.1021/es702913f.

[241] K. Zhang, G. Zhang, Z. Liu, J. Zhu, N. Zhu, and W. Jin, "Enhanced stability of membrane reactor for thermal decomposition of CO_2 via porous-dense-porous triple-layer composite membrane," *J. Membr. Sci.*, vol. 471, pp. 9–15, 2014, doi: 10.1016/j.memsci.2014.06.060.

[242] L. Nalbandian, A. Evdou, and V. Zaspalis, "$La_{1-x}Sr_xM_yFe_{1-y}O_{3-\delta}$ perovskites as oxygen-carrier materials for chemical-looping reforming," *Int. J. Hydrogen Energy*, vol. 36, no. 11, pp. 6657–6670, 2011, doi: 10.1016/j.ijhydene.2011.02.146.

[243] L. Nalbandian, A. Evdou, and V. Zaspalis, "$La_{1-x}Sr_xMO_3$ (M = Mn, Fe) perovskites as materials for thermochemical hydrogen production in conventional and membrane reactors," *Int. J. Hydrogen Energy*, vol. 34, no. 17, pp. 7162–7172, 2009, doi: 10.1016/j.ijhydene.2009.06.076.

[244] N. Itoh, M. A. Sanchez, W.-C. Xu, K. Haraya, and M. Hongo, "Application of a membrane reactor system to thermal decomposition of CO_2," *J. Membr. Sci.*, vol. 77, no. 2–3, pp. 245–253, 1993, doi: 10.1016/0376-7388(93)85073-6.

[245] Y. Nigara, K. Watanabe, K. Kawamura, J. Mizusaki, and M. Ishigame, "Oxygen Permeation in ZrO_2 - CeO_2 - CaO for Application to Oxygen Separation from Thermally Decomposed H_2O," *J. Electrochem. Soc.*, vol. 144, no. 3, pp. 1050–1055, 1997, doi: 10.1149/1.1837529.

[246] H. Naito, "Hydrogen production from direct water splitting at high temperatures using a ZrO_2-TiO_2-Y_2O_3 membrane," *Solid State Ionics*, vol. 79, pp. 366–370, 1995, doi: 10.1016/0167-2738(95)00089-O.

[247] M. Tou, R. Michalsky, and A. Steinfeld, "Solar-Driven Thermochemical Splitting of CO_2 and In Situ Separation of CO and O_2 across a Ceria Redox Membrane Reactor," *Joule*, vol. 1, no. 1, pp. 146–154, 2017, doi: 10.1016/j.joule.2017.07.015.

[248] M. Tou, J. Jin, Y. Hao, A. Steinfeld, and R. Michalsky, "Solar-driven co-thermolysis of CO_2 and H_2O and in-situ oxygen removal across a non-stoichiometric ceria membrane," *React. Chem. Eng.*, 2019, doi: 10.1039/C8RE00218E.

[249] X. Dong, W. Jin, N. Xu, and K. Li, "Dense ceramic catalytic membranes and membrane reactors for energy and environmental applications," *Chem. Commun.*, vol. 47, no. 39, p. 10886, 2011, doi: 10.1039/c1cc13001c.

[250] A. H. Bork, A. J. Carrillo, Z. D. Hood, B. Yildiz, and J. L. M. Rupp, "Oxygen Exchange in Dual-phase $La_{0.65}Sr_{0.35}MnO_3$-CeO_2 Composites for Solar Thermochemical Fuel Production," *ACS Appl. Mater. Interfaces*, vol. 12, no. 29, pp. 32622–32632, 2020, doi: 10.1021/acsami.0c04276.

[251] S. Brendelberger, J. Vieten, M. J. Vidyasagar, M. Roeb, and C. Sattler, "Demonstration of thermochemical oxygen pumping for atmosphere control in reduction reactions," *Sol. Energy*, vol. 170, pp. 273–279, 2018, doi: 10.1016/j.solener.2018.05.063.

[252] H. Giesche, "Mercury Porosimetry: A General (Practical) Overview," *Particle & Particle Systems Characterization*, vol. 23, no. 1, pp. 9–19, 2006, doi: 10.1002/ppsc.200601009.

[253] T. Takeshita and K. Yamaji, "Important roles of Fischer–Tropsch synfuels in the global energy future," *Energy Policy*, vol. 36, no. 8, pp. 2773–2784, 2008, doi: 10.1016/j.enpol.2008.02.044.

Appendix A - State of the art

Table SA-1: Summary of cations effect on reduction extent, fuel production and thermal stability of ceria used in thermochemical cycling applications. Symbols +, - and ≈ represent an increase, decrease and no significant variation of the properties due to the cation addition compared with pure ceria, respectively

Cation	Reduction extent	Fuel production	Thermal stability
Monovalent			
Li^{+}	+	+	
Divalent			
Ca^{2+}	-		
Cu^{2+}	+	≈	
Mg^{2+}	+	+	++
Sr^{2+}	-		
Trivalent			
Co^{3+}	++	-	--
Dy^{3+}	≈	-	+
Er^{3+}	+	-	-
Gd^{3+}	-	-	
La^{3+}	+	≈	
Nd^{3+}	-	-	+
Pr^{3+}	+	-	
Sc^{3+}	+	+	+
Sm^{3+}	+	≈	
Tb^{3+}	+	+	-
Y^{3+}	-	-	
Tetravalent			
Cr^{4+}	+	≈	
Ge^{4+}	+		
Hf^{4+}	+	+	-
Rh^{4+}	+		
Si^{4+}	+	-	-
Sn^{4+}	++	-	
Ti^{4+}	+	-	
Zr^{4+}	++	-	-
Pentavalent			
Nb^{5+}	+	-	
Ta^{5+}	+	+	-
V^{5+}	-	-	-
Multiple oxidation states			
Fe	++		
Mn	++	-	-
Ni	≈	≈	

Table SA-2 Comparison of the performance of current perovskites studied for thermochemical cycles

Material	Synthesis Method	Experimental Conditions	Production (µmol/g)		Ref.
			O_2	H_2/CO	
$La_{0.7}Sr_{0.3}Mn_{0.7}Cr_{0.3}O_3$	Modified Pechini	Reduction: 1350 °C under N_2 Oxidation: H_2O between 50 and 84%; 1000 °C during 60 min	~98	~107	[141]
$LaFe_{0.75}Co_{0.25}O_3$	Solid-state	Reduction: 1300 °C under Ar Oxidation: 50% CO_2 in Ar at 1000 °C	59	117	[134]
$LaCoO_3$	Solid-state	Reduction: 1300 °C under Ar Oxidation: 50% CO_2 in Ar at 1000 °C	369	123	[134]
$Ba_{0.5}Sr_{0.5}FeO_3$	Solid-state	Reduction: 1000 °C under Ar Oxidation: 50% CO_2 in Ar at 1000 °C	582	136	[134]
$La_{0.6}Sr_{0.4}Co_{0.2}Cr_{0.8}O_3$	Pechini	Reduction: 1200 °C under Ar Oxidation: 50% CO_2 in Ar at 800 °C		157	[151]
$La_{0.4}Ca_{0.6}Mn_{0.6}Al_{0.4}O_3$	Modified Pechini	Reduction: 1400 °C under Ar Oxidation: 40% H_2O in Ar at 1000 °C	231	429	[143]
$BaCe_{0.25}Mn_{0.75}O_3$	Modified Pechini	Reduction: 1350 °C under Ar Oxidation: 40% H_2O in Ar at 1000 °C		135	[154]
$La_{0.5}Sr_{0.5}MnO_3$	Solid-state	Reduction: 1400 °C under Ar Oxidation: H_2O at 1000 °C	298	195	[137]
$La_{0.35}Sr_{0.75}MnO_3$	Commercial powder	Reduction: 1400 °C under Ar Oxidation: H_2O at 1050 °C	166	124	[121]
$La_{0.5}Ca_{0.5}MnO_3$	Solid-state	Reduction: 1400 °C under Ar Oxidation: 50% CO_2 at 1050 °C	311	210	[125]
$La_{0.5}Ba_{0.5}MnO_3$	Solid-state	Reduction: 1400 °C under Ar Oxidation: 50% CO_2 at 1050 °C	203	185	[125]
$La_{0.5}Sr_{0.5}Mn_{0.4}Al_{0.6}O_3$	Pechini	Reduction: 1400 °C under Ar Oxidation: 50% CO_2 at 1050 °C	246	279	[125]
$La_{0.5}Sr_{0.5}Mn_{0.83}Mg_{0.17}O_3$	Solid-state	Reduction: 1400 °C under Ar Oxidation: 50% CO_2 at 1050 °C	214	209	[125]
$La_{0.5}Sr_{0.5}MnO_3$	Pechini	Reduction: 1400 °C under Ar Oxidation: 50% CO_2 at 1050 °C	256	256	[142]
$Y_{0.5}Sr_{0.5}MnO_3$	Pechini	Reduction: 1400 °C under Ar Oxidation: 50% CO_2 at 1050 °C	539	101	[142]
$La_{0.6}Sr_{0.4}Mn_{0.6}Al_{0.4}O_3$	Modified Pechini	Reduction: 1400 °C under Ar Oxidation: 40% CO_2 at 1000 °C		307	[136]
$La_{0.6}Ca_{0.4}Mn_{0.6}Al_{0.4}O_3$	Modified Pechini	Reduction: 1240 °C under Ar Oxidation: 50% CO_2 at 850 °C	165	230	[135]
$La_{0.6}Sr_{0.4}Mn_{0.6}Al_{0.4}O_3$	Modified Pechini	Reduction: 1240 °C under Ar Oxidation: 50% CO_2 at 850 °C	190	245	[135]
$La_{0.6}Ca_{0.4}Mn_{0.8}Ga_{0.2}O_3$	Modified Pechini	Reduction: 1300 °C Oxidation: H_2O at 900 °C	212	401	[145]
$La_{0.5}Sr_{0.5}Mn_{0.95}Sc_{0.05}O_3$		Reduction: 1400 °C under Ar Oxidation: 40% CO_2 at 1100 °C	417	545	[146]
$La_{0.6}Sr_{0.4}Mn_{0.8}Fe_{0.2}O_3$	Modified Pechini	Reduction: 1350 °C under N_2 Oxidation: CO_2 at 1000 °C	286	329	[147]
$La_{0.6}Sr_{0.4}CoO_3$	Modified Pechini	Reduction: 1300 °C Oxidation: 40% H_2O at 900 °C	718	514	[150]
$La_{0.6}Ca_{0.4}CoO_3$	Modified Pechini	Reduction: 1300 °C Oxidation: 40% H_2O at 900 °C	715	587	[148]
$Y_{0.5}Ca_{0.5}MnO_3$	Solid state	Reduction: 1400 °C Oxidation: CO_2 at 1100 °C	573	671	[130]

Appendix B - Selection of reactive materials for two-step thermochemical cycles

Table SB-1: O_2 and CO production yield during thermogravimetric analysis of perovskites for investigating the composition influence on the redox behavior

	Cycle 1		Cycle 2	
	O_2 produced (µmol/g)	**CO produced (µmol/g)**	**O_2 produced (µmol/g)**	**CO produced (µmol/g)**
LSMMg-P2	269	214	111	215
LSMMGa-P2	231	195	101	196
LSMAl/Cr-P2	232	164	100	165
LSMCr-P2	215	134	76	139
LSM-P2	232	190	104	195
LSMAl-P2	302	200	109	203
LCMGa-P2	287	215	175	200
LCMMg-P2	394	154	121	173
LCMCr-P2	249	111	78	125
LCMAl-P2	449	162	95	171
LCM-P2	325	175	107	182
LMCo	43	62	60	99
LSCo	1191	1141	658	998
YSrM	127	118	106	106
YLaM	54	86	60	107
YCeM	47	30		
YLaSrM	145	135	75	137
PrSrM25	668	171	96	170
PrSrM50	268	153	90	160
PrSrM75	146	150	79	156
SmSrM50	373	168	101	175
SmSrM75	117	177	95	180
CeO_2	55	85	54	98
$CeZr15O_2$	116	144	79	152
$CeZr37O_2$	176	72	47	69
$CeZrAlO_2$	129	86	78	57
BaCeMn	220	154	217	110

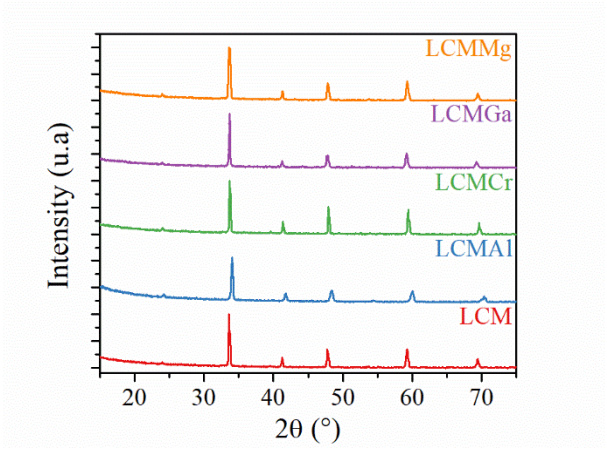

Figure SB-1: XRD patterns of LCM, LCMAl, LCMCr, LCMGa and LCMMg powders after sintering at 1400 °C for 1 h before cycling

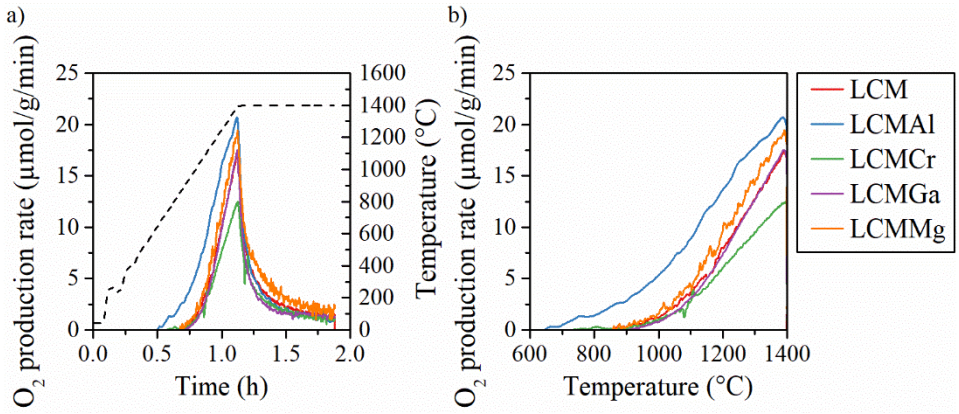

Figure SB-2: O_2 production rate as a function of a) time and b) temperature for lanthanum manganese doped calcium perovskites

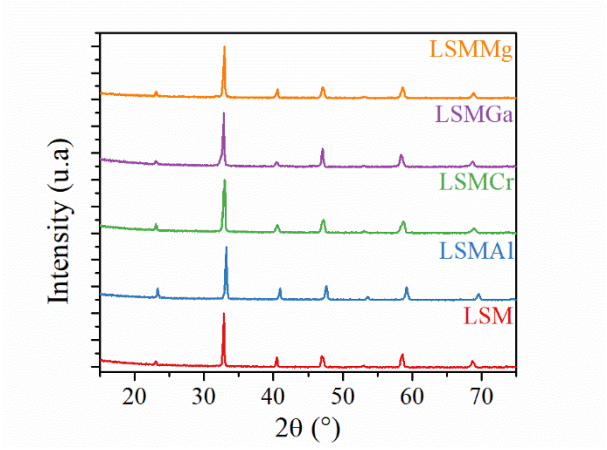

Figure SB-3: XRD patterns of LSM, LSMAl, LSMCr, LSMGa and LSMMg powders after sintering at 1400 °C for 1 h before cycling

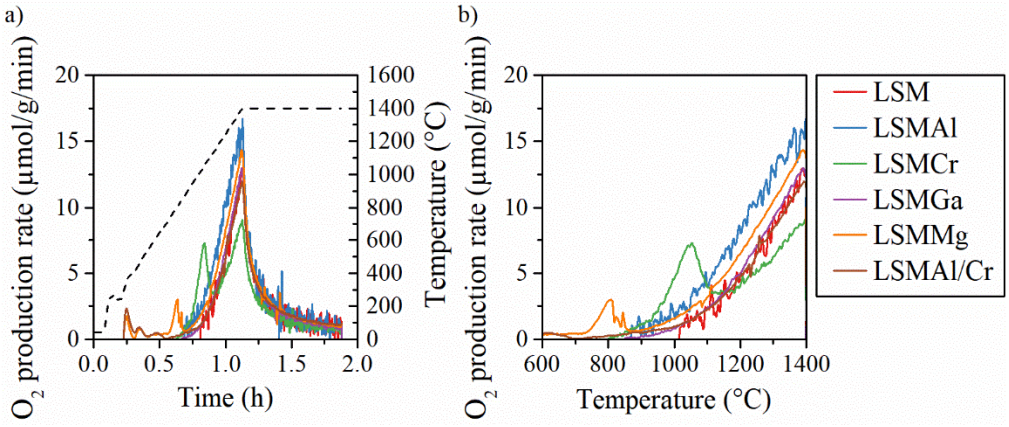

Figure SB-4: O_2 production rate as a function of a) time and b) temperature for lanthanum manganese doped strontium perovskites

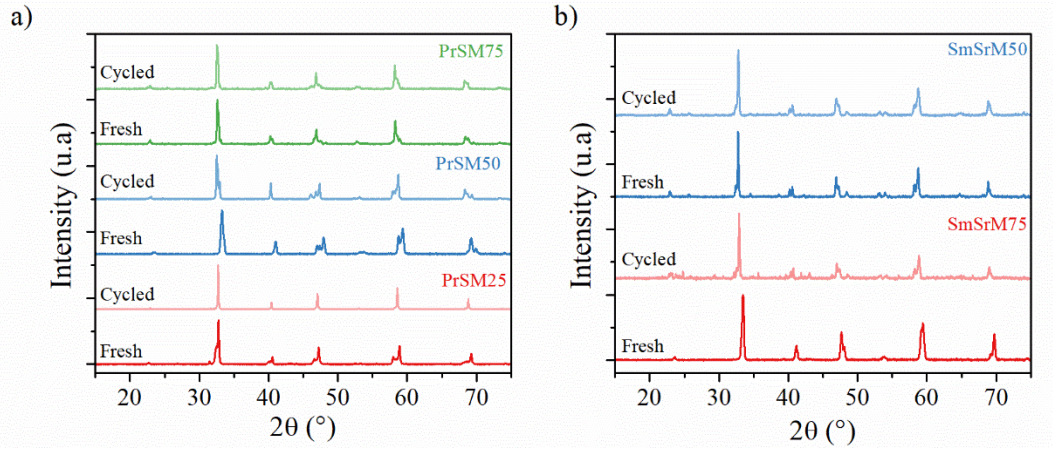

Figure SB-5: XRD patterns of fresh and cycled perovskites: a) PrSrM75, PrSrM50 and PrSrM25 and b) SmSrM50 and SmSrM75 powders

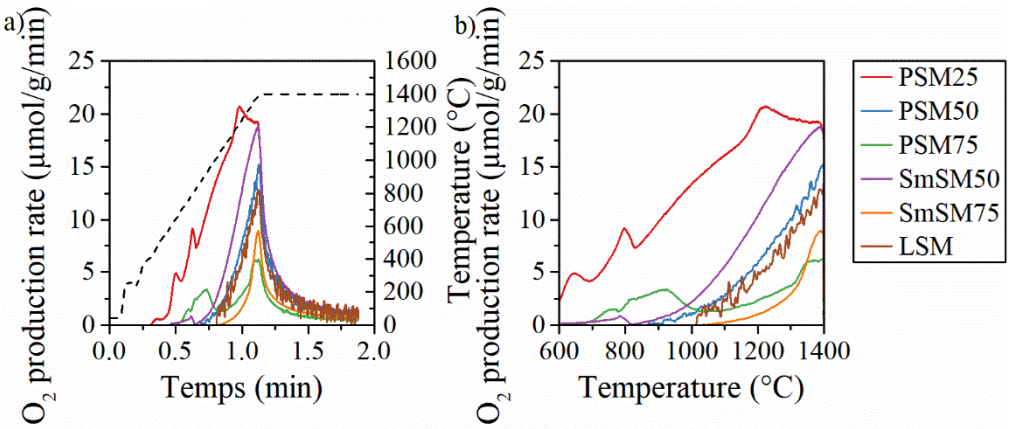

Figure SB-6: O_2 production rate as a function of a) time and b) temperature for strontium manganese perovskites

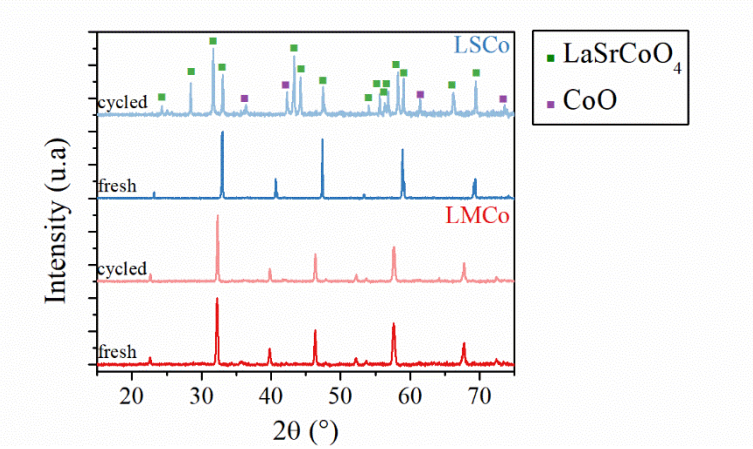

Figure SB-7: XRD patterns of fresh and cycled LMCo (red lines) and LSCo (blue lines) powders

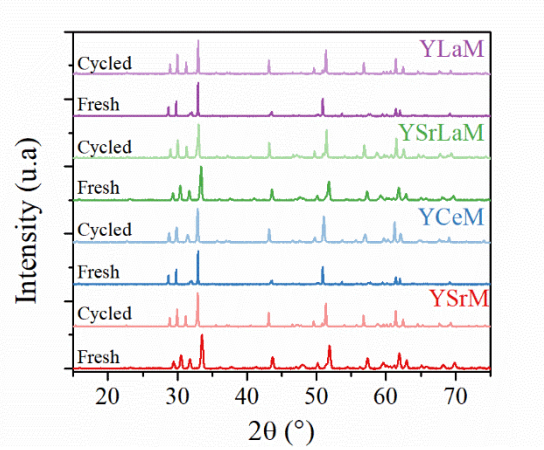

Figure SB-8: XRD patterns of fresh and cycled YSrM (red lines), YCeM (blue lines), YSrLaM (green lines) and YLaM (purple lines) powders

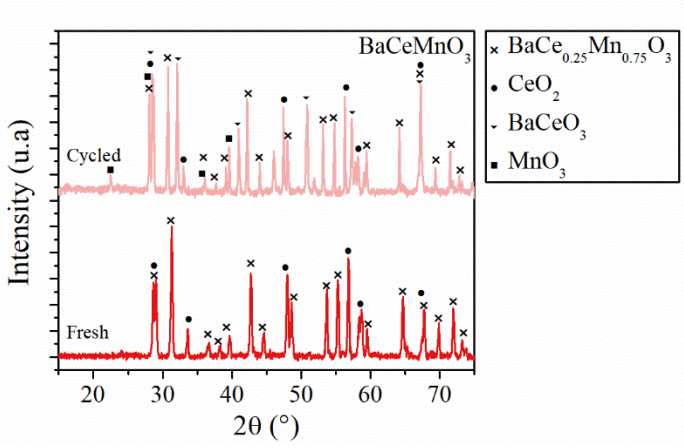

Figure SB-9: XRD patterns of fresh and cycled BaCeMn powder

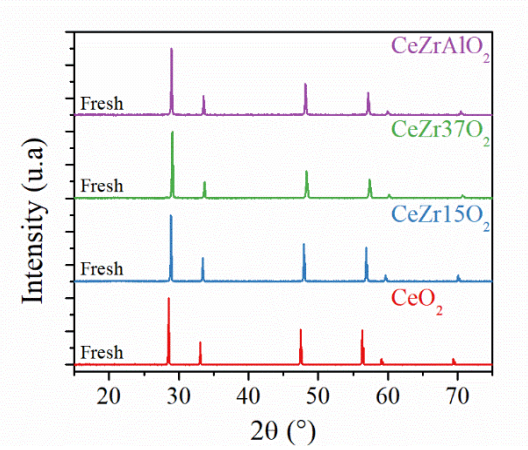

Figure SB-10: XRD patterns of fresh CeO_2, $CeZr15O_2$, $CeZr37O_2$ and $CeZrAlO_2$

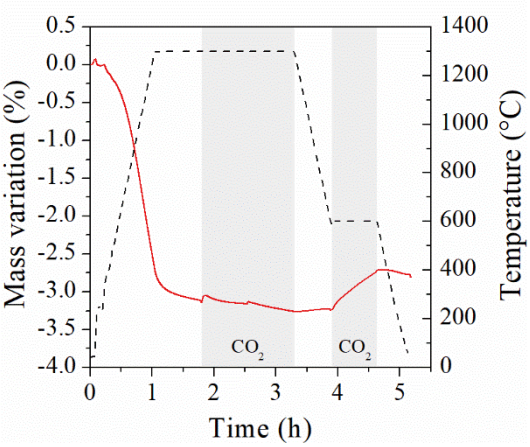

Figure SB-11: Thermogravimetric reduction and re-oxidation profiles (solid lines) and associated temperatures (dashed lines) for CSMF material (the first oxidation under 50% CO_2 was performed at 1300 °C and the second one at 600 °C)

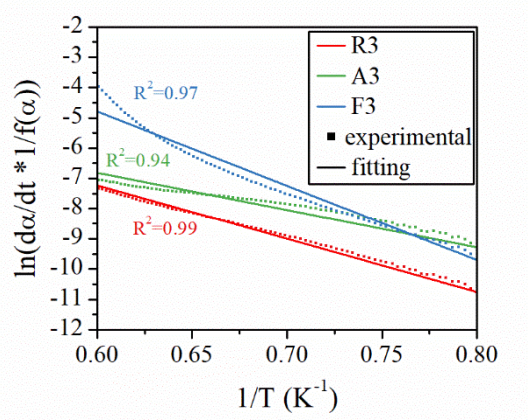

Figure SB-12: Example of linear regression with R3, A3 and F3 kinetic models on LSMMg-P1

Appendix C - Thermochemical performance evaluation of reticulated porous ceria structures in a monolithic solar reactor

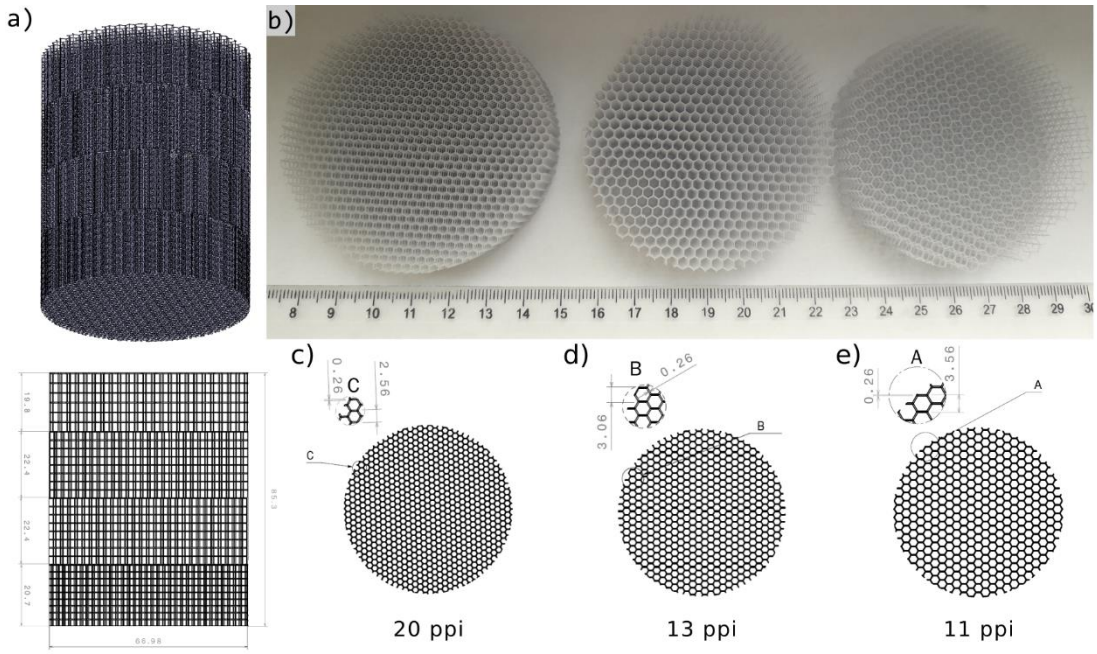

Figure SC-1: a) Design of the ordered 3D structures and b) images of the polymeric templates (left to right: 20 ppi, 13 ppi and 11 ppi), c) 20 ppi template; d) 13 ppi template and e) 11 ppi template

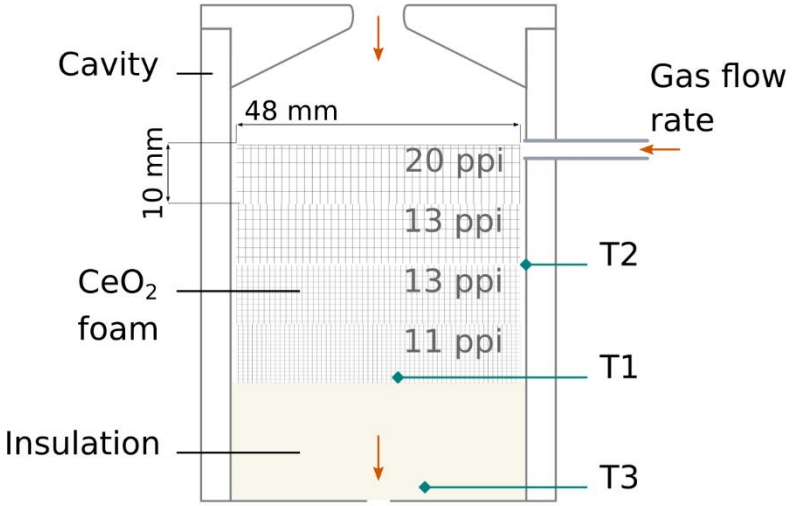

Figure SC-2: Schematic representation of the solar cavity containing the ordered porous ceria foam

Table SC-1: Operating parameters and fuel production performance for the CF-10 and CF-20 foams (T_{red} is the reduction temperature, P_{red} the reduction pressure and T_{ox} the oxidation temperature; gas flow-rates are given at normal conditions)

	Reduction step parameters				Oxidation step parameters						
Cycle #	**T_{red} (°C)**	**P_{red} (hPa)**	**Ar flow rate during reduction (L/min)**	**O_2 produced (µmol/g)**	**Oxidant gas**	**Oxidation temperature regime**	**T_{ox} (°C)**	**Oxidant gas molar fraction**	**Oxidant gas flow rate (total flow rate) (L/min)**	**Fuel produced (µmol/g)**	**Peak fuel production rate (mL/g/min)**
CF-10 foam (m=55.6954 g)											
1	1378	870	1.2	105	H_2O	Isothermal	967	0.17	0.25 (1.45)	208	0.57
2	1417	870	1.2	109	H_2O	Isothermal	1006	0.17	0.25 (1.45)	216	0.76
3	1404	870	1.2	106	CO_2	Isothermal	1034	0.25	0.40 (1.60)	213	1.43
4	1407	880	1.2	97	CO_2	Isothermal	1032	0.25	0.40 (1.60)	188	1.32
5	1400	872	1.2	107	CO_2	Isothermal	1079	0.25	0.40 (1.60)	212	1.10
6	1412	868	1.2	88	CO_2	Isothermal	1114	0.25	0.40 (1.60)	120	0.59
7	1407	866	1.2	84	CO_2	Isothermal	1121	0.25	0.40 (1.60)	161	0.53
8	1380	170	1.2	102	CO_2	Isothermal	907	0.25	0.40 (1.60)	203	1.61
9	1408	870	1.2	88	CO_2	Isothermal	1213	0.25	0.40 (1.60)	136	0.48
10	1408	879	1.2	98	CO_2	Isothermal	1059	0.25	0.40 (1.60)	194	0.81
11	1453	870	1.2	116	CO_2	Isothermal	1050	0.25	0.40 (1.60)	226	1.18
12	1404	876	1.2	98	CO_2	Isothermal	869	0.25	0.40 (1.60)	197	3.49
13	1403	872	1.2	78	CO_2	Isothermal	1011	0.25	0.40 (1.60)	151	0.91
14	1405	880	1.2	86	CO_2	Isothermal	1055	0.25	0.40 (1.60)	152	1.00
15	1402	885	1.2	96	CO_2	Isothermal	954	0.25	0.40 (1.60)	191	2.69
16	1458	878	1.2	119	CO_2	Isothermal	1061	0.25	0.40 (1.60)	237	1.40
17	1405	875	1.2	77	H_2O	Isothermal	1057	0.17	0.25 (1.45)	129	0.12
18	1407	851	1.2	110	CO_2	Dynamic	1020-904	0.25	0.40 (1.60)	241	2.31
19	1227	872	1.2	39	CO_2	Dynamic	998-764	0.25	0.40 (1.60)	82	1.23
20	1413	866	1.2	116	CO_2	Dynamic	1062-828	0.25	0.40 (1.60)	250	1.95
21	1410	863	1.5	125	CO_2	Dynamic	1005-799	0.25	0.40 (1.60)	254	2.48
22	1401	863	1.5	102	CO_2	Dynamic	1042-833	0.25	0.40 (1.60)	208	2.29
23	1240	870	2.0	58	CO_2	Dynamic	1185-724	0.29	0.40 (1.40)	115	0.43
24	1408	869	2.0	123	CO_2	Dynamic	988-850	0.50	1.00 (2.00)	250	6.25
25	1410	862	2.0	110	CO_2	Dynamic	993-836	0.50	1.00 (2.00)	217	5.41
26	1407	862	1.2	114	CO_2	Dynamic	1008-796	1.00	2.00 (2.00)	254	8.36

Reduction step parameters						Oxidation step parameters					
Cycle #	**T_{red} (°C)**	**P_{red} (hPa)**	**Ar flow rate during reduction (L/min)**	**O_2 produced (µmol/g)**	**Oxidant gas**	**Oxidation temperature regime**	**T_{ox} (°C)**	**Oxidant gas molar fraction**	**Oxidant gas flow rate (total flow rate) (L/min)**	**Fuel produced (µmol/g)**	**Peak fuel production rate (mL/g/min)**
27	1407	861	1.2	108	CO_2	Dynamic	1018-791	1.00	2.00 (2.00)	237	7.27
28	1403	861	1.2	120	CO_2	Dynamic	1007-797	1.00	2.00 (2.00)	252	9.43
29	1402	859	1.2	104	CO_2	Dynamic	1014-770	1.00	2.00 (2.00)	201	8.08
30	1401	858	1.2	90	CO_2	Dynamic	1010-839	0.25	0.40 (1.60)	160	2.09
31	1405	106	1.2	128	CO_2	Dynamic	1001-772	0.25	0.40 (1.60)	258	2.57
32	1403	110	1.2	141	CO_2	Dynamic	986-825	0.67	2.00 (3.00)	283	9.93
33	1409	116	1.2	130	CO_2	Dynamic	1020-752	0.50	1.00 (2.00)	262	4.51
34	1403	116	1.2	127	CO_2	Dynamic	1010-834	0.50	1.00 (2.00)	241	5.22
35	1401	114	1.2	141	CO_2	Dynamic	1015-775	1.00	2.00 (2.00)	284	7.55
36	1402	116	1.2	142	CO_2	Dynamic	1013-744	1.00	2.00 (2.00)	282	7.47
37	1328	92	0.8	85	CO_2	Dynamic	1002-812	0.50	1.00 (2.00)	171	3.55
CF-20 foam (m=55.9245 g)											
1	1410	876	1.2	110	CO_2	Isothermal	1064	0.25	0.40 (1.60)	186	1.10
2	1408	877	1.2	67	CO_2	Isothermal	1162	0.25	0.40 (1.60)	81	0.34
3	1411	879	1.2	60	CO_2	Isothermal	1056	0.25	0.40 (1.60)	121	0.89
4	1409	872	1.2	87	CO_2	Isothermal	955	0.25	0.40 (1.60)	197	2.05
5	1412	876	1.2	95	H_2O	Isothermal	1053	0.17	0.25 (1.45)	118	0.30
6	1401	910	1.2	90	H_2O	Isothermal	870	0.17	0.25 (1.45)	250	1.20
7	1410	870	1.2	106	CO_2	Isothermal	903	0.25	0.40 (1.60)	210	3.38
8	1410	874	1.2	118	CO_2	Isothermal	705	0.25	0.40 (1.60)	273	5.02
9	1424	110	1.2	174	CO_2	Isothermal	1048	0.25	0.40 (1.60)	296	1.68
10	1407	878	1.2	108	H_2O	Isothermal	858	0.17	0.25 (1.45)	222	0.83
11	1409	872	1.2	123	CO_2	Dynamic	1016-893	0.25	0.40 (1.60)	261	2.67
12	1407	869	1.2	126	CO_2	Dynamic	996-847	0.25	0.40 (1.60)	260	2.69
13	1456	872	1.2	149	CO_2	Dynamic	997-845	0.25	0.40 (1.60)	301	3.33
14	1454	870	1.2	135	CO_2	Dynamic	1004-673	0.25	0.40 (1.60)	266	1.34

Table SC-2: Operating parameters and fuel production performance for the CF-NG, CF-MG and CF-HG foams (T_{red} is the reduction temperature, P_{red} the reduction pressure and T_{ox} the oxidation temperature; gas flow-rates are given at normal conditions)

	Reduction step parameters				Oxidation step parameters						
Cycle #	**T_{red} (°C)**	**P_{red} (hPa)**	**Ar flow rate during reduction (L/min)**	**O_2 produced (µmol/g)**	**Oxidant gas**	**Oxidation temperature regime**	**T_{ox} (°C)**	**Oxidant gas molar fraction**	**Oxidant gas flow rate (total flow rate) (L/min)**	**Fuel produced (µmol/g)**	**Peak fuel production rate (mL/g/min)**
CF-HG (m= 65.23 g)											
1	1342	0.883	1.2	85	CO_2	Isothermal	1023	0.25	0.40 (1.60)	154	1.0
2	1332	0.880	1.2	80	CO_2	Dynamic	1089-801	0.25	0.40 (1.60)	161	1.7
3	1277	0.880	1.2	57	CO_2	Dynamic	1067-796	0.25	0.40 (1.60)	113	1.5
4	1262	0.876	1.2	45	CO_2	Dynamic	1040-786	0.50	1.00 (2.00)	94	3.0
5	1331	0.858	1.2	77	CO_2	Isothermal	974	0.25	0.40 (1.60)	135	1.0
6	1327	0.874	1.2	74	CO_2	Isothermal	828	0.25	0.40 (1.60)	135	2.3
7	1323	0.873	1.2	69	CO_2	Isothermal	836	0.50	1.00 (2.00)	144	4.7
8	1332	0.867	1.2	82	CO_2	Isothermal	831	1.00	2.00 (2.00)	169	6.3
9	1363	0.871	1.2	93	CO_2	Dynamic	1072-805	0.25	0.40 (1.60)	185	1.7
10	1365	0.109	1.2	158	CO_2	Dynamic	1065-670	0.25	0.40 (1.60)	308	2.4
11	1364	0.105	1.2	152	CO_2	Dynamic	1039-780	1.00	2.00 (2.00)	341	6.6
12	1367	0.875	1.2	85	H_2O	Dynamic	1176-669	0.17	0.25 (1.45)	165	1.8
13	1363	0.905	1.2	95	H_2O	Dynamic	1071-706	0.17	0.25 (1.45)	169	6.5
14	1358	0.906	1.2	81	H_2O	Dynamic	1183-644	0.17	0.25 (1.45)	163	4.3
CF-MG (m= 65.30 g)											
1	1364	0.868	1.2	67	CO_2	Dynamic	1053-800	0.25	0.40 (1.60)	21	1.5
2	1362	0.871	1.2	89	CO_2	Isothermal	694-623	0.25	0.40 (1.60)	185	4.6
3	1409	0.871	1.2	131	CO_2	Dynamic	1052-803	0.25	0.40 (1.60)	259	1.7
4	1367	0.863	1.2	88	CO_2	Isothermal	991	0.25	0.40 (1.60)	171	1.0
5	1372	0.865	1.2	87	CO_2	Isothermal	983	0.25	0.40 (1.60)	167	0.9
6	1373	0.865	1.2	94	CO_2	Isothermal	858	0.25	0.40 (1.60)	195	2.3
7	1376	0.866	1.2	94	CO_2	Dynamic	1064-819	0.25	0.40 (1.60)	183	1.2
8	1374	0.107	1.2	152	CO_2	Dynamic	1062-756	0.25	0.40 (1.60)	300	2.1
9	1370	0.105	1.2	159	CO_2	Dynamic	975-693	0.25	0.40 (1.60)	267	2.2
10	1370	0.873	1.2	89	H_2O	Dynamic	1007-691	0.11	0.25 (2.25)	181	0.7
11	1377	0.909	1.2	92	H_2O	Dynamic	1060-640	0.17	0.25 (1.45)	201	0.6

	Reduction step parameters					Oxidation step parameters					
Cycle #	**T_{red} (°C)**	**P_{red} (hPa)**	**Ar flow rate during reduction (L/min)**	**O_2 produced (µmol/g)**	**Oxidant gas**	**Oxidation temperature regime**	**T_{ox} (°C)**	**Oxidant gas molar fraction**	**Oxidant gas flow rate (total flow rate) (L/min)**	**Fuel produced (µmol/g)**	**Peak fuel production rate (mL/g/min)**
12	1366	0.872	1.2	88	CO_2	Dynamic	1049-686	0.20	0.30 (1.50)	207	1.0
13	1370	0.860	1.2	92	H_2O	Dynamic	999-790	0.17	0.25 (1.45)	180	1.1
14	1369	0.875	1.2	87	H_2O	Dynamic	1037-614	0.17	0.25 (1.45)	185	1.0
15	1364	0.869	1.2	88	H_2O	Dynamic	997-783	0.11	0.25 (2.25)	199	0.8
16	1365	0.909	1.2	86	H_2O	Dynamic	980-690	0.17	0.24 (1.44)	187	1.2
17	1423	0.108	1.2	183	CO_2	Dynamic	1056-831	1.00	2.00 (2.00)	390	8.6
18	1371	0.876	1.2	100	CO_2	Dynamic	1045-825	0.25	0.40 (1.60)	184	1.2
CF-NG (m= 52.36 g)											
1	1379	0.871	1.2	81	CO_2	Dynamic	1015-811	0.25	0.40 (1.60)	182	2.6
2	1377	0.872	1.2	90	CO_2	Dynamic	994-795	0.25	0.40 (1.60)	190	3.2
3	1432	0.871	1.2	137	CO_2	Dynamic	1018-826	0.25	0.40 (1.60)	272	4.1
4	1381	0.871	1.2	89	CO_2	Isothermal	876	0.25	0.40 (1.60)	181	4.7
5	1380	0.113	1.2	138	CO_2	Dynamic	1041-862	0.25	0.40 (1.60)	238	3.2
6	1374	0.869	1.2	81	H_2O	Dynamic	1088-634	0.17	0.24 (1.44)	150	1.7
7	1378	0.867	1.2	79	CO_2	Dynamic	1122-811	0.25	0.40 (1.60)	200	2.1
8	1379	0.87	1.2	92	CO_2	Isothermal	883	0.25	0.40 (1.60)	205	3.3
9	1390	0.192	1.2	144	CO_2	Dynamic	1053-816	0.25	0.40 (1.60)	304	2.7
10	1437	0.872	1.2	119	CO_2	Dynamic	1070-855	0.25	0.40 (1.60)	241	2.1
11	1375	0.864	1.2	83	CO_2	Dynamic	1026-883	0.25	0.40 (1.60)	173	1.8
12	1375	0.867	1.2	89	CO_2	Dynamic	1007-835	0.50	1.00 (2.00)	194	4.2
13	1376	0.869	1.2	84	CO_2	Dynamic	1038-875	1.00	2.00 (2.00)	193	5.0
14	1374	0.872	1.2	133	CO_2	Dynamic	982-796	0.25	0.40 (1.60)	226	3.0
15	1377	0.874	1.2	86	CO_2	Dynamic	1011-748	0.25	0.20 (0.80)	170	1.2
16	1374	0.108	1.2	123	CO_2	Dynamic	1006-811	0.25	0.40 (1.60)	219	2.3
17	1385	0.856	1.2	91	H_2O	Dynamic	1026-766	0.18	0.27 (1.47)	179	0.7
18	1385	0.893	1.2	90	H_2O	Dynamic	1054-697	0.39	0.45 (1.15)	174	0.9
19	1050	0.893	1.2	10	H_2O	Dynamic	911-796	0.18	0.26 (1.46)	7	0.1
20	1376	0.857	1.2	86	CO_2	Dynamic	1051-744	0.25	0.40 (1.60)	186	1.5
21	1377	0.1094	1.2	142	CO_2	Dynamic	1044-815	1.00	2.00 (2.00)	300	6.6

	Reduction step parameters					Oxidation step parameters					
Cycle #	**T_{red} (°C)**	**P_{red} (hPa)**	**Ar flow rate during reduction (L/min)**	**O_2 produced (µmol/g)**	**Oxidant gas**	**Oxidation temperature regime**	**T_{ox} (°C)**	**Oxidant gas molar fraction**	**Oxidant gas flow rate (total flow rate) (L/min)**	**Fuel produced (µmol/g)**	**Peak fuel production rate (mL/g/min)**
22	1380	0.116	1.2	132	H_2O	Dynamic	1055-669	0.25	0.43 (1.73)	235	1.1
23	1410	0.863	1.2	111	CO_2	Dynamic	1052-823	1.00	2.00 (2.00)	252	5.4
24	1408	0.864	1.2	104	CO_2	Dynamic	1052-864	0.67	2.00 (3.00)	225	4.7
25	1411	0.862	1.2	124	CO_2	Dynamic	1054-839	0.50	2.00 (4.00)	231	4.6
26	1350	0.863	1.2	65	CO_2	Dynamic	1058-806	0.50	2.00 (4.00)	134	2.9
27	1408	0.863	1.2	111	CO_2	Dynamic	1044-895	0.67	2.00 (3.00)	214	3.4
28	1408	0.863	1.2	104	CO_2	Dynamic	1064-891	0.67	2.00 (3.00)	207	4.7
29	1413	0.109	1.2	154	CO_2	Dynamic	1049-867	1.00	2.00 (2.00)	341	7.5
30	1407	0.868	1.2	101	CO_2	Dynamic	1040-849	0.75	3.00 (4.00)	242	6.6
31	1400	0.871	1.2	91	CO_2	Dynamic	1052-886	0.50	1.00 (2.00)	191	3.2
32	1402	0.110	1.2	146	CO_2	Dynamic	899-753	1.00	2.00 (2.00)	316	9.3

Table SC-3: Operating parameters and fuel production performance for the CF-LSMMg and CF-CSM foams (T_{red} is the reduction temperature, P_{red} the reduction pressure and T_{ox} the oxidation temperature; gas flow-rates are given at normal conditions)

	Reduction step parameters				**Oxidation step parameters**						
Cycle #	**T_{red} (°C)**	**P_{red} (hPa)**	**Ar flow rate during reduction (L/min)**	**O_2 produced (µmol/g)**	**Oxidant gas**	**Oxidation temperature regime**	**T_{ox} (°C)**	**Oxidant gas molar fraction**	**Oxidant gas flow rate (total flow rate) (L/min)**	**Fuel produced (µmol/g)**	**Peak fuel production rate (mL/g/min)**
CF-LSMMg (m=88.2178 g)											
1	1398	0.871	1.2	166	CO_2	Dynamic	1011-777	0.25	0.40 (1.60)	145	0.8
2	1403	0.867	1.2	89	CO_2	Dynamic	904-688	0.25	0.40 (1.60)	89	0.7
3	1411	0.101	1.2	222	CO_2	Dynamic	1045-988	1.00	2.00 (2.00)	387	4.3
4	1399	0.910	1.2	87	H_2O	Dynamic	1040-671	0.17	0.25 (1.45)	149	0.2
5	1406	0.098	1.2	206	CO_2	Dynamic	1061-757	1.00	2.00 (2.00)	359	4.3
6	1403	0.873	1.2	89	CO_2	Dynamic	1008-753	1.00	2.00 (2.00)	172	2.1
7	1409	0.100	1.2	203	H_2O	Dynamic	1034-781	0.24	0.80 (3.30)	234	1.4
8	1407	0.910	1.2	72	H_2O	Dynamic	959-615	0.50	0.80 (1.60)	166	1.1
9	1407	0.102	1.2	202	CO_2	Dynamic	1050-774	0.67	2.00 (3.00)	298	3.6
10	1407	0.096	1.2	153	CO_2	Dynamic	1041-680	1.00	1.00 (1.00)	344	2.3
CF-CSM (m=82.9748 g)											
1	1407	0.144	2	235	CO_2	Dynamic	1056-760	1.00	2.00 (2.00)	250	2.4
2	1407	0.141	2	103	CO_2	Dynamic	1047-765	0.67	2.00 (3.00)	219	2.1
3	1407	0.143	2	174	CO_2	Dynamic	953-604	1.00	2.00 (2.00)	230	2.2
4	1407	0.870	1.2	48	CO_2	Dynamic	1049-798	1.00	2.00 (2.00)	146	1.3
5	1410	0.865	1.2	63	CO_2	Dynamic	953-760	1.00	2.00 (2.00)	114	1.2

Table SC-4: Operating parameters and fuel production performance for the CF-OG and CF-OGP foams (T_{red} is the reduction temperature, P_{red} the reduction pressure and T_{ox} the oxidation temperature; gas flow-rates are given at normal conditions)

	Reduction step parameters				**Oxidation step parameters**						
Cycle #	**T_{red} (°C)**	**P_{red} (hPa)**	**Ar flow rate during reduction (L/min)**	**O_2 produced (µmol/g)**	**Oxidant gas**	**Oxidation temperature regime**	**T_{ox} (°C)**	**Oxidant gas molar fraction**	**Oxidant gas flow rate (total flow rate) (L/min)**	**Fuel produced (µmol/g)**	**Peak fuel production rate (mL/g/min)**
CF-OG (m=28.7318 g)											
1	1410	0.111	1.2	150	CO_2	Dynamic	1046-860	0.25	0.40 (1.60)	222	2.2
2	1404	0.089	1.2	102	CO_2	Dynamic	1071-841	1.00	2.00 (2.00)	227	3.3
3	1403	0.874	1.2	83	CO_2	Dynamic	1066-892	0.25	0.40 (1.60)	84	0.8
4	1407	0.871	1.2	53	CO_2	Dynamic	947-805	0.25	0.40 (1.60)	101	1.0
5	1410	0.090	1.2	105	CO_2	Dynamic	953-770	1.00	2.00 (2.00)	212	3.3
6	1407	0.111	1.2	116	CO_2	Dynamic	1050-856	1.00	2.00 (2.00)	214	2.7
7	1406	0.872	1.2	55	H_2O	Dynamic	1026-790	0.17	0.25 (1.45)	87	0.4
8	1406	0.940	1.2	51	H_2O	Dynamic	962-713	0.17	0.25 (1.45)	78	0.4
9	1405	0.872	1.2	72	CO_2	Dynamic	1058-781	0.25	0.40 (1.60)	96	0.7
10	1408	0.093	1.2	93	CO_2	Dynamic	1049-879	0.67	2.00 (3.00)	199	2.7
11	1406	0.092	1.2	114	H_2O	Dynamic	1019-724	0.17	0.25 (1.45)	166	0.8
12	1405	0.905	1.2	44	H_2O	Dynamic	1058-803	0.35	0.54 (1.54)	103	0.4
13	1404	0.906	1.2	53	H_2O	Dynamic	1055-797	0.24	0.41 (1.71)	85	0.4
CF-OGP (m=40.8051 g)											
1	1406	0.102	1.2	181	CO_2	Dynamic	1058-839	0.25	0.40 (1.60)	255	1.9
2	1404	0.105	1.2	124	CO_2	Dynamic	1047-820	1.00	2.00 (2.00)	284	3.2
3	1415	0.109	1.2	159	CO_2	Dynamic	953-715	1.00	2.00 (2.00)	333	4.0
4	1409	0.865	1.2	91	CO_2	Dynamic	1050-764	0.25	0.40 (1.60)	163	1.1
5	1408	0.108	1.2	151	H_2O	Dynamic	1052-749	0.17	0.25 (1.45)	243	1.1
6	1409	0.905	1.2	80	H_2O	Dynamic	1040-790	0.17	0.25 (1.45)	147	0.6
7	1407	0.911	1.2	80	H_2O	Dynamic	951-715	0.17	0.25 (1.45)	144	0.7
8	1411	0.871	1.2	104	CO_2	Dynamic	955-737	0.25	0.40 (1.60)	189	1.7
9	1407	0.096	1.2	139	CO_2	Dynamic	1055-834	1.00	2.00 (2.00)	294	3.5
10	1411	0.873	1.2	88	CO_2	Dynamic	1047-889	0.25	0.40 (1.60)	96	0.9
11	1420	0.102	1.2	154	CO_2	Dynamic	1058-834	0.25	0.40 (1.60)	258	1.9
12	1406	0.101	1.2	131	CO_2	Dynamic	1049-805	1.00	2.00 (2.00)	283	3.5

Reduction step parameters						Oxidation step parameters					
Cycle #	**T_{red} (°C)**	**P_{red} (hPa)**	**Ar flow rate during reduction (L/min)**	**O_2 produced (µmol/g)**	**Oxidant gas**	**Oxidation temperature regime**	**T_{ox} (°C)**	**Oxidant gas molar fraction**	**Oxidant gas flow rate (total flow rate) (L/min)**	**Fuel produced (µmol/g)**	**Peak fuel production rate (mL/g/min)**
13	1407	0.096	1.2	143	CO_2	Dynamic	1049-804	1.00	2.00 (2.00)	313	4.0
14	1408	0.101	1.2	132	CO_2	Dynamic	956-826	1.00	2.00 (2.00)	248	4.9
15	1405	0.911	1.2	83	H_2O	Dynamic	1055-725	0.35	0.54 (1.54)	154	0.8

In order to investigate the redox behavior of dual-phase compositions, TGA was performed with ceria-perovskite powder mixtures (Figure SC-3, 4 and Table SC-5). Four compositions were investigated: ceria powder mixed with 10 wt% of LSMMg, 50 wt% of LSMMg, 10 wt% of CSM, 50 wt% of CSM, and 10 wt% of $Y_{0.5}Sr_{0.5}MnO_3$ (YSM as an alternative material to CSM), abbreviated as CeO_2-10% LSMMg, 50% LSMMg, CeO_2-10% CSM, CeO_2-50% CSM, and CeO_2-10% YSM, respectively. The O_2 production yield was increased for CeO_2-10%YSM, CeO_2-50% LSMMg, CeO_2-10% CSM and CeO_2-50% CSM in comparison with pristine ceria. Accordingly, the CO production yield was also increased, highlighting the beneficial impact on the redox activity of dual phase composition. Among these materials, CSM provides a higher CO production yield than YSM, thus CSM and LSMMg were selected as perovskite coatings on ceria foam.

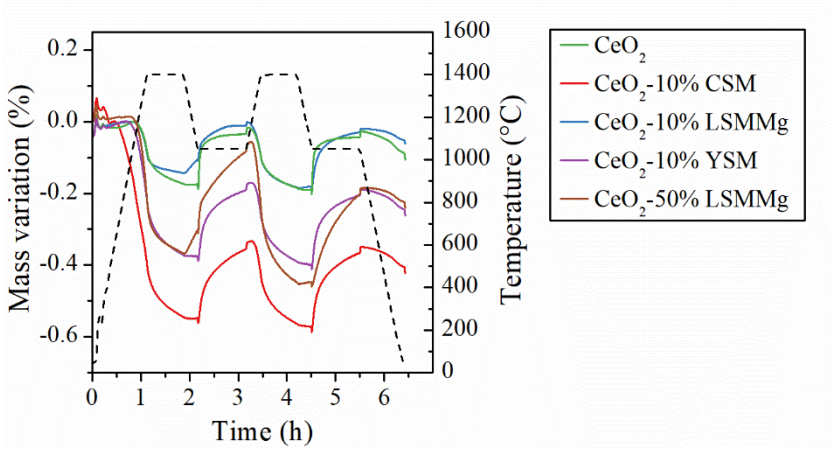

Figure SC-3: Thermogravimetric profiles along with the temperature during thermochemical cycling of powder mixtures: CeO2, CeO2-10% CSM, CeO2-10% LSMMg, CeO2-10% YSM and CeO2-50% LSMMg

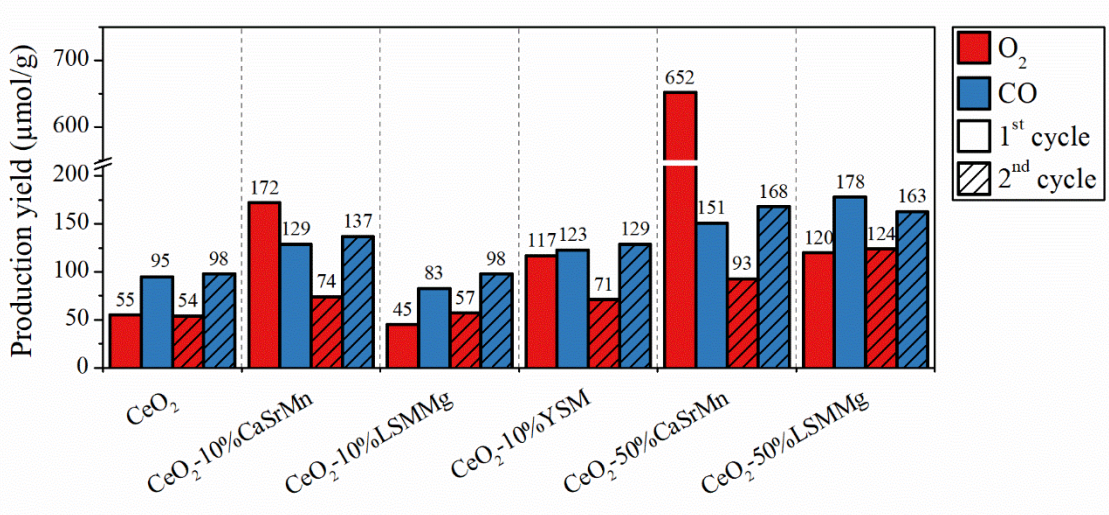

Figure SC-4: O_2 and CO production yields produced during the thermogravimetric analysis during cycling with CeO_2, CeO_2-10% CSM, CeO_2-10% LSMMg, CeO_2-10% YSM, CeO_2-50% CSM and CeO_2-50% LSMMg

Table SC-5: O_2 and CO production yields during two thermochemical cycles in TGA for dual phase powder compositions

Powder composition (wt%)	1st cycle		2nd cycle	
	O_2 yield (µmol/g)	CO yield (µmol/g)	O_2 yield (µmol/g)	CO yield (µmol/g)
CeO_2	55	95	54	98
CeO_2-10% YSM	117	123	71	129
CeO_2-10% LSMMg	45	83	57	98
CeO_2-50% LSMMg	120	178	124	163
CeO_2-10% CSM	172	129	74	137
CeO_2-50% CSM	652	151	93	166

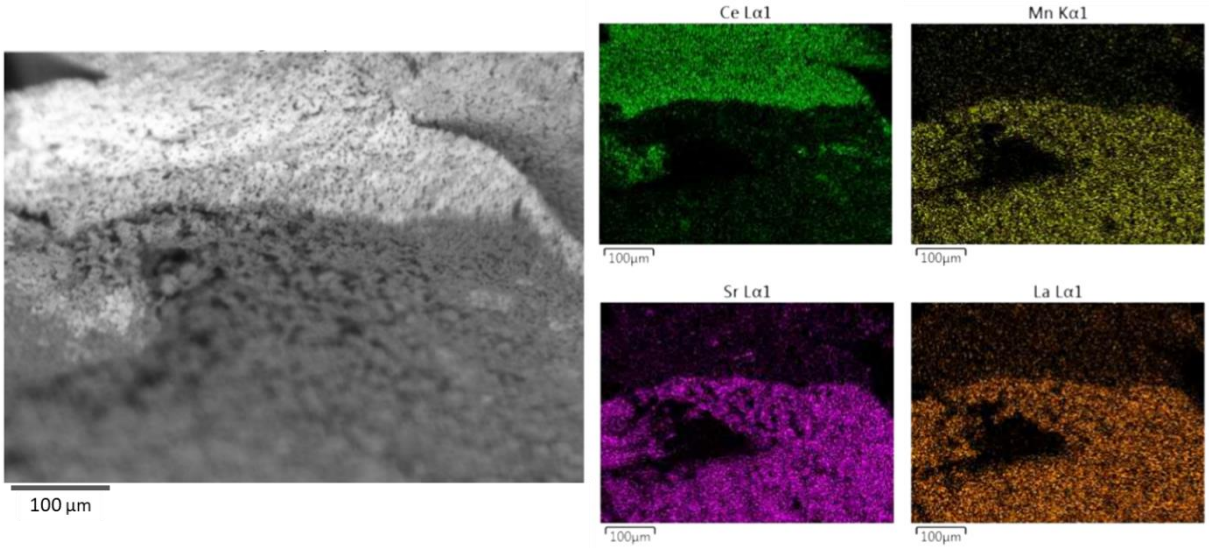

Figure SC-5 EDS mapping of the LSMMg-coated ceria foam

It is important to note that finding a flat area relevant for EDS analysis is quite difficult. The complex (sinuous and curved) shape of the ceria foams explains the blurred effect observed on the foreground as well as the perspective effect. The difference in composition between the dark and bright areas is clearly evidenced by the EDS mapping. The small dark grains correspond to the LSMMg coating layer while the upper part of the image with light grains corresponds to CeO_2.

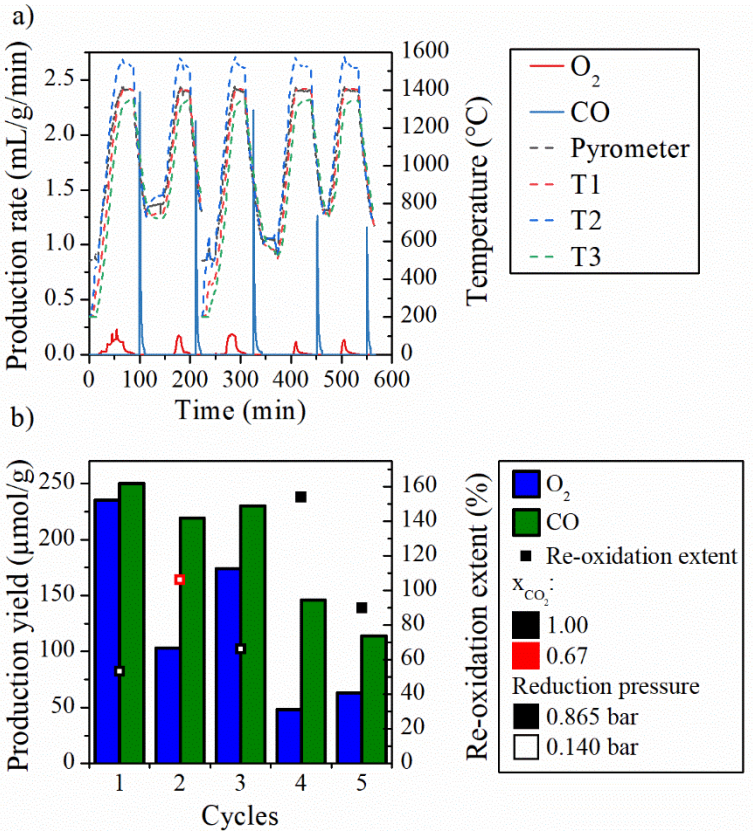

Figure SC-6: a) Evolution of O_2 and CO production rates and b) associated O_2 and CO production yield along with the reoxidation extent, during five successive thermochemical cycles performed with the composite CF-CSM foam.

The aim of adding a thin layer of perovskite at the ceria surface is to boost the reduction ability of ceria, because the larger reducibility of the perovskite phase compared to ceria is expected to promote oxygen diffusion in ceria. That is why the composite was compared to pure ceria and not to pure LSMMg in Figure SC-7. The promotional effect of the perovskite coating is actually reflected by the enhanced O_2 yield. Indeed, the theoretical O_2 yield for the composite can be obtained from the productivity of the individual compounds weighted by their mass fraction (90% CeO_2, 10% LSMMg). The TGA results (see chapter 2) show that the O_2 production from LSMMg in the first cycle is 4.89 times higher than for CeO_2. The same factor was applied to estimate the expected O_2 production from LSMMg (1st cycle) in the solar reactor, given that the O_2 yield from pure ceria is known (86 µmol/g, Figure SC-7). Then, the global expected O_2 production in the 1st cycle was 77 µmol/g (86*0.9) for CeO_2 and 42 µmol/g (86*4.89*0.1) for LSMMg, thus corresponding to 119 µmol/g for the total in LSMMg-CeO_2 foam, which is lower than the experimentally measured value (166 µmol/g, Figure SC-7), thereby suggesting the synergistic effect of the composite layered structure.

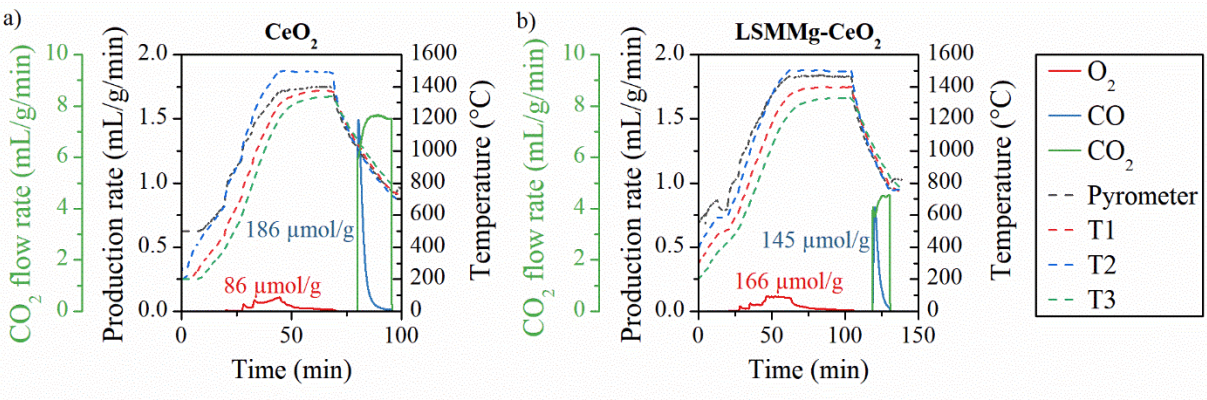

Figure SC-7: Thermochemical cycle with reduction at T1~1400 °C under atmospheric pressure followed by oxidation at ~1010 °C - 800 °C under 25mol% of CO_2 for a) pure ceria foam and b) CF-LSMMg (Cycle #1)

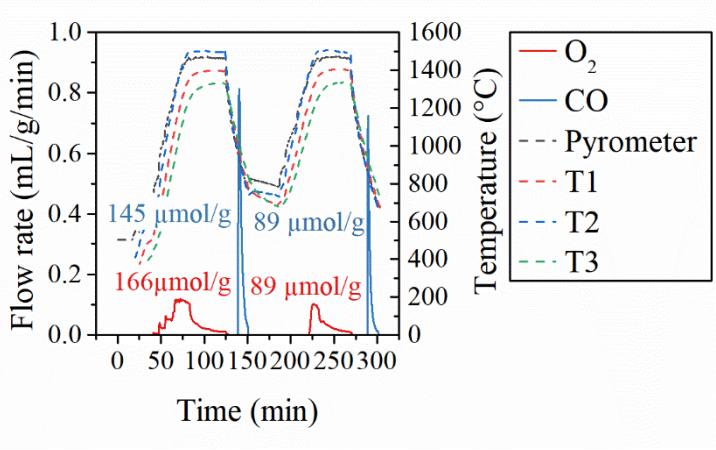

Figure SC-8: Evolution of O_2 and CO production rates during the two first consecutive cycles performed with LSMMg-CeO_2 foam (Cycles #1 and #2)

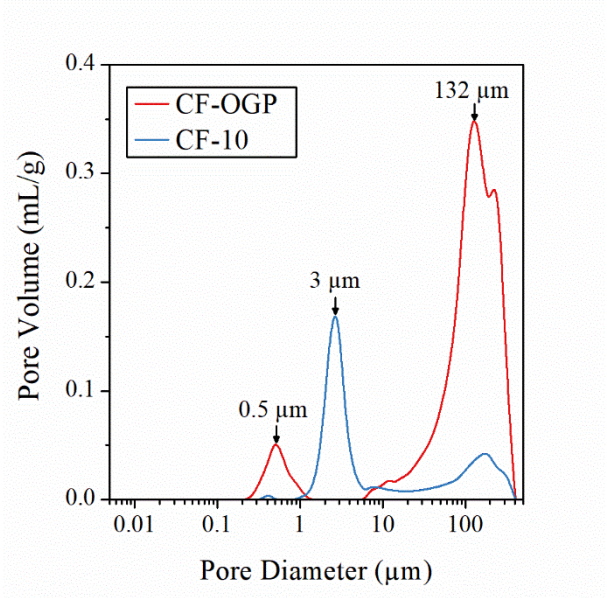

Figure SC-9: Pore size distribution measured by mercury porosimetry for CF-OGP and CF-10 ceria foams

The mercury porosimetry measurement is based on the Washburn equation (53):

$$D = -\frac{4\gamma \cos\theta}{P} \tag{53}$$

where γ is the surface tension of Hg, θ the contact angle Hg/solid, D the pore diameter (capillary shape hypothesis) and P the applied pressure. As mercury is a non-wetting liquid for most ceramics (high contact angle), it only penetrates in porous structures under pressure. The pore size distribution is determined by measuring the volume of mercury that progressively penetrates the porous solid as a function of the applied pressure. Large pores are filled first at low pressure, followed by smaller pores when the pressure increases (stepwise intrusion). However, in reality pores do not have perfect cylindrical shape and constrictions or ink-bottle shapes pores can lead to measurement artefacts. In fact, as the method measures the size of constrictions or pore entrances, the associated pore volume integrates also the volume of the underlying cavity whose size cannot be measured. Indeed, at pressure P_i, a pore with diameter D_i can be filled by Hg only if there exists a path from the surface toward the pore with a diameter superior (or equal) to D_i. For example, in Figure SC-10.a, the pore volume beyond the throat cannot be filled by Hg because the applied pressure (P_1) is lower than the pressure required to fill the throat (P_{throat}). When the pressure is increased until P_{throat}, Hg fills the throat, as illustrated in Figure SC-10.b. Finally, when the pressure overpasses P_{throat} (corresponding to P_2 in Figure SC-10.c), the pore volume on the opposite side of the surface is instantaneously filled. The pressure profile as a function of the depth of the pore is represented in Figure SC-10.d. Thus, this mechanism leads to high Hg volume variation for a pressure close to P_{throat} that is not associated to the global pore diameter, but rather to the pore having a throat with D_{throat} diameter [252].

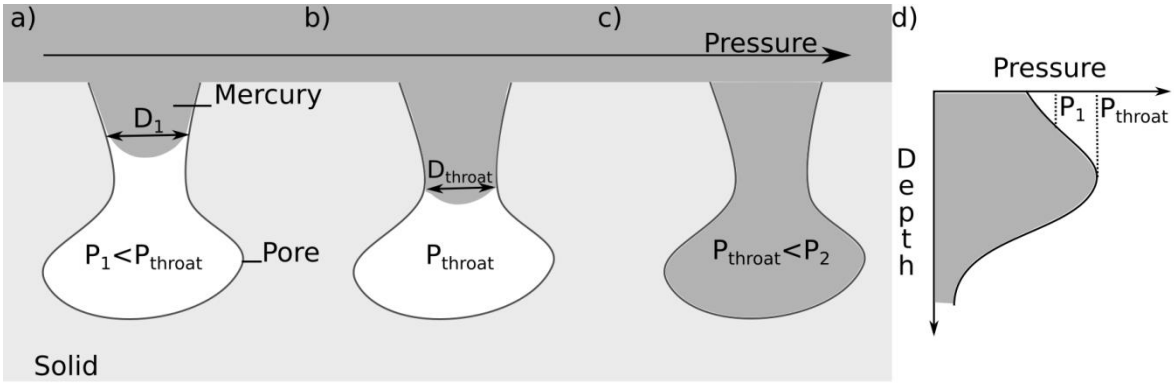

Figure SC-10: Schematic representation of the mercury porosimetry measurement, showing ink-bottle pores filled with Hg for a) a pressure $P_1<P_{throat}$ b) a pressure P_{throat}, c) a pressure $P_2>P_{throat}$ and d) pressure profile required to fill the pore as a function of the pore depth

Table SC-6: Data used to calculate the cycle efficiency and the instant solar-to-fuel energy conversion efficiency

Foam	Cycle	δ_{red}	ΔH (kJ/mol)	n_{CO} (mol)	ΔT (K)	P_{solar} (J/s)	CO peak production rate (mL/min/g)
CF-20	8	0.0323	462	0.015	705	1350	5.02
CF-10	32	0.0413	457	0.016	418	1350	9.93
CF-NG	32	0.0501	453	0.017	503	1350	9.26
CF-MG	17	0.0563	449	0.025	367	1350	8.57
CF-HG	11	0.0523	451	0.022	325	1350	6.60
CF-LSMMg	3	0.0774	440	0.035	366	1350	4.30
CF-CSM	1	0.0809	439	0.021	351	1350	2.38
CF-OG	5	0.0361	459	0.006	457	1350	3.30
CF-OGP	3	0.0547	450	0.014	462	1350	4.01

Appendix D - Solar redox cycling of structured ceria particulate materials in direct and indirect heating solar reactor

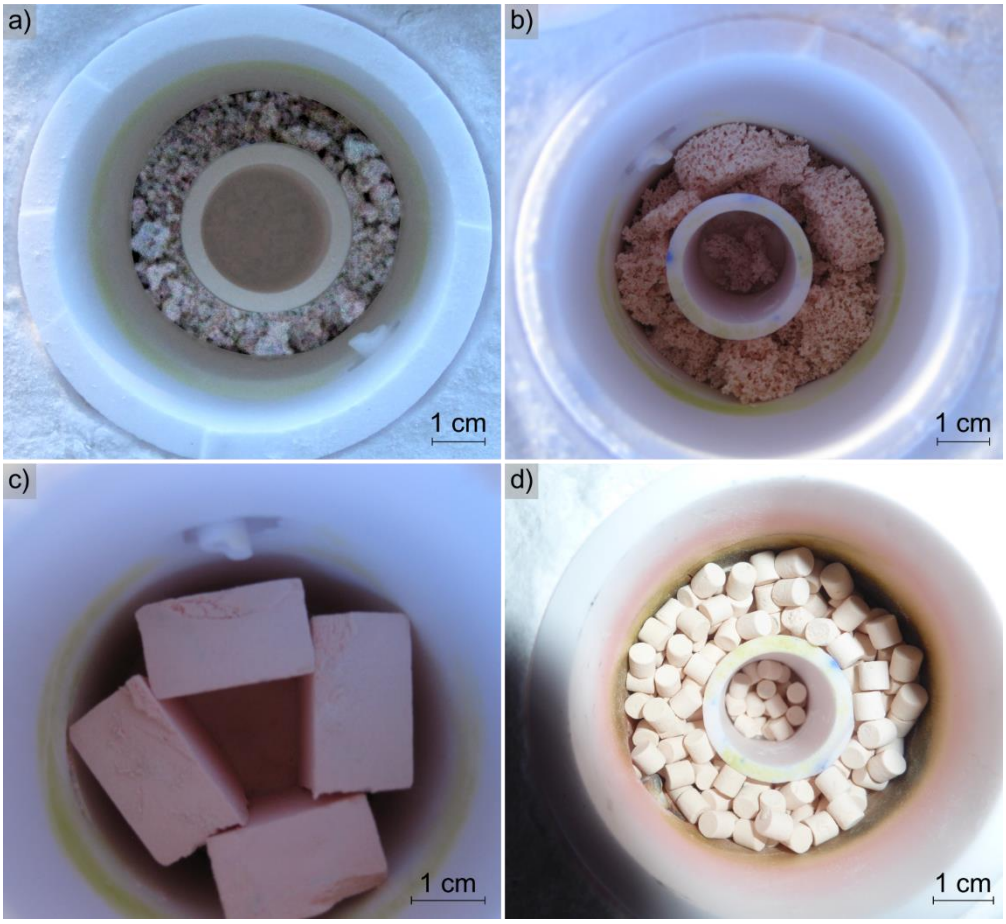

Figure SD-1: Images of the investigated reactive ceria materials: a) CTCe19, b) CeF, c) CeFB and d) CeP

Figure SD-2: Image of CeMS material

Table SD-1: O_2 and H_2 production yields during the investigated two-step thermochemical cycles in indirectly-heated tubular solar reactor (oxidation was performed during free cooling with steam injection starting at the mentioned temperature) for CTCe17, CTCe19 and CeF

Cycle #	Reduction step			Oxidation step				
	T_{red} (°C)	Ar flow rate during reduction (L/min)	O_2 produced (µmol/g)	T_{ox} (°C)	Oxidant gas (molar fraction)	Oxidant gas flow rate (total flow rate) (L/min)	Fuel produced (µmol/g)	Peak fuel production rate (mL/g/min)
CTCe17								
1	1330	0.25	26.9	880	H_2O (0.45)	0.21 (0.46)	62.0	0.6
2	1400	0.25	74.4	1050	H_2O (0.45)	0.21 (0.46)	157.0	1.4
3	1400	0.25	71.5	1050	H_2O (0.45)	0.21 (0.46)	162.3	1.4
4	1400	0.25	70.7	1050	H_2O (0.50)	0.25 (0.50)	140.1	1.3
5	1400	0.25	63.2	1050	H_2O (0.50)	0.25 (0.50)	135.1	1.3
6	1400	0.25	61.0	950	H_2O (0.50)	0.25 (0.50)	133.9	1.5
CTCe19								
1	1400	0.25	63.1	1050	H_2O (0.45)	0.21 (0.46)	125.9	1.1
2	1400	0.25	52.7	1050	H_2O (0.45)	0.21 (0.46)	113.6	1.0
3	1450	0.25	88.9	1050	H_2O (0.45)	0.21 (0.46)	171.1	1.6
4	1400	0.25	47.6	1150	H_2O (0.45)	0.21 (0.46)	101.2	0.6
5	1400	0.25	49.4	1050	H_2O (0.45)	0.21 (0.46)	104.4	0.9
6	1400	0.25	44.8	950	H_2O (0.45)	0.21 (0.46)	114.1	1.1
7	1400	0.25	72.5	1050	H_2O (0.45)	0.21 (0.46)	133.2	1.3
8	1400	0.50	56.1	1050	H_2O (0.29)	0.21 (0.71)	118.9	1.3
9	1400	0.25	56.1	950	H_2O (0.45)	0.21 (0.46)	117.3	1.3
CeF								
1	1400	0.25	44	1050	H_2O (0.45)	0.21 (0.46)	95.4	0.7
2	1400	0.25	49.8	1050	H_2O (0.45)	0.21 (0.46)	115.2	0.8
3	1400	0.25	52.0	950	H_2O (0.45)	0.21 (0.46)	112.0	1.2
4	1400	0.25	52.4	1150	H_2O (0.45)	0.21 (0.46)	102.5	0.5
5	1450	0.25	72.2	1050	H_2O (0.45)	0.21 (0.46)	147.4	0.7

Table SD-2: Operating parameters along with oxygen and fuel production amounts for the investigated reactive materials including CTCe, CeF, CeFB, CeP and CeMS (oxidation was performed during free cooling with oxidant gas injection starting at the mentioned temperature) in directly-heated solar reactor. The asterisk (*) indicates an overpressure (0.930 bar instead of 0.865 bar) during the oxidation reaction due to the reactor configuration

Cycle #	**Reduction step parameters**				**Oxidation step parameters**				
	$T1_{red}$ (°C)	**Pressure (bar)**	**Ar flow rate during reduction (L/min)**	**O_2 produced (µmol/g)**	**$T1_{ox}$ (°C)**	**Oxidant gas (oxidant molar fraction)**	**Oxidant gas flow rate (total flow rate) (L/min)**	**Fuel produced (µmol/g)**	**Peak fuel production rate (mL/g/min)**
CTCe19									
1	1107	0.865	1.2	25	1040	CO_2 (0.25)	0.40 (1.60)	56	1.2
2	1414	0.871	1.2	65	1043	CO_2 (0.25)	0.40 (1.60)	131	1.8
3	1413	0.870	1.2	68	1060	CO_2 (0.25)	0.40 (1.60)	122	1.6
4	1405	0.871	1.2	75	1056	CO_2 (1.00)	2.00 (2.00)	148	2.9
5	1411	0.110	1.2	94	1049	CO_2 (0.25)	0.40 (1.60)	190	2.9
6	1410	0.864	1.2	64	949	CO_2 (0.25)	0.40 (1.60)	114	3.1
7	1409	0.871	1.2	68	1088	CO_2 (0.25)	0.40 (1.60)	122	1.5
8	1414	0.874	1.2	64	1032	H_2O (0.18)	0.27 (1.47)	116	0.7
9	1413	0.870	1.2	68	1062	CO_2 (0.25)	0.40 (1.60)	121	1.8
10	1413	0.870	1.2	60	1031	H_2O (0.18)	0.27 (1.47)	119	0.8
11	1423	0.913	1.2	65	1035	H_2O (0.18)	0.27 (1.47)	129	0.8
12	1410	0.870	1.2	68	1054	CO_2 (0.25)	0.40 (1.60)	126	1.8
13	1413	0.871	1.2	64	1054	CO_2 (0.24)	0.20 (0.85)	127	0.9
14	1410	0.871	1.2	67	1043	H_2O (0.39)	0.45 (1.15)	125	0.8
15	1412	0.905	1.2	69	1043	H_2O (0.50)	0.45 (0.90)	122	0.6
16	1405	0.911	1.2	64	1049	H_2O (0.26)	0.45 (1.75)	112	0.9
CeF									
1	1412	0.869	1.2	76	1051	CO_2 (0.25)	0.40 (1.60)	131	1.3
2	1413	0.874	1.2	71	1055	CO_2 (0.25)	0.40 (1.60)	137	1.2
3	1413	0.871	1.2	72	1029	H_2O (0.18)	0.27 (1.47)	129	0.5
4	1411	0.911	1.2	66	1041	H_2O (0.18)	0.27 (1.47)	117	0.4
5	1411	0.863	1.2	72	1050	H_2O (0.39)	0.45 (1.15)	130	0.6
6	1411	0.909	1.2	67	940	H_2O (0.18)	0.27 (1.47)	119	0.9
7	1405	0.901	1.2	53	1031	H_2O (0.50)	0.45 (0.90)	101	0.4
CeFB									
1	1410	0.865	1.2	159	1044	CO_2 (0.25)	0.40 (1.60)	302	3.1
2	1417	0.867	1.2	146	1046	CO_2 (0.25)	0.40 (1.60)	292	2.9
3	1410	0.869	1.2	160	1047	H_2O (0.18)	0.27 (1.47)	288	1.3

Cycle #	Reduction step parameters				Oxidation step parameters				
	$T1_{red}$ (°C)	**Pressure (bar)**	**Ar flow rate during reduction (L/min)**	**O_2 produced (µmol/g)**	**$T1_{ox}$ (°C)**	**Oxidant gas (oxidant molar fraction)**	**Oxidant gas flow rate (total flow rate) (L/min)**	**Fuel produced (µmol/g)**	**Peak fuel production rate (mL/g/min)**
4	1413	0.909	1.2	146	1039	H_2O (0.39)	0.45 (1.15)	277	1.6
5	1411	0.902	1.2	145	960	H_2O (0.18)	0.27 (1.47)	268	2.0
6	1411	0.905	1.2	135	1031	H_2O (0.18)	0.27 (1.47)	254	1.1
7	1410	0.906	1.2	123	1060	H_2O (0.26)	0.45 (1.75)	230	1.1
CeP									
1	1391	0.878	1.2	89	1059	CO_2 (0.25)	0.40 (1.60)	173	1.3
2	1400	0.877	1.2	104	1048	CO_2 (1.00)	2.00 (2.00)	208	4.4
3	1401	0.873	1.2	112	1050	CO_2 (0.25)	0.40 (1.60)	195	1.5
4	1407	0.098	1.2	162	1054	CO_2 (1.00)	2.00 (2.00)	315	7.5
5	1403	0.872	1.2	117	1055	H_2O (0.18)	0.27 (1.47)	201	1.0
6	1408	0.911	1.2	100	1047	H_2O (0.40)	0.58 (1.46)	193	1.0
7	1405	0.912	1.2	103	1052	H_2O (0.39)	0.45 (1.15)	193	0.8
8	1410	0.915	1.2	105	955	H_2O (0.18)	0.27 (1.47)	188	1.3
9	1403	0.869	1.2	103	954	CO_2 (0.25)	0.40 (1.60)	152	2.4
10	1403	0.083	1.2	154	1050	CO_2 (1.00)	2.00 (2.00)	308	7.8
11	1403	0.083	1.2	148	959	CO_2 (1.00)	2.00 (2.00)	293	9.5
CeMS									
*1**	1409	0.414	1.2	116	1077	CO_2 (0.25)	0.40 (1.60)	120	0.6
2	1410	0.868	1.2	85	1051	CO_2 (0.23)	0.30 (1.30)	105	0.9
3	1410	0.870	1.2	56	960	CO_2 (0.23)	0.30 (1.30)	104	1.1
4	1409	0.871	1.2	104	1050	CO_2 (0.25)	0.40 (1.60)	172	0.7
5	1412	0.104	1.2	133	1052	CO_2 (1.00)	2.00 (2.00)	297	1.8
6	1418	0.875	1.2	106	764	H_2O (0.17)	0.25 (1.45)	140	1.1
7	1411	0.123	1.2	141	1045	H_2O (0.17)	0.25 (1.45)	256	0.7
8	1415	0.918	1.2	89	1040	H_2O (0.17)	0.25 (1.45)	156	0.4
9	1412	0.915	1.2	90	1051	H_2O (0.37)	0.54 (1.44)	170	0.5
10	1409	0.107	1.2	151	1053	CO_2 (1.00)	2.00 (2.00)	331	1.8
11	1410	0.875	1.2	85	1064	CO_2 (0.25)	0.40 (1.60)	128	0.5
12	1407	0.102	1.2	142	1053	CO_2 (1.00)	2.00 (2.00)	306	1.2
13	1408	0.099	1.2	136	1046	CO_2 (0.67)	2.00 (3.00)	246	1.2
14	1408	0.873	1.2	71	1066	CO_2 (0.25)	0.40 (1.60)	114	0.4
15	1419	0.083	1.2	136	1051	CO_2 (1.00)	2.00 (2.00)	282	1.3
16	1412	0.871	1.2	80	953	CO_2 (0.25)	0.40 (1.60)	139	0.6

Cycle #	Reduction step parameters				Oxidation step parameters				
	$T1_{red}$ (°C)	**Pressure (bar)**	**Ar flow rate during reduction (L/min)**	**O_2 produced (µmol/g)**	**$T1_{ox}$ (°C)**	**Oxidant gas (oxidant molar fraction)**	**Oxidant gas flow rate (total flow rate) (L/min)**	**Fuel produced (µmol/g)**	**Peak fuel production rate (mL/g/min)**
17	1408	0.089	1.2	122	950	CO_2 (1.00)	2.00 (2.00)	267	1.7
18	1410	0.870	1.2	72	912	H_2O (0.17)	0.25 (1.45)	96	0.3
19	1410.9	0.912	1.2	57	1061	H_2O (0.17)	0.25 (1.45)	113	0.3

Another reactor configuration was designed to realize a fluidized bed or spouted bed with CeMS particles. The reactor configuration was modified to this end as illustrated in Figure SD-3. An alumina bottom part was placed in the cavity in order to obtain a conic cavity, necessary to fluidize particles. A thin insulating layer along with supporting alumina particles (~2 mm in size) were placed at the bottom of the cavity to avoid the reactive CeMS particles to escape from the cavity via the bottom injection tube. The gas input was placed at the cavity bottom whereas the gas exit was at the window output. A gas flow rate of 0.2 L/min was maintained to protect the Pyrex window. However, this configuration was not well adapted to obtain a fluidized bed. Depending on the gas flow rate input in the cavity, the CeMS particles were either immobile or propelled out from the cavity. Therefore, this configuration was not used and the configuration presented in Figure 4-3 was preferred.

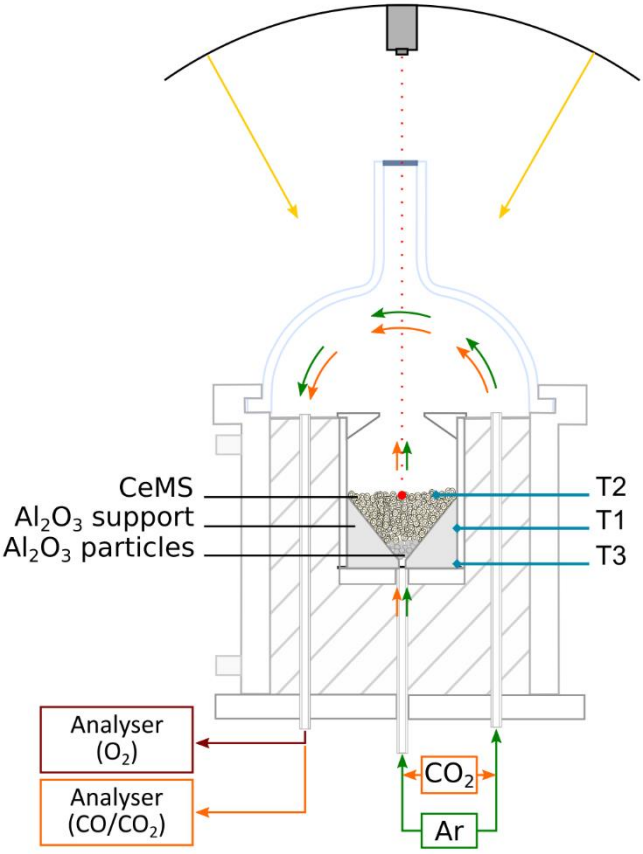

Figure SD-3: Schematic representation of the reactor with conic configuration for CeMS material

Two other configurations were designed (Figure SD-4) for CeMS materials. The first one (Figure SD-4.a) was used during cycle #1. It is similar to Figure 4-3 but the alumina bottom part was placed in the cavity in order to obtain a conic cavity. However, this configuration creates a pressure increase in the cavity (due to the small exit tube diameter: 1.6 mm), making it inappropriate. The second configuration (Figure SD-4.b) was used during cycles #2 and #3. Unlike the previous configuration, the gas flow rates were injected at the cavity bottom to avoid pressure increase in the cavity. An ended tube was placed in the middle of the cavity to allow both an homogeneous heating of the reactive material and particles sweeping by the gas. However, the gas flow input from the bottom of the cavity overturned the alumina ended tube.

Therefore, for all the other cycles, the reactor configuration presented in Figure 4-3 was preferred.

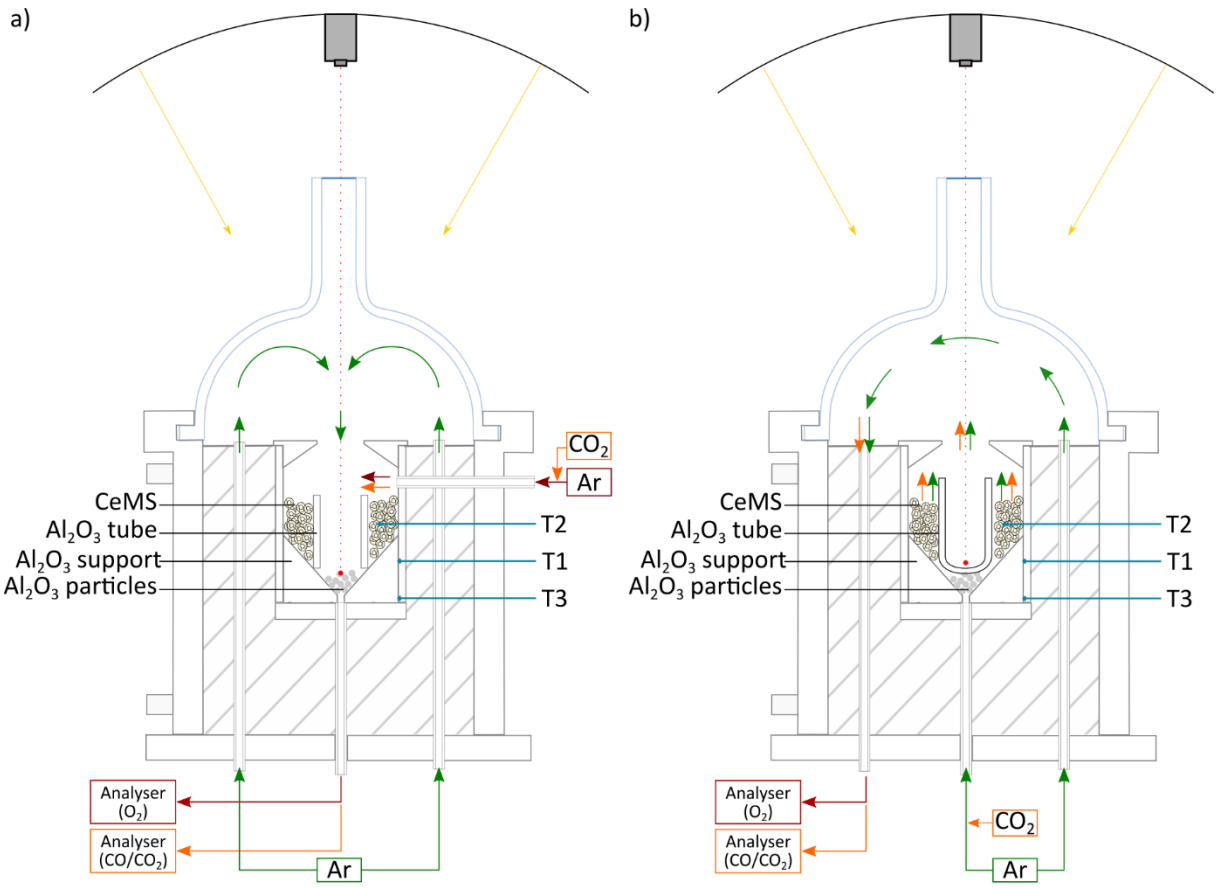

Figure SD-4: Schematic configuration of the reactor used for CeMS during a) cycle #1 and b) cycles #2 and #3

When the CeP and CeMS reactive materials were removed from the solar-heated cavity, few particles that were in contact with alumina tube and directly irradiated by concentrated sunlight, showed a color change (from off-white to green, Figure SD-5) and a melting with alumina part of the cavity, as illustrated for CeP. XRD analysis confirmed the formation of $CeAlO_3$ by reaction between ceria and alumina (Figure SD-6). Such reaction might be attributed to the high temperature underwent by the reacted particles (as they were at the top of the cavity) in contact with alumina. However, due to the small amount of reactive material that had reacted with alumina, no performance decline attributed to this reaction could be observed.

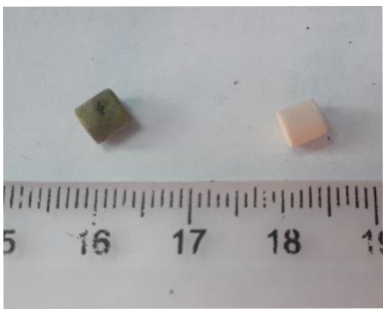

Figure SD-5: Comparison of between CeP materials after cycling: CeP which was in contact with alumina walls (left) and CeP which was not in contact with alumina (right)

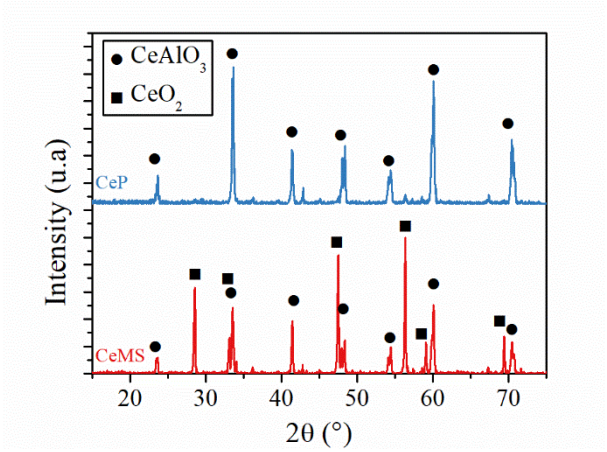

Figure SD-6: XRD patterns of sintered materials CeP (blue) and CeMS (red), recovered from the upper part of the cavity after cycling in the direct heating solar reactor

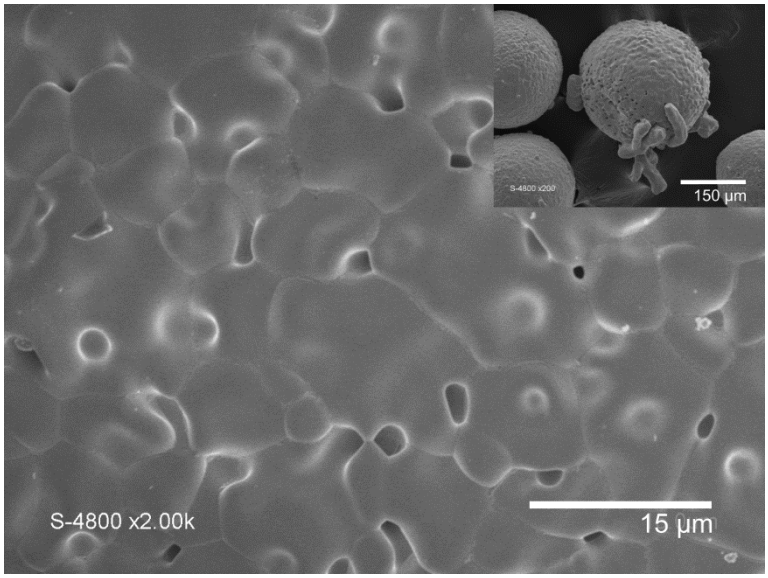

Figure SD-7: SEM images of CeMS particles which have reacted with alumina tube of the cavity

Appendix E - Solar membrane reactor for continuous and isothermal redox splitting of CO_2 and H_2O

Figure SE-1 presents the steady-state O_2 and CO production rates (left), and the O_2 and CO evolution with time along with the temperatures (right). During the heating ramp, the O_2 production rate increases rapidly (starting at 800 °C, measured at T4) up to a peak and decreases to reach an almost stable O_2 production rate. When the temperature decreases, the O_2 production decreases quickly because the reduction is thermodynamically unfavorable. On the contrary, during reactor cooling, the oxidation is thermodynamically favored, thus the CO production rate increases. The total O_2, CO and H_2 amounts produced by the UC, PCC1 and PCC2 membranes were calculated by the integration of associated production rates. The data are reported in Table SE-1.

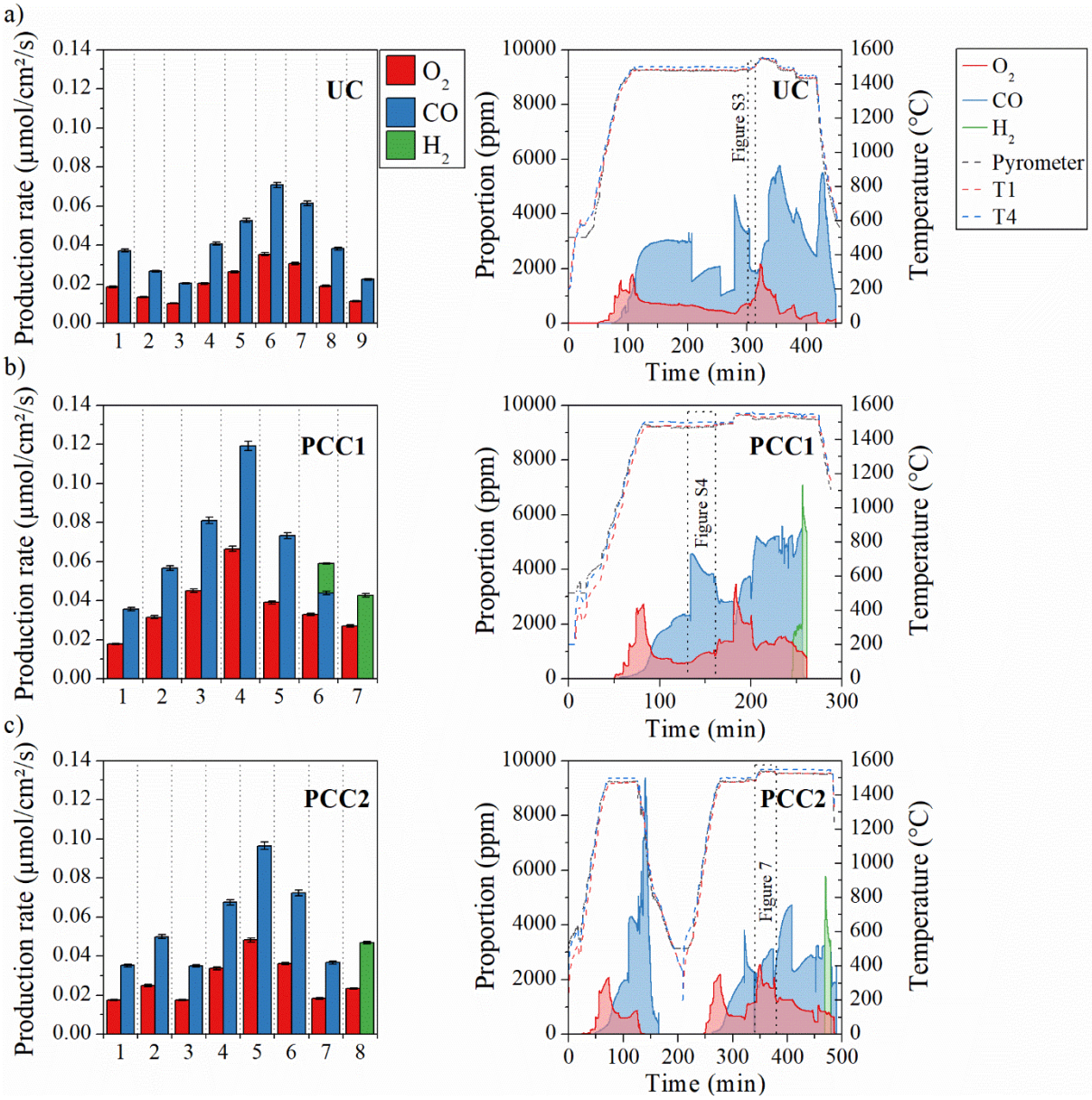

Figure SE-1: O_2, CO and H_2 production rates in steady state conditions for all the operating conditions investigated (left) and production rates evolution over all the successive experimental conditions (right) for a) UC, b) PCC1 and c) PCC2 membranes; dotted zones correspond to O_2 and CO evolutions further investigated in the indicated figure inset.

Table SE-1: O_2, CO and H_2 amounts produced by each investigated membrane

Membrane	O_2 amount produced (mL)	CO amount produced (mL)	H_2 amount produced (mL)
UC	291.2	453.8	--
PCC1	257.6	302.4	10.1
PCC2	689.9	1153.6	9.2

Figure SE-2 illustrates the O_2 and CO production rates during three temperature dwells after modification of $Q_{ox,\ tot}$ from 1.0 L/min to 0.4 L/min. After the decrease of $Q_{ox,\ tot}$, the CO production rate suddenly decreases, due to the less favorable oxidation reaction. It should be underlined that after the decrease of $Q_{ox,tot}$, the temperature measured by T4 increases by 10 °C, which is attributed to the decrease of the heat losses. At 1550 °C (T4) with $Q_{ox,\ tot}$=0.4 L/min, the O_2 decreases while the CO production rate increases to a steady state value

(0.061 µmol/cm^2/s). Decreasing the temperature to 1500 °C (T4) leads to a transient increase of the CO production rate due to thermodynamically favored oxidation reaction and a decrease of the O_2 production rate. Once the temperature stabilized at 1500 °C, the O_2 production rate increases whereas the CO production rate decreases to the steady state values. A similar behavior is observed when decreasing the temperature from 1500 °C to 1450 °C (T4).

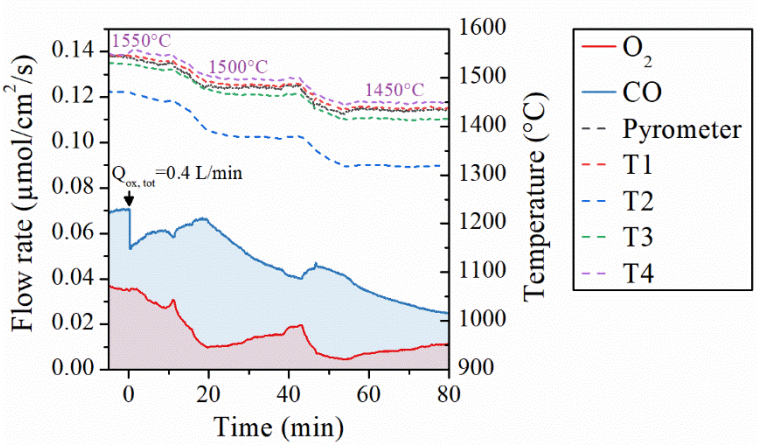

Figure SE-2: Transient evolution of O_2 and CO production rates along with reactor temperatures, during three temperature dwells at 1550 °C, 1500 °C and 1450 °C (corresponding to conditions #7, 8, 9)

Figure SE-4 illustrates the O_2 and CO production rates at 1500 °C with x_{CO2}=1.00 after modification of $Q_{ox,\,tot}$ from 0.4 L/min to 1.0 L/min, with similar x_{CO2} and temperature. During the ~40 s after the change of $Q_{ox,tot}$, a difference exists between the gas flow rate input in the membrane and the gas flow rate analyzed (Figure SE-3), due to the volume swept between the gas flow controller and the gas analyzer. Once the inlet gas has totally filled the membrane volume, the outlet CO concentration drops, due to dilution effect when increasing the inlet gas flow rate to 1.0 L/min. The gas flow sweeping the inner side of membrane is assumed to approach a plug flow model (given the tubular geometry of the system), as evidenced by the step in the CO concentration resulting from the stepwise increase of the inlet gas flow rate (03). Two distinct periods can be observed. In the first period, the gas concentration analyzed at the outlet corresponds to the previous $Q_{ox,tot}$ due to time lag. It is indicated as a hatched area in Figure SE-4. The second period corresponds to a continuous increase of the gas flow rate from initial to final total gas flow rate (grey area in Figure SE-4). In this case, it was assumed that the gas flow rate increased linearly from 0.4 L/min to 1.0 L/min to smooth the change in CO concentration due to the change of the inlet gas flow rate. The CO production rate starts to increase 30 s after $Q_{ox,tot}$ change (grey area). This sharp increase is attributed to the re-oxidation of the membrane material due to the CO:CO_2 ratio decrease and the enhancement of the oxidant gas access to the reactive surface. Then, the CO production rate slowly decreases to the stabilized value reached after ~5-6 min. In parallel, the O_2 production rate increases smoothly to the stabilized value, highlighting the enhancement of O_2 diffusivity due to $Q_{ox,tot}$ increase. Increasing the feeding gas flow rate ($Q_{ox,tot}$) in the membrane also leads to a decrease of the temperature inside the membrane (T4 decreases by 16 °C), given that the energy required to heat the injected gas increases. However, the temperature at the membrane outside presents a slight decrease (7 °C and 6 °C for temperatures measured by the pyrometer and by T1,

respectively). Therefore, the temperatures measured by the pyrometer, T1 and T4 become very similar when $Q_{ox,tot}$=1.0 L/min.

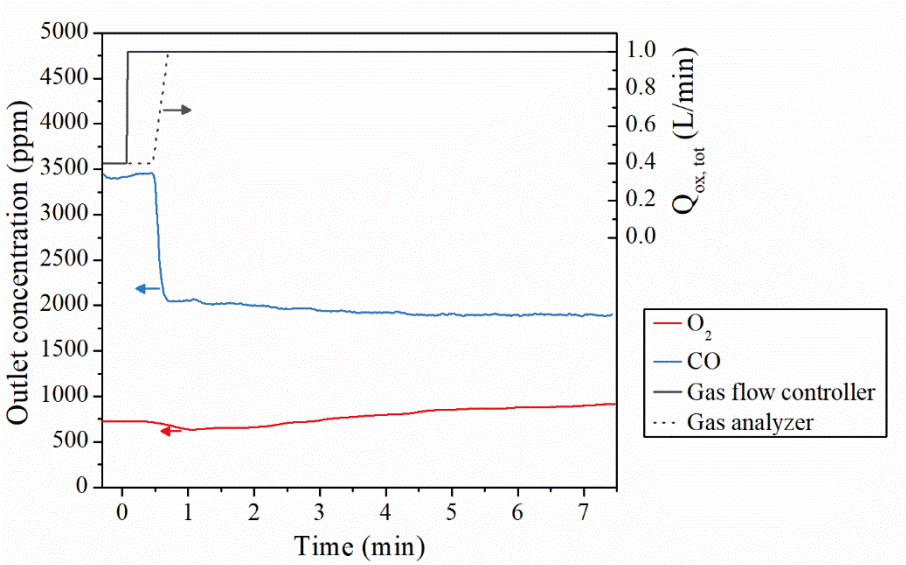

Figure SE-3: O_2 and CO proportions at 1500 °C with x_{CO2}=1.00 along with $Q_{ox,tot}$ in the gas flow controller (solid grey line) and in the gas analyzer (dotted grey line) for UC membrane (condition #5)

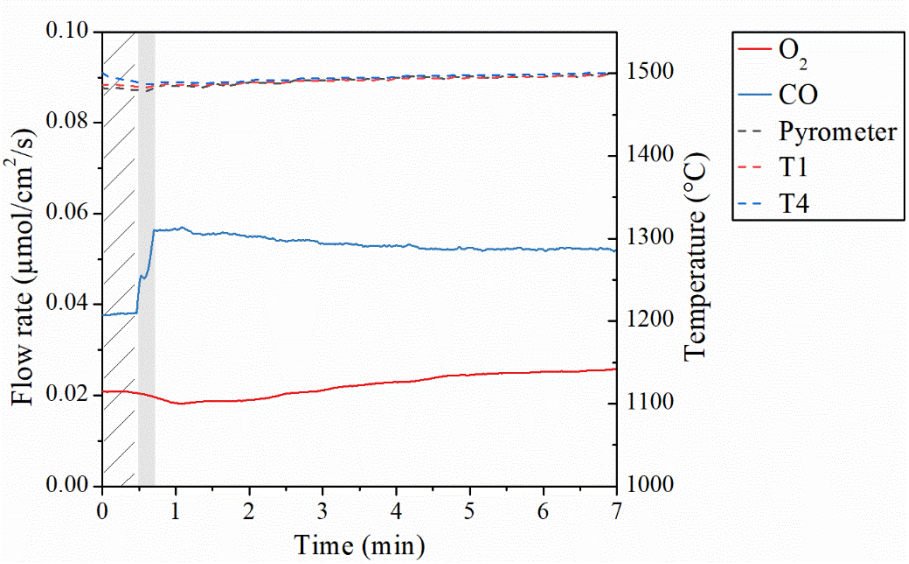

Figure SE-4: O_2 and CO evolution (solid lines) at 1500 °C with x_{CO2}=1.00 and $Q_{ox,tot}$ fixed at 1.00 L/min, along with the temperatures (dashed lines) for UC membrane (condition #5)

When the CO_2 molar fraction is modified, the oxygen flux through the membrane is not at equilibrium anymore, thus the O_2 and CO production rates evolve to reach the new steady-state values. Figure SE-5 presents the O_2 and CO production rates at 1500 °C (T4) with $Q_{ox,tot}$=0.4 L/min and x_{CO2}=1.00. The O_2 and CO production rates were previously stabilized with x_{CO2}=0.50 and similar temperature and $Q_{ox,tot}$. When the CO_2 molar fraction is increased from 0.50 to 1.00, the membrane surface is instantaneously re-oxidized, leading to a drastic increase of the CO production rate. Then, the CO production rate decreases smoothly until a stable value, higher than the one previously achieved with x_{CO2}=0.50. In the meantime, the O_2

production rate increases slowly to a stable value (half the CO production rate denoting equilibrium is achieved) due to an enhancement of oxygen diffusivity.

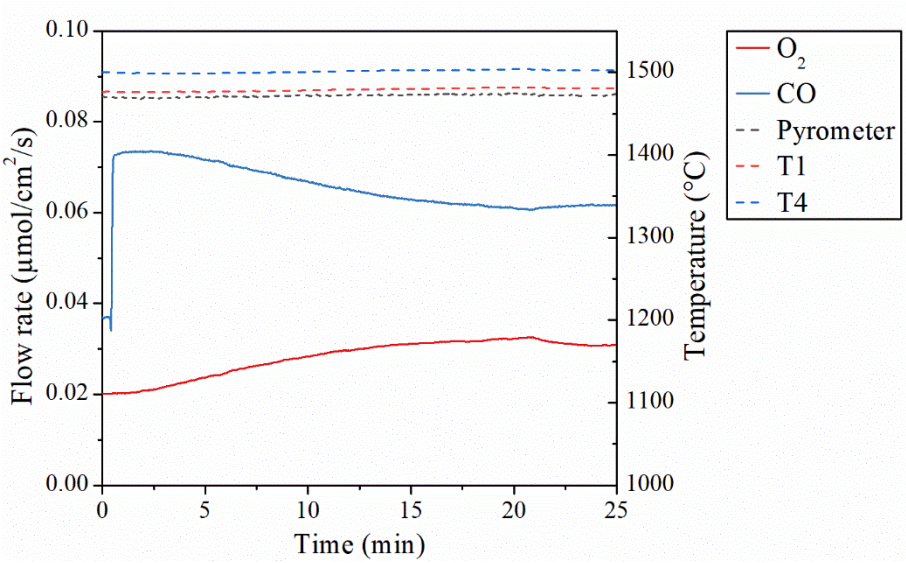

Figure SE-5: O_2 and CO evolution at 1500 °C with $Q_{ox\ tot}$=0.4 L/min after modification of the CO_2 molar fraction from 0.50 to 1.00, for PCC1 membrane

Appendix F - Résumé en français

Production de combustibles solaires par dissociation de CO_2 et H_2O via des cycles thermochimiques

F.a Introduction

Le changement et le réchauffement climatique causés par l'utilisation de combustibles fossiles pour la production d'énergie est l'un des plus grands défis auxquels l'humanité fait face. Pour résoudre ce problème, la communauté scientifique a attiré l'attention sur la nécessité de réduire les gaz à effet de serre. Par conséquent, une économie neutre en carbone doit être développée, en particulier avec une diminution drastique des émissions de CO_2 du secteur de l'énergie. En effet la production mondiale d'énergie est essentiellement basée sur la combustion de carburants fossiles, ce qui conduit à des problèmes associés à la limitation des ressources fossiles ainsi que les émissions de gaz à effet de serre dues à leur combustion. De nombreuses études se sont penchées sur la capture et la séquestration du CO_2. Cependant ces technologies sont uniquement applicables pour des émissions de CO_2 centralisées et non pour des émissions diffuses comme celles du secteur du transport, empêchant une réduction drastique des émissions de CO_2 dans l'atmosphère. De plus, l'utilisation directe de carburants renouvelables pour atteindre une économie neutre en carbone semble plus adaptée. Le dihydrogène est un vecteur énergétique intéressant car sa conversion ne produit que de l'eau. De plus, l'atome d'hydrogène est l'un des éléments les plus abondant sur la Terre, cependant il n'existe que combiné avec du carbone (hydrocarbures) ou avec de l'oxygène (eau). Par conséquent, le dihydrogène peut être produit à partir d'une grande variété de sources (eau, carburants fossiles, biomasse). Par la suite, le « dihydrogène » sera désigné par le terme « hydrogène » ou H_2 par soucis de simplification. A ce jour, la production d'hydrogène est essentiellement basée sur l'utilisation d'énergie fossile (ex : oxydation partielle ou reformage du méthane) et dans une moindre mesure, d'électricité non-décarbonée ou issue du nucléaire (ex : électrolyse). Par conséquent, des voies de production d'hydrogène durables doivent être développées. La manière la plus simple de produire de l'hydrogène à partir de ressources décarbonées, sans émissions de gaz à effet de serre, est la dissociation de l'eau en hydrogène et en oxygène. Etant donné que l'hydrogène est un vecteur énergétique, sa production nécessite un apport d'énergie qui doit aussi être durable pour obtenir une production d'énergie verte. Dans cette optique, l'énergie solaire est particulièrement intéressante car son utilisation n'implique pas d'émission de CO_2, sa source n'est pas limitée et elle accessible sur l'ensemble du globe, cependant elle est intermittente, diffuse et répartie de façon non-homogène. Par conséquent, la conversion de l'énergie solaire en énergie chimique via la production de carburants solaires permet de s'affranchir des problèmes d'intermittences à travers un stockage long-terme de l'énergie solaire en carburants chimiques. En effet, les carburants solaires peuvent être facilement stockés, transportés sur de longues distances et utilisés à la demande.

Les procédés thermochimiques réalisant la dissociation de l'eau couplés avec des systèmes à énergie solaire concentrée apparaissent comme des solutions intéressantes pour produire de l'hydrogène durable. De la même manière, ce procédé est aussi capable de dissocier le CO_2, ainsi valorisé en CO et formant du syngaz lorsqu'il est combiné à H_2, le syngaz pouvant être transformé en hydrocarbure synthétique avec le procédé Fischer-Tropsch.

Les cycles thermochimiques utilisant des oxydes métalliques sont constitués de deux étapes (Figure SF-1). Premièrement, l'oxyde métallique est réduit à haute température à l'aide d'énergie solaire produisant de l'oxygène lors de la création de lacunes en oxygène dans la maille cristallographique, comme représenté dans la réaction (54). L'énergie solaire concentrée peut être utilisée comme source d'énergie externe pour atteindre les hautes températures nécessaires à la réaction de réduction. La seconde étape est une réaction exothermique durant laquelle le matériau réactif est réoxydé par H_2O ou CO_2, comme illustré respectivement par les réactions (55.a) et (55.b). L'hydrogène ainsi produit peut être directement utilisé comme vecteur énergétique (pile à combustible par exemple), tandis que le syngaz (mélange de H_2 et CO) peut être converti en hydrocarbure liquide de synthèse via le procédé Fischer-Tropsch [253]. L'oxyde métallique n'est pas consommé lors du procédé global de dissociation de H_2O et CO_2 ; il agit comme un catalyseur de la réaction globale.

$$\mathrm{M}_x\mathrm{O}_y \rightarrow \mathrm{M}_x\mathrm{O}_{y-\delta} + \frac{\delta}{2}\mathrm{O}_2 \tag{54}$$

$$\mathrm{M}_x\mathrm{O}_{y-\delta} + \delta\mathrm{H}_2\mathrm{O} \rightarrow \mathrm{M}_x\mathrm{O}_y + \delta\mathrm{H}_2 \tag{55a}$$

$$\mathrm{M}_x\mathrm{O}_{y-\delta} + \delta\mathrm{CO}_2 \rightarrow \mathrm{M}_x\mathrm{O}_y + \delta\mathrm{CO} \tag{55b}$$

Les seuls entrants dans le procédé thermochimique sont des ressources abondantes et peu chères (H_2O et CO_2) ainsi que de l'énergie solaire, rendant le procédé neutre en carbone. Les procédés thermochimiques de dissociation de H_2O et CO_2 ont une efficacité théorique élevée et ne nécessitent pas d'utiliser de l'électricité. Par conséquent, ces procédés thermochimiques représentent une voie idéale à long terme pour décarboner la production mondiale d'énergie. A ce jour, des verrous technologiques doivent être levés pour développer à grande échelle la production de H_2 ou de syngaz par des procédés thermochimiques solaires.

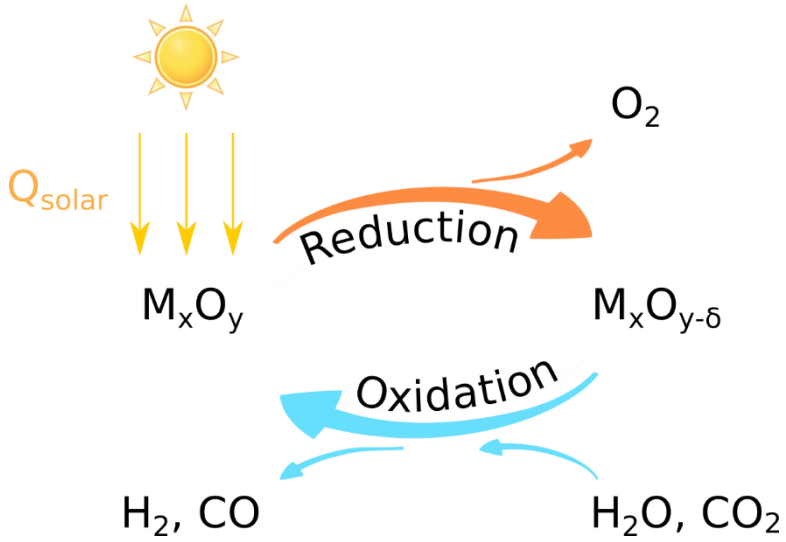

Figure SF-1 : Schéma de principe des cycles thermochimiques solaires utilisant des oxydes non-stœchiométriques

L'efficacité des cycles thermochimiques est actuellement trop faible pour une utilisation commerciale à court terme. A ce jour, en utilisant par exemple des mousses en cérine dans un réacteur de taille laboratoire, l'efficacité de conversion de l'énergie solaire en énergie chimique est de ~5% [46], alors qu'une efficacité d'au moins 20% est requise pour être concurrentielle avec l'électrolyse combinée au photovoltaïque et devenir industrialisable. Dans ce but, l'efficacité thermique du réacteur solaire ainsi que la production de carburant à partir des matériaux réactifs doivent être améliorées. L'amélioration de l'ensemble du procédé nécessite une augmentation du rendement de production de carburant ainsi que des vitesses de production, tandis que les températures de réaction doivent être réduites pour diminuer les pertes thermiques. De plus le matériau réactif employé dans les cycles thermochimiques doit être thermiquement stable pour garder une production constante de carburant au cours des cycles redox.

Cette thèse a été réalisée dans le cadre du projet SUNFUEL (N°ANR-16-CE06-0010), financé par l'Agence Nationale de la Recherche. Ce projet a pour but de développer la conversion thermochimique solaire de H_2O et CO_2 pour la production de carburants solaires à haute valeur ajoutée, en utilisant des oxydes non stœchiométriques comme intermédiaires réactifs. Associés au laboratoire PROMES-CNRS (coordinateur du projet), où cette thèse a été réalisée, l'Institut Européen des Membranes (IEM) et l'entreprise ALSYS-CTI ont été partenaires du projet SUNFUEL. Une autre thèse, réalisée en parallèle à l'IEM, a été dédiée à la préparation et la caractérisation de matériaux poreux revêtus ainsi que des membranes denses pour la production de carburant. Les différentes tâches du projet sont les suivantes :

i) évaluation d'oxydes à base de pérovskites et de cérine, comme matériaux candidats pour les cycles thermochimiques ;

ii) synthèse de matériaux réactifs sous forme de structures poreuses ou de membranes denses ;

iii) conception et construction de prototypes de réacteurs solaires flexibles selon deux concepts et modes opératoires différents :

- configuration monolithique pour réaliser des cycles redox avec une variation de température,
- configuration membrane utilisant une membrane conductrice mixte ions/électrons pour un fonctionnement continu et isotherme.

L'objectif principal du projet était de démontrer le procédé de dissociation de CO_2 et H_2O en utilisant les deux configurations de réacteur solaire et de comparer les performances des deux réacteurs. L'entreprise ALSYS-CTI était en charge de fournir les matériaux réactifs sous forme de mousses cylindriques et de membranes tubulaires, tandis que le laboratoire IEM était responsable de la réalisation des couches poreuse et denses de pérovskites, de la caractérisation et l'optimisation des propriétés des matériaux et de l'étude des mécanismes de transport de l'oxygène dans les membranes densifiées. L'étude détaillée des performances thermochimiques des matériaux redox intégrés dans les réacteurs solaires développés a été réalisée par le laboratoire PROMES-CNRS.

Ce manuscrit de thèse se concentre sur l'étude et l'optimisation de la production de carburants solaires par dissociation de CO_2 et H_2O en utilisation des matériaux redox non-stœchiométriques comme porteurs d'oxygène. Les différents points clefs impliqués dans les procédés thermochimiques ont été étudiés, incluant : la composition chimique et la microstructure/morphologie des porteurs d'oxygène, le design des réacteurs et les conditions opératoires contrôlant les performances du procédé solaire en fonction de la configuration (cycles redox avec variation de température versus thermolyse isotherme utilisant une membrane conductrice d'oxygène).

F.b Etat de l'art

F.b.1 Cérine et dopants associés

La cérine est considérée comme le matériau de référence pour les cycles thermochimiques en raison i) de sa capacité à produire des lacunes en oxygène tout en maintenant sa structure cristallographique sur une large gamme de conditions et ii) de son oxydation thermodynamiquement favorable. Cependant son taux de réduction limité restreint la production de carburant. Afin d'améliorer sa réductibilité, de nombreux dopants ont été étudiés qui augmentent la mobilité de l'oxygène au sein de la cérine. Les dopants les plus prometteurs sont les cations Zr^{4+}, Hf^{4+} et Sc^{3+}, leur incorporation étant généralement bénéfique à la réaction de réduction, en augmentant la quantité d'oxygène produite (Figure SF-2). Cependant, cela a généralement un effet négatif sur l'étape d'oxydation avec une diminution à la fois du taux et de la vitesse de réoxydation. Le processus de dopage avec des cations nécessite d'être très vigilant à la solubilité, au diagramme de phases et à la stabilité de la phase formée.

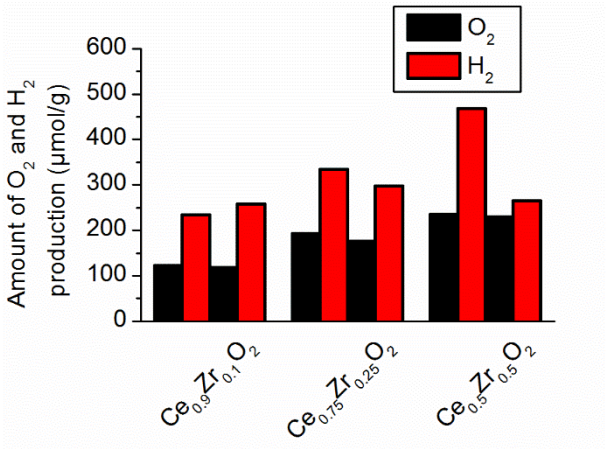

Figure SF-2 : Quantités de O_2 et H_2 produites durant deux cycles thermochimiques utilisant de la poudre $Ce_{1-x}Zr_xO_2$ (x=0.1, 0.25 et 0.5) avec des température de réduction et d'oxydation de 1400 °C et 1050 °C respectivement [93]

F.b.2 Pérovskites

Les pérovskites sont des matériaux prometteurs pour la production de carburants solaires par voie thermochimique. Ces matériaux ont une importante stabilité thermique et une non-stœchiométrie accessible permettant d'importants échanges en oxygène. De plus, leur température de réduction peut être abaissée par rapport à la cérine, tout en conservant une bonne capacité de production de carburant. Le principal inconvénient associé à l'utilisation des pérovskites, est le faible taux de réoxydation obtenu, causé par la faible cinétique réactionnelle et les limitations thermodynamiques. Les nombreuses possibilités de formulation de pérovskites et la découverte de nouveaux matériaux permettent d'ajuster les propriétés redox afin d'optimiser les productions de carburant. Les pérovskites composées de lanthane-manganèse, lanthane-cobalt, yttrium-manganèse associées à différents dopants (Al, Ga, Ba, Mg, Sr, Ca, Ce, Cr, Fe) sont les principaux matériaux utilisés pour les cycles thermochimiques.

F.b.3 Morphologie et microstructure des matériaux réactifs

Un autre paramètre influençant les productions de combustible est la morphologie associée à la mise en forme du matériau réactif. Différentes morphologies ont été étudiées dans la littérature, comme des fibres, des feutres, des poudres nanostructurées et des mousses réticulées (avec une ou plusieurs échelles de porosité). Les fibres et les feutres offrent d'importantes surfaces d'échange qui favorisent la réaction d'oxydation. Cependant, l'absorption du rayonnement solaire dans le volume de ces matériaux est faible, et conduit à des gradients de température importants dans les matériaux qui limitent l'efficacité de l'étape de réduction. A l'opposé, les mousses poreuses réticulées, avec des pores de taille millimétrique permettent une bonne absorption des radiations solaires, ce qui favorise l'étape de réduction. Toutefois, l'oxydation est limitée par la faible surface spécifique. Pour améliorer les vitesses d'oxydation, des pores de taille micrométrique peuvent être introduits dans la structure des mousses. Ceci permet d'augmenter la surface spécifique en conservant l'absorption volumétrique du flux solaire. Les poudres nanostructurées présentent une importante surface spécifique ce qui promeut l'étape d'oxydation (Figure SF-3), mais la nanostructure a une propension à être endommagée à haute température. De plus, le procédé de mise en forme requiert une étape supplémentaire pour la préparation de matériaux adaptés à une intégration dans les réacteurs, ce qui peut impacter l'aspect économique du procédé. Le design optimal ainsi que la stabilité thermique des matériaux réactifs avec des morphologies et des

microstructures contrôlées représente un défi pour une implémentation industrielle à large échelle dans des réacteurs solaires utilisant des températures élevées pour la production de carburant.

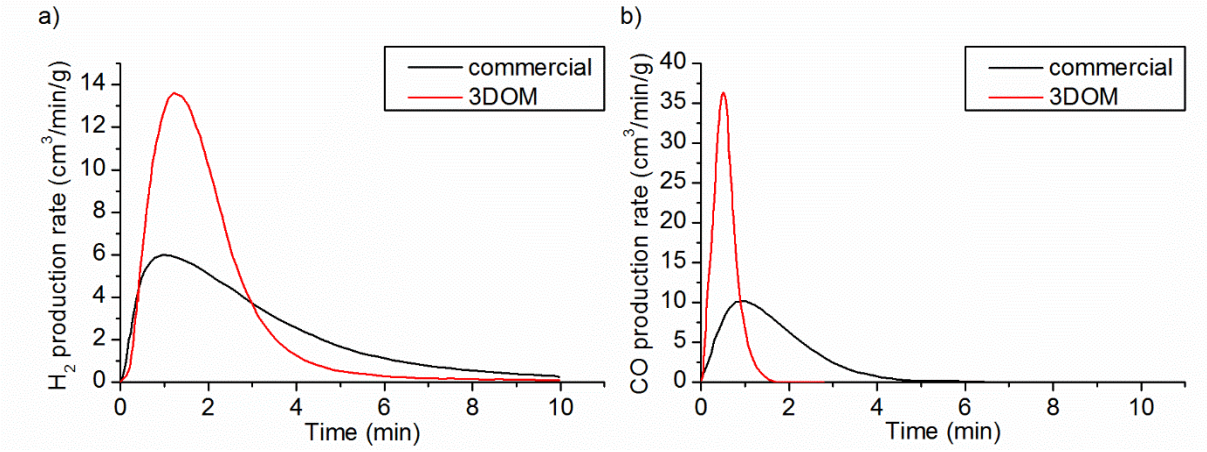

Figure SF-3: Comparaison de performances entre des structures ordonnées 3D (3DOM) et des poudres commerciales de cérine CeO_2 : a) vitesse de production de H_2 et b) vitesse de production de CO, avec une oxydation à 1100 °C [163]

F.c Sélection de matériaux réactifs appropriés aux cycles thermochimiques

Une large gamme de compositions de matériaux a été testée dans cette étude pour identifier les matériaux adaptés aux cycles thermochimiques.

F.c.1 Méthode de synthèse des poudres

Premièrement, l'influence des paramètres de synthèse de la méthode Pechini modifiée utilisée pour la préparation des poudres réactives a été étudiée. Il a été mis en exergue qu'un large excès de citrate (méthode P2) conduit à une augmentation de l'aptitude au frittage des poudres, ce qui est approprié pour réaliser des couches supportées poreuses bien consolidées et des membranes denses. Par contre, la méthode P1 , qui utilise une quantité de citrate stœchiométrique, s'avère plus adaptée à la synthèse de matériaux réactifs stables pour les cycles thermochimiques, dus à leur faible aptitude au frittage [182].

F.c.2 Etude de la composition des poudres

Il a été démontré que dans les pérovskites $A_{1-x}Sr_xMnO_3$, les cations Sm^{3+} et Pr^3 sur le site A permettent d'augmenter le taux de réduction en comparaison avec La^{3+}, mais le taux de réoxydation n'est lui pas amélioré. Le taux de substitution de Sr^{2+} impacte le taux de réduction car cela modifie l'état d'oxydation de Mn. Parmi les pérovskites lanthane-manganèse, le dopant Ca^{2+} sur le site A permet d'augmenter la quantité d'oxygène produit par rapport à Sr^{2+} mais pas la quantité de carburant. Pour $La_{1-x}Sr_xMnO_3$ (LSM), l'incorporation des dopants Ga^{3+}, Al^{3+} et Mg^{2+} sur le site B, conduit à une augmentation des quantités d'oxygène et de carburant produits. Par contre, le dopage avec Cr ou Al/Cr est néfaste pour les performances thermochimiques de LSM (Figure SF-4).

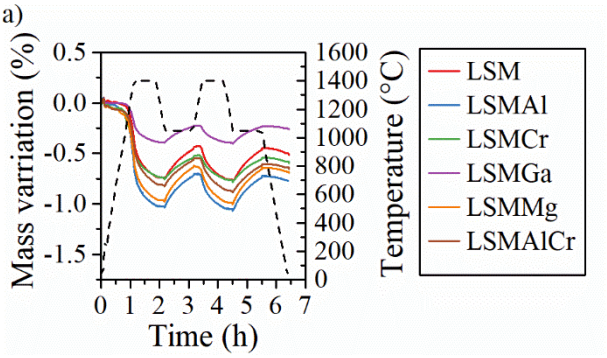

Figure SF-4: Analyses thermogravimétriques de $La_{0.5}Sr_{0.5}Mn_{1-y}B_yO_3$ lors de 2 cyclages redox (avec B=Ga^{3+}, Al^{3+}, Cr, Cr/Al et Mg^{2+})

Concernant la cérine dopée, l'augmentation du taux d'incorporation de Zr^{4+} améliore le taux de réduction. La concentration optimale de Zr^{4+} s'établit autour de 15% car cela augmente à la fois les taux d'oxygène et de carburant produits.

F.c.3 Cinétique et thermodynamique des cycles thermochimiques

Il a été mis en évidence que l'énergie d'activation de la réaction de réduction de LSMMg est corrélée au taux de réduction du matériau réactif. De plus, l'énergie d'activation augmente avec l'augmentation de la non-stœchiométrie lors de la progression de la réaction de réduction, comme illustré par la Figure SF-5. Cependant la cinétique de réduction ne permet pas d'anticiper le taux et la vitesse de réoxydation, ce qui est aussi un facteur déterminant pour l'adéquation d'un matériau dans les cycles thermochimiques.

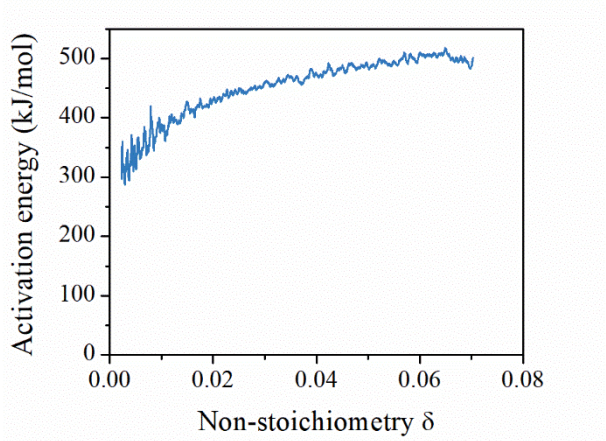

Figure SF-5: Evolution de l'énergie d'activation de la réaction de réduction en fonction de la non-stœchiométrie (δ) de l'oxyde $La_{0.5}Sr_{0.5}Mn_{0.9}Mg_{0.1}O_{3-\delta}$

Par la suite, la détermination des propriétés thermodynamiques a permis de prévoir les taux de réduction et de réoxydation théoriques, bien que les valeurs expérimentales puissent être plus faibles que les valeurs déterminées à l'équilibre thermodynamique en raison de limitations cinétiques. Par conséquent, il est essentiel de combiner des études cinétique et thermodynamique, afin d'obtenir l'aperçu le plus complet du comportement redox du matériau sélectionné.

F.c.4 Evaluation des performances thermochimiques de structures poreuses réticulées en cérine dans un réacteur monolithique

La capacité du réacteur monolithique SUNFUEL (Figure SF-6) à réaliser des cycles thermochimiques en deux étapes avec des mousses réactives à porosité ouverte en cérine a été démontrée. Une étude exhaustive des paramètres opératoires du réacteur a été réalisée pour identifier les conditions optimales permettant de maximiser la production de carburant. La flexibilité du réacteur a été évaluée en testant des conditions opératoires nombreuses et variées. La robustesse du procédé solaire a été démontrée par l'utilisation du système sur des durées prolongées à hautes températures sous flux solaire concentré. Des vitesses et des taux de production élevés ont été atteints avec des mousses préparées par ALSYS-CTI, ayant une absorption solaire volumique via des pores ouverts de taille millimétrique et des microstructures poreuses adaptées favorisant des réactions de surface solide-gaz. De plus, ces mousses ont démontré une bonne stabilité de leurs performances thermochimiques.

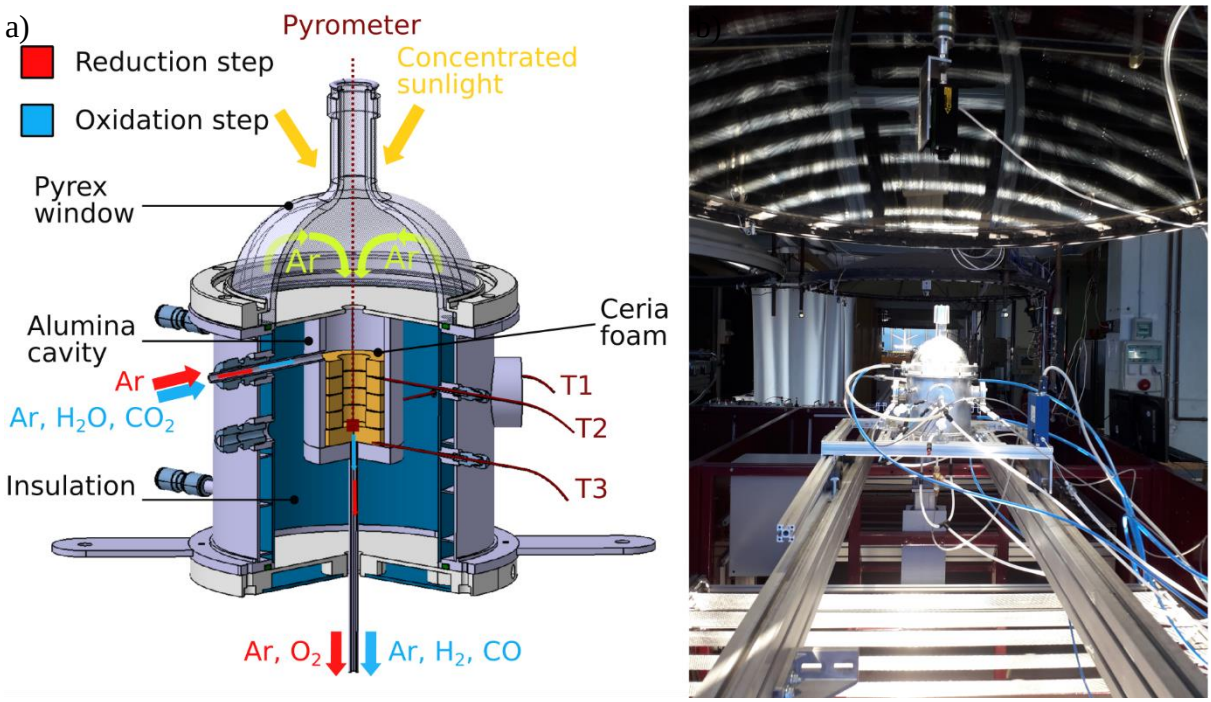

Figure SF-6: a) Schéma illustratif du réacteur solaire monolithique de 1.5 kW développé pour la production de H_2 ou de CO par des cycles redox avec de la cérine produisant H_2 et CO ; b) photographie du réacteur solaire SUNFUEL en fonctionnement

F.c.5 Influence des conditions opératoires de la configuration monolithique

D'après la thermodynamique, la non-stœchiométrie en oxygène atteinte par le matériau réactif dépend de la température et la pression partielle en oxygène. L'augmentation de la température de réduction améliore significativement le taux de réduction du matériau réactif, par conséquent la quantité de carburant produit est aussi améliorée (Figure SF-7). Cependant la température ne peut être augmentée indéfiniment car il y a un risque de sublimation du matériau réactif pour les températures trop élevées. L'impact de la pression totale lors de la réduction a été étudié, et il a pu être observé que la diminution de la pression permet aussi d'augmenter les quantités d'oxygène et de carburant produits. En effet, la diminution de la pression totale permet de diminuer la pression partielle d'oxygène, ce qui favorise thermodynamiquement la réaction de réduction. Le débit d'argon lors de l'étape de réduction a aussi été étudié, il a été observé que son augmentation

améliore la non-stœchiométrie finale atteinte, dû à la diminution de la pression partielle en oxygène. Cependant diminuer la pression partielle d'oxygène en baissant la pression totale apparait plus favorable que d'augmenter le débit d'argon car des débits trop élevés d'argon sont nécessaires pour diminuer significativement la pression partielle d'oxygène lors de la réduction.

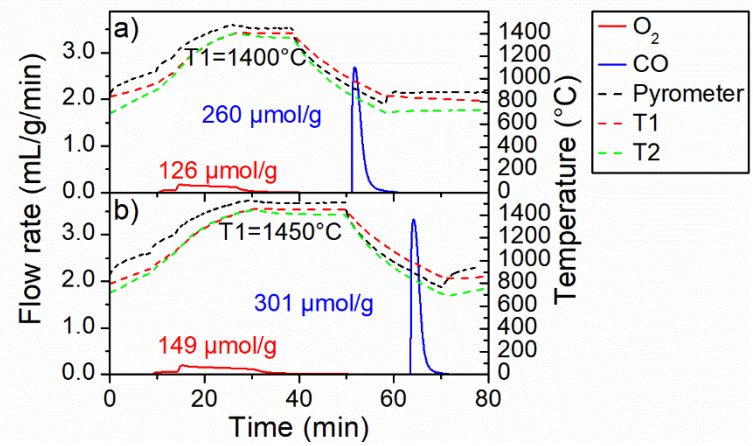

Figure SF-7: Evolution des vitesses de production de O_2 et CO associées à la température pour deux cycles thermochimiques avec une température de réduction de a) 1400 °C et b) 1450 °C sous pression atmosphérique avec une mousse en cérine (CF-20)

Concernant l'étape d'oxydation, les influences de la fraction molaire d'oxydant, des débits de gaz, du type de gaz oxydant et de la température sur les quantités de carburant produit ainsi que les cinétiques de réaction ont été étudiées. Il a été démontré que la diminution de la température permet d'augmenter les cinétiques d'oxydation, en raison d'une réaction d'oxydation thermodynamiquement favorisée par la baisse de température. De plus, un régime isotherme est moins favorable à l'étape d'oxydation qu'un refroidissement libre, bien que ce dernier augmente la différence de température entre les étapes d'oxydation et de réduction. L'augmentation de la fraction molaire de CO_2 améliore significativement la cinétique de l'étape d'oxydation en augmentant le pic de production en CO tout en diminuant la durée de réaction (Figure SF-8). Cela peut être attribué au ratio CO:CO_2 qui diminue avec l'augmentation de la fraction molaire de CO_2 et à un accès amélioré du gaz oxydant à la surface réactive, favorisant ainsi l'étape d'oxydation. Concernant le type de gaz oxydant, la dissociation du CO_2 est plus favorable que la dissociation de H_2O. Cependant elle nécessite un apport d'énergie supplémentaire pour séparer CO de CO_2 en sortie alors que la séparation de H_2 de H_2O est plus simple et donc peu couteuse. L'augmentation du débit total de gaz oxydant contribue aussi à améliorer la cinétique de la réaction d'oxydation. Une vitesse de production de CO de 9,9 mL/min/g a été atteinte en optimisant les conditions opératoires, dépassant significativement les vitesses de production de CO précédemment reportées dans la littérature.

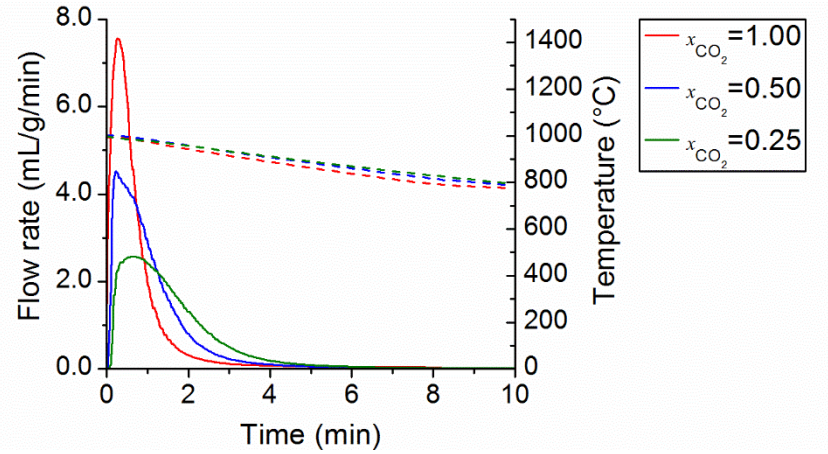

Figure SF-8: Evolution de la vitesse de production de CO pour trois fractions molaires de CO_2 avec une mousse en cérine (CF-10)

F.c.6 Influence des structures poreuses utilisées comme matériaux réactifs

Différentes mousses réactives à porosité ouverte ont été testées. Aucune différence significative des performances thermochimiques n'a été observée avec les mousses 10 ppi et 20 ppi (nombre de pores par pouce), tandis qu'un gradient axial de la taille des pores induit une intensification des gradients thermiques mais sans impacter les taux de carburant produit. Des mousses en cérine avec un revêtement pérovskites ont été étudiées et l'intérêt des revêtements $La_{0.5}Sr_{0.5}Mn_{0.9}Mg_{0.1}O_3$ (LSMMg) et $Ca_{0.5}Sr_{0.5}MnO_3$ (CSM) sur les performances thermochimiques a été prouvé. Les deux revêtements améliorent l'échange en oxygène des matériaux à composition biphasique durant l'étape de réduction en comparaison avec les deux compositions prises individuellement. La mousse de cérine revêtue de LSMMg permet d'améliorer les quantités de carburant produit dans des conditions opératoires adaptées en comparaison avec une mousse en cérine pure (Figure SF-9). Par contre, la mousse en cérine revêtue de CSM présente une diminution du taux de production de CO. Pour les deux mousses en cérine revêtues, les vitesses de production de carburant sont plus faibles que celles obtenues pour la cérine pure en raison de l'effet barrière du revêtement sur la diffusion des espèces gazeuses.

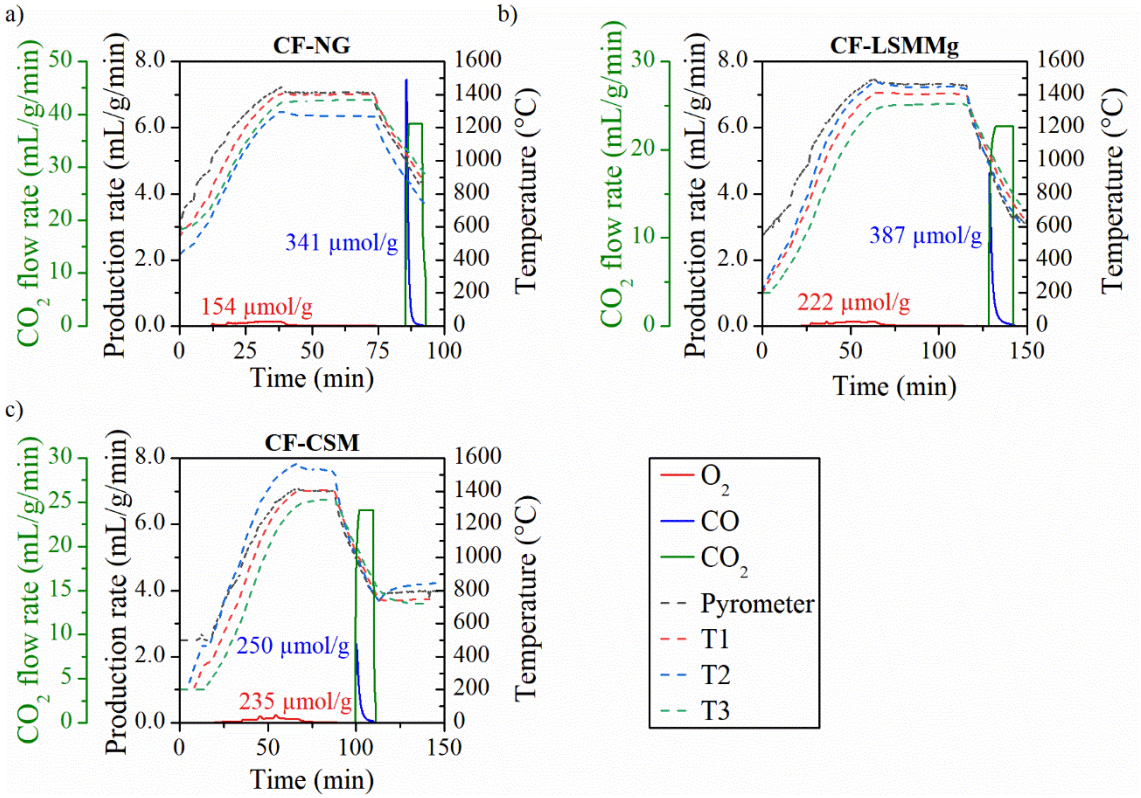

Figure SF-9 : Cycles thermochimiques réalisés à T~1400 °C sous 0.100 bar (étape de réduction) suivi d'une oxydation commençant à 1050 °C sous 100% de CO_2 pour a) mousse en cérine pure (CF-NG), b) mousse en cérine revêtue de LSMMg (CF-LSMMg) et c) mousse en cérine revêtue de CSM (CF-CSM)

Des mousses en cérine à géométrie ordonnée préparées par fabrication additive (technique de réplication utilisant des supports polymère 3D imprimés) ont aussi été étudiées dans le réacteur solaire. La géométrie ordonnée permet d'augmenter le taux de réduction par rapport à des mousses non ordonnées dans des conditions similaires. Cependant, l'étape d'oxydation n'est pas améliorée par la géométrie ordonnée. En effet la réoxydation est incomplète, et ceci peut être attribué à la méthode de synthèse qui génère une microstructure différente. De plus, la densité des structures ordonnées est plus faible que celle des mousses réticulées, diminuant ainsi la quantité de matériau réactif chargée dans la cavité. L'addition de porogène naturel (particules de bois) durant la synthèse améliore significativement les vitesses de production de carburant, comme illustré par la Figure SF-10. Ceci est attribué à l'augmentation du nombre des pores de taille micrométrique. Les performances du réacteur peuvent être encore améliorées en optimisant la géométrie des mousses en cérine, la taille des pores et les microstructures pour maximiser l'absorption des radiations solaires et obtenir un chauffage uniforme.

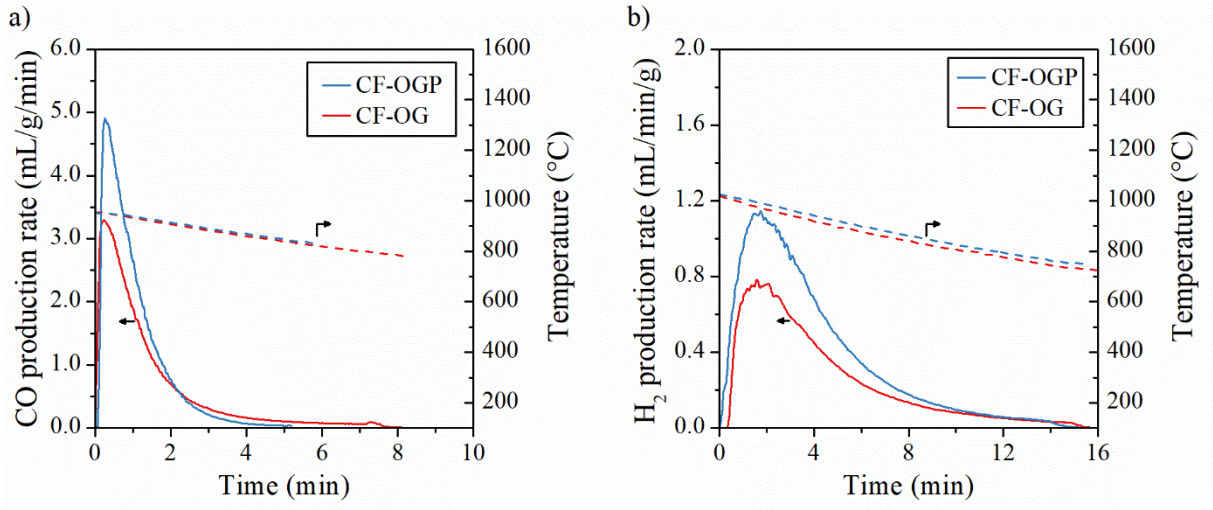

Figure SF-10 : Comparaison des performances des mousses en cérine à géométrie ordonnée avec (CF-OGP) et sans (CF-OG) porogène : a) Vitesse de production de CO avec une oxydation commençant à 950 °C et b) vitesse de production de H_2 avec une oxydation commençant à 1050 °C

F.d Cyclage redox solaire de matériaux particulaires structurés en cérine dans des réacteurs solaires à chauffage direct et indirect

Les performances d'une série de matériaux réactifs en cérine avec différentes morphologies et microstructures ont été comparées pour la production de CO et H_2 en réacteur solaire. Ces matériaux, présentés sur les Figures SF11-SF12, sont notamment des particules imitant la structure du liège (CTCe19), des mousses poreuses réticulées (CeF), des plaques fibreuses commerciales (CeFB), des pastilles frittés (CeP) et des microsphères poreuses (CeMS). Leurs performances thermochimiques ont été étudiées en lit fixe dans des réacteurs solaires à chauffage direct et indirect.

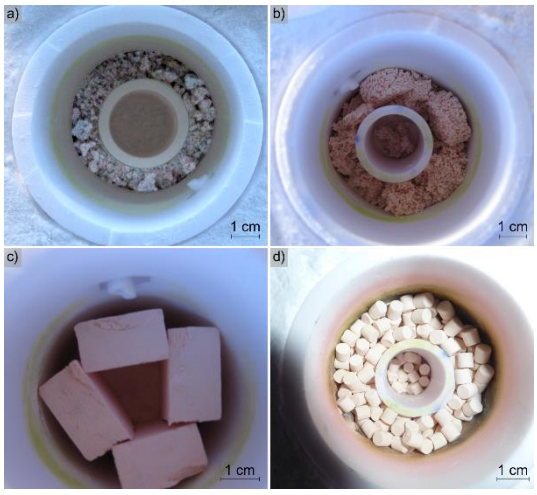

Figure S F-11: Images d'une série de matériaux réactifs en cérine testés dans le réacteur solaire : a) CTCe19, b) CeF, c) CeFB et d) CeP

Figure SF-12: Image du matériau réactif CeMS constitué de microsphères de cérine

F.d.1 Comparaison des réacteurs à chauffage direct et indirect

Les performances thermochimiques des différentes structures en cérine ont été comparées dans des réacteurs solaires à lit fixe à chauffage direct (réacteur de type cavité) et indirect (réacteur tubulaire). Les performances obtenues avec les deux réacteurs sont similaires. Pour CTCe19, on obtient par exemple 63 µmol/g de O_2 et 126 µmol/g de CO dans le réacteur indirect contre 67 µmol/g de O_2 et 125 µmol/g de CO dans le réacteur solaire à chauffage direct. Cependant, l'efficacité de la conversion d'énergie solaire-en-carburant est meilleure dans le réacteur à chauffage direct, car une quantité plus importante de matériau réactif est cyclée pour une puissance solaire injectée similaire. En contrepartie, le réacteur à chauffage indirect permet de diminuer les problèmes de frittage causés par l'irradiation directe des matériaux réactifs. Bien évidemment, des pertes thermiques inhérentes au chauffage du tube en alumine servant d'intermédiaire au chauffage des particules, sont difficilement évitables avec un réacteur à chauffage indirect. Par conséquent, le design optimum du réacteur solaire dépend des matériaux réactifs utilisés et de leur sensibilité au frittage (particules, structures 3D, structure monolithique, etc..).

F.d.2 Comparaison des performances des matériaux

Le matériau CeFB présente le plus important taux de réduction (non-stœchiométrie en oxygène moyenne allant jusqu'à δ~0,055), conduisant par conséquent à des productions de CO importantes (> 300 µmol/g pour le premier cycle, puis diminuant par la suite, comme présenté sur la Figure SF-13). Cela est attribué à la faible conductivité thermique du matériau et à l'important gradient de température mesuré dans sa hauteur. Il a été démontré que les fibres présentes sur la surface directement irradiée atteignent des températures bien supérieures à la température ciblée (1400 °C). Ceci est cohérent avec les analyses thermogravimétriques réalisées avec une température contrôlée de 1400 °C, mettant en évidence des productions de O_2 et CO conformes à celles obtenues pour d'autres matériaux de cérine sous des conditions similaires. En outre, le déclin de la quantité de carburant produit au fil des cycles dénote d'un matériau réactif non-adapté pour obtenir des performances stables sur de nombreux cycles.

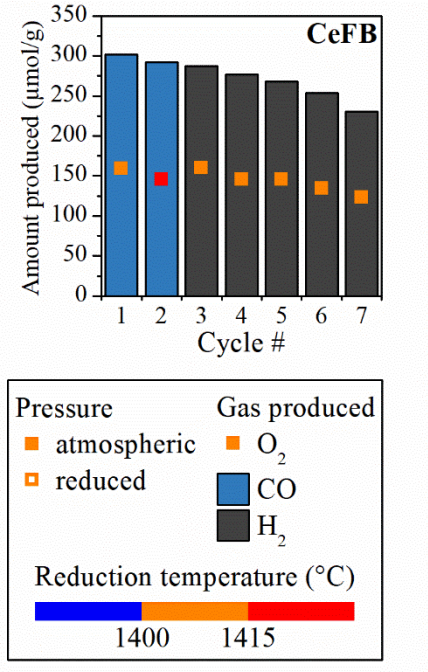

Figure SF-13: Evolution de la production de O_2 et de combustible pour CeFB au cours des cycles, les symboles carrés représentent les productions de O_2, les barres d'histogramme font référence aux quantités de carburant produit.

Les matériaux CTCe19, CeF et CeP ont une bonne résistance au frittage, sans aucun déclin de leurs performances au cours des cycles et une réoxydation complète (production de carburant de ~130 µmol/g pour une réduction à 1400 °C à pression atmosphérique, donnant δ~0,022-0,026). CTCe19 présente une vitesse de production de combustible plus importante que les autres matériaux, associée à la microstructure favorable de ce matériau céramique imitant la structure du liège. La morphologie dérivée de la structure du liège améliore l'activité redox, démontrant la pertinence d'étudier ce type de matériau pour la dissociation de H_2O et CO_2. De plus, différentes voies de synthèse pour ces éco-céramiques en cérine ont été étudiées (imprégnations multiples avec l'eau comme solvant *versus* infiltration unique avec l'acétone comme solvant). La première méthode en milieu aqueux conduit à des taux de production de carburants plus importants (74 µmol//g de O_2 et 157 µmol/g de H_2) et une vitesse de production de H_2 plus élevée (typiquement 1,4 mL/min/g) que la deuxième méthode impliquant l'acétone (respectivement, 63 µmol/g, 126 µmol/g et 1,1 mL/min/g).

Concernant les microsphères de cérine, leur structure très poreuse est attrayante, mais leur importante coulabilité conduit à l'échappement de particules réactives hors de la cavité. La production globale de combustible basée sur la masse initiale de CeMS est donc quelque peu inférieure à celle des autres matériaux testés, malgré sa structure poreuse. La géométrie uniforme des particules CeMS peut cependant être particulièrement bien adaptée pour des réacteurs à lit fluidisé, afin de favoriser l'accès du gaz oxydant à la surface réactive et ainsi la cinétique de réaction.

Enfin, il a été démontré que les pastilles commerciales (pellets) de cérine peuvent aussi être utilisées comme matériaux réactifs pour les cycles thermochimiques, étant données les vitesses de production de carburant atteintes (jusqu'à 9,5 mL/min/g), comme illustré par la Figure SF-14.

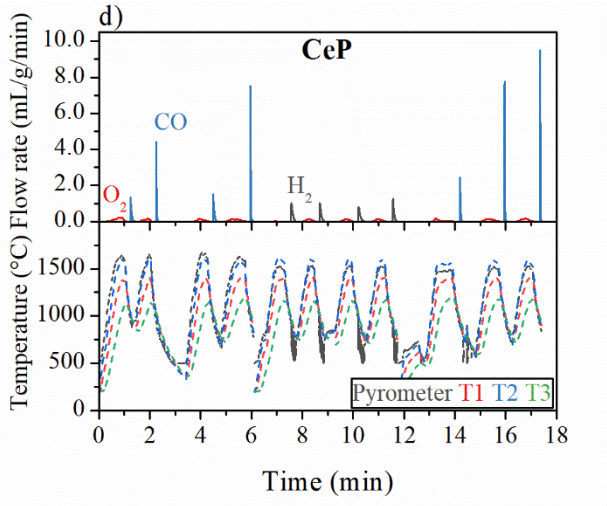

Figure SF-14 : Vitesse de production de O_2 et de carburants, avec les températures associées, pour CeP

F.e Réacteur solaire membranaire pour la dissociation redox isotherme et continue de CO_2 et H_2O

Les cycles thermochimiques à deux étapes nécessitent une variation de la température entre les étapes de réduction et d'oxydation, effectuées en alternance. Les variations de température induisent des pertes thermiques dues aux étapes de chauffage/refroidissement, et une production discontinue de H_2 ou CO. En outre, le cyclage thermique peut endommager les composants internes du réacteur en céramique et le matériau réactif (stress thermique). Par conséquent, un procédé capable de dissocier CO_2 ou H_2O en réalisant les deux étapes simultanément est intéressant car il permet de produire des carburants solaires de manière continue et isotherme.

Une membrane conductrice mixte ionique-électronique agit comme un échangeur d'oxygène entre les deux étapes et l'oxygène est transféré via la membrane pour une production séparée de O_2 et CO (ou H_2), comme présenté sur la Figure SF-15. Le côté de la réduction est maintenu à faible pression partielle d'oxygène, et la membrane libère de l'oxygène en créant des lacunes en oxygène à sa surface. Selon la loi de Fick de diffusion, les ions oxygène absorbés à partir du CO_2 (ou H_2O) du côté oxydation de la membrane tendent à migrer vers le côté réduction pour équilibrer les lacunes en oxygène créées en surface de la membrane. Du côté oxydation, les lacunes en oxygène sont comblées par la dissociation de CO_2 (ou H_2O), produisant ainsi CO (ou H_2). Les réactions ont lieu simultanément, ce qui permet de produire des carburants solaires en continu. De plus la séparation des produits, O_2 et CO (ou H_2), par la membrane permet d'éviter toute recombinaison.

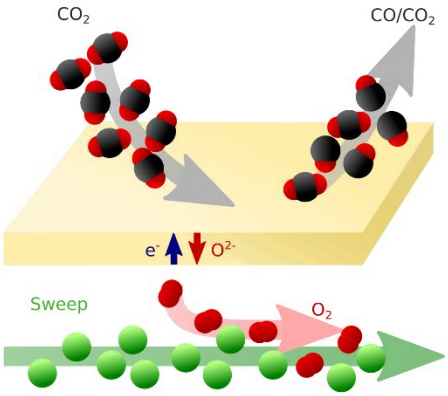

Figure SF-15: Représentation schématique de la dissociation de CO_2 avec une membrane conductrice mixte ions-électrons: le côté de la réduction est maintenu à une faible pression partielle d'oxygène par un balayage de gaz inerte pour favoriser le transfert d'ions oxygène et d'électrons à travers la membrane

Des combustibles solaires ont été produits en conditions isotherme (1500 °C) avec une seule étape de thermolyse directe activée par l'énergie solaire, en utilisant une membrane réactive en cérine ou en cérine revêtue de matériaux pérovskites (sur ses deux faces). Au total, 1,91 L de CO et 0,02 L de H_2 ont été produits, démontrant la capacité du réacteur solaire SUNFUEL à produire des carburants solaires à l'aide d'un procédé membranaire redox continu combiné avec une séparation *in-situ* des produits. Toutes les membranes testées sous forme de doigt de gant (épaisseur ~ 1,8 mm) ont été capables de produire en continu des carburants solaires, sur une durée allant jusqu'à 8,5 h. La réutilisation des membranes durant plusieurs journées s'avère possible sous réserve d'opérer un refroidissement à température ambiante lent et contrôlé (afin d'éviter les chocs thermiques).

F.e.1 Influence des conditions opératoires de la configuration membrane du réacteur solaire

L'influence des principaux paramètres opératoires du réacteur solaire en configuration membrane a été étudiée. L'augmentation de la température (dans le domaine 1450-1550 °C) améliore la vitesse de production de CO grâce à l'augmentation de la mobilité de l'oxygène à travers la membrane (Figure SF-16). L'augmentation du débit total de gaz du côté de la réaction d'oxydation de la membrane ou de la fraction molaire d'oxydant (dans le domaine 0,25-1,00) améliore la production de CO car la réoxydation de la membrane est favorisée. En résumé, la vitesse de production de carburant est favorisée à haute température, et avec un débit total de gaz et une fraction molaire d'oxydant élevés du côté de la réaction d'oxydation. La vitesse maximale de production de CO atteinte par la membrane en cérine pure est de 0,071 µmol/cm^2/s, avec un taux de conversion de CO_2 de 0,25 %. Toutefois, l'augmentation du débit total de gaz et/ou de la fraction molaire de CO_2 diminue le taux de conversion du gaz oxydant. La vitesse de production de combustible peut être encore améliorée en diminuant la pression partielle d'oxygène du côté de la réaction de réduction en utilisant soit un pompage mécanique, soit un pompage thermochimique. Concernant l'influence du gaz oxydant, la dissociation de CO_2 est plus favorable que la dissociation de H_2O. De surcroit, l'utilisation de H_2O comme gaz oxydant cause un stress thermique probablement dû à la condensation indésirable dans les parties refroidies, ce qui conduit à la fracturation des membranes. Cependant, la production de H_2 devra être étudiée plus en détail afin i) d'optimiser le fonctionnement en mode continu de la membrane et ii) de réduire les gradients thermiques le long de la membrane tubulaire.

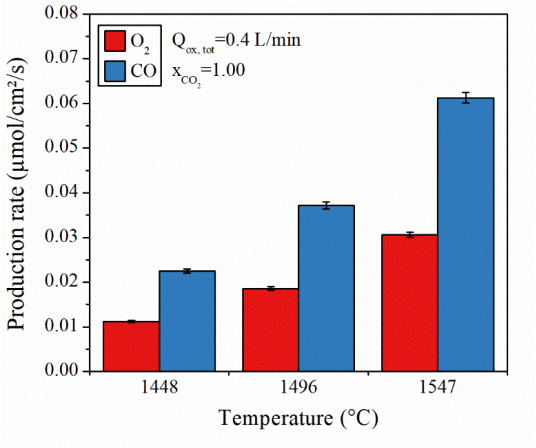

Figure SF-16: Vitesse de production de O_2 et CO pour une membrane en cérine pure pour trois températures différentes

F.e.2 Performances de membranes en cérine revêtues de couches de pérovskites

Des membranes innovantes utilisant des revêtements pérovskites ont été évaluées dans le réacteur solaire. Ces membranes sont constituées d'un support tubulaire en cérine revêtu de pérovskites. Un revêtement en CSM a été déposé sur la surface externe du support tandis qu'un revêtement en LSMMg a été déposé sur la surface interne, comme illustré sur la Figure SF-17.

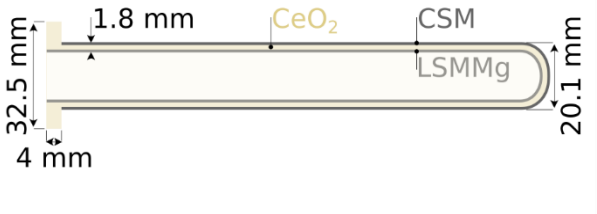

Figure SF-17: Représentation schématique d'une membrane tubulaire en cérine revêtue de pérovskites CSM et LSMMg

Les revêtements CSM et LSMMg améliorent les vitesses de production de O_2 et CO (Figure SF-18) car ils favorisent la création de lacunes en oxygène au sein de la cérine, améliorant ainsi les performances thermochimiques des membranes en cérine. La vitesse de production maximale de CO atteint 0,13 µmol/cm^2/s avec une membrane revêtue à 1550 °C (avec une fraction molaire de CO_2 de 1,00 et un débit total du côté de la réaction d'oxydation de 1 NL/min). En outre, la vitesse de production de CO dépend aussi de l'homogénéité des dépôts de pérovskites. En effet la membrane revêtue désignée PCC1 sur la Figure SF-18 offre une production 38% plus importante que celle de la membrane PCC2. Ce résultat est attribué à la meilleure homogénéité des revêtements en pérovskite. Cependant, la rupture des membranes après plusieurs heures d'utilisation, notamment après injection de vapeur d'eau et principalement à cause du stress thermique associé, souligne la nécessité d'améliorer leur résistance thermomécanique pour permettre des durées d'utilisation plus importantes.

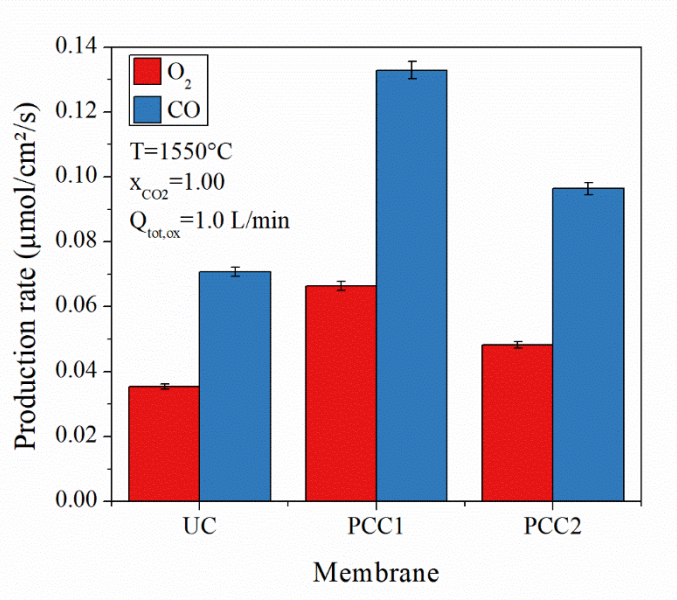

Figure SF-18: Comparaison des vitesses de production de O_2 et CO à 1550 °C, pour une membrane en cérine pure (UC) et pour deux membranes similaires en cérine revêtues de pérovskites (PCC1 et PCC2)

F.f Conclusion

Les cycles thermochimiques représentent une solution viable pour la production de carburants solaires par dissociation de H_2O et CO_2, et contribuer ainsi à atteindre une économie neutre en carbone à long terme. Ce travail a permis d'optimiser les cycles thermochimiques en étudiant les différents aspects impactant les performances thermochimiques, et notamment : la composition chimique et la morphologie des matériaux réactifs, les conditions opératoires et les configurations de réacteurs solaires utilisées.

Une étude expérimentale a été réalisée afin de sélectionner les matériaux réactifs adaptés aux cycles thermochimiques. Pour cela, l'activité redox de pérovskites et de cérine dopées a été examinée à l'aide d'analyses thermogravimétriques. De plus, des études cinétique et thermodynamique ont permis d'améliorer la compréhension des mécanismes mis en jeu lors des cycles thermochimiques. Ainsi le matériau pérovskite de formulation $La_{0.5}Sr_{0.5}Mn_{0.9}Mg_{0.1}O_3$ (LSMMg) a été sélectionné comme le plus adapté de par sa bonne réactivité et sa stabilité chimique.

Par la suite, une étude paramétrique de la configuration monolithique du réacteur solaire SUNFUEL a été réalisée. La diminution de la pression et/ou l'augmentation de la température durant l'étape de réduction améliore significativement le taux de réduction atteint par le matériau réactif. Concernant l'étape d'oxydation, l'augmentation de la fraction molaire d'oxydant ou du débit total de gaz, ainsi que la diminution de la température d'oxydation augmentent la vitesse de production de carburant.

Les mousses réticulées poreuses en cérine fournies par ALSYS-CTI ont été intégrées dans le réacteur solaire et ont permis d'obtenir la vitesse de production de CO la plus élevée (9,9 mL/min/g) dans des conditions opératoires optimales (réduction à 1400 °C avec une pression de ~100 mbar et une étape d'oxydation avec un refroidissement libre à partir de 1050 °C et sous CO_2 pur). D'autres mousses poreuses réticulées en cérine ont été revêtues avec un dépôt de

pérovskite par l'IEM pour étudier les performances thermochimiques des mousses à composition biphasique. Dans des conditions opératoires adaptées, les mousses en cérine avec un dépôt de LSMMg ont permis de produire une quantité de CO plus importante que les mousses en cérine pure, malgré une vitesse de production de CO plus faible. Cela a permis de mettre en évidence la pertinence de l'utilisation des revêtements en pérovskites dans les cycles thermochimiques. L'intérêt des mousses présentant une géométrie ordonnée pour améliorer les performances thermochimiques a été démontré, de même que l'utilisation de porogène lors de la synthèse des mousses.

Par la suite, plusieurs types de matériaux structurés en cérine sous forme divisée ont été testés en lit fixe dans des réacteurs solaires à chauffage direct et indirect pour tester leur capacité à dissocier H_2O et CO_2. D'importantes vitesses de production de carburant (9,5 mL/min/g) ont été obtenues avec des pastilles commerciales en cérine. Des microstructures alternatives comme des microsphères poreuses et des matériaux biomimétiques en cérine ont aussi été étudiées dans le réacteur solaire. Les matériaux testés présentent une bonne stabilité thermique couplée à des vitesses de production de carburant élevées (jusqu'à 3,1 mL/min/g).

Enfin, la configuration membrane du réacteur SUNFUEL a été étudiée en réalisant une étude paramétrique détaillée et en utilisant différentes membranes (en cérine pure, avec ou sans revêtements pérovskites). Pour la première fois, la dissociation redox isotherme et continue de CO_2 (et H_2O) avec une membrane conductrice en oxygène a été démontrée dans un réacteur solaire utilisant un flux solaire concentré réel. La capacité des membranes à fonctionner au cours de journées complètes sous flux solaire a été démontrée, soulignant leur capacité à résister à de très hautes températures (jusqu'à 1550 °C).

Production de combustibles solaires par dissociation de CO_2 et H_2O via des cycles thermochimiques

Résumé Cette étude se focalise sur le développement de procédés de dissociation de H_2O et CO_2 par voie thermochimique utilisant des oxydes métalliques non-stœchiométriques et l'énergie solaire concentrée pour la production de carburants solaires. Les procédés redox se décomposent en deux réactions distinctes : tout d'abord, une réduction thermique à haute température de l'oxyde métallique avec la création de lacunes en oxygène dans la structure cristallographique, entrainant une production d'oxygène ; puis, une réoxydation de l'oxyde métallique par H_2O et/ou CO_2, conduisant à la production de H_2 et/ou CO. La cérine et les pérovskites ont été étudiées comme matériaux réactifs pour les cycles thermochimiques. Pour augmenter l'efficacité des cycles, différents paramètres ont été étudiés, comme la composition chimique et la morphologie de l'oxyde réactif, les conditions opératoires, ainsi que la configuration du réacteur solaire. Dans un premier temps, les activités redox, la cinétique et la thermodynamique de différentes pérovskites ont été étudiées expérimentalement pour les cycles redox. Par la suite, les performances thermochimiques de différents matériaux réactifs sous forme de structures poreuses ou de particules ont été étudiées dans des réacteurs solaires (configuration monolithique ou lit fixe) permettant de réaliser des cycles thermochimiques en deux étapes. Une étude paramétrique détaillée a permis d'optimiser les taux et vitesses de production de combustibles. La vitesse de production de CO la plus élevée (9.9 mL/min/g) a été obtenue avec des mousses réticulées en cérine. Enfin, un réacteur solaire membranaire a été développé pour produire en conditions isothermes et en continu du CO (ou H_2) par dissociation de CO_2 (ou H_2O) avec une membrane réactive et perméable à l'oxygène. La vitesse de production la plus élevée atteint 0.133 µmol/cm^2/s à 1550 °C en utilisant une membrane en cérine revêtue de pérovskite.

Mot clés : cycles thermochimiques redox, réacteur solaire, énergie solaire concentrée, cérine, pérovskites, membrane perméable à l'oxygène.

Solar fuels production by CO_2 and H_2O splitting via thermochemical processes

Abstract This study is focused on the development of thermochemical H_2O and CO_2 splitting processes using non-stoichiometric metal oxides and concentrated solar energy to produce solar fuels. The redox process involves two distinct reactions: first, a thermal reduction at high temperature of the metal oxide with creation of oxygen vacancies in its crystallographic structure, resulting in released oxygen; second, the re-oxidation of the metal oxide by H_2O and/or CO_2, yielding H_2 and/or CO. Both ceria and perovskite materials have been investigated as reactive oxides for thermochemical cycles. To increase the process efficiency, different aspects were investigated, such as chemical composition and morphology of the metal oxide, operating parameters, and solar reactor configuration. The redox activities, kinetics and thermodynamics of different perovskite materials were first investigated experimentally for two-step thermochemical cycles. Then, the thermochemical performance of various reactive materials shaped as porous structures or particulate media were investigated in solar reactors (monolithic or packed-bed configurations) adapted for two-step thermochemical cycles. A detailed parametric study was performed to determine the fuel production rates and yields. The highest CO production rate (9.9 mL/min/g) was achieved with ceria reticulated foams. Finally, a solar membrane reactor was developed for isothermal and continuous production of CO (or H_2) by CO_2 (or H_2O) splitting with a reactive and oxygen-permeable membrane. The highest CO production rate reached 0.133 µmol/cm^2/s at 1550 °C using a perovskite-coated ceria membrane.

Keywords: two-step thermochemical cycles, solar reactor, concentrated solar power, ceria, perovskites, oxygen permeable membrane.